



**HAL**  
open science

# Grain-scale investigation of sand-pile interface under axial loading conditions using x-ray tomography

Jeanne Doreau Malioche

► **To cite this version:**

Jeanne Doreau Malioche. Grain-scale investigation of sand-pile interface under axial loading conditions using x-ray tomography. Material chemistry. Université Grenoble Alpes, 2018. English. NNT: 2018GREAI066 . tel-01968753

**HAL Id: tel-01968753**

**<https://theses.hal.science/tel-01968753>**

Submitted on 3 Jan 2019

**HAL** is a multi-disciplinary open access archive for the deposit and dissemination of scientific research documents, whether they are published or not. The documents may come from teaching and research institutions in France or abroad, or from public or private research centers.

L'archive ouverte pluridisciplinaire **HAL**, est destinée au dépôt et à la diffusion de documents scientifiques de niveau recherche, publiés ou non, émanant des établissements d'enseignement et de recherche français ou étrangers, des laboratoires publics ou privés.

## **THÈSE**

Pour obtenir le grade de

### **DOCTEUR DE LA COMMUNAUTE UNIVERSITE GRENOBLE ALPES**

Spécialité : 2MGE : Matériaux, Mécanique, Génie civil, Electrochimie

Arrêté ministériel : 25 mai 2016

Présentée par

**Jeanne DOREAU-MALIOCHE**

Thèse dirigée par **Gaël COMBE**, Professeur des Universités, UGA  
Codirigée par **Gioacchino VIGGIANI**, Professeur des Universités, UGA

préparée au sein du **Laboratoire Sols, Solides, Structures-Risques**  
dans l'**École Doctorale I-MEP2 - Ingénierie – Matériaux, Mécanique,  
Environnement, Energétique, Procédés, Production**

## **Grain-scale investigation of sand-pile interface under axial loading conditions using x-ray tomography**

Thèse soutenue publiquement le **28 Septembre 2018**,  
devant le jury composé de :

**Monsieur Pascal VILLARD**

Professeur des Universités, Université Grenoble Alpes, Président

**Monsieur J. David FROST**

Full Professor, Georgia Institute of Technology, School of Civil & Environmental  
Engineering, Rapporteur

**Monsieur Steinar NORDAL**

Full Professor, Norwegian University of Science and Technology, Department of  
Civil and Environmental Engineering, Rapporteur

**Monsieur Michel BORNERT**

Ingénieur en Chef des Ponts, Eaux et Forêts, Ecole des Ponts ParisTech,  
Examineur

**Monsieur Gaël COMBE**

Professeur des Universités, Université Grenoble Alpes, Directeur de thèse

**Monsieur Gioacchino VIGGIANI**

Professeur des Universités, Université Grenoble Alpes, Co-directeur de thèse



# Abstract

This doctoral work presents an experimental investigation into the deformation mechanisms governing the macroscopic response of sand-pile interface during monotonic installation and subsequent axial loading cycles. An innovative approach combining x-ray tomography and advanced image analysis tools is employed to extract information at different scales, including at the micro-scale. A quantitative analysis of the behavior of individual sand grains in the vicinity of the pile offers valuable three-dimensional (3D) data set against which theoretical or numerical approaches could be tested.

A series of tests is run on an instrumented close-ended conical model pile installed by monotonic jacking in a dense calcareous sand sample. Following the installation, the model pile is submitted to a large number of axial displacement-controlled loading cycles (a few thousands cycles) under constant radial stress. The tests are performed in a mini-calibration chamber that allows the acquisition of high resolution x-ray images at different stages of the loading. The chamber is admittedly not representative of field pile testing conditions for the main following reasons: the calibration chamber-to-pile diameter ratio and the sand particle-to-pile diameter ratio are far below the ratios recommended in the literature to limit scale effects on the interface response. Consequently, the results presented in this work can not, and should not, be directly extrapolated to field pile design. And yet, such a setup is able to reproduce trends similar to those obtained at the macro-scale on large-scale experiments and allows the observation of full-field mechanisms taking place at the micro-scale.

3D images resulting from the reconstruction of the x-ray scans are used to identify and follow the evolution of individual sand grains. Full-kinematics are measured thanks to a 3D Digital image Correlation (DIC) code, "TomoWarp2". Image processing tools are also employed to measure local porosity changes and the production of fines by grain crushing at the interface.

During pile installation, different zones where grains displacements concentrate are identified. A recirculation of the grains alongside the pile is also observed. Globally, the sand mass exhibits a dilative behavior except within a relatively thin layer (about 3 to  $4 \cdot D_{50}$  thickness) around the model pile where grain crushing occurs. During subsequent loading cycles, the macroscopic response of sand-pile interface shows a two-phases evolution, with a non negligible increase of shaft resistance in the latter phase. For these two phases, the measurement of grain kinematics reveals a different behavior of the sand mass associated with a significant densification at the interface. In the first phase, the sand mass contracts radially within a region of thickness  $4 \cdot D_{50}$ . This mechanism is likely due to inter-granular the collapse of the hoop stresses developed during pile installation. In the second phase, sand grains hardly move and the sand mass reaches a threshold density for which the friction on the shaft resistance increases significantly.

*To my parents*

## *Acknowledgements*

Un grand merci à mes deux encadrants qui m'ont accompagnée, soutenue, appris tellement de choses et offert leur confiance pendant presque quatre ans. Bien que très occupés et très sollicités tous les deux, ils ont toujours su être présents quand j'en avais besoin. Gaël, merci pour ta gentillesse, ta patience, ton humour et ton franc-parler parfois déconcertant. Pour la DEM, c'est sans rancune! Cino, malgré la grande qualité de mon italien, je préfère poursuivre en français. Merci d'avoir accepté une française venue de New-York avec un statut étonnant. Merci pour tes conseils avisés, ta sympathie et ta simplicité. J'ai été très heureuse, et chanceuse, de pouvoir travailler avec vous deux.

Besides my supervisors, I would like to thank my jury. Prof David Frost and Prof Steinar Nordal, Mr Michel Bornert and Prof Pascal Villard. It was an honour and a pleasure to have you as jury members. Thank you for your time, your comments and for the fruitful discussion we had about my PhD work.

Switching back to french... Merci à tous mes collègues de 3SR qui ont contribué à rendre cette aventure plus facile et agréable. Matias, Pascal, Jean-Benoît, Eddy, Christophe, Soha, merci pour votre disponibilité et votre aide quand il s'agissait de se battre avec le tomographe, les images, la mini-chambre de calibration et ces chers grains de sable Glageon. Merci à mes collègues du 330, Maxime et Thibault, pour les bons moments que nous avons partagés, pour les vidéos drôles, pour les bons goûters et surtout pour votre authenticité. Merci aux 'amis grenoblois' qui, aux quatre coins de Grenoble, de la France, voire même de l'Europe, m'ont apporté leur bonne humeur et leur soutien. Mireille, merci pour ta présence, ta sincérité, ton grain de folie et nos drôles de courses à pieds. Une belle rencontre! Merci à l'incroyable groupe cosmopolite des 'Phd seeds' qui a rendu cette expérience quelque peu déjantée, unique et inoubliable.

Merci à mes parents sans qui je ne serais pas là où je suis aujourd'hui. Ils m'ont tout appris. Ce travail, que je leur dédie, n'est qu'une infime récompense comparé à tout l'amour qu'ils me donnent chaque jour. Merci à mes frères et soeurs et à leurs enfants qui sont à eux tous une source de bonheur et d'énergie qui n'a pas de prix. Merci à ma nouvelle famille albanaise qui, même de loin, m'a apporté tout son soutien et sa gentillesse. Finalement, merci à mon collègue, à mon ami, à celui qui partage ma vie. Dorjan, merci pour ton soutien quotidien, ton grand coeur, ta prévenance et toute l'énergie que tu dépenses à rendre ma vie plus simple et plus légère. Faleminderit për gjithçka. Ti je i jashtëzakonshem. Unë jam me fat.

# Contents

<b>Acknowledgements</b>	<b>iv</b>
<b>1 Introduction</b>	<b>1</b>
<b>2 Literature review</b>	<b>4</b>
2.1 General description of cyclic loading . . . . .	4
2.2 Effect of axial cyclic loading on sand-pile interface: macroscopic observations . . . . .	5
2.2.1 Full-scale behavior . . . . .	5
2.2.2 Physical modeling . . . . .	6
2.3 Understanding the mechanisms that control the macroscopic axial cyclic response . . . . .	9
2.3.1 Local effective stress around the shaft . . . . .	9
2.3.2 Volumetric behavior and grain crushing . . . . .	11
2.4 Towards the numerical modeling of soil-pile interface: a need for micro-scale investigation . . . . .	13
<b>3 X-ray tomography and advanced image analysis tools</b>	<b>19</b>
3.1 X-ray tomography for high resolution 3D imaging . . . . .	20
3.1.1 General description of x-ray Computed Tomography . . . . .	20
3.1.2 3SR x-ray tomograph . . . . .	21
3.1.3 Optimum image acquisition settings . . . . .	22
3.1.4 3D reconstruction . . . . .	23
3.2 Image pre-processing: identification of individual sand grains . . . . .	25
3.2.1 Definition of different phases in the 3D images . . . . .	25
3.2.2 Segmentation of the 3D images and labeling of individual grains . . . . .	29
3.3 Measurement of soil density / porosity . . . . .	31
3.4 Measurements of full-kinematics thanks to 3D-Digital image Correlation . . . . .	33
3.4.1 Digital Image Correlation: general principles and methodology . . . . .	34
3.4.2 3D-Digital Image Correlation: continuum approach . . . . .	35
3.4.3 3D-Digital Image Correlation: discrete approach . . . . .	38
3.4.4 Optimal set of parameters for 3D-Digital Image Correlation . . . . .	39
3.5 Grains orientations . . . . .	40
<b>4 Physical modeling</b>	<b>43</b>
4.1 Tested material . . . . .	43
4.2 Small-scale physical model . . . . .	48
4.2.1 Description of the mini-calibration chamber . . . . .	48
4.2.2 Loading device . . . . .	48
4.2.3 Instrumentation . . . . .	49
4.3 Instrumented model pile . . . . .	50
4.3.1 Description of the model pile . . . . .	50
4.3.2 Shaft surface roughness . . . . .	51

4.4	Testing procedure . . . . .	52
4.4.1	Sample preparation . . . . .	52
4.4.2	Sample Confinement . . . . .	53
4.4.3	Pile installation . . . . .	55
4.4.4	Displacement-controlled two-ways loading cycles . . . . .	56
4.5	Comparison with field pile testing conditions and scale effects . . . . .	57
4.6	Experimental program and tests naming . . . . .	58
<b>5</b>	<b>Macroscopic response of sand-pile interface</b>	<b>61</b>
5.1	Typical response during pile installation . . . . .	61
5.1.1	Evolution of the loads applied to the pile . . . . .	61
5.1.2	Reproducibility of the results . . . . .	63
5.1.3	Typical response when the loading is stopped for image acquisition . . . . .	66
5.2	Typical evolution of tip and shaft resistance during loading cycles . . . . .	67
5.2.1	Identification of two different phases in shaft resistance evolution. . . . .	67
5.2.2	Problems encountered with the instrumentation of the model pile. . . . .	70
5.3	Influence of the amplitude of displacement applied during loading cycles . . . . .	71
5.3.1	Influence of the amplitude on the two phases in shaft resistance evolution . . . . .	71
5.3.2	Variation of the amplitude within a single test . . . . .	74
5.4	Effect of boundary conditions . . . . .	81
5.5	Cyclic response of a molded pile . . . . .	83
5.6	Conclusions . . . . .	83
<b>6</b>	<b>Image-based analysis of sand-pile interface</b>	<b>85</b>
6.1	Image analysis data reporting . . . . .	85
6.2	Mechanical processes during pile installation . . . . .	87
6.2.1	Soil displacement pattern during pile installation . . . . .	87
	Global behavior of the soil: continuum DIC . . . . .	87
	Characterization of different zones of displacements around the pile: discrete DIC . . . . .	88
6.2.2	Grains orientations . . . . .	90
6.2.3	Volumetric and shear behaviors . . . . .	94
6.2.4	Grain crushing . . . . .	96
6.3	Mechanical processes during cyclic loading . . . . .	98
6.3.1	3D displacement fields . . . . .	98
6.3.2	Porosity changes . . . . .	102
6.3.3	Grain crushing . . . . .	105
6.4	Behavior of sand-pile interface across the scales: discussion . . . . .	108
6.5	Conclusions . . . . .	109
<b>7</b>	<b>Summary, conclusions &amp; perspectives</b>	<b>111</b>
7.1	Summary . . . . .	111
7.2	Conclusions . . . . .	111
7.2.1	Macro-scale observations . . . . .	111
7.2.2	Image-based analysis . . . . .	112
7.3	Perspectives . . . . .	113
	<b>Bibliography</b>	<b>115</b>

# List of Figures

2.1	Schematic illustrating the characteristic parameters of cyclic loading, from Tsuha et al. (2012) . . . . .	5
2.2	Main features of a cyclic stability diagram, after Poulos (1989) . . . . .	5
2.3	Interaction diagram for full-scale piles, from Jardine and Standing (2000). Numbers within the graph area represent the number of cycles for each test . . . . .	6
2.4	a) Shaft capacity measured during monotonic loading, prior to and after cyclic loading and b) evolution of lateral shaft friction with the number of cycles, after Bekki et al. (2014)	8
2.5	Degradation of stationary horizontal stress with cycling at during load tests: (a) one-way compression load test; (b) two-way compression-tension load test, after White and Lehane (2004) . . . . .	9
2.6	Scheme of multiple yield surface, from Tsuha et al. (2012) . . . . .	10
2.7	Schematic explaining the different phases in shaft friction evolution in the case of low consolidation stress, from Bekki et al. (2013) . . . . .	12
2.8	Schematic development of concentric zones around the pile shaft involving different degrees of particle crushing and their relationship to stress regime (not to scale), from Yang et al. (2010) . . . . .	13
2.9	a) Moulding of the sand before extraction, b) frozen sample, and c) slice showing fine particles at the interface obtained by x-ray tomography, after (Silva et al., 2013) . . . . .	13
2.10	Comparison of numerical circumferential stresses at $h/R = 0.5$ level above the tip during penetration and experimental results obtained by Jardine et al. (2013), from Zhang et al. (2014) . . . . .	14
2.11	a) Maximum coordination number for a particle to be able to break; loading conditions on a particle assumed to be equivalent to the one of a diametrical compression test; configuration after breakage and b) Evolution of average radial stresses in representative cycles: strain (-0.1, +0.1%), from Lobo-Guerrero and Vallejo (2005) . . . . .	15
2.12	a) View of the virtual calibration chamber and the model pile. b) Contact normal forces exceeding average normal force (the lines thickness is proportional to the magnitude of the normal force), from Butlanska et al. (2014) . . . . .	16
2.13	a) Configuration of soil tank and pile; b) Incremental soil displacements at the end of the given cycle (mm): strain (-0.1, +0.1%), 1st-50th cycles; c) Evolution of average radial stresses in representative cycles: strain (-0.1, +0.1%), after Cui and Bhattacharya (2016) . . . . .	17
2.14	Schematic illustration of the hierarchical computational framework for multi-scale modeling of granular material, from Zhao (2008) . . . . .	18
3.1	a) 3SR x-ray device including the cabin and the control panel. b) Setup installed in front of the x-ray source within the cabin . . . . .	22
3.2	JIMA calibration chart used for the selection of the optimum spot size . . . . .	23
3.3	Example of 3D-reconstructed images after pile installation a) in global tomography and b) in local tomography . . . . .	24

3.4	Horizontal slice taken through a 3D reconstructed image recorded in local tomography: a) before the correction of the misalignments and b) after correction in X-Act . . .	25
3.5	Illustration of beam hardening artifact on a horizontal slice a) in global tomography and b) in local tomography . . . . .	26
3.6	Illustration of the definition of the different phases in a gray image: a) Image subset (2D, 16 bit) recorded in local tomography showing grains, pores and fines. The same subset displayed with a different color scale helps differentiating the three phases (grains: red, pores: blue, fines: green). b) Histogram associated with the image subset indicating the two threshold values selected manually to isolate each phase . . . . .	27
3.7	Result of the multiplication between the original gray-scale image subset and the binary masks created for each phase: a) voids, b) fines and c) grains . . . . .	28
3.8	Selection of a manual threshold to identify (and next separate) grains in the framework of discrete DIC. a) Histogram showing the manual threshold and the Otsu threshold. b) Differences between the binary data produced with Otsu and manual threshold values: red circles show the difference in the size of the contacts between grains and the blue stars show that with a manual threshold the grain phase is intentionally underestimated . . . . .	28
3.9	Image subsets taken from x-ray images recorded in local tomography, with a voxel size of $40 \mu\text{m}$ . Different fractions of silica sands were imaged: a) $D_{50} = 2.4\text{mm}$ , b) $D_{50} = 1.5\text{mm}$ , c) $D_{50} = 1.0\text{mm}$ , d) $D_{50} = 650\mu\text{m}$ and e) $D_{50} = 338\mu\text{m}$ . The first row shows the raw gray-scale image subsets. The second row shows the binarized image subsets. The third row shows a zoom in the binary data to highlight the poor quality of the binary data when decreasing the mean particle size . . . . .	29
3.10	Diagram showing the segmentation process on a sub-volume. a) Gray-scale sub-volume and a 2D slice taken from it. b) Sub-volume and slice after binarization. c) Sub-volume and slice segmented and labeled showing a grain split into two particles (over-segmentation). d) 2D Euclidean distance map of the binarized slice displayed as a landscape and zoom showing two possible local maxima detected as markers for watershed segmentation . . . . .	30
3.11	Example of sample characterization at the initial state. a) Evolution of the porosity measurement as the cubic sub-volume on which it is measured increases from one voxel to a cube measuring $100 \text{ pixel}^3$ and selection of the REV size. b) 3D porosity field for the selected REV of $50 \text{ pixel}^3$ . . . . .	32
3.12	Local density changes at the interface: sketch showing the subdomains over which the percentage of each phase (grains, fines and pores) is estimated. These subdomains are hollow cylinders with a thickness of 5 voxels ( <i>i.e.</i> , $0.2 \text{ mm}$ ), coaxial to the pile . . . . .	34
3.13	Flow chart explaining the different steps of continuum DIC implemented in Tomowarp2 (existing code employed in this work). The example is given in 2D for clarity and show the displacement field and the maximum shear strain field for an incremental displacement of the pile tip of $1.0 \text{ mm}$ . . . . .	36
3.14	Flow chart showing the main steps of the implementation of the 3D discrete DIC in Tomowarp2 . . . . .	38
3.15	Example of slices through the maximum shear strain field obtained with a tri-linear spline interpolation in the sub-pixel search. Please note that the color contrast was enhanced for clarity . . . . .	40
3.16	Scheme illustrating the measurement of the orientation $\theta$ of a single Glageon grain. $e_{\min}^{\vec{}}$ , $e_{\text{med}}^{\vec{}}$ and $e_{\max}^{\vec{}}$ are the minimum, the intermediate, and the maximum eigenvectors of the inertia tensor, respectively . . . . .	42

4.1	a) 3D-reconstructed volume of an oedometer sample of Glageon sand (granular fraction: 1.250 - 1.600 mm) at ESRF, Grenoble, by Dano and coworkers (2018) at a voxel size of 6.5 $\mu\text{m}$ . b) Horizontal slice taken through the reconstructed volume showing the angularity of Glageon sand grains . . . . .	44
4.2	Grains morphology based on the dimensions of the bounding box . . . . .	44
4.3	Preliminary shape analysis of Glageon sand grains based on the bounding boxes: a) aspect ratio, b) elongation and c) flatness. d) Ratio between the volume of the grains over the volume of their bounding box. The red curve show the Gaussian fit associated with a deviation $\sigma$ and a mean $\mu$ . . . . .	46
4.4	Example of two grains extracted from the reconstructed volume of Figure 4.1. The grains are displayed in different orientations to show that one is rather elongated and the other one platy but both have a longer dimension . . . . .	47
4.5	a) Deviatoric response of Glageon sand and b) Volumetric deformation curves for different confining pressures (100 kPa and 200 kPa) . . . . .	48
4.6	Grain size distribution before and after triaxial compression at different isotropic confining pressure on dense sample of Glageon sand . . . . .	48
4.7	Scheme of the mini-calibration chamber mounted on the loading device . . . . .	49
4.8	Design of the model pile: a) drawing made by DOERLER Mesures and b) schematic of the different parts of the model pile . . . . .	50
4.9	Calibration of the load measured by a) the head load sensor (total load applied to the pile) and b) the strain gauges (tip load). Full symbols represent compression and empty symbols represent tension . . . . .	51
4.10	Definition of the maximum roughness $R_t$ and the normalized roughness $R_n$ , from Tehrani et al. (2016) . . . . .	52
4.11	Shear stress measured during two monotonic direct shear tests conducted with a constant normal stress of 100 kPa and 200 kPa . . . . .	52
4.12	Parts needed to build the tested sand sample: a) sample holder and cell support, b) cylindrical cell and c) blocking piece . . . . .	53
4.13	Different steps of sample preparation: a) sand deposition within a cylindrical mold, b) mold removal for the measurement of sample height and diameter and c) cell assembly . . . . .	54
4.14	Experimental arrangement before pile installation for a test conducted outside the tomograph . . . . .	54
4.15	Porosity at the initial state for test P-GLAG-16: a) 3D field of porosity, b) Vertical slice through the 3D field, and c) horizontal slices taken at different elevations through the 3D field (H1, H2, H3, H4) . . . . .	55
4.16	Typical head load profile during pile installation . . . . .	56
4.17	a) Typical displacement imposed to the pile during loading cycles; b) Typical shaft resistance evolution within a cycle. (red and black dots represent an x-ray scan acquisition)	57
5.1	Evolution of the loads applied on the pile during the initial embedment for test P-GLAG-01 . . . . .	62
5.2	Evolution of tip and shaft resistance during pile installation, after Tali (2011) . . . . .	62
5.3	Horizontal stress measurement at different distances from the pile tip during monotonic installation, from White & Lehane (2004) . . . . .	63
5.4	Load profiles during pile installation for different tests showing the reproducibility of the results (initial relative density between 85 % and 110 %): a) head load, b) tip resistance and c) shaft resistance. Note that the tip resistance and shaft resistance could not be recorded during test P-GLAG-12 . . . . .	65
5.5	Photograph showing the pile surface after a typical test in the mini-calibration chamber	66

5.6	a) Different zones developing around the pile during cavity expansion and b) size effect curves for several vertical stress values (cc: calibration chamber, ff: free-field), after Salgado et al. (1998) . . . . .	66
5.7	a) Incremental loading steps applied to the pile during scanning for test P-GLAG-00. The circles represents the steps when the loading was interrupted for scanning. b) Sketch of the region of interest analyzed by x-ray tomography during pile embedment	67
5.8	Evolution of a) head and b) tip load during displacement-controlled loading cycles for test P-GLAG-02 (amplitude of $\pm 0.5$ mm). Arrows indicate the loading path within a single cycle . . . . .	69
5.9	Evolution of shaft resistance during displacement-controlled loading cycles for test P-GLAG-02 (amplitude of $\pm 0.5$ mm) . . . . .	69
5.10	Evolution of the maximum friction measured with increasing number of cycles for tests P-GLAG-02, P-GLAG-03, P-GLAG-04 . . . . .	70
5.11	Deviation of the measurements given by the instrumented model pile: a) inconsistent shaft resistance values during test P-GLAG-05, b) tip load deviation during test P-GLAG-06 and its linear fit (inside the tomograph) . . . . .	71
5.12	Evolution of the force measured using the strain gauges with temperature. . . . .	72
5.13	Evolution of shaft resistance during loading cycles for test P-GLAG-11 (amplitude of $\pm 1.0$ mm) . . . . .	73
5.14	Evolution of the degradation of shaft resistance with the amplitude of loading cycles, from Le Kouby (2003). The degradation factor $D_\tau$ was defined as the ratio between the limit shaft resistance after and prior to cyclic loading . . . . .	73
5.15	Evolution of shaft resistance when changing the amplitude of cycles from $\pm 0.5$ mm to $\pm 1.0$ mm: a) maximum peak shaft resistance "kept in memory" at $\pm 0.5$ mm, b) smoothing of the first maximum peak shaft resistance and c) new maximum peak shaft resistance reached at $\pm 1.0$ mm - test P-GLAG-14 . . . . .	75
5.16	Schematic showing the modified direct shear device of Laboratoire 3SR . . . . .	76
5.17	Evolution of the shear stress when changing the amplitude of cycles from $\pm 0.5$ mm to $\pm 1.0$ mm and to $\pm 2.0$ mm: a) maximum peak shear stress visible at $\pm 0.5$ mm, b) smoothing of the first maximum peak shear stress and new maximum peak shear stress visible at $\pm 1.0$ mm, c) smoothing of the second maximum peak shear stress and new maximum peak shear stress visible at $\pm 2.0$ mm. Please, note that the key is common to the three plots . . . . .	77
5.18	Evolution of the axial shear strain with cumulative shear displacement when changing the amplitude of cycles from $\pm 0.5$ mm to $\pm 1.0$ mm and to $\pm 2.0$ mm (associated with the test presented in Figure 5.17) . . . . .	78
5.19	Image of an isotropically compressed sample in the $1\gamma 2\epsilon$ device, with zoom on a small amount of grains to show the speckle pattern on their visible face, after Tolomeo et al. (2017) (the frame is 599.4 mm x 444.7 mm). $\sigma_n$ and $\gamma$ are the vertical stress and the shear angle imposed, respectively . . . . .	79
5.20	Evolution of the shear stress when changing the magnitude of the shear angle from $\pm 2^\circ$ to $\pm 7^\circ$ : a) maximum peak shear stress at $\pm 2^\circ$ , b) smoothing of the first maximum peak shear stress, and c) new peak shear stress at $\pm 7^\circ$ . Please, note that the key is common to the three plots . . . . .	80
5.21	Test under constant volume boundary conditions (test P-GLAG-06): a) head load, b) tip resistance, c) shaft resistance and d) confining pressure evolution . . . . .	82
5.22	Evolution of shaft resistance during loading cycles for test P-GLAG-15 (pre-installed model pile) . . . . .	83

6.1	Vertical slices taken at different angular position within the 3D field of vertical displacements. These results were obtained with continuum DIC, for the increment 2-3 mm of test P-GLAG-00 . . . . .	86
6.2	Horizontal slices taken within the 3D field of horizontal displacements in both x and y directions. These results were obtained with continuum DIC, for the increment 2-3 mm of test P-GLAG-00 . . . . .	86
6.3	a) Coordinate reference system for image analysis data reporting. b) Schematic showing how a subdomain is defined for averaging micro-scale measurements on the circumference of the sample . . . . .	87
6.4	Vertical slices taken through the 3D field of vertical displacements obtained with continuum DIC (node spacing: 20 pixels, correlation window size: 40 voxels) for an incremental displacement of the pile tip of 1 mm until a maximum displacement of 14 mm (test P-GLAG-00) . . . . .	88
6.5	Vertical slices taken through the 3D field of horizontal displacements obtained with continuum DIC (node spacing: 20 pixels, correlation window size: 40 voxels) for an incremental displacement of the pile tip of 1 mm until a maximum displacement of 14 mm (test P-GLAG-00) . . . . .	89
6.6	Typical individual grain displacements from discrete DIC, plotted in a vertical plane passing through the pile axis, when the pile tip moved up from $h = 37mm$ to $h = 38mm$ (increment 2-3 mm): a) vertical displacements; b) horizontal displacements; c) individual displacement vectors for the same loading increment. These results are from test P-GLAG-00. Dashed lines delimit the different zones of displacement . . . . .	89
6.7	Individual grain rotations plotted in a vertical plane passing through the pile axis, when the pile tip moved up from $h = 37mm$ to $h = 38mm$ (increment 2-3 mm) during test P-GLAG-00. The color scale represents the rotation intensity in degrees . . . . .	91
6.8	Distribution of grains orientations and its representation using Legendre polynomials expansion truncated at the 4th order ( $P( x ) = 2p(x)$ ) a) prior to and b) after pile installation . . . . .	92
6.9	a) Radial evolution of the ratio between $\tilde{a}$ and $\tilde{a}_{initial}$ showing the change in anisotropy prior to and after pile installation. b) Schematic illustrating the fabric formed following pile penetration at different locations around the pile tip and the pile shaft. In this figure, $\tilde{a}_{initial}$ was obtained over all grains at the initial state and its value is 0.095 . . . . .	93
6.10	Distribution of grains orientations and its representation using Legendre polynomials expansion truncated at the 4th order after pile installation. The level of anisotropy was estimated by determining $\tilde{a}$ over two subdomains located around the pile tip corresponding to the regions 1 and 2 in Figure 6.9b . . . . .	94
6.11	Vertical slices selected through the measured 3D field of porosity a) before and b) after pile installation, for test P-GLAG-16. c) Same vertical slice through the 3D reconstructed volume showing the global volume change of the sample after pile installation . . . . .	95
6.12	Vertical slices through the 3D deviatoric strain field ( <i>i.e.</i> , maximum shear strain) calculated from continuum DIC kinematics for test P-GLAG-00 . . . . .	96
6.13	Photograph of the sample when the setup was disassembled after pile installation. A light-gray powder can be seen around the pile, which is delimited by the dashed line. A zoom into the material sampling at the interface shows the powder produced by grain crushing . . . . .	96
6.14	Evolution of the thickness of the layer of soil alongside the pile where grain crushing occurs and vertical slice showing this layer after pile installation during test P-GLAG-09 . . . . .	97

6.15 Typical individual grain displacements from discrete DIC, plotted in a vertical plane passing through the pile axis and showing the evolution of displacement intensity (DI) during loading cycles: a) vertical displacements, b) horizontal displacements between cycles 10 and 50; c) vertical displacements, d) horizontal displacements between cycles 500 and 1000. These results are from test P-GLAG-03 (amplitude  $\pm 0.5$  mm) . . . . . 98

6.16 Individual displacement vectors obtained for the same loading increments as Figure 6.15, plotted in a vertical plane passing through the pile axis: a) between cycles 10 and 50 and b) between cycles 500 and 1000. Note that the scale is different in figures a and b 99

6.17 Mean radial displacements obtained from discrete DIC for different loading stages: a) cycles 1-10, b) cycles 10-50, c) cycles 50-100 and d) cycles 500-1000. Radial displacements are averaged within a toroidal subdomain of soil obtained by revolution of the rectangular cross-section shown in 6.15a. These results are from test P-GLAG-03 (amplitude  $\pm 0.5$  mm) . . . . . 100

6.18 Mean radial displacements obtained from discrete DIC for different loading stages: a) cycles 1-5, b) cycles 10-20, c) cycles 70-100 and d) cycles 100-150. Radial displacements are averaged within a toroidal subdomain of soil obtained by revolution of the rectangular cross-section shown in 6.15a. These results are from test P-GLAG-09 (amplitude  $\pm 1.0$  mm) . . . . . 101

6.19 Evolution of the standard deviation of the radial displacements for the elevation H1 during cycles: a) test P-GLAG-03 of Fig. 6.17, b) test P-GLAG-09 of Fig. 6.18 . . . . . 102

6.20 Radial evolution of grain (without fines) and pore phases volume during loading cycles for test P-GLAG-03 (amplitude of displacement  $\pm 0.5$  mm, initial relative density of 84 %). The x-axis scale is such that a radial distance of 7 is equal to one pile radius. For a given curve, each symbol represents one measurement obtained by thresholding the gray-scale image at a distance  $r$  from the shaft (over a cylindrical subdomain as defined in Section 3.3) . . . . . 103

6.21 Radial evolution of grain (without fines) and pore phases volume during loading cycles for test P-GLAG-09 (amplitude of displacement  $\pm 1.0$  mm, initial relative density of 85 %). The x-axis scale is such that a radial distance of 7 is equal to one pile radius. For a given curve, each symbol represents one measurement obtained by thresholding the gray-scale image at a distance  $r$  from the shaft (over a cylindrical subdomain as defined in Section 3.3) . . . . . 104

6.22 a) Density evolution at different distances "r" from the pile surface when increasing the number of loading cycles and b) zoom into the first 150 cycles. The results obtained for test P-GLAG-03 are plotted with filled symbols and the one obtained for test P-GLAG-09 are plotted with empty symbols. To meaningfully compare the two tests, the initial percentage measured for the first cycle was subtracted from all values . . . . . 104

6.23 Radial evolution of grain (without fines) and pore phases volume for two different x-ray scans recorded after 150 cycles during test P-GLAG-09. The measurements done on two scans show the reproducibility of the methodology described in Section 3.3 . . . 105

6.24 Radial evolution of the quantity of fines during loading cycles for test P-GLAG-03 (amplitude of displacement  $\pm 0.5$  mm, initial relative density of 84 %). The x-axis scale is such that a radial distance of 7 is equal to one pile radius. For a given curve, each symbol represents one measurement obtained by thresholding the gray-scale image at a distance  $r$  from the shaft (over a cylindrical subdomain as defined in Section 3.3 . . . 106

6.25	Radial evolution of the quantity of fines during loading cycles for test P-GLAG-09 (amplitude of displacement $\pm 1.0$ mm, initial relative density of 85 %). The x-axis scale is such that a radial distance of 7 is equal to one pile radius. For a given curve, each symbol represents one measurement obtained by thresholding the gray-scale image at a distance $r$ from the shaft (over a cylindrical subdomain as defined in Section 3.3 . . .	106
6.26	Radial evolution of the quantity of fines for two different x-ray scans recorded after 150 cycles during test P-GLAG-09. The measurements on two scans show the reproducibility of the methodology described in Section 3.3 . . . . .	107
6.27	Sketch showing the high densification of the sand ahead of the pile tip during test P-GLAG-11. The numbers placed on the curve showing the typical evolution of shaft resistance indicate when the loading was interrupted for x-ray scanning. The two vertical slices (on the right) were taken through the 3D images recorded after the tenth cycle, when the tip was at 0 mm (scan 1) and at -1.0 mm (scan 4). The zooms into the slices illustrate the densification at the tip . . . . .	107
7.1	Sketch showing a possible modification of the mini-calibration chamber for the application of active radial boundary conditions . . . . .	114

# List of Tables

4.1	Glageon sand index properties . . . . .	45
4.2	Testing program to characterize Glageon sand . . . . .	47
4.3	Sensors precision. . . . .	50
4.4	Summary of model pile tests conducted in the mini-calibration chamber . . . . .	59
4.5	Specific objectives and technical issues encountered for each test . . . . .	60
6.1	Coefficient $\tilde{a}$ measured locally at different locations in the 3D image recorded at the initial state. . . . .	92

## Chapter 1

# Introduction

This PhD work examines the mechanisms that govern the macroscopic response of a displacement pile installed in a crushable calcareous sand by monotonic jacking. Local density changes, full-kinematics and grain crushing are investigated quantitatively during both pile installation and subsequent axial displacement-controlled cyclic loadings. This research project follows a preceding experimental PhD work (Silva Illanes, 2014) using the large and highly instrumented calibration chamber of Laboratoire 3SR, within the framework of the ANR project SOLCYP (French acronym for National Project in Piles under Cyclic Solicitations). This chapter describes the background and the main objectives of the study and presents the organization of the thesis.

Pile foundations are submitted to both long-term cyclic loads due to their environment (such as waves, wind or temperature fluctuations) and in-service cyclic loads (such as traffic or vibrations). These specific loading conditions were shown to influence the shaft resistance depending on the number and on the level of the applied cyclic loads. Although current regulations account for the potential effects of cyclic loading on the bearing capacity of foundations, there is still a lack of understanding of the mechanisms driving the macroscopic response of sand-pile interfaces under axial cyclic loading.

Sand-pile interfaces behavior involve complex mechanisms that are coupled across a range of scales. At the macro-scale the effect of cyclic loading manifests itself by a loss or a gain in shaft capacity. Although the macro-scale is of primary interest for pile foundations practical design, the macroscopic behavior of the sand-pile interface is related to mechanisms that take place at underlying scales. At the micro-scale, structural properties of individual sand grains and full-kinematics (translation and rotation) are essential to interpret macroscopic observations. At an intermediate scale, commonly called meso-scale, the volumetric behavior of the interface can be studied to better understand how the individual sand grains behave collectively. A number of small-scale laboratory investigations have been reported on related topics of sand kinematics, grain crushing, local porosity changes and macroscopic interface behavior (White and Bolton, 2004; Silva et al., 2013; Arshad et al., 2014; Martinez and Frost, 2017). However, these studies suffered from some of the following limitations: (i) use of plain strain devices and 2D imaging tools, (ii) studies limited to the installation of a pile or to a non-displacement pile<sup>1</sup>, (iii) postmortem analyses, (iv) lack of quantitative data on the observed grain crushing or density changes. These limitations can be overcome by the combined use of 3D small-scale physical model and non-intrusive full-field measurement techniques such as x-ray Computed Tomography (CT) and 3D Digital Image Correlation (DIC), as proposed in the present study.

---

<sup>1</sup>In the case of non-displacement piles the soil is excavated and the resulting hole filled with concrete (or a pre-cast concrete pile is installed and grouted in). At the laboratory scale, for non-displacement piles the soil is directly deposited around the pile.

## Objectives

The first objective of this PhD work is to identify key mechanisms taking place at the scale of individual sand grains that can lead to changes in shaft resistance of a displacement pile, when it is submitted to a relatively high number of axial loading cycles. The second objective is to provide a detailed analysis of the sand grains behavior in the vicinity of the model pile under different testing conditions that could be used to validate theoretical or numerical models. Particle-scale simulations such as DEM (Discrete Element Modeling) offers new possibilities to simulate grain-scale phenomena controlling sand-pile interface behavior. However, these models remain incomplete if they can not be compared to experimental data. Current comparisons are often limited to macroscopic responses or to micro-mechanisms observed during pile installation. In the present work, an innovative experimental approach is proposed to overcome these limitations.

To achieve the above objectives, this study required a reduced physical model, referred to as "mini-calibration chamber", that could be combined with x-ray tomography and high resolution image analysis. The laboratory arrangements employed by Silva Illanes (2014), including the mini-calibration chamber, was adopted and further developed in this research work. The chamber is admittedly not representative of field pile testing conditions for the main following reasons: the calibration chamber - to - pile diameter ratio and the sand particle - to - pile diameter ratio are far below the ratios recommended in the literature to limit scale effects on the interface response. And yet, such a setup is able to reproduce the same trends obtained at the macro-scale on large-scale experiments and allows the observation of full-field mechanisms taking place at the micro-scale. The dissertation includes a discussion of the influence of the specific testing conditions adopted in this experimental work on the results obtained at different scales.

## Outline of the thesis

The thesis is organized in seven chapters; the current **Chapter 1** provides the introduction and sets out the background to this PhD work.

**Chapter 2** reviews the most important findings that have informed advances in understanding and designing displacement piles when submitted to axial loading cycles. This review covers numerous experimental campaigns that were conducted at different scales, including full-scale pile tests, large calibration chamber tests, centrifuge tests and 2D interface shear tests. Particular emphasis is given to the effect of axial cyclic loading on the pile shaft resistance. This chapter also reports the mechanisms identified in the literature that are controlling the macroscopic response of sand-pile interface under cyclic loading. Finally, chapter 2 highlights the need for the development of advanced experimental tools providing quantitative micro-scale data against which numerical models could be tested and validated.

**Chapter 3** introduces briefly x-ray computed tomography and the x-ray tomograph of Laboratoire 3SR used in this work . Further details are provided on the acquisition system, the method employed for the reconstruction of 3D images, as well as the selection of optimum parameters allowing the visualization of the interface at a relatively high resolution. The second part of this chapter focuses on the way 3D images are manipulated to extract quantitative information at the grain-scale. A particular attention is paid to the process used to isolate each individual sand grains. The method employed to follow local density changes during both pile installation and loading cycles is also described, including a mesoscopic approach of porosity measurement and a grain-scale approach to take into account the volume of fines produced by grain crushing. Then, chapter 3 details the measurements of full-kinematics using two different approaches of 3D Digital Image Correlation (DIC): continuum DIC (following a pattern made up with pores and grains) and discrete DIC (following

individual grains). Finally, the technique used to measure the orientation of each grain is described.

**Chapter 4** focuses on the specific characteristics of the calcareous sand employed in this study, Glageon sand. Then, the mini-calibration is presented along with the loading system and the model pile. The testing procedure including a first embedment of the pile by monotonic jacking followed by a series of displacement-controlled loading cycles is also described. Chapter 4 discusses in what extend the results obtained in this study can be compared with other experimental observations conducted with large-scale tests. The experimental program and the objectives of each individual test are provided at the end of this chapter.

**Chapter 5** presents the results obtained at the macro-scale thanks to the mini-calibration chamber. First, the evolution of the loads applied on the pile during the first embedment phase is analyzed. Then, results showing different regimes in shaft resistance evolution during loading cycles are presented. Finally, the effect of several testing parameters on the macroscopic response are investigated: amplitude of the displacement applied during loading cycles, boundary conditions and method of installation.

**Chapter 6** contains the analysis of grain kinematics, volumetric behavior and grain crushing during both pile installation and subsequent loading cycles. A link between the mechanisms observed at the micro-scale and the macroscopic response of the interface is proposed.

Finally, **Chapter 7** summarizes the work described in this thesis, drawing out the principal results and advances in the understanding of particle-scale behavior of sand-pile interface under cyclic loading. The perspectives for future work are also discussed.

## Chapter 2

# Literature review

In addition to usual constant loading, foundations are subjected to variable loads including the so-called "cyclic" loads. This type of loading is described as "cyclic" for its repetitive character in terms of amplitude and frequency. Cyclic loads have various possible origins: environmental (wind, waves, vibrations, temperature or pressure fluctuations, etc.) or anthropic (operating machines, traffic, etc.). Their impact on foundations highly depends on their frequency and on the number of cycles. These two parameters vary significantly from one structure to another. The load frequency for emptying of tanks may be weekly, while for waves it may be around ten seconds. A storm may imply a few thousands cycles whereas railway of high speed trains may involve millions of cycles. Different aspects of pile behavior during cyclic loading are of interest for foundations design: (i) the effect of cyclic loading on the axial load capacity (both in tension and compression); (ii) the number of cycles that a pile can withstand before failure; and (iii) the accumulated displacement at the pile tip during loading.

A remarkable collaborative research project, SOLCYP, recently proposed a methodological approach and a set of calculation methods to take into account the effect of cyclic loads on pile foundation in Puech and Garnier (2017). Many studies mentioned in the following sections were conducted within this research project.

### 2.1 General description of cyclic loading

Chan and Hanna (1980), Tsuha et al. (2012), Jardine and Standing (2012) among others reported that the applied cyclic loads can be described by means of the following parameters:

- the number of cycles ( $N$ )
- the period of the cycles ( $T$ )
- the mean value of the cyclic load ( $Q_{mean}$ )
- the amplitude of the cyclic load ( $Q_c$ )
- the maximum and the minimum load values in the cycle ( $Q_{max}$  and  $Q_{min}$ )

Figure 2.1 illustrates these different parameters in the ideal case of cyclic loading, which means a case of constant amplitude and regular period. If this ideal case is generally employed for laboratory testing, field conditions are admittedly more irregular and, in some cases, highly random. Two types of cyclic loading should be distinguished: *one-way* loading that involves applying cyclic loads of only one sign (tension or compression) to the head of the pile and *two-way* loading that involves both compression and tension head loads with the potential to be more damaging than one-way loading.

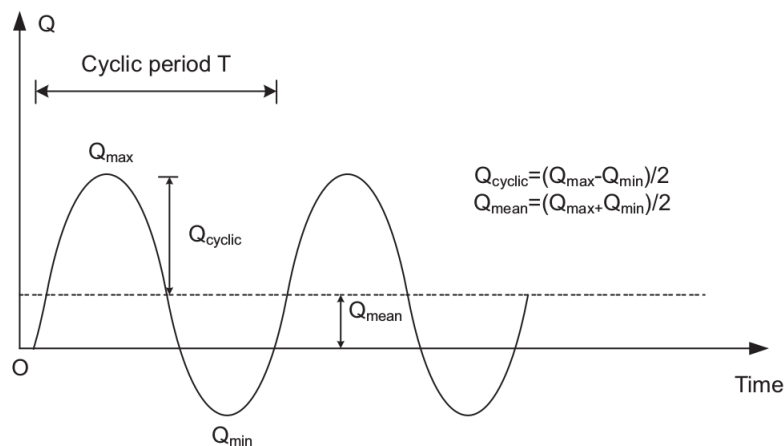


Figure 2.1: Schematic illustrating the characteristic parameters of cyclic loading, from Tsuha et al. (2012)

## 2.2 Effect of axial cyclic loading on sand-pile interface: macroscopic observations

### 2.2.1 Full-scale behavior

Field experiments showed that driven piles in sand have three possible responses to axial cyclic loading depending on the cyclic parameters defined in the previous section: stable, unstable and meta-stable. These three types of response were used to build the concept of cyclic stability diagram, also called interaction diagram, as introduced by Poulos (1989). The cyclic stability diagram allows the evaluation of the behavior of a pile submitted to axial cyclic loading as a function of the number of cycles and the cyclic loads as illustrated in Figure 2.2, with  $P_0$  = mean load,  $P_c$  = cyclic load,  $Q_c$  = static compressive capacity and  $Q_t$  = static tensile capacity. Such diagram defines three zones: a stable zone (A), a metastable zone (B) and an unstable zone (C). It is then possible to determine whether the applied load is critical or not for the soil-pile interface considered. This diagram is obviously a function of the type of pile and of the type of soil.

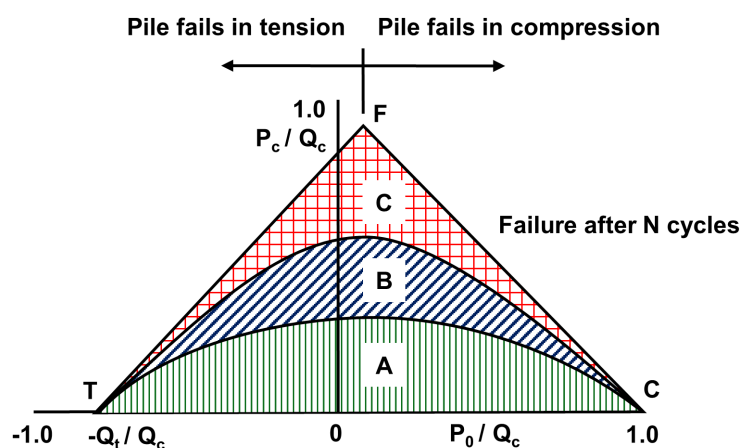
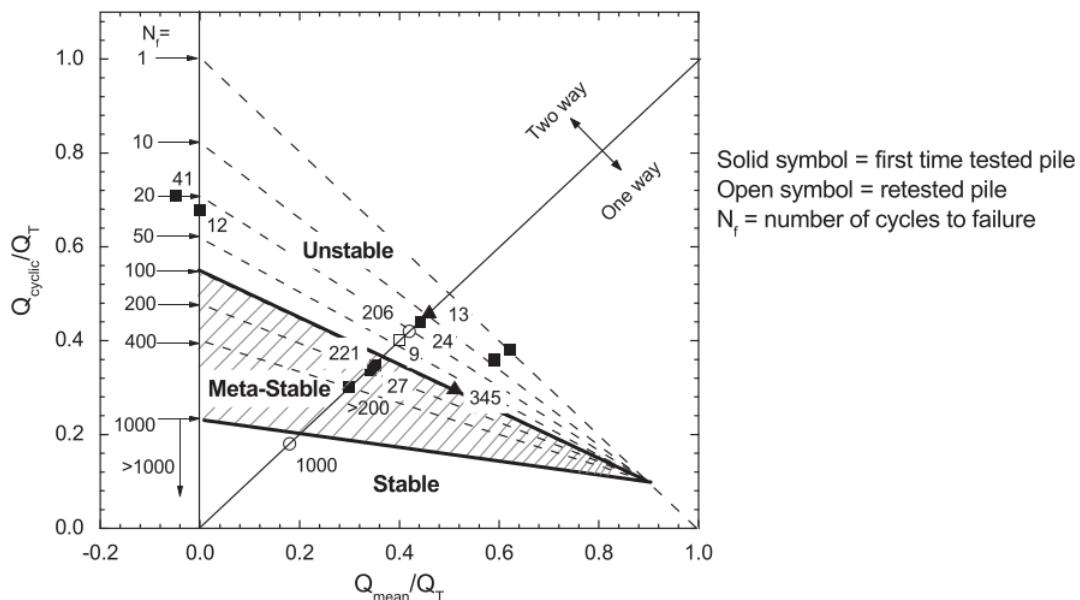


Figure 2.2: Main features of a cyclic stability diagram, after Poulos (1989)

For instance, Jardine and Standing (2000) used the stability diagram to characterize cyclic shaft failure conditions based on load-controlled tests conducted on seven open-tube steel piles, driven above and below the water table in clean medium-to-dense marine sand, at Dunkerque, France (see Figure 2.3). The Authors described thoroughly the three types of cyclic response:

- **Stable:** axial displacements stabilize or accumulate slowly over hundreds of cycles, under one-way or two-way loading. In such a case, shaft capacity can benefit from cyclic loading.
- **Unstable:** axial displacements accumulate rapidly under one-way or two-way loading leading to shaft failure within a few tens of cycles and a marked decrease of shaft capacity.
- **Meta-Stable:** axial displacements accumulate at a moderate rate without stabilization. Shaft failure develops for 100 to 1000 cycles.



**Figure 2.3:** Interaction diagram for full-scale piles, from Jardine and Standing (2000). Numbers within the graph area represent the number of cycles for each test

As part of the national project SOLCYP, an other experimental campaign of axial cyclic loading tests was conducted on the Loon-Plage site, near Dunkerque. Five bored piles installed in dense to very dense Flanders sands (the same sand formation as Dunkerque site) were submitted to extensive series of static and cyclic one-way tests, in compression. The results reported by Benzaria et al. (2013) showed that the non-damage zone (stable zone) is very limited in the case of bored piles, which highlights the importance of the method of pile installation.

## 2.2.2 Physical modeling

Full-scale experimental studies of pile submitted to cyclic loading offer an efficient and attractive approach but they are unfortunately difficult to carry out, for obvious financial reasons. Such tests are thus often covering only particular testing parameters and they are all conducted on the same pile, which makes their interpretation more complex. Physical modeling (*i.e.*, laboratory experiments) offers a good alternative for replicating the behavior of sand-pile interactions under controlled and

repeatable conditions.

A laboratory test of soil-pile interface can simply be a direct shear interface test under appropriate conditions. Boulon and Foray (1986) showed that active boundary conditions, *i.e.*, constant normal stiffness (CNS) conditions, can reproduce an infinite surrounding soil mass. The normal stiffness imposed to the interface ( $k$ ) was defined by Boulon and Foray (1986) as in Eq. 2.1, where  $E_p$  is the pressuremetric modulus,  $R_0$  the pile radius,  $\Delta\sigma_n$  is the variation of normal stress acting on the interface, and  $\Delta[u]$  is the variation of normal displacement.

$$k = \frac{2E_p}{R_0} = \frac{\Delta\sigma_n}{-\Delta[u]} \quad (2.1)$$

A number of studies on the related topics of cyclic shear behavior (Ooi and Carter, 1987; Johnston et al., 1987; Tabucanon et al., 1995; Mortara et al., 2007; Pra-ai and Boulon, 2016) showed that cyclic loading induces a significant normal stress reduction with increasing number of cycles. 2D-direct shear tests allow the variation of many parameters such as boundary conditions, amplitude of cyclic loading, roughness of the interface, loading rate, etc. However, such a test does not take into account the possible 3D effects induced by pile installation and subsequent cycles, especially in terms of stress (re)distribution.

Calibration chamber testing is a well established tool for the understanding of *in situ* testing. It is assumed that the results obtained are comparable to in situ results, provided that the tested material is identical to the field and that in situ stresses conditions are correctly reproduced in the chamber. This assumption is not strictly valid due to the limited size of laboratory chambers compared to the large body of soil to be modeled. It is well-known that boundary conditions have an important effect on calibration chamber results (*e.g.*, Parkin and Lunne, 1982; Foray, 1991; Schnaid and Houlsby, 1991). However, by choosing appropriate scales (size of the chamber, pile diameter, mean-particle size) and relevant boundary conditions, calibration chamber results prove to be in good agreement with full-scale observations. A number of laboratory studies considerably advanced the understanding of the effect of cyclic loading on sand-pile interface by means of calibration chamber testing.

Tsuha et al. (2012) conducted model pile tests in dense siliceous sand (Fontainebleau NE34) within the large calibration chamber of Laboratoire 3SR, Grenoble, France. The design of the chamber and of the closed-ended stainless steel Mini-ICP pile (Mini-Imperial College Pile) are fully described in Jardine et al. (2009). Mini-ICP pile was installed with jacking cycles and submitted to multiple static and cyclic tests involving one-way, two-way load and displacement controlled loading. The cyclic tests exhibited a range of stable, unstable and meta-stable responses broadly comparable to that observed in the field in Figure 2.3. Under stable conditions, up to 1000 cycles can be sustained and an overall increased in shaft capacity was observed. Under unstable conditions, shaft failure (defined when accumulated axial displacements reached 10% of the pile diameter, *i.e.*, 3.6mm for Mini-ICP pile) occurred in less than 100 cycles with a marked degradation of shaft capacity. Finally, under meta-stable conditions, shaft capacity may decrease depending on the level of loading imposed but piles can sustain several hundreds of cycles without reaching failure.

Using the same experimental arrangement as Tsuha et al. (2012), Silva Illanes (2014) reported results of driven and jacked piles submitted to axial load-controlled and displacement-controlled loading cycles. Load-controlled tests results were consistent with the stability diagrams proposed by Tsuha et al. (2012). Displacement-controlled tests were performed with different boundary conditions for a large number of loading cycles (up to 100 000 cycles). Different regimes were identified

in the evolution of shaft resistance during cyclic loading. Tests under constant volume (zero strain) exhibited a continuous degradation of shaft resistance during the first 3000 loading cycles and a stabilization for the following cycles. For tests conducted under constant normal load, a sharp decrease in shaft resistance was measured for few thousands of cycles after which, shaft resistance started increasing again. Axial cyclic loading tests performed in the calibration chamber of UR Navier-CERMES (France) filled with Fontainebleau sand produced similar results (Bekki et al. 2014; 2016). The Authors reported a gain in shaft capacity by performing post-cyclic measurements as shown in Figure 2.4a. Although a decrease of shaft resistance was observed in the first hundreds of cycles, the Authors reported that a large number of two-way displacement-controlled loading cycles can lead to a significant gain in shaft capacity as illustrated by Figure 2.4b.

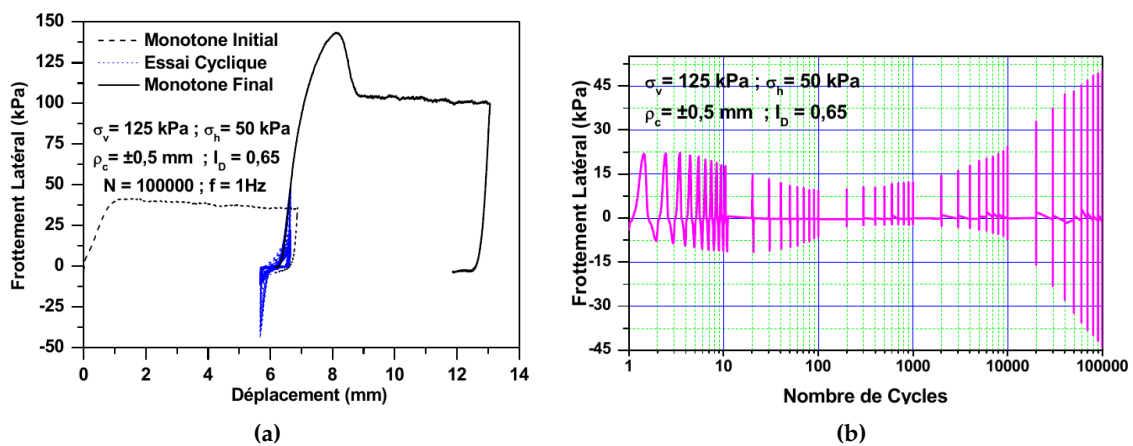


**Figure 2.4:** a) Shaft capacity measured during monotonic loading, prior to and after cyclic loading and b) evolution of lateral shaft friction with the number of cycles, after Bekki et al. (2014)

Li et al. (2012) investigated the influence of cyclic axial loads on the performance of pile foundations for different installation methods (cyclic jacking, monotonic jacking and pre-jacking, *i.e.*, bored) in the case of both force-controlled and displacement-controlled loading conditions. Tests were conducted at 50g in the Turner beam centrifuge at Cambridge University. Relative to "classical" calibration chamber testing, centrifuge testing has the advantage of replicating in situ stress conditions. The results showed that the pile head maximum force reduces during displacement-controlled loading with increasing number of cycles, but at a reducing rate. During force-controlled loading, more permanent settlement is accumulated. Pre-jacked pile head stiffness increases with increasing number of cycles while that of jacked piles remains almost constant. The Authors suggested that for pre-jacked piles, head load transfers from the shaft to the base due to densification of the soil beneath the pile tip.

The numerous results obtained from experimental campaigns conducted at different scales, from full scale tests to small-scale physical models, lead to similar conclusions regarding the macroscopic response of sand-pile interface submitted to loading cycles. It is generally observed that loading cycles result in a significant degradation of shaft capacity. Fewer results are found for a large number of loading cycles (higher than several hundreds). However, the existing studies all agree that there are different regimes in the evolution of shaft capacity during loading cycles, depending on the level of cycling and on the boundary conditions employed.

## 2.3 Understanding the mechanisms that control the macroscopic axial cyclic response

In addition to technical and financial feasibility, experimental modeling offers the possibility to investigate the complex mechanisms driving the macroscopic response of sand-pile interface. Local observations and measurements can be compared with the global interface response under well-defined testing conditions. Three main aspects were reported in the literature as potential explanations to the cyclic shear evolution of sand-pile interfaces: changes in effective stress around the shaft, local volumetric changes, and grain crushing.

### 2.3.1 Local effective stress around the shaft

White and Lehane (2004) analyzed the distribution of lateral stresses acting on piles during installation and subsequent load-controlled cyclic centrifuge tests and provided a further understanding of the mechanism called "friction fatigue". Friction fatigue theory was introduced by Heerema (1980) to describe pile driving behavior in clay, assuming that shaft friction, at a given soil horizon, decreases with increasing penetration of the pile tip. The results showed that cyclic installation methods lead to a significant degradation of shaft friction, varying in the case of one-way or two-way installation method. It was also observed that, for a given installation method, the degradation during subsequent cyclic loading followed the same decay pattern as that during installation. This is illustrated by Figure 2.5 and plotted for a relative position to the pile tip of  $h/\text{pile diameter}=1$ . The Authors attributed this phenomenon to the contraction of a thin layer around the pile, confined by the far field soil with a relatively high lateral stiffness.

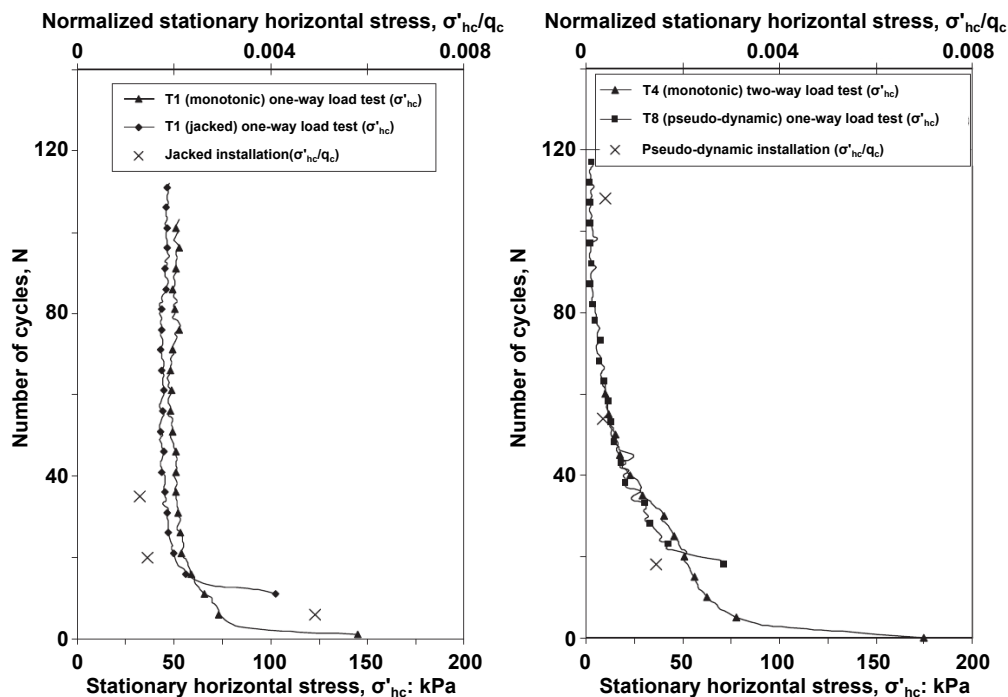


**Figure 2.5:** Degradation of stationary horizontal stress with cycling at during load tests: (a) one-way compression load test; (b) two-way compression-tension load test, after White and Lehane (2004)

By means of highly instrumented Mini-ICP piles and a set of stress sensors placed in the sand mass around the pile, Tsuha et al. (2012) related the local effective stress conditions to the three types of macroscopic response of piles under axial cyclic loading. The Authors conducted the analysis of effective stress paths based on the multiple yield surface framework proposed by Tatsuoka et al. (1997) (see Fig. 2.6). The small kinematic  $Y_1$  yield surface corresponds to a fully recoverable elastic behavior for fine silica sand. Tatsuoka et al. (1997) defined  $Y_2$  surface as the "threshold condition" that can trigger a re-direction of the strain increment vector and corresponds to cyclic loading without significant strain accumulation.  $Y_3$  surface is associated with increasing plastic and irrecoverable behavior. Tsuha et al. (2012), reported that, under stable conditions, the stress paths remain within  $Y_2$  limit without any local slip at the interface. Only minor top-down degradation was observed. Under unstable conditions, local slip developed at the interface and was linked to shear zone compaction and marked reduction of radial effective stress resulting in a highly inelastic behavior in the soil mass. Finally, under meta-stable conditions interface slip may develop depending on the level of cycling and a markedly plastic behavior was observed concentrated close to the shaft.

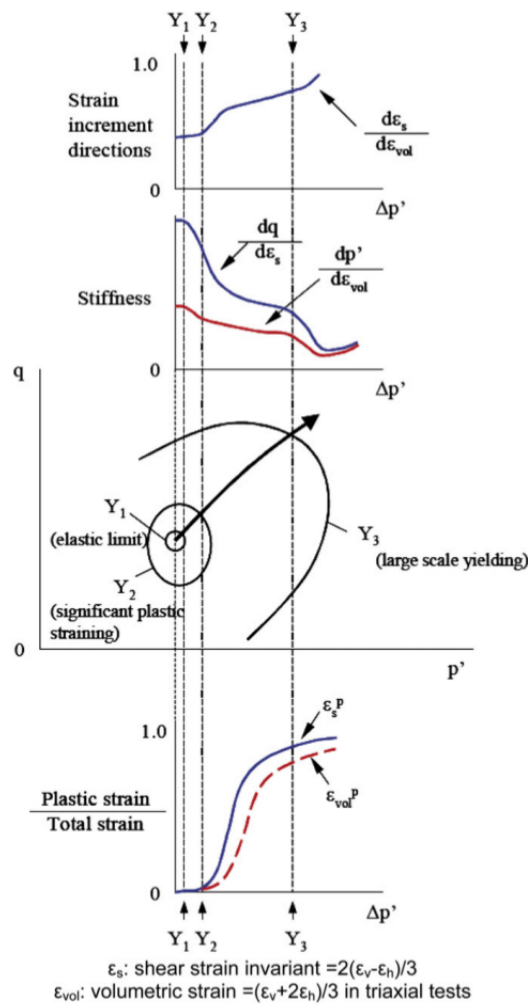


Figure 2.6: Scheme of multiple yield surface, from Tsuha et al. (2012)

### 2.3.2 Volumetric behavior and grain crushing

The mechanisms controlling interface load transfer degradation during cyclic loading were investigated at the particle scale by DeJong et al. (2003). The Authors studied the effect of particle characteristics, cementation, mean stress and of the amplitude of displacement on the load transfer degradation. A series of interface shear tests conducted under constant normal stiffness were analyzed by means of Particle Image Velocimetry (PIV). Three different regions of deformation were identified: slip between the interface and the shear zone, the shear zone itself (5-10 particle diameters thickness) and a region above the shear zone undergoing horizontal compression against the end walls of the shear device. The shear zone thickness was shown to increase with cumulative relative displacement and the cyclic reduction of normal stress was linked to the global contraction of the shear band. Calcareous sand exhibited a higher shear band thickness decreasing with cycling. Further analysis on the behavior at the interface within an individual cycle was presented by DeJong et al. (2006). During a single cycle, the volume change in the shear band included an initial contraction until the so-called transformation point (*i.e.*, the point when the volumetric response changes from contractive to dilative) at a stress ratio of about 0.5 followed by a dilation until the cyclic limit.

From a series of centrifuge tests on instrumented model piles, Dijkstra et al. (2010) also reported that local density change at sand-pile interface correlates well with the change of base and shaft resistances during cyclic loading. The tests performed on loose and dense saturated sand samples involve pile installation by jacking and four subsequent series of 10 displacement-controlled cycles with respectively 0.5, 1.0, 1.5 and 2.0 mm amplitude. Density measurements based on electrical resistivity changes were made at three different depth alongside the shaft. The main observation was that an increase in sand density near the pile is coupled to a decrease in shaft resistance during cycles. The Authors suggested that cyclic loading leads to the collapse of stress build-up and loosening occurring during pile installation.

If the cyclic degradation of the interface has been observed and thoroughly analyzed by a number of researchers, fewer analyses were proposed for the cyclic hardening reported by Silva Illanes (2014) and Tali (2011) in the case of a large number of loading cycles. Bekki et al. (2013), interpreted the different phases of shaft friction evolution using a relatively simple mechanical model, based on the concept of constant stiffness of the soil surrounding an interface zone around a probe, as illustrated in Figure 2.7,  $k_0$  being the stiffness of the soil. This interpretation was made assuming that no significant grain crushing occurs at the interface. The Authors suggested that the mobilization of shaft friction during cyclic loading is driven by the combined evolution of the normal component of the effective stress  $\sigma'_n$  and the local densification of the interface zone. The first phase of cyclic degradation was linked to the decrease in  $\sigma'_n$ , corresponding to a decrease of the interface thickness. After a given amount of loading cycles, the maximum degradation is reached,  $\sigma'_n$  decreases and the sand contracts at a lower rate. The authors attributed this result to a "prevented dilatancy" which becomes predominant and results in a cyclic hardening for the following cycles.

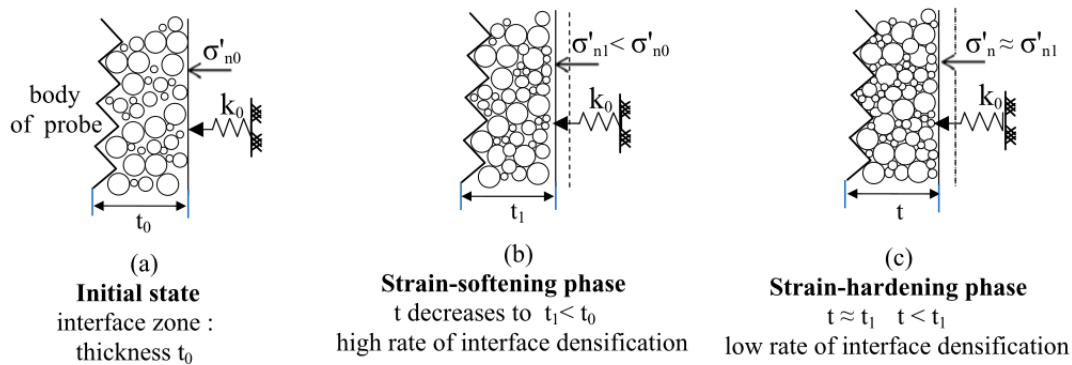


**Figure 2.7:** Schematic explaining the different phases in shaft friction evolution in the case of low consolidation stress, from Bekki et al. (2013)

A combination of particle-scale analyses of sand-pile interface after installation and of ring-shear tests, conducted by Yang et al. (2010), offered new insights on how stress level and displacement history may affect the shearing characteristics along the pile shaft. The Authors' analysis lead to the following main conclusions:

- Considerable grain crushing takes place beneath the pile tip during installation, provided the sand is sufficiently dense and pressurized.
- The crushed material moves radially as the pile penetrates, which creates concentric zones around the shaft as described in the schematic of Figure 2.8. Significant abrasion was also observed alongside the shaft.
- The thickness of the shear zone developed near the tip scales with the mean grain size. The shear zone thickness increases alongside the shaft, particularly when installation is not monotonic, and is augmented by later static and cyclic loading.

More recently, postmortem analysis of frozen sand samples recovered at sand-pile interface using x-ray tomography gave a further insight on the link between grain crushing and the axial cyclic loading (Silva et al., 2013). After pile installation by non-monotonic jacking, and an ageing period of two weeks, the pile was submitted to 20 000 two-way displacement-controlled loading cycles. Samples were extracted after testing at depths ranging between 30 cm and 98 cm, *i.e.*, beneath the pile tip (see Figs. 2.9a, b). X-ray images revealed a thin layer of pseudo-cemented sand with a high content of fine particles resulting from grain breakage. These fine particles were interlocked between intact grains as show in Figure 2.9. The shear band thickness was related to the depth alongside the pile and consequently to the loading history as reported by Yang et al. (2010).

The aforementioned studies contributed substantially to the understanding of the mechanisms that govern cyclic shear interface behavior and load transfer degradation. However, the results suffer from some of the following limitations: (i) the analyzes were conducted postmortem (sampling at the interface after testing); (ii) displacement and strain fields were obtained using 2D imaging tools and plane-strain devices; (iii) measurements were obtained locally at given locations alongside the pile shaft or around the pile.

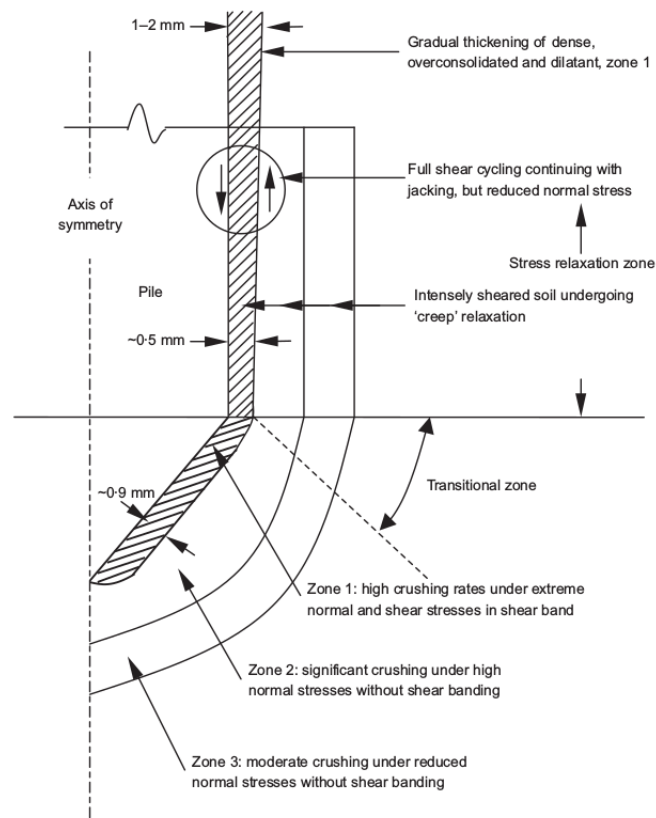


**Figure 2.8:** Schematic development of concentric zones around the pile shaft involving different degrees of particle crushing and their relationship to stress regime (not to scale), from Yang et al. (2010)

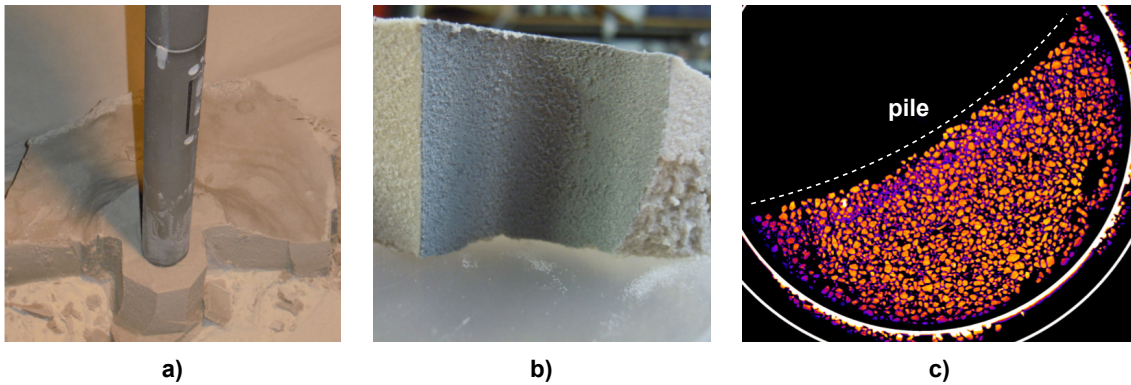


**Figure 2.9:** a) Moulding of the sand before extraction, b) frozen sample, and c) slice showing fine particles at the interface obtained by x-ray tomography, after (Silva et al., 2013)

## 2.4 Towards the numerical modeling of soil-pile interface: a need for micro-scale investigation

Modeling numerically the effects of cyclic loading on soil-pile interface is vital to reproduce the highly non-linear behavior of the interface and to improve predictive capabilities for foundations

design. The complex mechanisms driving the macroscopic response of the interface described in section 2.3 make this task non-trivial. This section presents a non-exhaustive list of examples of numerical models applied to the soil-pile interface behavior during both pile installation and cyclic loading.

D'Aguiar et al. (2011) employed a 3D finite-element model (implemented in the finite element software GEFDYN) and an elastoplastic soil constitutive model (Hujeux's model) to investigate the effect of the soil initial state, including initial relative density and initial mean stress, and the amplitude of the first pre-loading cycle on the load transfer mechanisms that can lead to a reduction in shaft resistance. In this model, a non-displacement pile was used, which means that the effects of pile installation were neglected. The model was based on the centrifuge pile tests performed by Fioravante (2002). The numerical results showed that the model captures well the mechanisms governing friction fatigue including including a decrease of the maximum shear stress depending on the level of cycling and a contraction of the soil.

A different finite-element (FE) approach, implemented in Abaqus, complemented by a simple breakage constitutive model (the so-called "student model" of breakage mechanics, as proposed by Einav, 2007) was adopted by Zhang et al. (2014) to simulate the cone-ended pile penetration tests in sand. The breakage constitutive model was coded as a user subroutine in Abaqus to deliver updated stresses and breakage increments to the general FE model. A detailed analysis of circumferential and vertical stresses around the pile during penetration was conducted and the numerical results were compared to the experimental results obtained by Jardine et al. (2013) (a typical stress prediction is shown in Fig. 2.10). The numerical results follow broadly similar trends and show fair quantitative agreement with the experimental measurements. Several limitations were underlined by the Authors: the installation procedure was simplified (monotonic instead of cyclic) and the shear zone abrasion was not addressed.

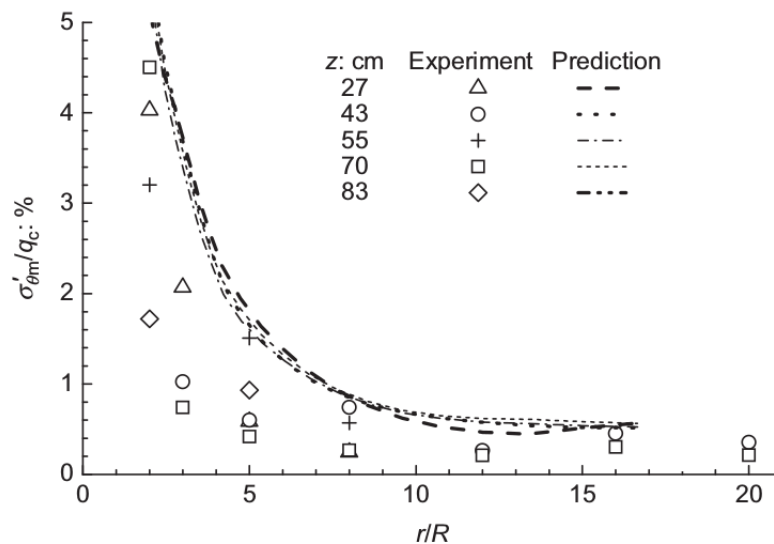


**Figure 2.10:** Comparison of numerical circumferential stresses at  $h/R = 0.5$  level above the tip during penetration and experimental results obtained by Jardine et al. (2013), from Zhang et al. (2014)

Even though finite-element approaches help greatly in replicating of sand-pile interface behavior for practical design, they remain limited to a small number of cycles and do not take into account the particle-scale interactions directly linked to the macro-scale complexity of the interface response. In this sense, discrete element method (DEM) is obviously a more appropriate tool to simulate the micro-mechanics, which underlies the global response of a granular assembly under mechanical loading. Originally proposed by Cundall and Strack (1979), DEM explicitly simulates granular materials as assemblies of individual particles. Inter-particle interactions are modeled by contact laws, where the normal and tangential contact forces are dependent on the overlap and on the relative displacement between two particles in contact.

A detailed DEM study of the penetration of driven piles in granular materials was proposed by Lobo-Guerrero and Vallejo (2005; 2007). A discrete element model was enhanced by including a simplified tensile failure criterion in order to take into account, and to visualize, grain crushing around a penetrating pile. The particles were idealized as discs with a thickness  $L$  and a diameter  $D$ . Only particles with a coordination number smaller or equal to 3 were allowed to break. The loading conditions were simplified as shown in Figure 2.11a. A particle was able to break when its tensile strength ( $\sigma_t$ ) was higher than a threshold arbitrarily defined by the Authors. The results showed that crushing starts and concentrates in a region below the tip of the pile (see Fig. 2.11b). As the pile passes through the region containing crushed particles, a migration of the generated fragments to the sides around the shaft was observed.

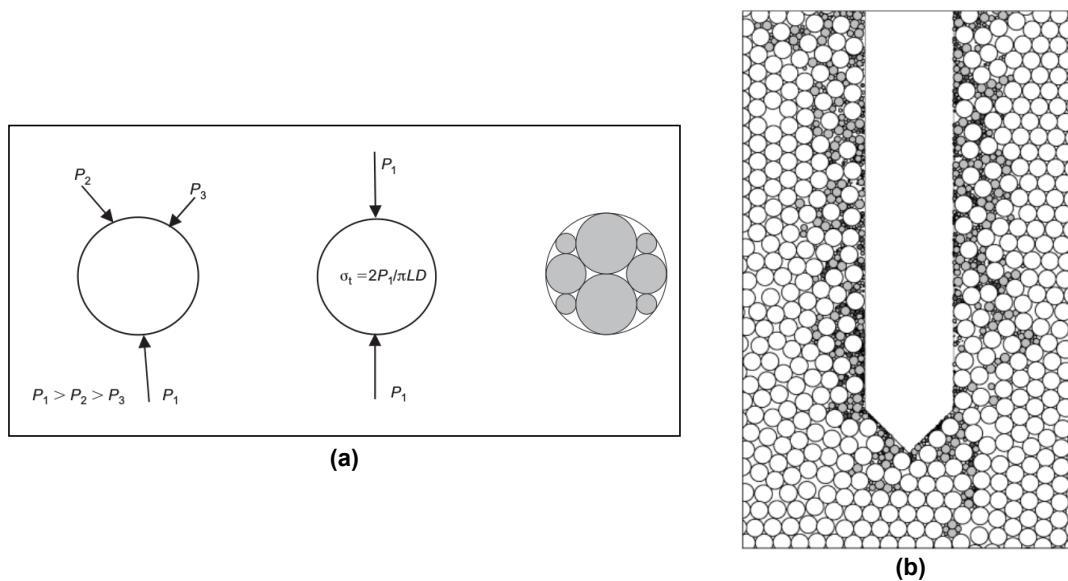


**Figure 2.11:** a) Maximum coordination number for a particle to be able to break; loading conditions on a particle assumed to be equivalent to the one of a diametrical compression test; configuration after breakage and b) Evolution of average radial stresses in representative cycles: strain (-0.1, +0.1%), from Lobo-Guerrero and Vallejo (2005)

More recently, the studies of Butlanska et al. (2014) and Wang and Zhao (2014) also demonstrated the ability of DEM to capture the main micro-mechanisms governing pile penetration. Both studies proposed a multi-scale analysis of sand-pile interface, including the evolution of the stress and strain fields around a virtual pile. The main advantages of these two models are the three-dimensional approach and the consideration of grain breakage, respectively. For instance, Butlanska et al. (2014) simulated a CPT test in a virtual calibration chamber thanks to the PFC3D Itasca Consulting Group

code, as illustrated in Figure 2.12a. This model gave access to the 3D contact forces network developed around the pile (see Fig. 2.12b). The Authors showed that the strong force network concentrate around the pile tip and is strongly affected by the boundary conditions (constant stress or constant volume). Coupled discrete-continuum simulations incorporating 3D aspects (see for instance Jin and Zhou, 2010; Zhou et al., 2012) can also be a viable alternative for sand-pile interface numerical modeling. In such a model, "coupled discrete-continuum simulations" means that both discrete elements and finite elements are used *at the same scale*. For instance, the sand near the pile is modeled using DEM, while the sand away from the pile is modeled using FEM. The numerical results produced by all these models at the particle-scale agree well with small-scale experimental results obtained during pile installation in sand (see for instance White and Bolton, 2004; Arshad et al., 2014; Silva and Combe, 2015).

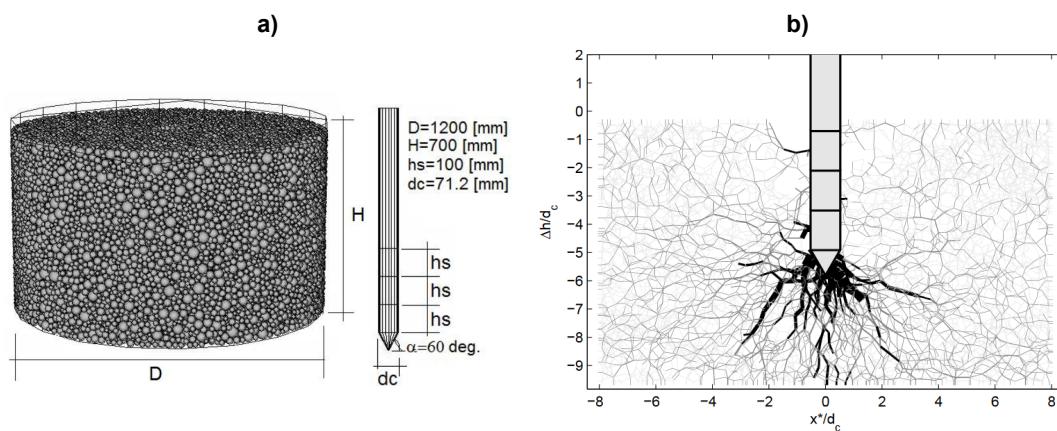


**Figure 2.12:** a) View of the virtual calibration chamber and the model pile. b) Contact normal forces exceeding average normal force (the lines thickness is proportional to the magnitude of the normal force), from Butlanska et al. (2014)

Fewer DEM studies can be found in related topics of sand-pile interface submitted to cyclic loading. Cui and Bhattacharya (2016) investigated the mechanisms inducing soil stiffness changes around a wind turbine monopile submitted to a large number (few thousands) of lateral cyclic loadings by means of 3D DEM as illustrated in Figure 2.13a. The results obtained by DEM simulations were in good agreement with the results of small-scale physical models: granular soil stiffness increases during cyclic loading; a convective soil flow and a soil densification takes place around the monopile (see Fig.2.13b); the average radial stress on the pile increases under cyclic loading (see Fig.2.13c). Similarly, Duan and Cheng (2016) proposed a DEM centrifuge model of a monopile submitted to lateral cyclic loads using PFC 2D (ITASCA software). Predicted accumulated permanent pile lateral displacements induced by the lateral cyclic loads, agreed well with experimental observations. To the author's knowledge, no equivalent DEM study was developed for axially loaded sand-pile interfaces.

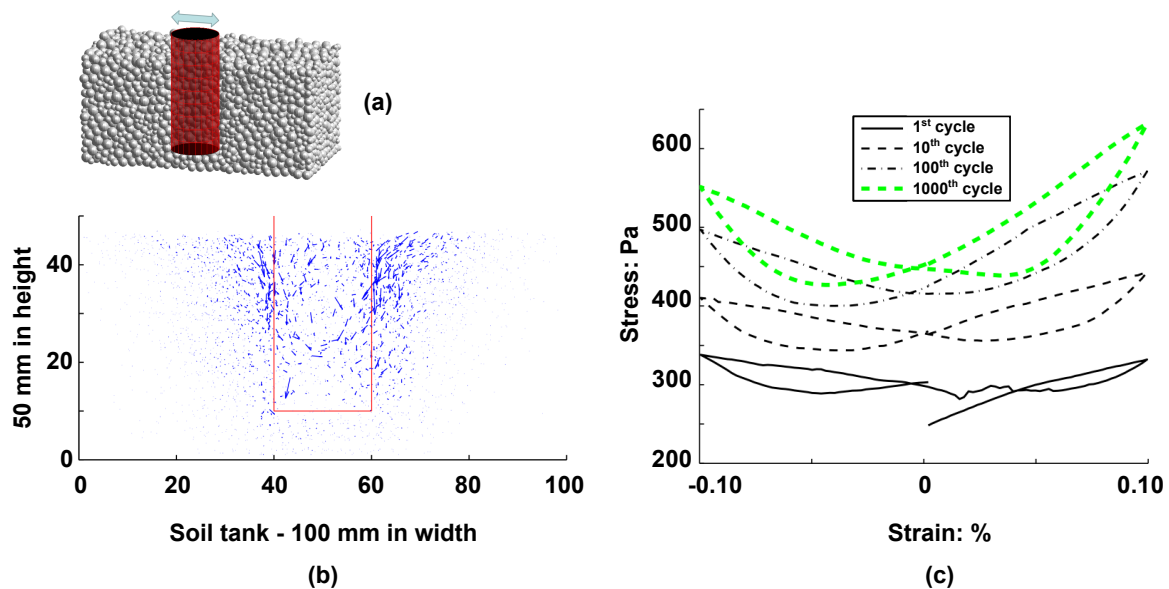


**Figure 2.13:** a) Configuration of soil tank and pile; b) Incremental soil displacements at the end of the given cycle (mm): strain (-0.1, +0.1%), 1st-50th cycles; c) Evolution of average radial stresses in representative cycles: strain (-0.1, +0.1%), after Cui and Bhattacharya (2016)

It is important to note that all the aforementioned DEM studies were based on some of the simplifications listed below:

- 2D
- highly idealized particles (discs or spheres)
- a low ratio of particle diameter to pile diameter leading to potential scale effects
- absence of particle crushing, or fines produced by grain breakage not considered
- an installation method closer to the one of a bored pile (particles virtually removed to leave place to the pile)
- a separated analysis of pile installation and of subsequent loading cycles

Despite these simplifications, the different applications of DEM to soil-pile interface problems showed that it is possible to replicate satisfactorily various mechanisms observed in reduced physical model pile tests and in full-scale tests. DEM models provide valuable and detailed particle-scale information, such as: grain kinematics, stress and strain fields, contact forces network, and fabric evolution. Once the ability of DEM to capture the response of a simplified test is demonstrated, the model can be extended to more realistic cases. For instance, particle shape and grain crushing can be taken into account, as proposed by Falagush et al. (2015). However, without detailed (full-field) micro-mechanical measurements obtained experimentally, it is not possible to achieve quantitative numerical conclusions regarding the particle-scale phenomena driving the macroscopic response of sand-pile interface. This fundamental need for a grain-scale investigation in the modeling of the interface behavior was underlined by a number of researchers: *e.g.*, DeJong et al. (2006), O'Sullivan

et al. (2008), Wang and Zhao (2014), Cui and Bhattacharya (2016).

Finally, multi-scale numerical models are promising tools to simulate different scales explicitly. In a multi-scale framework, a rigorous coupling between the finite element method (FEM) and the discrete element method (DEM) is implemented at different scales (e.g., Zhao J.D., 2015 and Desrues et al., 2015). In such a model (see Figure 2.14), to solve a boundary value problem, the macroscopic geometric domain is first discretized into a FEM mesh. A DEM assembly is then embedded at each Gauss integration point of the mesh serving as a local Representative Volume Element (RVE). At each load step, the RVE takes its memory of the past loading history as initial conditions and receives the global deformation from the FEM at the specific Gauss point as input boundary conditions. It is solved to derive the local incremental stress-strain relation (e.g., stress and tangential stiffness matrix) required for advancing the global FEM computation. Such a multi-scale approach could possibly benefit from grain-scale data provided by experiments such as those using x-ray imaging. Although very challenging, image-based data could be used to create a REV containing realistic grains. Thus the numerically modeled micro-structure would be more representative of the great randomness and heterogeneity of a real granular system.

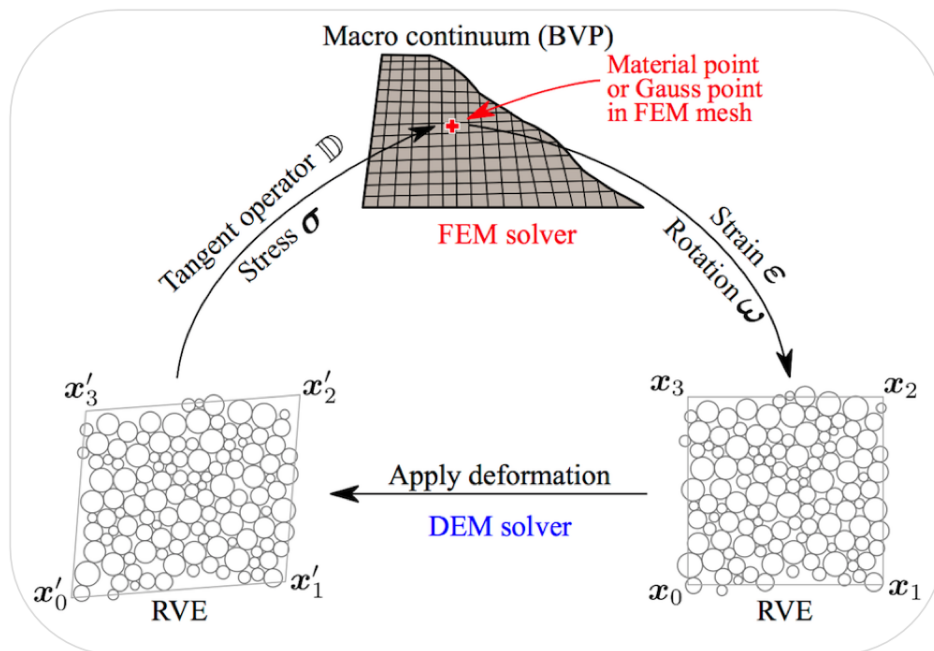


**Figure 2.14:** Schematic illustration of the hierarchical computational framework for multi-scale modeling of granular material, from Zhao (2008)

## Chapter 3

# X-ray tomography and advanced image analysis tools

Small-scale phenomena such as shear banding, grain crushing or cracks formation, which are not necessarily visible from just looking at the specimen, can be revealed thanks to x-ray imaging. X-ray tomography has been successfully used as a quantitative experimental tool for strain localization investigation (see for instance Batiste et al., 2004; Lenoir et al., 2007; Andò et al., 2013a). When a phenomenon is associated with significant density changes within the scanned specimen, the affected regions of the specimen have a different x-ray attenuation coefficient prior to and after deformation. However, if a phenomenon occurs without significant volumetric changes, *i.e.*, density changes, then it is invisible to x-rays. Advanced image analysis tools, such as 3D-Digital Image Correlation (DIC), have been developed to complement the information provided by x-ray images.

X-ray imaging is a key tool in this research work, in which the deformation mechanisms governing the sand-pile interface response are investigated at the grain-scale during pile installation and subsequent loading cycles. The focus is on image-based measurements that track the sand grains in the vicinity of the pile. A particular effort was made to obtain quantitative results that could be used to validate numerical models. This study has been made possible thanks to advanced image acquisition and analysis tools directly available at Laboratoire 3SR, in Grenoble. The majority of the image processing was conducted thanks to the open-source image processing software Fiji (Schindelin et al., 2012) and the 3D visualization was done using the open-source, multi-platform data analysis and visualization software ParaView (Ahrens et al., 2005).

### Layout of the chapter

This chapter starts with a brief introduction to x-ray computed tomography (Section 3.1.1) and, particularly, to the x-ray tomograph employed in this work (Section 3.1.2). The settings selected for the acquisition and the reconstruction of 3D images are detailed in Sections 3.1.3 and 3.1.4.

Since one of the main objectives of this work is to provide a detailed analysis of the sand-pile interface at the scale of a sand grain, it is first required to identify and define each grain in the 3D images. Section 3.2 shows how the solid phase (intact grains and fines produced by grain crushing) can be separated from the void phase by using an appropriate thresholding method. The method employed to separate each individual grain from its neighbors is presented afterwards (3D segmentation and labeling). When the grains are identified, it is possible to characterize them geometrically by means of their main dimensions and their center of mass. The processed images in which the grains, the voids and the powder produced by grain crushing are identified are used as an input for a set of full-field measurements techniques described in the next sections.

First, a method to follow the density changes, both at the scale of the sample and locally at the scale of the grains, is described in Section 3.3. Section 3.4 presents DIC as a tool for measuring the full

kinematics between different loading steps, which means between different 3D images. A first approach referred as *continuum DIC*, the most commonly used, is described in Section 3.4.2. Continuum DIC tracks a sub-volume from one image to another. This sub-volume forms a 3D pattern containing different grains and pores. The granular nature of the material is not taken into account and the 3D displacement field within a sub-volume and between two adjacent sub-volumes is assumed to be continuous, which is why this approach is referred as continuum. A second approach referred as *discrete DIC* is detailed in Section 3.4.3. In this approach, the grains are followed individually between two configurations. The sub-volume is centered on a grain and follows the actual shape of the grain being tracked, which is why the approach is referred as discrete. These two sections specifically focus on the methods implemented in the DIC code Tomowarp2 developed by S. Hall and coworkers (Hall et al., 2010). The selection of a set of parameters optimizing the quality of the DIC-based analyses is explained in Section 3.4.4. Finally, Section 6.2.2 introduces a method aiming at characterizing the anisotropy of the granular media prior to and after mechanical loading, based on the distribution of the orientations of the sand grains.

### 3.1 X-ray tomography for high resolution 3D imaging

#### 3.1.1 General description of x-ray Computed Tomography

X-ray Computed Tomography (x-ray CT) provides nondestructive three-dimensional maps of the x-ray attenuation within an object. X-ray is an electromagnetic waveform with a wavelength ranging from a few picometers to a few nanometers. The energy of an x-ray is usually expressed in eV ( $1\text{eV} = 1.602 \times 10^{-19}\text{ J}$ ). X-rays photons are produced by striking a material with high-speed electrons (the kinetic energy is transformed into electromagnetic radiation). Therefore, the maximum energy of an x-ray photon equals the entire kinetic energy of the electron. The energy of each photon,  $E$ , is proportional to its frequency,  $\nu$ , and is described as shown in Equation 3.1, where  $h$  is Planck's constant ( $6.63 \times 10^{-34}\text{ J s}$ ),  $c$  is the speed of light ( $3 \times 10^8\text{ m/s}$ ) and  $\lambda$  the wavelength of the x-ray. There are two types of x-rays: hard x-rays and soft x-rays. Hard x-rays are on the lower wavelength of the spectrum. They have higher energy and consequently penetrate matter easily. On the contrary, soft x-rays have wavelengths ranging between 10 nm and 0.1 nm. They are referred as "soft" since they are easily absorbed by matter.

$$E = h\nu = \frac{hc}{\lambda} \quad (3.1)$$

As the x-rays go through an object, the signal is attenuated by three different processes: photoelectric absorption, Compton scattering and pair-production. For geomaterials, the photoelectric absorption, which corresponds to the transfer of the total energy of a photon to an inner electron causing the electron to be ejected, is the main mechanism. When a monochromatic x-ray beam goes through a homogeneous object, the measured attenuation is linearly related to the thickness of the object along that path and is described by the Beer-Lambert law (Eq. 3.2) where  $I_0$  is the x-ray intensity before crossing the object,  $z$  is the depth within the object and  $\mu$  is the attenuation coefficient of the material. The attenuation coefficient was shown to be dependent on the atomic number of the scanned matter (a material with a high atomic number will have a higher attenuation coefficient, see Als-Nielsen and McMorrow, 2001).

$$I(z) = I_0 \exp^{-\mu z} \quad (3.2)$$

The use of x-ray imaging in experimental geomechanics dates back to the early 1960s, in Cambridge, where x-ray radiographies, *i.e.*, 2D images, were employed for measuring strain field in granular soil (Roscoe et al, 1963). In the case of x-ray CT, x-ray radiographies are recorded at different angular positions around a specimen. These radiographies are called projections. A 3D image of the specimen is reconstructed using the projections thanks to a specific algorithm (filtered back projection in this study). Section 3.1.4 gives further details about the reconstruction process. Originally used for medical purpose, x-ray CT is now widely used in geomechanics. This technique was pioneered at 3SR by Desrues and coworkers in the early 1980s to study strain localization in sand (see Viggiani and Hall, 2012).

### 3.1.2 3SR x-ray tomograph

X-ray CT allows the visualization of the micro-structure of a specimen during a test, *i.e.*, while it deforms under loading. The 3SR x-ray tomograph requires to interrupt the loading during the acquisition of a scan. This limitation can be overcome by synchrotron x-ray radiation for which a more powerful source (and thus a higher photon flux) provides fast scanning at a high spatial resolution. In this study, it was however possible to follow the entire process controlling sand-pile interface behavior prior to, during and after pile installation or loading cycles, at the scale of the sand grains. Performing such a test while scanning is extremely challenging and requires a specific testing arrangement as described in Chapter 4.

The 3SR device was supplied by RX-Solutions (Annecy) and bought in 2007 with funds from ANR Project MicroModEx as well as Laboratoire 3SR (see Fig. 3.1a). This device differs from ordinary x-ray scanners. It has been designed to host relatively large and complex equipments within the x-ray cabin. It also allows connections to the outside of the cabin without risk. For instance, it is possible to keep data acquisition, pressure or temperature control during scanning. Figure 3.1b shows the experimental equipment used for this study within the x-ray tomograph. The source and the detector can be translated vertically and horizontally which allows for scanning different regions within a specimen. It is also possible to translate the specimen closer to the source (*i.e.*, zoom in) and increase the spatial resolution of the x-ray images. Further technical details and various examples of studies conducted using the 3SR device can be found in Viggiani et al. (2015).

The x-ray beam generated by the source<sup>1</sup> has a conical shape and is polychromatic. The voltage and the current applied to the x-ray tube can be controlled by the user depending on the scanned object. Increasing the voltage increases the mean photons energy, which means they cross matter easier. The current controls the number of photons emitted, so the flux of photons. The 3SR source allows for voltages ranging between 40 and 150 kV and currents up to 500  $\mu$ A. As an example, a voltage of 100 kV means that an electrical potential is applied across the x-ray tube. Under such conditions, the electrons that strike the target have 100 keV of kinetic energy. Thus, the highest energy photons that can be produced is of 100 keV.

The source of 3SR can work with three different "spot" sizes (the spot is the starting point of the beam): small, medium and large. The higher the power given to the x-ray tube, the larger is the size of the "spot". The size of the "spot" has to be carefully selected since it partially defines the spatial resolution of the images by determining the number of possible source detector-paths that can intersect a given point in the scanned object. The higher the number of paths, the more the image

---

<sup>1</sup>Hamamatsu L8121-03 micro-focus x-ray source

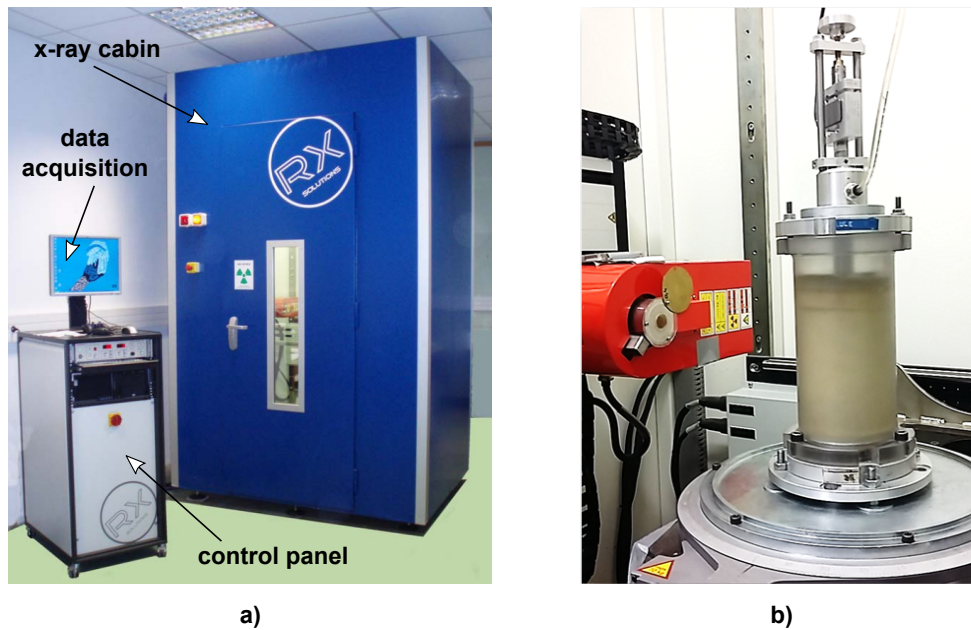


**Figure 3.1:** a) 3SR x-ray device including the cabin and the control panel. b) Setup installed in front of the x-ray source within the cabin

will be blurry. Thus, the size of the spot should be smaller than the smallest feature to be resolved in the x-ray images. The source of 3SR allows a minimum voxel size of  $5\ \mu\text{m}$ .

### 3.1.3 Optimum image acquisition settings

An accurate interpretation of x-ray images relies on an adequate scanning configuration, a careful calibration and a selection of suitable acquisition settings.

During one scan, projections are recorded at 1024 angular positions. In this work, the acquisition was done using two different modes: "global tomography" and "local tomography". In "global tomography", the whole sample is imaged, which means that we have a "global" vision of the phenomena occurring during a test. However, to access information at the grain scale, the resolution of the images should be high enough to actually resolve individual grains. This constraint does not allow a field of view including the whole sample. The images are thus limited to a reduced field of view focused on the pile tip and shaft, which corresponds to a "local tomography".

In global tomography, a voltage of 120 kV and a current of  $400\ \mu\text{A}$  were selected, leading to a power of 48 W. These choices were made in order to obtain clear images and photons with an energy high enough to penetrate the 70 mm-diameter sand specimen mounted within the mini-calibration chamber. The targeted voxel size with such a power was  $70\ \mu\text{m}$ . The optimum "spot" size was selected thanks to a calibration chart JIMA (Japan Inspection Instruments Manufacturers' Association) shown in Figure 3.2. Depending on the spot size and on the power of the x-ray source, the chart allows the identification of the minimum size of pattern that can be resolved. Based on this calibration, the size of the spot was set to "large" in global tomography. The size of the images obtained is  $1160 \times 1200 \times 1822$  voxels. At each angular position, 8 frames were recorded and averaged to limit the amount of blur in the image. With a frame rate of 1.00 (one frame recorded per second, adjusted to

avoid pixel saturation and receive enough signal), one entire scan took about 2 hours and a half.

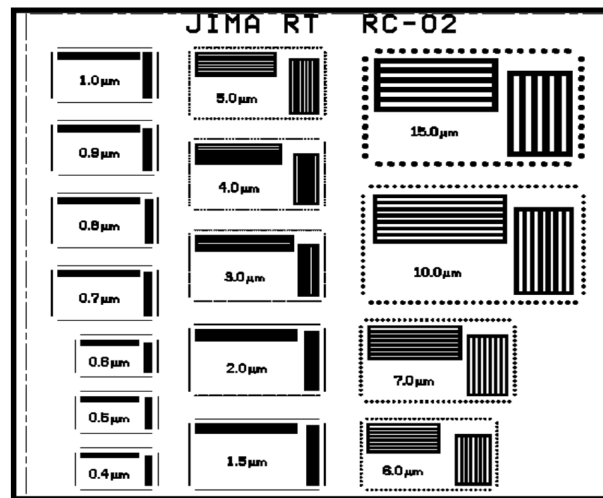


**Figure 3.2:** JIMA calibration chart used for the selection of the optimum spot size

In local tomography, the voltage was reduced to 150 kV and the current to 200  $\mu\text{A}$ , leading to a power of 30 W. The highest voxel size possible was 40  $\mu\text{m}$ . For such a voxel size and such a power, the spot size was set to "medium". When working in local tomography, the axis of rotation of the x-ray device does not stop at each angular position, rather it rotates continuously. This setting limits the artifacts created by the parts of the scanned object which are going out of the field of view during rotation but tends to blur the images. To increase the quality of the images, the number of averaged frames and the frame rate were increased and respectively set to 14 and 1.75. One complete scan took about 3 hours (2 hours and 55 minutes).

Prior to a test, the x-ray source and the detector are calibrated. A first filter, called "black filter" is applied to the recorded data on the detector. This filter aims at removing the electronic noise on the detector. It consists of taking several black frames with x-rays turned off. It is necessary to update this filter often, since the background noise changes in time, especially with the temperature of the detector. A second filter called "flat filter" (or gain) is then applied. This filter aims at homogenizing the response of each pixel to a given received intensity. It also corrects the defective pixels by replacing their value by the mean of their neighbor's. This filter consists of taking white frames with x-rays turned on and set at the working voltage and about the third of the working current. No object should interact with the beam during the acquisition of the white images.

### 3.1.4 3D reconstruction

3D images were reconstructed thanks to the projections recorded during a scan with the X-Act software, provided by RX-Solutions. These projections are 2D and represents an integration of all x-ray attenuation coefficients encountered along the path of the beam until it reaches the detector. The reconstruction was performed using a filtered back projection algorithm implemented in the software. Further details on the principles of 3D x-ray images reconstruction can be found in Hsieh (2003). An example of 3D-rendering after pile installation is shown in Figure 3.3.

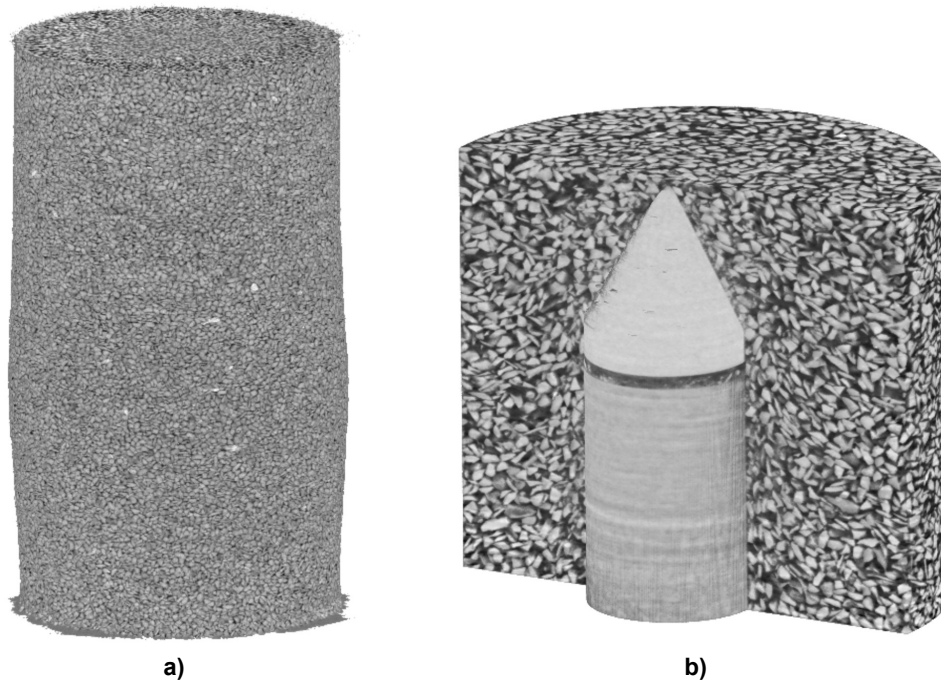


**Figure 3.3:** Example of 3D-reconstructed images after pile installation a) in global tomography and b) in local tomography

A qualitative interpretation of x-ray images is generally straightforward when adequate acquisition settings are applied. However, various scanning artifacts, described for example by Ketcham and Carlson (2001), can highly affect the data for quantitative analysis. Some of these artifacts can be corrected, or reduced, during the reconstruction using X-Act.

First, during a scan, the projection of the x-ray spot can derive or the scanned specimen can deform. To correct these drifts, an additional series of projections is recorded at the end of the scan and correlated to the projections recorded during the scan, at the same angular positions. Second, a blur (object edges are duplicated) can be produced on the images in the case of a geometrical misalignment (between the source, the specimen and the detector). This artifact is usually due to a bad calibration of the imaging system and is more pronounced for high zoom values. The differential displacements creating a blur on the images were reported to correlate well with temperature changes by Andò (2013), which means that they are amplified in the case of long duration scans. Figure 3.4 gives an example of a slice taken through a 3D reconstructed image recorded in local tomography. Figure 3.4a shows the slice before applying any correction. The edges of the grains are duplicated, leading to a global blur of the image as highlighted by the zoom into some grains. Figure 3.4b shows that by correcting the misalignments mentioned previously (in this specific case an offset of 3 voxels in the x direction and a tilt of  $-0.02^\circ$  around z were needed) the edges of the grains become sharper and the image relatively clear.

The linear relation given by Beer-Lambert law mentioned previously (Eq. 3.2) does not work for polychromatic beams, as it is the case for the scanner at 3SR. Since low-energy photons are more easily absorbed than high-energy photons, the beam tends to become relatively harder as it goes through the object. This phenomenon is called "beam hardening". The effect of beam hardening can be reduced by using metallic filters, such as copper and aluminum, which absorb the low-energy components of the spectrum. Despite the use of a flat copper filter placed in front of the source, beam

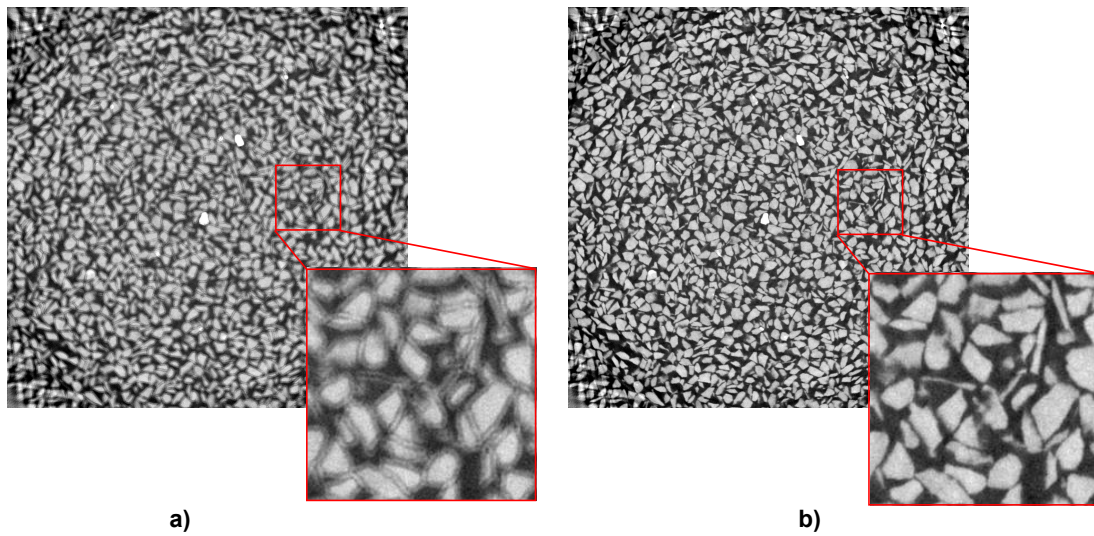


**Figure 3.4:** Horizontal slice taken through a 3D reconstructed image recorded in local tomography: a) before the correction of the misalignments and b) after correction in X-Act

hardening remains a visible artifact for the scans obtained in this work as illustrated by Figure 3.5. On the boundaries of the horizontal slice taken through the 3D reconstruction, pixel intensities are higher (brighter) than in the center, especially in global tomography. However, in most of the measurements described in Sections 3.3, beam hardening is not important enough to affect the results.

## 3.2 Image pre-processing: identification of individual sand grains

This section details the upstream work of image processing that is needed for the analysis of the 3D images at the grain scale. The methodology was adapted to the particular material employed in this study: Glageon sand, a calcareous sand (its mechanical and index properties are detailed in Chapter 4). Glageon grains are angular and produce fines when they wear or break. These specific features add complexity to the processing of the images described in this section.

### 3.2.1 Definition of different phases in the 3D images

As shown in the example of the image subset obtained in local tomography (see Fig. 3.6a), three phases are observed in the gray-scale images: pores (low gray level), intact grains (high gray level) and, possibly, fines produced by grain crushing. These fines are smaller than the pixel size, therefore they cannot be resolved at the spatial resolution of the images. However, as they partially fill voxels, they can be associated to an intermediate mean gray level. Figure 3.6a also shows the same image subset with a different color scale to help differentiating the three phases. The definition of the different phases is a crucial step in the analysis of the grain-scale mechanisms taking place during mechanical loading. To track the evolution of each phase in terms of volumetric changes or kinematics, it is imperative to isolate them from each other. The definition of each phase relies on the selection of a threshold value, which means a gray level ( $T$ ). Based on the value of  $T$ , voxels with a gray level above  $T$  will be attributed to one phase whereas voxels with a gray level below  $T$  will be attributed to a second phase. The selection of  $T$  is relatively delicate and requires a particular attention.

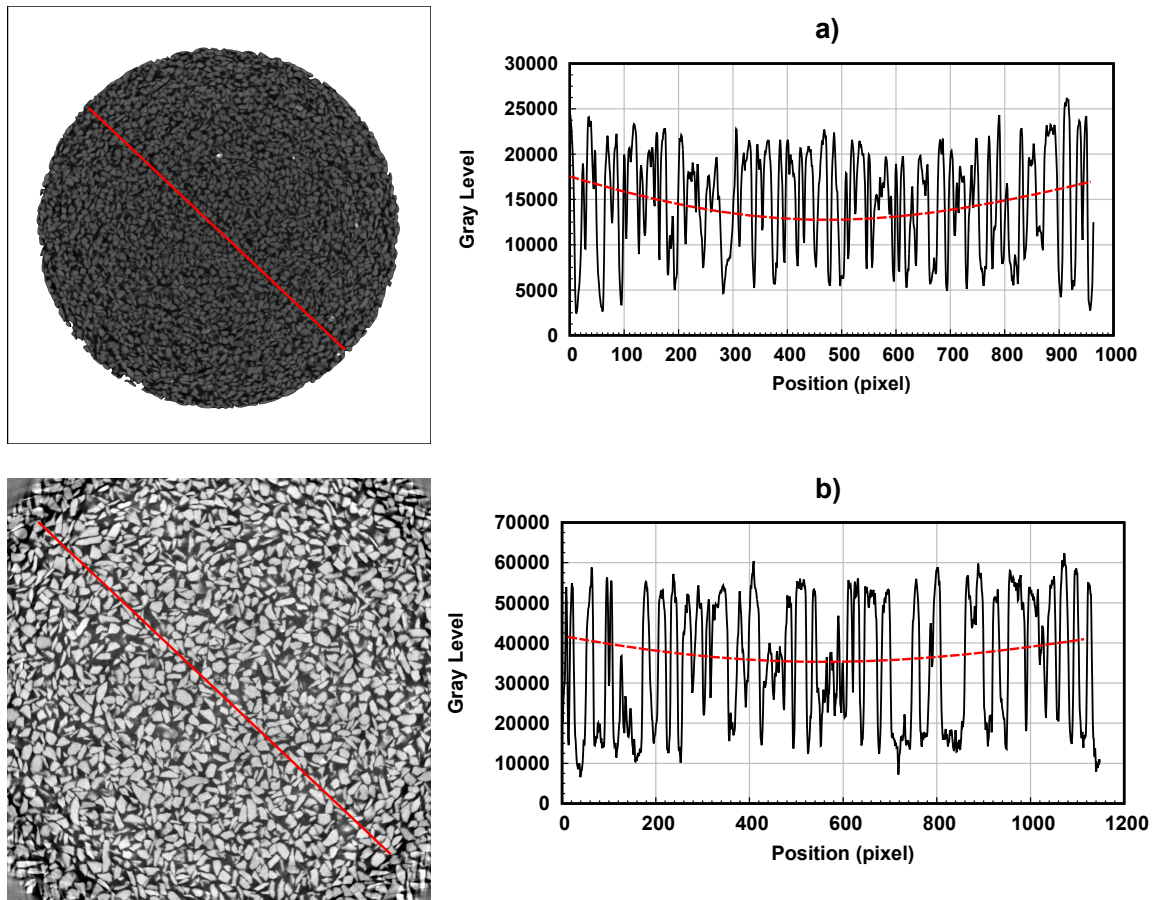


**Figure 3.5:** Illustration of beam hardening artifact on a horizontal slice a) in global tomography and b) in local tomography

In the case of two-phases media (solid and air), there are essentially two ways to select an appropriate gray level threshold value for isolating phases: an automatic thresholding method such as Otsu method (Otsu, 1979) or the determination of a threshold based on the physical measurement of the solid volume during sample preparation. In this study, neither of the two methods actually works. An automatic thresholding generally works when the histogram of the gray-scale image exhibits a clear distinct peak for each phase. In the case of Glageon sand, the presence of fines leads to an histogram with two peaks separated by a plateau (see Fig. 3.6b). Thus, this method tends to overestimate the solid phase and enlarges contacts between grains. For images acquired in local tomography, the latter method does not allow a fair comparison with the macroscopic measurement of the solid volume as only a part of the specimen is being scanned. An other source of error comes from partial volume effect. Partial volume effect occurs at the interface between two phases (*e.g.*, grains and pores) and refers to a blurring of the object edges. This artifact is mainly due to the finite size of a voxel, which includes parts of multiple phases. In the case of Glageon sand, any pixel at the interface between a grain and a pore will have an intermediate gray value similar to the one associated with the fines. Partial volume effect is visible in Figure 3.6a: a thin layer of green voxels surrounding grains having similar gray level as the fines.

Given the aforementioned limitations, the separation of the different phases was done manually. In this study, two different cases should be distinguished.

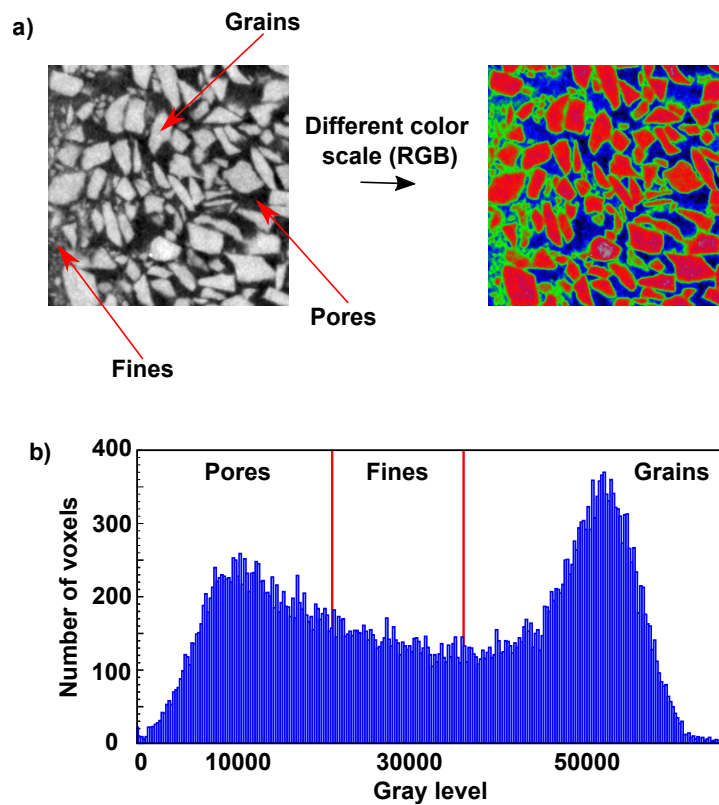


**Figure 3.6:** Illustration of the definition of the different phases in a gray image: a) Image subset (2D, 16 bit) recorded in local tomography showing grains, pores and fines. The same subset displayed with a different color scale helps differentiating the three phases (grains: red, pores: blue, fines: green). b) Histogram associated with the image subset indicating the two threshold values selected manually to isolate each phase

**Case 1:** The first case corresponds to the separation of the intact grains from the fines and from the voids. By considering three phases, two different threshold values must be selected. This case applies to the analysis of the volumetric changes of each phase (see Section 3.3). As an example, Figure 3.6b indicates the two threshold values selected for the image subset. Once the threshold are fixed, the image can be converted into binary data (binarization). The binarized image can then be used as a mask on the gray image. Figures 3.7a, b, c show the image subset after applying a mask corresponding respectively to the voids, the fines and the grains. Figure 3.7b, corroborates the fact that partial volume effect leads to an overestimation of the quantity of fines.

**Case 2:** The second case corresponds to the separation of the intact grains from the voids, *i.e.*, fines are not taken into account. This case applies to the tracking of individual grains through images in the framework of discrete DIC (see Section 3.4.3). To better isolate individual grains, the solid phase is voluntarily underestimated in order to reduce the size of contacts between grains. Figure 3.8a shows that the manual threshold is higher than the one given by the Otsu method. It is acknowledge that this arbitrary selected threshold is user-dependent. In the binarized images one can note that few grains seem to be "erased" with the manual threshold (see Fig. 3.8b, blue stars). This is a "wrong impression" simply due to the 2D configuration of the figure.

Before selecting Glageon sand as an adequate material for this experimental work, preliminary

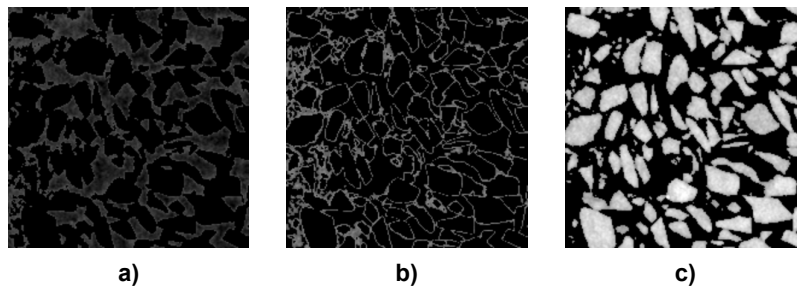


**Figure 3.7:** Result of the multiplication between the original gray-scale image subset and the binary masks created for each phase: a) voids, b) fines and c) grains

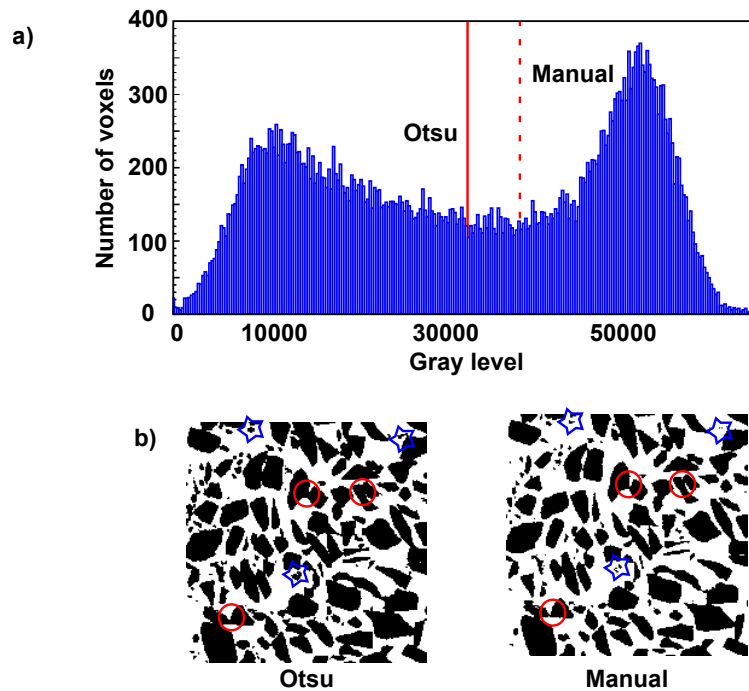


**Figure 3.8:** Selection of a manual threshold to identify (and next separate) grains in the framework of discrete DIC. a) Histogram showing the manual threshold and the Otsu threshold. b) Differences between the binary data produced with Otsu and manual threshold values: red circles show the difference in the size of the contacts between grains and the blue stars show that with a manual threshold the grain phase is intentionally underestimated

tests were conducted with different types of sand in order to choose the optimum mean grain size, which allows individual grains identification for a voxel size of  $40 \mu\text{m}$  (in local tomography). The sands employed for the calibration were silica sands chosen for their grading. Different granular fractions were sieved and scanned with identical scanning conditions as the one used for model-pile tests described in Chapter 4:  $D_{50} = 2.4\text{mm}$ ,  $D_{50} = 1.5\text{mm}$ ,  $D_{50} = 1.0\text{mm}$ ,  $D_{50} = 650\mu\text{m}$  and  $D_{50} = 338\mu\text{m}$ . Figure 3.9 shows images subsets for these granular fractions and their binarized versions. When zooming in the binary data, it can be seen that for grains with a mean particle size less than  $1.0 \text{ mm}$ , the grains are not well defined and inter-granular contacts are relatively large. These two features do not allow the identification of each grain by means of segmentation (see Section 3.2.2). A mean particle size close to  $1.0 \text{ mm}$  was then selected as a good compromise for the studied

material: Glageon sand has  $D_{50} = 1.125mm$ .

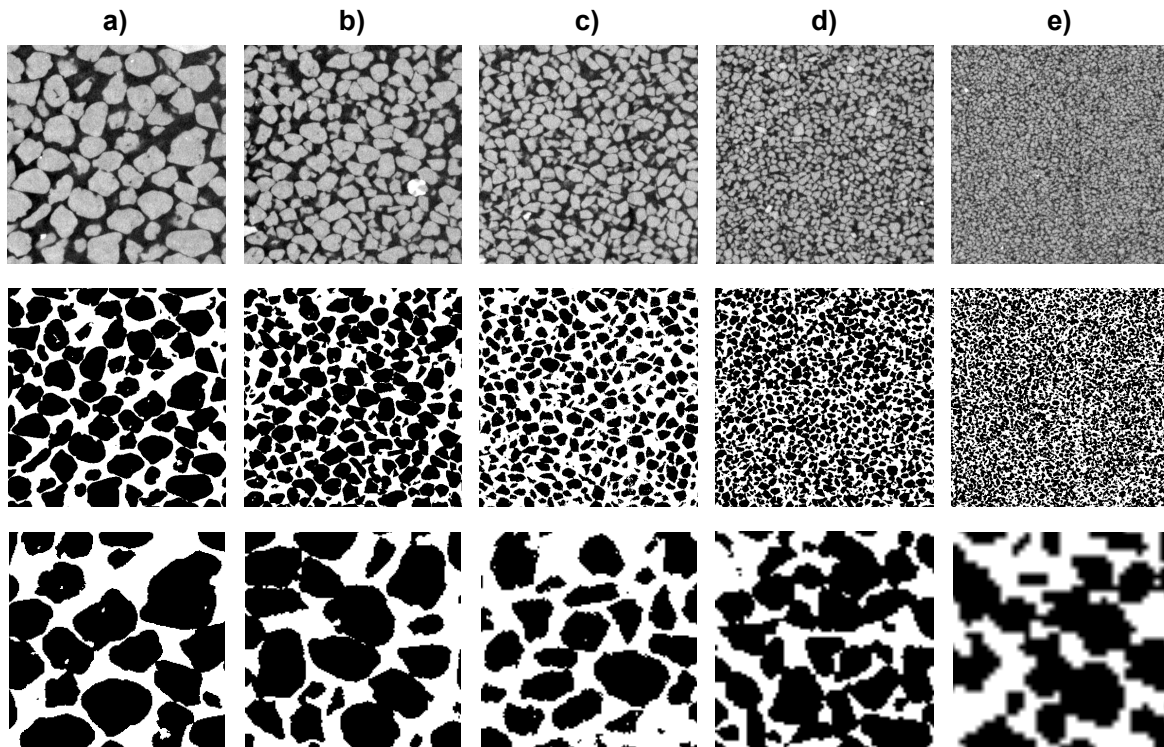


**Figure 3.9:** Image subsets taken from x-ray images recorded in local tomography, with a voxel size of  $40\ \mu m$ . Different fractions of silica sands were imaged: a)  $D_{50} = 2.4mm$ , b)  $D_{50} = 1.5mm$ , c)  $D_{50} = 1.0mm$ , d)  $D_{50} = 650\ \mu m$  and e)  $D_{50} = 338\ \mu m$ . The first row shows the raw gray-scale image subsets. The second row shows the binarized image subsets. The third row shows a zoom in the binary data to highlight the poor quality of the binary data when decreasing the mean particle size

### 3.2.2 Segmentation of the 3D images and labeling of individual grains

Once the image was binarized following the method used for "Case 2" presented in Section 3.2.1, it was possible to separate the grains from each other thanks to a watershed algorithm implemented in the highly optimized commercial code Visilog<sup>2</sup>. Despite its optimization, the code needed several hours to perform the complete segmentation process for the size of the studied images and the number of grains to be considered (several hundreds of thousands). An example of 3D segmentation is given in Figure 3.10. Figure 3.10a shows the gray-scale sub-volume to be segmented and a slice taken through this sub-volume. Figure 3.10b shows the same sub-volume and slice after binarization. Visilog takes the binary data as the input for segmentation. The watershed algorithm implemented in Visilog is based on the definition of markers within each grain. These markers are defined as the local maxima of the Euclidean distance map calculated on the binarized image. The map indicates, for each voxel in a grain of the originally binary sub-volume, the shortest distance to the nearest voxel in the background (*i.e.*, pores). A solid voxel touching a void voxel has a small value, whereas a voxel inside a grain will have a relatively high value. The 3D image of markers is then obtained by merging local maxima in the Euclidean distance map (*e.g.*, if the "merge tolerance" is set to 5, and a maximum is at a value of 10, then all voxels contiguous with that maximum having a value greater than or equal

<sup>2</sup>Copyright Noesis, see <http://www.noesisvision.com/>

to  $10^{-5}=5$  will be included in the marker). The definition of the markers can be erroneous in some cases: flat contact between two grains, a grain with an internal porosity or grain with a low compactness<sup>3</sup>. A not well-defined marker can lead to under-segmentation (two grains are merged into a single grain) or over-segmentation (one grain is split into two grains). This phenomenon is illustrated in Figure 3.10c showing the sub-volume and slice after segmentation. A grain circled in red on the slice is over-segmented and split into two different grains. To better understand this problem Figure 3.10d presents the Euclidean distance map of the binary slice. The map is displayed as a landscape where grains are hills and pores are valleys. A zoom into the distance map shows that the highest values of the over-segmented grain form a ridge with a thinner part indicated by the arrow in the figure. Thus, two markers can be defined on each side of the arrow resulting in the splitting of the grain.

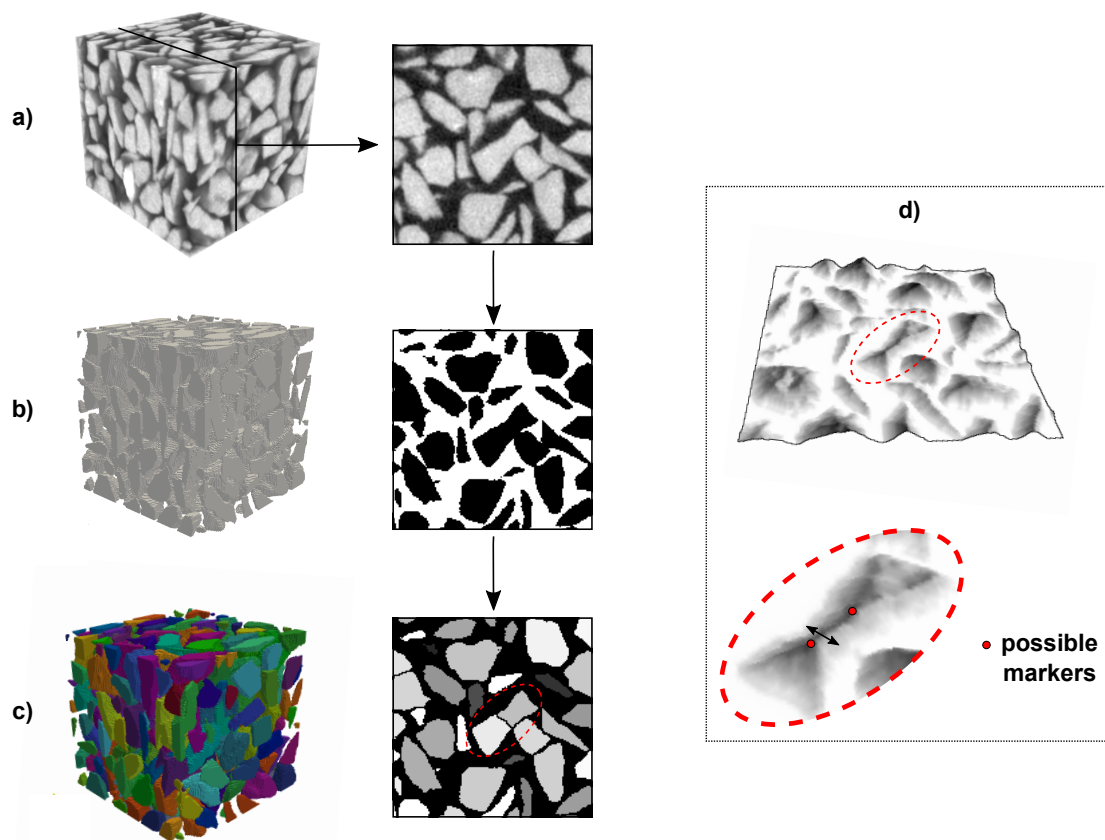


**Figure 3.10:** Diagram showing the segmentation process on a sub-volume. a) Gray-scale sub-volume and a 2D slice taken from it. b) Sub-volume and slice after binarization. c) Sub-volume and slice segmented and labeled showing a grain split into two particles (over-segmentation). d) 2D Euclidean distance map of the binarized slice displayed as a landscape and zoom showing two possible local maxima detected as markers for watershed segmentation

The watershed is analogous to the flooding of a landscape (the Euclidean distance map), with a source of water from each marker. The landscape is progressively flooded with markers expanding. When two different markers meet, the interface between the two markers defines the watershed

<sup>3</sup>The classical compactness of a solid is measured by the ratio between the  $area^3$  and the  $volume^2$  which is dimensionless and minimized by a sphere

point/line/surface, which is the output of the algorithm. The voxels belonging to the watershed point/line/surface are subtracted for the grains in the binary image. The result is a binary image with separated grains. Please note that the pile was masked and treated as voids (gray level equals to 0) in all the binary images for practical reasons.

Finally, the individual grains were labeled with a unique number (positive integer). Visilog assigns increasing values of labels as it traverses the volume from the bottom to the top. Each grain can be easily extracted from the volume by selecting only the voxels associated with its label. Visilog also provides geometrical features for each grain that can be used to track grains from one image to another: a bounding box and a center of mass. The bounding box is a parallelepiped adjusted to the volume of the grain. The center of mass is defined as the spatial average of all the voxels that make up the grain, weighting voxels equally. It is noteworthy that the center of mass of a voxel is considered to be in the middle of that voxel. Other features are available such as the maximum/minimum dimensions or the volume of the grains but are not used in this study.

### 3.3 Measurement of soil density / porosity

Initial soil density is known to have a major influence on both tip and shaft resistance of piles in sand. From pile penetrometer tests carried out on homogeneous sand in a large testing tank, Kérisel et al (1965) showed that deep foundations ultimate capacity is a function both of soil density and friction. Alawneh et al. (1999) investigated the effect of pile placement method (driven and jacked), initial sand conditions, pile surface roughness and pile end type (open or closed) on the ultimate uplift shaft resistance of piles in sand. The authors ranked initial sand density as the most important factor: an increase of sand density from 45% to 70% results in an average increase of the ultimate shaft resistance of 70% for driven piles and 100% for jacked piles. A number of other remarkable studies demonstrate the influence of soil initial state (density and stress level) on pile capacity: see for instance Foray (1991), Salgado et al. (1997) and Klotz and Coop (2001).

It was also shown that pile installation induces significant local density changes at the interface. Robinsky and Morrison (1964) studied sand displacement and compaction patterns around driven flat base model piles on loose to medium sand samples. By means of radiography technique they observed a zone approximating the shape of a cone beneath the pile where vertical compression and two-directional horizontal expansion take place. They also measured a vertical expansion within a thin zone around the pile shaft. From CPT tests in sand of different relative densities, Chong (1988) showed that the sand close to the shaft undergoes considerable loosening and that the sand beneath the tip undergoes densification for loose samples or loosening for dense samples. Similar observations were reported in subsequent studies by Nes (2004), Ngan-Tillard et al. (2005).

More recently, Dijkstra et al. (2010) and Dijkstra and Broere (2010) developed a new method to investigate soil density change during pile installation and cyclic loading based on electrical resistivity measurements. The results of a series of centrifuge tests on instrumented model piles showed that density change is correlated to the change in apparent shaft resistance for initially loose and dense saturated sand samples.

In this work, x-ray images were analyzed to characterize the state of the tested samples prior to testing. A detailed study of local porosity changes induced by pile installation and cyclic loading at the interface was also used to better understand the macroscopic response of sand pile interface. The results of this analysis are presented in Chapter 6. The methodology employed to measure porosity

was adapted through different scales: a mesoscopic approach was used for the overall sample characterization and a grain-scale approach was used for the analysis of local density changes.

### Mesoscopic approach: overall sample characterization

As described in Section 3.2.1, x-ray images allow the identification of different phases following the methodology presented for "Case 2": solid phase (grains + fines) and voids. The sample density can be described by estimating the porosity as the ratio between the void phase volume over the total volume.

To generate a 3D porosity field, the solid and void phases were integrated over sub-volumes in the 3D images obtained by x-ray tomography. These sub-volumes should be large enough to be representative of the granular material and small enough to give a "local" porosity measurement. The minimum size of a sub-volume which leads to stable porosity measurements over the sample was chosen as the optimal size, then the corresponding sub-volume was referred as Representative Elementary Volume (REV). The program used to find the REV was implemented by Andò (2013). It consists in defining a set of regularly spaced calculation nodes over the 3D image. For each node, the program grows a cubic sub-volume, centered on the node, over which is calculated the porosity. The porosity measurement is equal either to 0% (sub-volume corresponding to the solid phase) or 100% (sub-volume corresponding to the void phase) and evolves as the sub-volume grows. Once the sub-volume is large enough to be representative, the porosity measurement is expected to tend towards the macroscopic porosity of the sand sample (provided that the sample is relatively homogeneous).

In this study, the REV was found based on the 3D images recorded for the initial state of the test, when the sample did not yet experience any loading (apart from a mean stress of 100 kPa). At this stage, the sand sample was considered as having a relatively homogeneous density. Figure 3.11a illustrates the estimation of the REV size. This example shows that starting from a size of 50  $pixel^3$ , which means that there are about 30 grains within the sub-volume, the porosity measurements converge towards a common value of about 45%. This sub-volume size was selected as a good compromise for the REV for all the mesoscopic measurements of porosity.

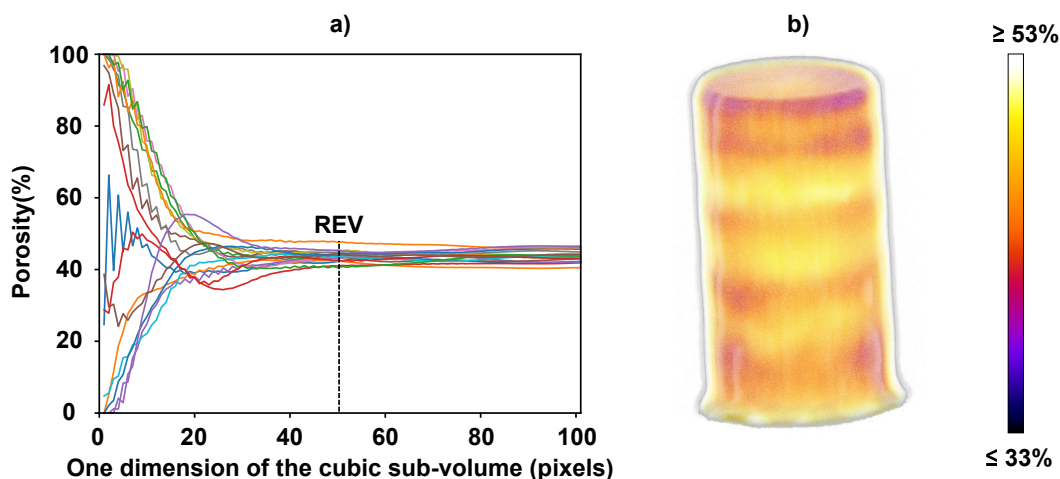


**Figure 3.11:** Example of sample characterization at the initial state. a) Evolution of the porosity measurement as the cubic sub-volume on which it is measured increases from one voxel to a cube measuring 100  $pixel^3$  and selection of the REV size. b) 3D porosity field for the selected REV of 50  $pixel^3$

Figure 3.11b shows an example of 3D porosity field for a sample at its initial state. Note that in this work, whenever the porosity field is presented as an image, it is always filtered for noise with a 3D median filter of radius 3 pixels. This filter replaces each voxel gray level with that of the median value of voxels inside a small sphere centered on that voxel.

Despite a careful calibration of the x-ray source, several artifacts described in section 3.1.4 can affect the porosity measurements. For instance, small variability in the x-ray beam leads to a shift in gray-level values between two scans. To fairly compare the porosity measurements made at each step of the loading, the histogram of the 3D images were normalized. The normalized gray level  $G_n$  of each voxel "v" can be expressed as in Eq. 3.3, where  $G_i$  is the initial gray level of "v",  $Peak_p$  is the gray level associated with the pores peak in the initial histogram, and  $Peak_g$  is the gray level associated with the grains peak in the initial histogram.

$$G_n(v) = \frac{G_i(v) - Peak_p}{2(Peak_g - Peak_p)} + 0.25 \quad (3.3)$$

Although very useful, the porosity fields obtained up to this point suffer from several limitations. First, the grid of calculation nodes defined over the image does not account for the presence of interfaces. The sub-volumes located at the interface between the sand and the pile can lead to inaccurate measurements since voxels belonging to the pile are considered as being part of the void phase (the pile was masked as mentioned in section 3.2.2). Second, the powder produced by grain crushing is not set apart from the intact grains. For these two main reasons, an alternative approach was developed to follow quantitatively local density changes at the interface.

#### Grain-scale approach: density changes at the interface

The grain-scale approach accounts for the three phases identified in the images: grains and fines are considered separately. This is no longer simply a question of density changes, but of production of fines by grain crushing. In the present study, density is expected to vary radially from the pile shaft. For this reason, the percentage of voxels belonging to each phase was estimated within 5-voxels-thickness hollow cylinders centered on the pile axis around the shaft as illustrated in Figure 3.12. The size of the cylinders was selected to get a sufficient resolution of the measurement of fines quantity.

### 3.4 Measurements of full-kinematics thanks to 3D-Digital image Correlation

DIC is a pattern recognition technique that compares two images (2D or 3D) recorded at two different time steps and provides a full-field measurement of kinematics. DIC has been increasingly used during the last 20-30 years in experimental geomechanics. In the field of soil-structure interaction, White and Bolton (2004) developed an innovative technique using PIV (Particle Image Velocimetry) to study the displacement and the strain paths experienced by the soil during the installation of a plane-strain model pile in a calibration chamber. The Authors reported a detailed analysis of pile penetration mechanisms and examined the influence of soil type, initial state, pile breadth and the use of a driving shoe. PIV is a DIC technique used primarily in fluid dynamics where the fluid is seeded with particles that follow the flow field. This technique was also employed for the investigation of static (pile, footing) and dynamic (projectile) penetration in granular media by means of transparent model soils (Lehane and Gill, 2004; Iskander, 2010; Liu and Iskander, 2010; Omidvar et al., 2015;

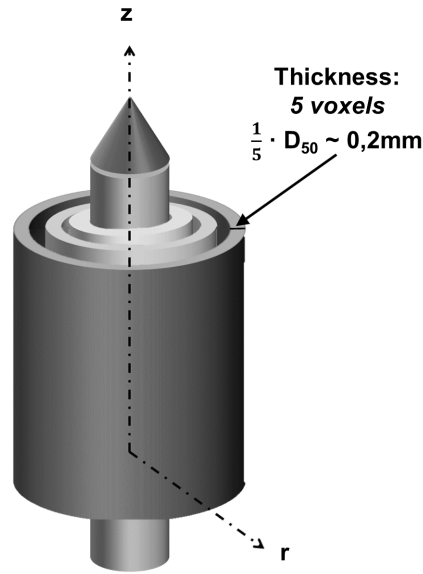


**Figure 3.12:** Local density changes at the interface: sketch showing the subdomains over which the percentage of each phase (grains, fines and pores) is estimated. These subdomains are hollow cylinders with a thickness of 5 voxels (*i.e.*, 0.2 mm), coaxial to the pile

Chen et al., 2017). Classical DIC was used in a thorough study of soil displacements resulting from cone penetration in sand conducted by Arshad et al. (2014). The results of a series of CPT tests performed in a half-circular chamber allowed the identification of different zones of displacements around the cone affected by the density and the crushability of the sand, as well as the depth of penetration. In the present work, DIC provided a number of results essential to the understanding of the mechanisms governing the sand-pile interface macroscopic response.

### 3.4.1 Digital Image Correlation: general principles and methodology

In DIC, two images are compared: a reference image ( $I_1$ ) and a deformed image ( $I_2$ ). The objective is to find a transformation operator,  $\Phi$  (4x4 matrix), that makes these two images as similar as possible, such as:

$$I_2(\Phi.X) = I_1(X) \quad (3.4)$$

$\Phi$  is an extension of the transformation gradient tensor  $F$  taking into account also the translation vector, which together with the rotations describe the rigid-body motion of the material:

$$\Phi = \begin{bmatrix} F_{zz} & F_{zy} & F_{zx} & t_z \\ F_{yz} & F_{yy} & F_{yx} & t_y \\ F_{xz} & F_{xy} & F_{xx} & t_x \\ 0 & 0 & 0 & 1 \end{bmatrix} \quad (3.5)$$

The basic steps involved in a DIC procedure are:

- the reference image  $I_1$  is divided in smaller image subsets referred as "correlation window" with calculation nodes defined at their center
- the transformation operator is applied to the correlation window

- if the transformation is not limited to a translation of an integer number of pixels, an interpolation of the gray-scale field is required
- a correlation function is defined in order to assess the similarity between the transformed subset in  $I_1$  and the image subset in  $I_2$
- the unknown components of the transformation operator are determined by maximizing the correlation function

The resolution of DIC relies on the selection of important parameters such as the spacing between each node of calculation and the size of the correlation window. The selection of these parameters is often a trial and error process, because it depends on a large number of factors including image texture, correlation method, as well as the complexity of the expected deformation pattern.

#### Correlation window

The size of the correlation window is of major importance. This parameter defines the resolution of the calculations. If the correlation window is too large, the resolution of the displacement field is reduced and the local aspect of the measurements is lost. Conversely, if the correlation window is too small, it does not contain enough information (the pattern being tracked might not be unique) and can lead to poor correlation.

#### Node spacing

A small spacing between nodes tends to smooth the field of displacements. However, if it is too small (relative to the noise in the displacement measurements) then the gradient of displacement can be dominated by noise and the strain field can not be well determined.

### **3.4.2 3D-Digital Image Correlation: continuum approach**

Continuum DIC is the most commonly used approach to track an image subset (2D) or a sub-volume (3D) between two configurations. In the present study, a typical sub-volume forms a 3D pattern including multiple grains, pores and possibly fines. In continuum DIC the similarity between two sub-volumes relies on the gray levels that make up the 3D pattern. The granular nature of the material is not taken into account. In addition, the 3D displacement field within a sub-volume and between two adjacent sub-volumes is assumed to be continuous, which is why this approach is referred as continuum.

The analyses based on continuum DIC were performed using the 3D-DIC code Tomowarp2 (Tudisco et al., 2017). The six steps listed below describe the specific methodology implemented in Tomowarp2 and are also illustrated in 2D in Figure 3.13.

1. definition of a grid of nodes uniformly distributed over the reference image
2. definition of a cubic correlation window centered on each node
3. calculation of the similarity between two image subsets for different displacements of the correlation window within a region, called search window, in the deformed image (the transformation operator is limited to a translation of an integer number of pixels)
4. the displacement giving the best correlation between the two image subsets is defined as the real displacement of the node considered (pixel search)

5. the displacement obtained being an integer number of pixels can be refined by using a sub-pixel method (sub-pixel search)
6. if required, the strain field can be deduced from the gradient of the derived displacements and a continuum assumption

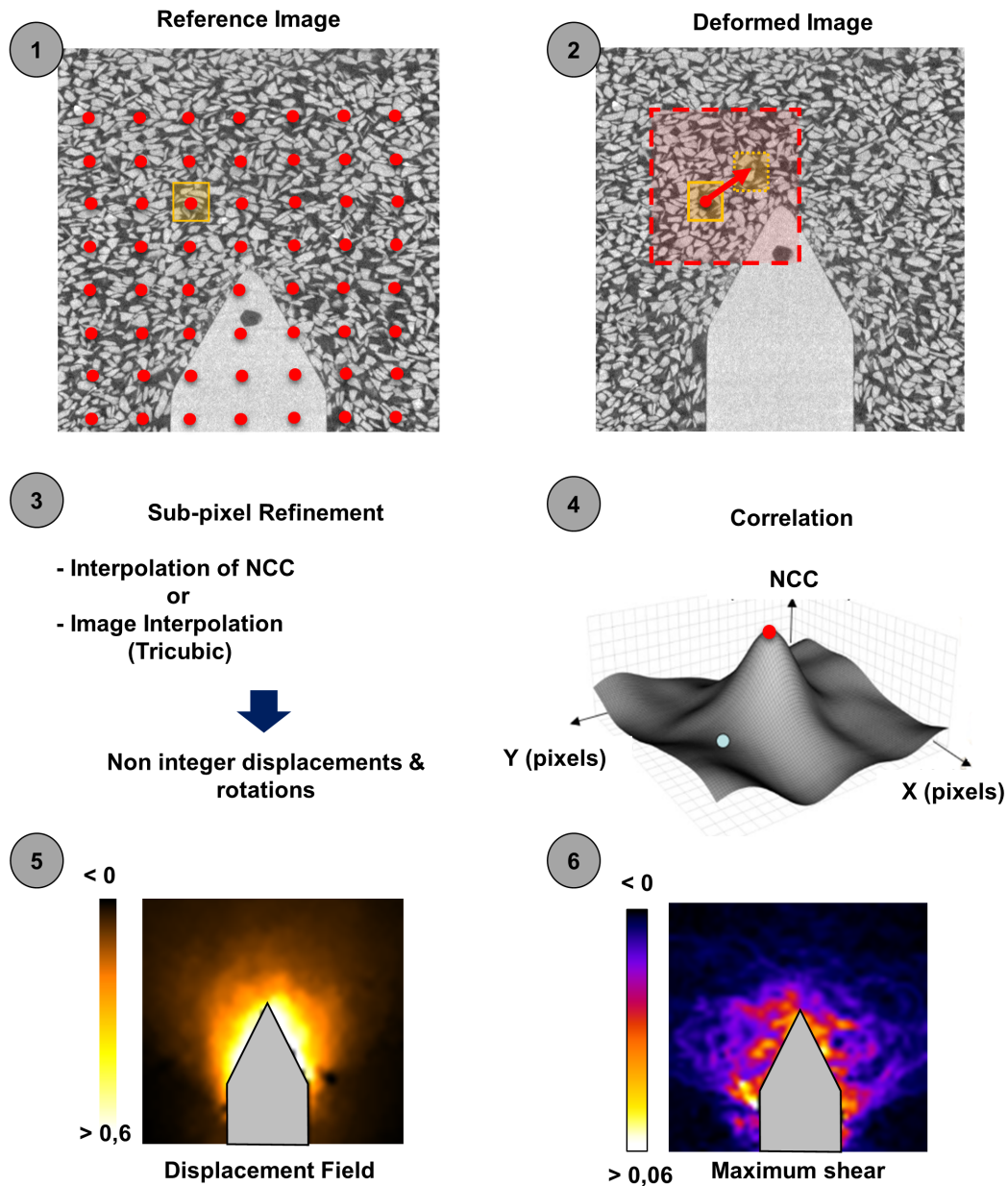


**Figure 3.13:** Flow chart explaining the different steps of continuum DIC implemented in Tomowarp2 (existing code employed in this work). The example is given in 2D for clarity and show the displacement field and the maximum shear strain field for an incremental displacement of the pile tip of 1.0 mm

There is a number of correlation functions that can be used to assess the degree of similarity between two images. The function used in Tomowarp2 is normalized-cross correlation (referred as NCC) defined in 3D by Eq. 3.6, where  $(x,y,z)$  are the spatial coordinates and  $(u,v,w)$  the Cartesian components of the displacement imposed to the correlation window to a new position in the deformed image ( $I_2$ ). The function is normalized to account for possible variations in lighting and contrast between  $I_1$  and  $I_2$  that can lead to erroneous correlation.

$$NCC(u, v, w) = \frac{\sum_{x,y,z} I_1(x, y, z) I_2(x + u, y + v, z + w)}{\sqrt{\sum_{x,y,z} I_1(x, y, z)^2 \sum_{x,y,z} I_2(x + u, y + v, z + w)^2}} \quad (3.6)$$

The maximum of the NCC function (or the minimum of 1-NCC) defines the best integer shift of the correlation window. X-ray images are, by nature, discretized into pixels, which means that the highest resolution that is reachable with Tomowarp2 is that of a pixel. This pixel resolution leads to a stepped displacement field and, as a consequence, to high strain values associated with the jumps. Two methods implemented in the code allow a sub-pixel resolution: interpolation of the correlation coefficient and gray-scale interpolation of the deformed image.

#### Interpolation of the correlation coefficient

This method consists in finding the maximum of the local variation in the correlation coefficient for test displacements (of 1 pixel) around the best integer displacement determined in the pixel search. The correlation coefficient is described by a quadratic function and interpolated for sub-pixel displacements over this neighborhood. The "new" maximum is determined using Newton's method and gives the "new" sub-pixel displacement of the image subset. This method is relatively fast but is limited to rigid body translation as a more complex transformation would require a gray-scale interpolation as in the following method.

#### Gray-scale interpolation

This method is based on the interpolation of the pixel values (gray-scale) of the deformed image with an optimization of the transformation (translation and rotation) of the deformed image to match the reference image (or vice-versa). The code uses a spline interpolation of the requested order (selected by the user). The optimization of the transformation is based on Powell's method (unconstrained optimization by quadratic approximation).

Tomowarp2 also provides the full-strain tensor field using a trilinear gradient function of the nodal displacements of cubic elements. The output are individual 3D fields of the each component of the strain tensor, as well as the three invariants of the strain tensor. The strain tensor  $E$  is determined through the strain gradient tensor  $G$  and the right Cauchy-Green deformation tensor  $C$  defined in Eq.3.7, where  $I$  is the identity tensor and  $\frac{\partial u}{\partial x}$  is the gradient of the displacements.

$$\begin{aligned} G &= I + \frac{\partial u}{\partial x} \\ C &= F^T F \\ E &= \frac{1}{2}(C - I) \end{aligned} \quad (3.7)$$

The maximum shear strain tensor is expressed as

$$\frac{1}{\sqrt{3}} \sqrt{2(\epsilon_{11} - \epsilon_{22})^2 + 2(\epsilon_{11} - \epsilon_{33})^2 + 2(\epsilon_{22} - \epsilon_{33})^2 + 3\epsilon_{21}^2 + 3\epsilon_{31}^2 + 3\epsilon_{32}^2} \quad (3.8)$$

In this PhD work, the volumetric strain obtained from DIC are not presented. During pile installation, DIC was performed on image pairs recorded after an incremental displacement of the pile of 1.0 mm. For such an incremental step, the volumetric strain field was dominated by noise.

### 3.4.3 3D-Digital Image Correlation: discrete approach

In the case of sand-pile interface, continuum DIC cannot take into account the possible discontinuities in displacement between the pile and the grains or between the grains themselves. Grain breakage is another important aspect that is not considered with the continuum approach; rather, the presence of broken grains tend to affect the correlation since the pattern in the reference image can not be tracked in the second image. Therefore, a discrete version of 3D-DIC has been developed in Tomowarp2 to track each individual grain from one configuration to an other (Hall et al 2010). The main difference with the continuum approach is that the correlation window is replaced by subsets centered on individual grains that follow the actual shape of the grains and include only a single grain. In discrete DIC the similarity between two sub-volumes relies on the gray levels that make up the 3D pattern (if the grain is not homogeneous) but most importantly on the actual shape of the grains.

Discrete DIC requires an upstream work of image pre-processing not needed for continuum DIC. An appropriate identification of individual grains is crucial to ensure a good correlation. This pre-processing was conducted using the method described in Section 3.2.2.

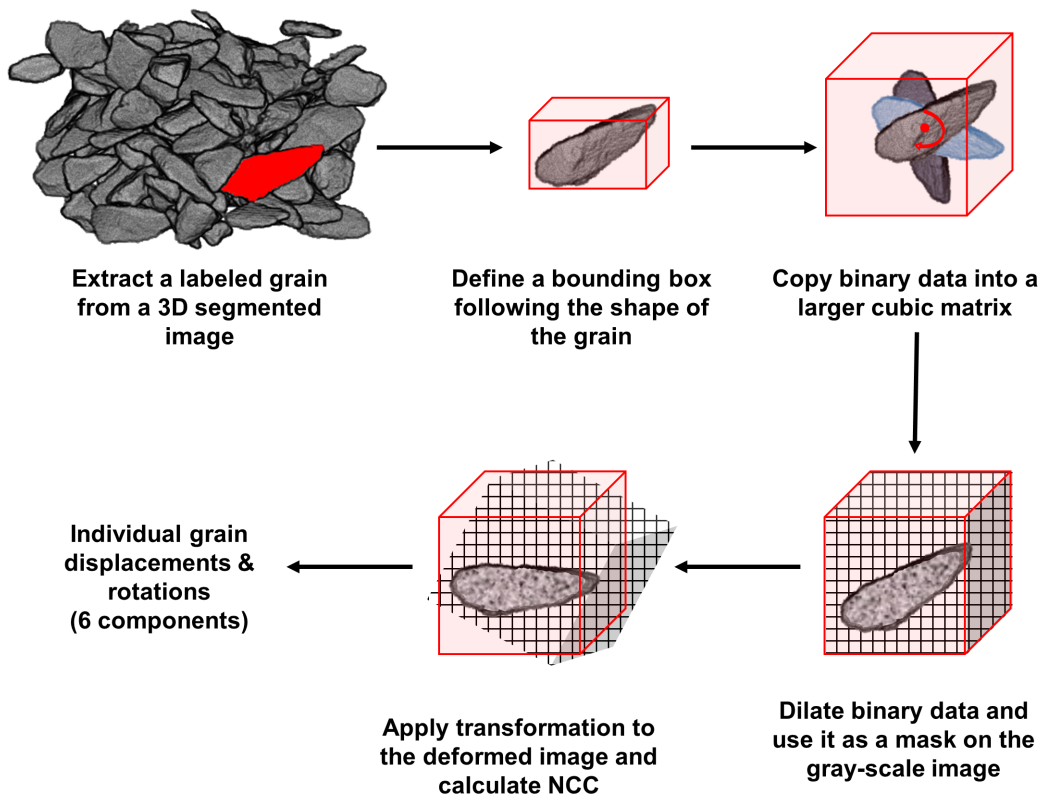


**Figure 3.14:** Flow chart showing the main steps of the implementation of the 3D discrete DIC in Tomowarp2

Once the grains are identified and labeled, discrete DIC can be performed following the steps described in Figure 3.14. In Tomowarp2, the correlation window defined for discrete DIC is the bounding box obtained thanks to Visilog (see Section 3.2.2). All the voxels in the bounding box that

do not have the same label value as the grain being tracked, which means parts of other grains, are removed. The information within the subset is binarized: the voxels part of the voids are treated as 0 and the voxels part of the grain are treated as 1. The binary data is copied into a larger cubic matrix allowing the 3D rotation of the grain around its center of mass. The binary data is then dilated and used as a mask on the gray image. The dilation ensures that all the information in the grain is considered. The rest of the procedure is the same as continuum DIC (NCC calculation and subpixel refinement). In addition, the discrete method implemented in TomoWarp2 provides the 3D rotation of each individual grain. The result is given as a rotation vector with three components describing the axis around which the grain rotates, the norm of which gives the angle of rotation. The DIC code uses the Rodrigues' rotation formula (Andò, 2013) to define such a rotation vector.

### 3.4.4 Optimal set of parameters for 3D-Digital Image Correlation

#### Continuum DIC

As mentioned previously, the selection of the size of the correlation window is of main importance in the resolution of DIC results. In this work, a cubic correlation window of 40 voxels (*i.e.*, it includes about 8 grains) was selected as a good compromise using a trial-and-error approach. The REV size (50 voxels) calculated for the measurement of porosity in Section 3.3 was used as a first guess for the determination of the size of the correlation window. At the interface, a window smaller than 40 voxels could not be tracked since its pattern was highly modified from one image to another due to grain crushing.

Without sub-pixel search, a typical DIC calculation takes about 30 min, whereas with sub-pixel search (including translation and rotation) it takes about 32 hours. This computational time was reduced by performing a two-steps calculation. In the first step, the DIC code was run with a relatively large node spacing (40 pixels) and a large search window (*e.g.*,  $\pm 10$  pixels). In the second step, the node spacing was reduced to 20 pixels and the search window was reduced to  $\pm 2$  pixels. Then, the DIC code was run by taking the output of the first step as an input, which means that the displacement field measured during the first step was used as a first clue for the second calculation. With these two steps, the computational time was at least divided by 2.

It is noteworthy that the order of the spline-interpolation used in the sub-pixel search to interpolate the gray-scale values has also a major effect on DIC results, as reported by Bornert et al. (2009). With a tri-linear interpolation, the code has a tendency to converge towards half-integer values, which results in mostly non-physical lines patterns in the strain fields. Figure 3.15 gives an example of such lines pattern in the 3D field of maximum shear strain measured during pile installation. In TomoWarp2, an order of interpolation of 3, *i.e.*, tri-cubic interpolation, is sufficient to remove this artifact and obtain a physically-reasonable result.

#### Discrete DIC

The performance of discrete DIC mainly depends on the pre-processing of the 3D images, and more precisely on the segmentation of the grains. If a successful segmentation is achieved and if all grains have relatively distinct shapes (which is the case of Glageon grains), then each individual grain should be tracked from one image to another. Only grains that break may not be found in the second image. The same problem as for continuum DIC arises with the choice of the order of spline interpolation for the sub-pixel search. Similarly to continuum DIC, a third order interpolation was employed.

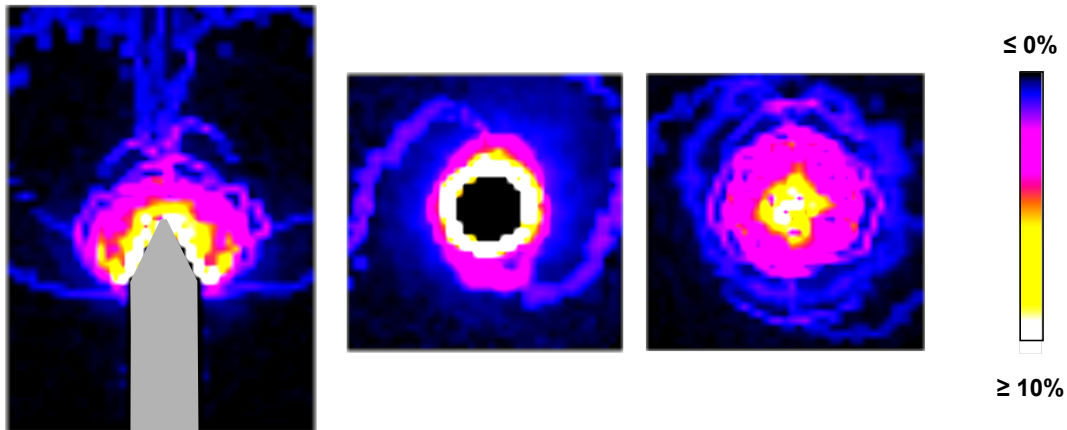


**Figure 3.15:** Example of slices through the maximum shear strain field obtained with a tri-linear spline interpolation in the sub-pixel search. Please note that the color contrast was enhanced for clarity

A parameter, specific to discrete DIC, that can potentially affect the results is the dilation applied to the binary mask presented in Figure 3.14. The dilation of the mask, *i.e.*, the binary data corresponding with the labeled grain, allows to capture all the gray-scale information (voxels) from the grain being tracked. However, the dilation should be small enough to minimize the possibility of capturing voxels that belong to other grains. In this study, a 3D dilation of 3 voxels was selected as a good compromise.

With these sets of parameters, the resolution reached for both continuum and discrete DIC was of 1 pixel, *i.e.*,  $40 \mu\text{m}$ , without sub-pixel search and  $10^{-3}$  pixel with sub-pixel search. The accuracy of the measured displacements estimated was 0.5 pixels, *i.e.*, about  $20 \mu\text{m}$ , by correlating two 3D images acquired for the same sample, at the initial state (*i.e.*, without any transformation between the two scans).

### 3.5 Grains orientations

It is well known that mechanical properties of a granular assembly is linked to the geometry of the granular skeleton, commonly referred to as fabric. Oda (1972) defined the term fabric of a cohesionless granular assembly to represent "the spatial arrangement of the particles and associated voids, including (i) the orientation of individual particle, (ii) the position of the particle and its the mutual relationship to other particles" (*i.e.*, inter-particle contacts). In Oda et al. (1985), the Author identifies the preferred orientation of non-spherical particles as a major source of fabric anisotropy, along with the change in inter-particle contacts orientation.

Numerous numerical studies using discrete element method propose a detailed analysis of fabric evolution of granular material during mechanical loading (*e.g.*, Fu and Dafalias, 2011). Experimentally, measuring accurately the orientation of individual grains and contacts becomes relatively complex. Advanced imaging techniques offer new possibilities to measure and quantify the fabric of a granular soil assembly at the micro-scale level, as proposed by Yang et al. (2008). The Authors investigated fabric anisotropy for different sand sample preparations (dry and wet), using coupon surfaces

analyzed by scanning electron microscopy (SEM) postmortem. Recently, Paniagua et al. (2018) proposed an innovative approach to link volumetric behavior to changes in soil fabric during a cone penetration test (CPTU) in silt. Volumetric changes were measured thanks to x-ray tomography and with 3D-DIC whereas the soil fabric was studied by means of high resolution 2D backscattered electron images ( $0.4\mu\text{m}/\text{pixel}$ ) obtained postmortem. In both studies, a postmortem approach is used, which implies three main limitations: (i) the soil specimen should be manipulated with minimum disturbance of the soil fabric, (ii) the selected sections should be representative of the rest of the soil mass, and (iii) the 2D measurements should be in agreement with the 3D nature of the problem studied. To the best of the author's knowledge, the work proposed by Paniagua et al. (2018) is the first experimental study investigating soil fabric in the field of pile testing.

In this PhD work, the orientations of individual sand grains were studied during a test and in 3D thanks to x-ray tomography. The measurements were made in the segmented and labeled 3D images by means of the inertia tensor following the method described by Wiebicke et al. (2015). The inertia tensor was calculated over all the voxels that make up the particle, attributing an equal weight to each voxel. The orientation of a grain was then determined based on the eigenvectors of the symmetric inertia tensor. The minor eigenvector, associated with the smallest eigenvalue, points in the longest direction of the grain, from the center of mass (it represents the axis around which the rotation of the grain is the less "energy-demanding"). The grains of Glageon sand are elongated and relatively flat as shown in Section 4.1. As expected, the inertia tensor of Glageon grains exhibits a relatively small minor eigenvector and two other eigenvectors of similar magnitude. As a result, the minor eigenvector ( $e_{min}^{\vec{}}$ ) was selected as a meaningful measure to characterize grains orientations prior to and after pile installation.

The orientation of a single grain,  $\theta$ , was defined as the angle between  $e_{min}^{\vec{}}$  and the vertical axis, which also represents the pile axis denoted  $\vec{z}$  (see Fig. 3.16). As a result of the axisymmetry around  $\vec{z}$ , the distribution of the orientations can be expressed by the probability density function of  $\cos(\theta) = x$ , denoted  $p(x)$ , with  $0 \leq \theta \leq \pi$ . By construction,  $p$  is an even function and is constant for an isotropic system. Such a function can be expanded in the series of Legendre polynomials, with only terms of even order, truncated after the 4<sup>th</sup> order

$$p(x) = 1 + A(3x^2 - 1) + B(35x^4 - 30x^2 + 3) \quad (3.9)$$

in which coefficients A and B are related to the moments of the distribution

$$\begin{aligned} A &= \frac{15}{4}(\langle x^2 \rangle - \frac{1}{3}) \\ B &= \frac{9}{64}(35\langle x^4 \rangle - 30\langle x^2 \rangle + 3) \end{aligned} \quad (3.10)$$

Coefficient "A" can be used to describe the anisotropy of the distribution as it is directly related to the difference between the second moment and its isotropic value. This method has been proposed in a number of numerical studies to analyze the inter-particle contact anisotropy in a granular assembly (e.g., Emam et al., 2006; Khalili et al., 2017). To characterize the level of anisotropy of grains orientations, the notation  $\tilde{a}$  was introduced:

$$\tilde{a} = \langle x^2 \rangle - \frac{1}{3} \quad (3.11)$$

It is important to specify that the resolution at which individual grains are imaged is of major

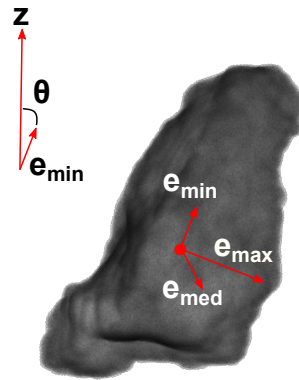


**Figure 3.16:** Scheme illustrating the measurement of the orientation  $\theta$  of a single Glageon grain.  $e_{\min}$ ,  $e_{\text{med}}$  and  $e_{\max}$  are the minimum, the intermediate, and the maximum eigenvectors of the inertia tensor, respectively

importance in the accuracy of the measurement of the inertia tensor. Wiebicke et al. (2015) studied the accuracy of the determination of the principal particle orientations using a high resolution greyscale image of an Hostun sand grain rotated via 4 different angles around a defined axis. These rotated images were scaled down to a minimum resolution corresponding to the one of a typical x-ray CT experiment. The Authors estimated an error of about  $1.8^\circ$  on the orientation of the minor eigenvector. This relatively good accuracy was attributed to the fact that the grain investigated had a clearly defined long axis. Thus, a similar level of accuracy can be expected for Glageon grains.

## Chapter 4

# Physical modeling

The previous chapter has described how the combined use of x-ray tomography and advanced image analysis tools provides both qualitative and quantitative data about kinematics at the scale of the sand grains. This chapter details small-scale physical modeling of a calibration chamber, referred as "mini-calibration chamber" is adapted to x-ray imaging. It is acknowledged that the size of the mini-calibration chamber does not respect the rules of similitude allowing a fair reproduction of field pile testing. However, the main objective of this work is to analyze the deformation mechanisms taking place at the grain-scale that govern the macroscopic response of sand-pile interface. Thanks to the reduced size of the chamber, it is possible to zoom into the specimen and to identify individual sand grains in the 3D x-ray images.

### Layout of the chapter

This chapter starts with a description of the material tested in this experimental work, its mechanical and index properties and highlights the reason why this specific material has been selected (Section 4.1). Section 4.2 describes the small scale physical model including the mini-calibration chamber, the loading device and the instrumentation used during a mechanical test. This section is followed by the presentation of the instrumented model pile (Section 4.3).

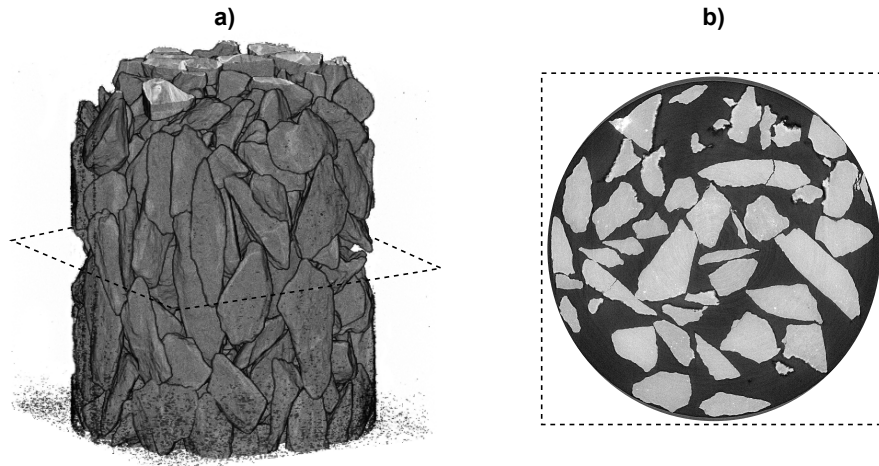
Section 4.4 presents the testing procedure for a model pile test: sample preparation, sample, confinement, pile installation and loading cycles. The main differences with field pile testing conditions are underlined in Section 4.5 in which the scale effects expected on the interface response are also discussed.

Finally, Section 4.6 summarizes the tests conducted in this work along with their main objectives and the difficulties encountered with the instrumentation of the pile.

## 4.1 Tested material

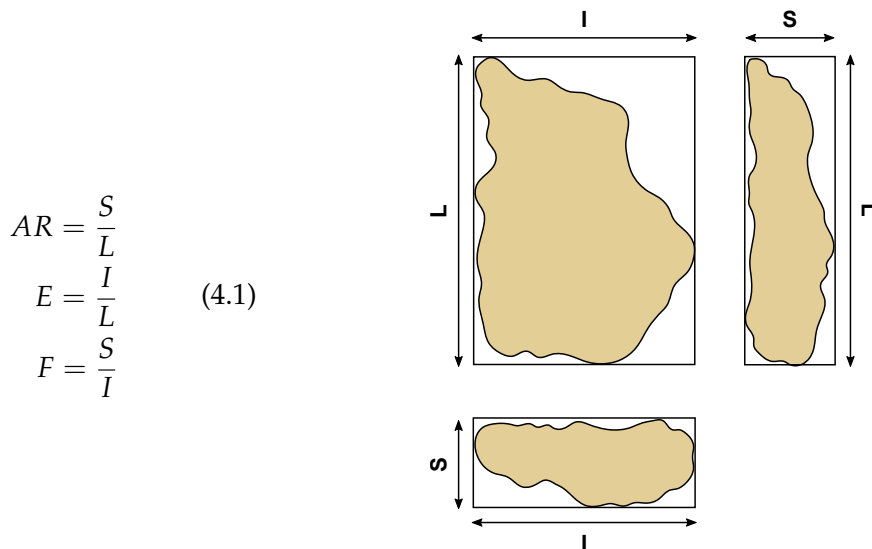
The soil used in this work is Glageon sand. This specific granular material was selected for its geometrical and mechanical properties which are particularly suitable for the present study. Glageon sand is a calcareous sand derived from a limestone rock (hard limestone from Givétien age) crushed in Bocahut quarry, in Glageon, France. The material was sieved in order to keep a fraction of uniformly graded particles with a size ranging from 1.000 mm to 1.250 mm. The remaining fraction was then carefully washed with water and dried in an oven for 48h. Thanks to such grading, the grains can be identified in the x-ray images and tracked individually from one loading step to another (see Section 3.2.2).

Figure 4.1a shows a 3D reconstructed volume of Glageon sand grains with a size ranging between 1.250 and 1.600 mm, during an oedometer test. This scan was recorded at a voxel size of  $6.5 \mu m$ , at



**Figure 4.1:** a) 3D-reconstructed volume of an oedometer sample of Glageon sand (granular fraction: 1.250 - 1.600 mm) at ESRF, Grenoble, by Dano and coworkers (2018) at a voxel size of  $6.5 \mu\text{m}$ . b) Horizontal slice taken through the reconstructed volume showing the angularity of Glageon sand grains

the European Synchrotron Radiation Facility (ESRF), Grenoble, by Dano and coworkers from Laboratoire 3SR. From the figure, it appears that Glageon grains are rather elongated. An horizontal slice taken through the reconstructed volume (4.1b) also highlights the angularity of such grains. In the present study, the shape of the grains was further analyzed on a sample scanned at the initial state (*i.e.*, before loading) in local tomography, with the x-ray device of 3SR. Although the granular fraction employed in this work is smaller than the one scanned at ESRF (1.000 to 1.250 mm against 1.250 to 1.600 mm), it is believed that the shape of the grains remain similar. The x-ray images acquired in this work were segmented as explained in Section 3.2.2 and the bounding box of each individual grain was extracted. Different shape parameters were estimated based on the dimensions of the bounding boxes (see Fig. 4.2): the aspect ratio (AR), the elongation (E) and the flatness (F) expressed as in Eq. 4.1, where  $L$  is the longest dimension of the box,  $S$  the smallest one and  $I$  the intermediate one.



**Figure 4.2:** Grains morphology based on the dimensions of the bounding box

The distributions of the shape parameters for all the grains of the volume scanned are plotted in Figure 4.3 and fitted with a Gaussian function, where  $\sigma$  is the deviation and  $\mu$  the mean. From Figure 4.3a it can be seen that most of the grains have an aspect ratio close to 0.5, which supports the fact that Glageon grains have a longer dimension and are rather elongated. However, it can be seen from Figures 4.3b, c that the flatness and the elongation are closer to 1.0. This result means that there are as many grains that are platy (as a slab) as elongated grains (as a rod). An example of a platy and an elongated grain taken from the volume in Figure 4.1 is given in Figure 4.4. It should be noted that the bounding boxes may not be reliable to measure the flatness and elongation in the case of Glageon grains. Indeed, due to the relatively complex shape of the grains, the size of the bounding boxes can be overestimated in one of the directions. Figure 4.3d shows the ratio between the volume of the grain (number of voxels making up the segmented grain) and the volume of the bounding box. It can be seen that most of the grains have a volume equal to 0.3 times the volume of the bounding box. To improve the estimation of the grains flatness and elongation, the bounding box should be defined with an orientation based on the inertia tensor of the grains. However, the objective of this preliminary shape analysis was to highlight the fact that following the orientation of the grains based on their longest dimension is actually a representative and meaningful measurement for the whole sample.

The shape and the angularity of the grains make them more vulnerable to crushing (see for instance Feia et al., 2017; Cho et al., 2006), which is the main reason why they were selected for this study. As shown by Nakata et al. (1999) and Coop et al. (2004), particle breakage is greater for uniformly graded than for well graded sands, which is also the reason why only the material from one sieve interval was used for this study.

It is well known that working on crushable sands is complex, mainly due to the sand erosion during its transportation or sample preparation. Wils et al. (2013) summarized the issues encountered in laboratory testing on crushable sands. One of the main difficulties is the estimation of accurate maximum and minimum void ratios. For calcareous sands, breaking of angular grains asperities releases small dust particles that do not lead to a visible change in grain size distribution considerably affect the densification process. The maximum void ratio of Glageon sand was evaluated following the method specified by ASTM D4254. The mold was filled with sand from a nil fall height using a funnel so that the falling grains do not have time to rearrange and compact. The maximum void ratio, was estimated following ASTM D698-12e2: nine layers of sand were deposited and each layer was tamped radially with 25 blows. In parallel, the minimum void ratio was estimated thanks to ASTM D4253-16 by using a vibratory table. Both methods gave similar results with limited amount of grain wear. Glageon sand index properties are summarized in Table 4.1.

**Table 4.1:** Glageon sand index properties

Specific Gravity ( $G_s$ )	$D_{50}$ : mm	Coefficient of uniformity $C_u$	$e_{max}$	$e_{min}$
2.65	1.125	1.25	1.070	0.839

The mechanical properties of the sand, were determined by performing a series of tests as summarized in Table 4.2. The triaxial compression tests were performed on dry sand sample, under drained conditions with a confining pressure of 100 kPa and 200 kPa.

The results of triaxial compression tests on Glageon sand are plotted in Figure 4.5. The samples were prepared dense as indicated in Table 4.2 following the same procedure as described in section

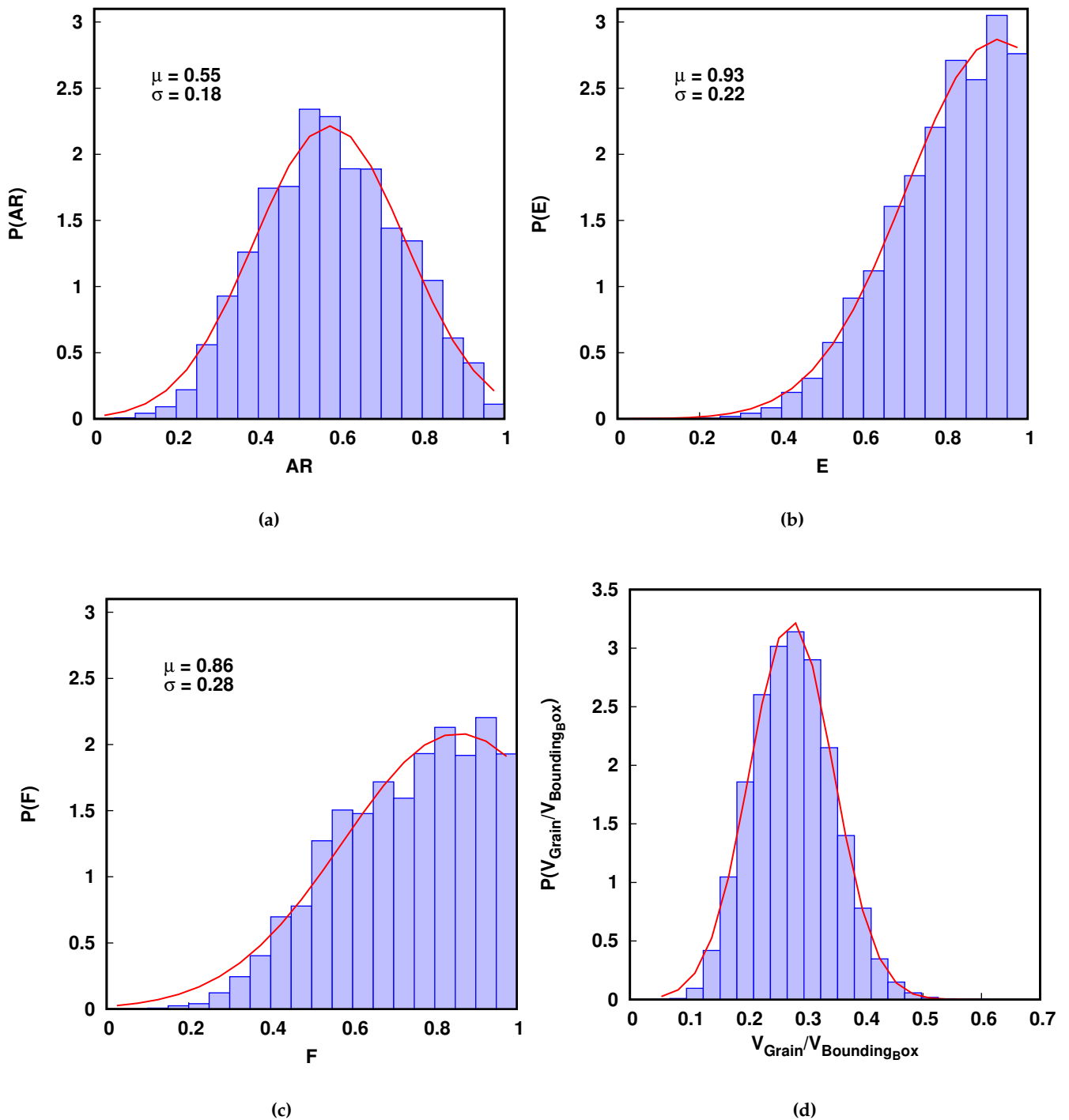


**Figure 4.3:** Preliminary shape analysis of Glageon sand grains based on the bounding boxes: a) aspect ratio, b) elongation and c) flatness. d) Ratio between the volume of the grains over the volume of their bounding box. The red curve show the Gaussian fit associated with a deviation  $\sigma$  and a mean  $\mu$

4.4.1. The three tests exhibit typical results for a dense granular material. Figure 4.5a shows a quasi-linear deviatoric stress evolution at low strain values, followed by a non-linear evolution until a

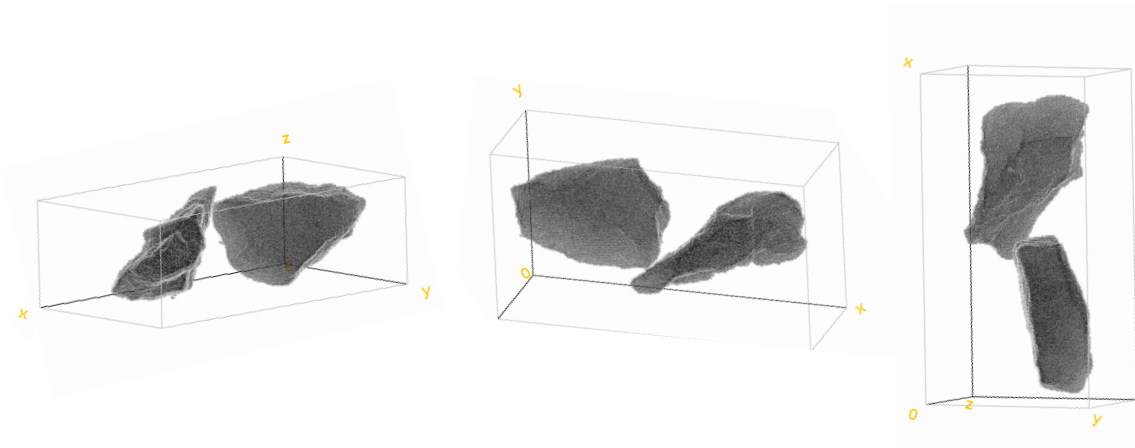


**Figure 4.4:** Example of two grains extracted from the reconstructed volume of Figure 4.1. The grains are displayed in different orientations to show that one is rather elongated and the other one platy but both have a longer dimension

**Table 4.2:** Testing program to characterize Glageon sand

Test Name	Conditions	Initial $D_r$ (%)
TRIAX-GLAG-00	Drained - 100 kPa	104
TRIAX-GLAG-01	Drained - 100 kPa	94
TRIAX-GLAG-02	Drained - 200 kPa	94

maximum deviatoric stress (reached at 12% and 17 % for a confining pressure of 100 kPa and 200 kPa respectively). The tests continue with a softening phase at a reducing rate. The tests were stopped at a maximum axial strain of 35 %. In the case of Glageon sand, it was not possible to reach a plateau of residual stress. The volumetric response, presented in Figure 4.5b, starts with a contraction followed by a continuous and significant dilation. Tests TRIAX-GLAG-01 and TRIAX-GLAG-00 show very similar deviatoric responses. The volumetric behavior is slightly different. This difference is likely due to the difference in initial relative density. TRIAX-GLAG-01 shows a more contractant behavior at the beginning of the loading, due to its lower initial relative density.

Figure 4.6 shows the grain size distribution obtained by sieving before and after triaxial testing. Youd (1972) stated that grain crushing is significant when the minimum increase of particles passing any sieve is more than 2 %. Based on this statement, it is clear that triaxial testing lead to grain crushing at both confining stress. Increasing the confining stress also results in a higher percentage of smaller particles. Grains passing the 1 mm sieve increased to 20 % and 40 % for the tests respectively conducted at 100 and 200 kPa. The percentage of grains passing through smaller sieves also increased significantly (2 to 10 %). This result suggests that different mechanisms of grain breakage occurred: fracture, attrition of small asperities and eventually wear of grains producing fines that were not quantified during sieving. The two tests performed at 100 kPa exhibit very similar responses and also show the reproducibility of the tests results.

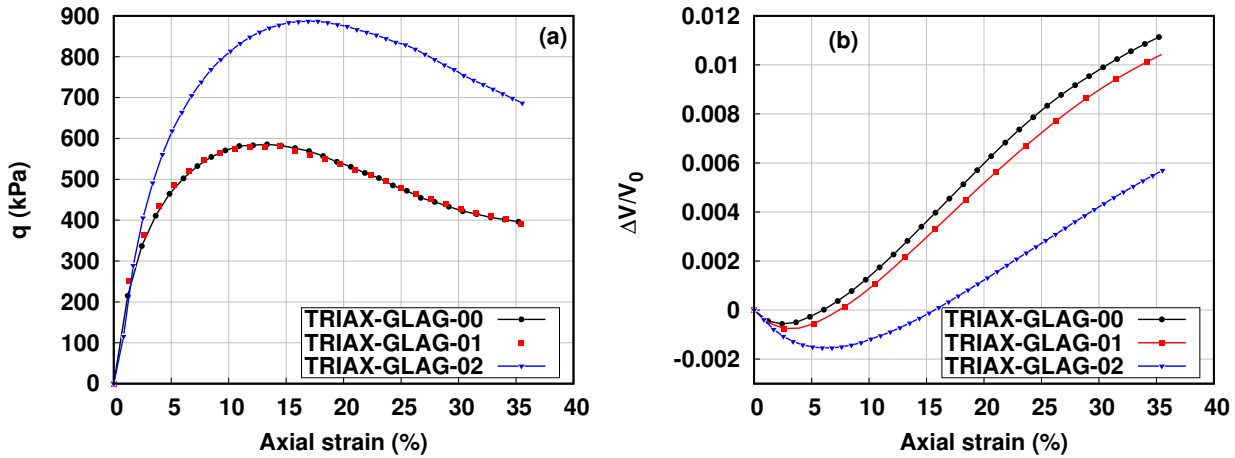


Figure 4.5: a) Deviatoric response of Glageon sand and b) Volumetric deformation curves for different confining pressures (100 kPa and 200 kPa)

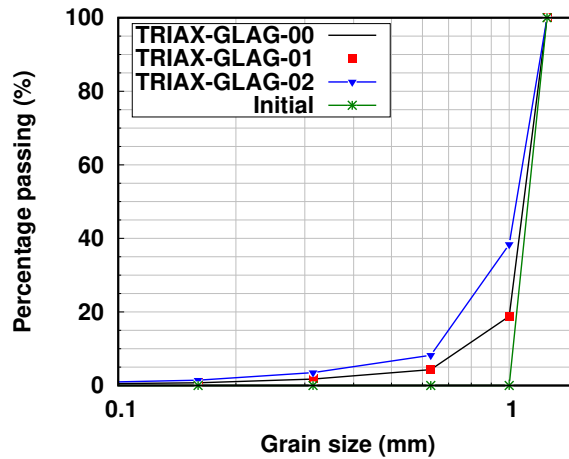


Figure 4.6: Grain size distribution before and after triaxial compression at different isotropic confining pressure on dense sample of Glageon sand

## 4.2 Small-scale physical model

### 4.2.1 Description of the mini-calibration chamber

The mini-calibration chamber was originally developed by Silva Illanes (2014), and was modified as part of this research work. It consists of a cylindrical Polycarbonate cell that allows the application of different magnitudes of uniform confining stress via externally applied pressurized fluid (in this case air or water) to the sand sample. Polycarbonate was selected for its relatively low x-ray absorption coefficient. Figure 4.7 shows a scheme of the experimental arrangement including the chamber, the model pile, the loading device and the load sensors.

### 4.2.2 Loading device

The loading device employed to apply monotonic and cyclic loadings to the model pile was a worm gear motor which drives a loading head up or down. For this study, two different devices were used.

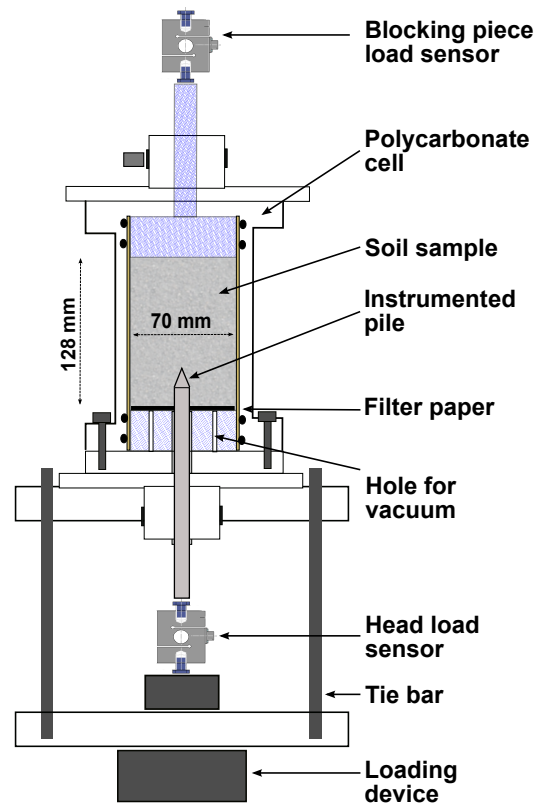


**Figure 4.7:** Scheme of the mini-calibration chamber mounted on the loading device

The first one was used at a speed of 0.06 mm/s (its minimum speed) to remain in the quasi-static domain. A second loading device, with a higher precision and a higher load capacity, was acquired later in this research work, allowing the application of a loading rate of 25  $\mu\text{m/s}$  (its maximum speed). The difference in the applied loading rate was considered to be negligible for the analysis of the tests.

The use of the mini-calibration chamber within a tomograph implies a very specific configuration of the setup. Indeed, no parasite object should pass in front of the x-ray source during the scan (cables, screws, etc). Thus, the entire loading device was suspended below the rotation stage of the tomograph by four tie bars. These bars were also linked to the cell to ensure the rotation of the entire setup during a scan. This means that the model pile was inserted upwards, from the bottom of the chamber.

### 4.2.3 Instrumentation

To measure the force applied by the loading device to the model pile, a force meter was installed on the top of the loading head and tied to the model pile head. This force meter was calibrated beforehand with a reference force meter (see Fig. 4.9a). Its maximum capacity is 1.0 kN. The axial displacement of the loading device and, thus, of the model pile was measured thanks to a linearly variable differential transformer (LVDT) placed on the loading head. The stroke of the LVDT is 1.0 cm. Finally, the confining stress around the sample was kept constant during a test at 100 kPa thanks to a pressure meter linked to the cell by a pipe. The precision of the measurements is given in Table 4.3.

## 4.3 Instrumented model pile

### 4.3.1 Description of the model pile

The model pile is a tubular aluminum probe with a length of 21.6 mm and a diameter of 14 mm (see Figure 4.8a). This diameter was the minimal diameter required by the designer, DOERLER Mesures, for the internal instrumentation of the pile. The tip is conical and has an apex angle of 60 degrees. It is linked to an inner rod instrumented with strain gauges as shown in Figure 4.8b. The model pile was calibrated as shown in Figure 4.9b. Its maximum capacity in compression is 1.5 kN. The precision of the strain gauges was estimated based on the standard deviation of the slope (0.64 V) and offset (3 V) measured during five different calibration tests. These gauges measure independently the load applied to the tip during a test. By subtracting the tip load from the head load measured by the head load sensor described in Figure 4.7, the shaft resistance was also measured during a test. The pile was made of aluminum instead of steel, as it is the case for typical field piles, since aluminum has a moderate x-ray attenuation.

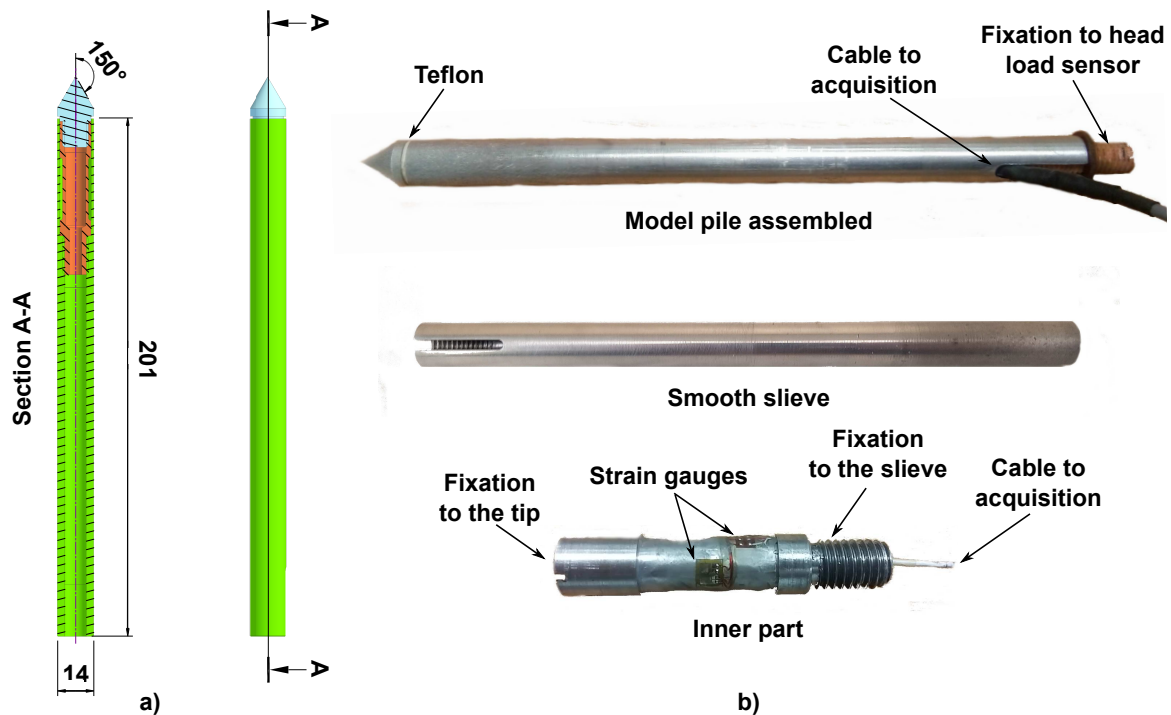


**Figure 4.8:** Design of the model pile: a) drawing made by DOERLER Mesures and b) schematic of the different parts of the model pile

**Table 4.3:** Sensors precision.

Sensor	Precision
Head Load	$\pm 5.0$ N
Tip Load	$\pm 4.6$ N
LVDT	0.005 mm

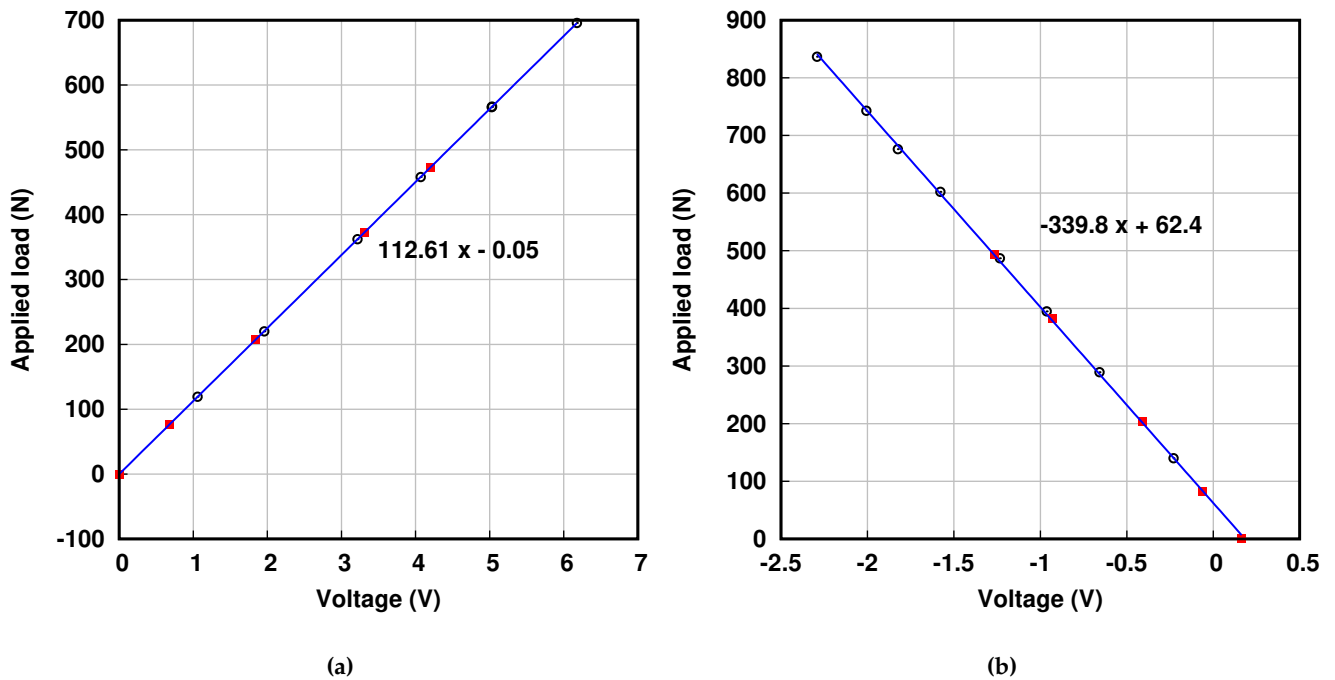


**Figure 4.9:** Calibration of the load measured by a) the head load sensor (total load applied to the pile) and b) the strain gauges (tip load). Full symbols represent compression and empty symbols represent tension

### 4.3.2 Shaft surface roughness

The model pile tests were performed on a pile having a smooth shaft surface. The roughness of the surface of a pile is typically quantified by the normalized roughness. The normalized roughness  $R_n$  was defined by Kishida and Uesugi (1987) as the ratio of the maximum roughness  $R_t$  (*i.e.*, the maximum vertical distance between a peak and a trough) to the mean grain size  $D_{50}$ , measured over a length  $L_m = D_{50}$  (see Fig. 4.10). In this study, measurements done over the shaft surface with a laser gave:  $R_t = 20\mu\text{m}$  and  $R_n = 0.018$ . According to Tehrani et al. (2016), a pile-soil interface is smooth when  $R_n \leq 0.02$ , which is the case of the model pile used in this work. This experimental choice was made in order to limit the amount of grain crushing at the interface to make the processing of the images easier. The use of rough interface is presented as one of the perspectives of this research work. Indeed, the roughness of sand-pile interface is known to be one of the most important factors affecting the unit shaft resistance (*e.g.*, Uesugi et al., 1988; Fioravante, 2002; Frost and DeJong, 2005; Martinez and Frost, 2014; Tehrani et al., 2016). Uesugi et al. (1988) showed the effect of the roughness of the interface on the formation of a shear band in the vicinity of the interface. The Authors noted that sand particles tend to slide along a smooth surface without large deformation. More recently, Hebler et al. (2015) investigated the effect of particle shape and size on CPT friction sleeve behavior over a range of counter-face surface roughness values. They noted that, for a conventional smooth CPT, some key aspects of interface shearing are eliminated, which results in a pure sliding failure mechanism.

Therefore, in this study, the friction mobilized by the shaft is far below the one measured in the field. Direct shear tests were performed on sand-aluminum interface under a constant normal stress of 100 kPa or 200 kPa. The samples were prepared with a similar initial relative density as for model

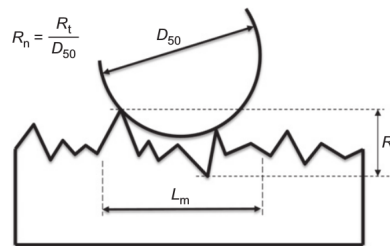


**Figure 4.10:** Definition of the maximum roughness  $R_t$  and the normalized roughness  $R_n$ , from Tehrani et al. (2016)

pile tests (85 %) and sheared against a perfectly smooth aluminum plate. Figure 4.11 shows the evolution the shear stress ( $\tau$ ) against the tangential displacement ( $w$ ) for both constant normal stress. From the estimation of the peak and the mean shear stresses (in both loading directions) the results give a peak interface friction angle of about  $16^\circ$  and a residual interface friction angle of about  $14^\circ$  whereas field piles have a roughness that leads to a typical residual interface friction angle of about  $30^\circ$  (e.g., Yang et al., 2010; Tehrani et al., 2016).

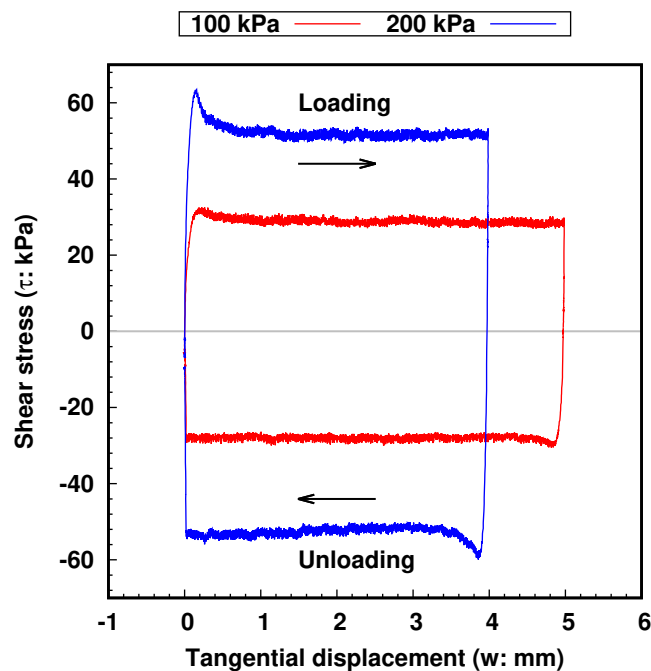


**Figure 4.11:** Shear stress measured during two monotonic direct shear tests conducted with a constant normal stress of 100 kPa and 200 kPa

## 4.4 Testing procedure

### 4.4.1 Sample preparation

Figure 4.12a shows the holder on which the sample was prepared. The holder is a Plexiglas cylinder with a hole at its center in order to insert the pile in the sand sample. Two other small holes were drilled in the holder to apply suction at the bottom of the sample. A filter paper was placed over the

holder to prevent the grains to fall down during sample preparation. The filter paper was chosen as it allows the application of the suction. A membrane was then cut to size and slipped over the system so that it covers the holder to prevent from water invasion when the sample is being confined. Due to their size and angular shape, the sand grains can damage the membrane during the test. For this reason, the latex membrane was chosen with a thickness of 0.5 mm. One rubber O-rings was needed to press the membrane against the holder and ensure a better sealing.

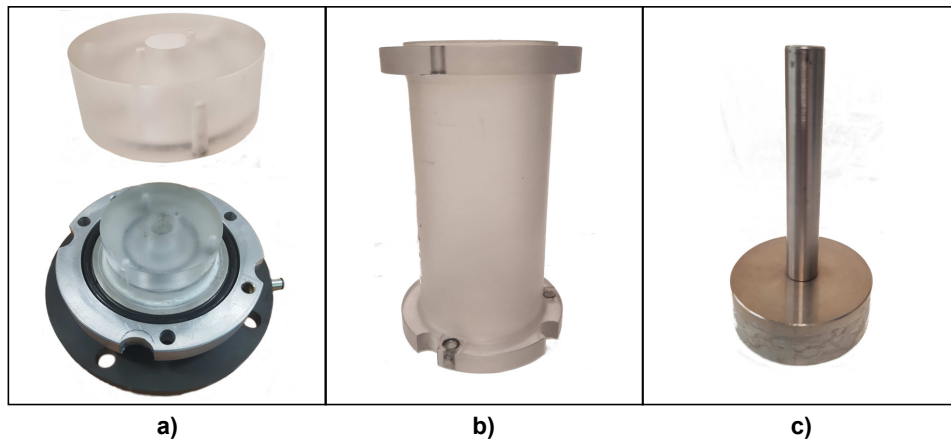


**Figure 4.12:** Parts needed to build the tested sand sample: a) sample holder and cell support, b) cylindrical cell and c) blocking piece

The cylindrical mold used in this work is shown in Figure 4.13a. The mold was closed around the holder and the membrane was folded back over it. Vacuum was applied on the circumference of the mold to press the membrane against it.

A preliminary study was conducted to select the most adequate method for sand deposition with a controlled density. Typical sand samples employed for model calibration chamber tests are prepared by pluviial deposition. In this study, dry pluviation was performed by pouring the sand grains with a funnel. Due to the size and the shape of Glageon grains, the minimum funnel diameter that could be used is about 2cm. With a smaller diameter, grains get blocked (a cohesive arch may form by angular grains) and do not flow homogeneously through the outlet. However, a diameter of 2 cm is already relatively large compared to the sample diameter and makes it very difficult to cover a wide range of relative densities despite the control of the falling height of the sand grains. Thus, it was decided to pour the sand layer by layer with a spoon and tamp it moderately for dense samples (relative density between 85 % and 110 %). After sand deposition, the sample was closed at its top by a metallic blocking piece as shown in Figure 4.12c. The sample being well sealed, the vacuum was stopped around the membrane and applied at the bottom of the sample. The sample could stand under its own weight and the mold was carefully removed (see Fig. 4.13b). The sample height and diameter were measured for the estimation of initial relative density. The cell was finally mounted around the sand sample and filled with water before being closed at its top (see Fig. 4.13c).

#### 4.4.2 Sample Confinement

Following sample preparation, the cell assembly was mounted on the loading device inside or outside the tomograph as described in Figure 4.14. Before applying any mechanical loading, the sample was confined isotropically at 100 kPa.

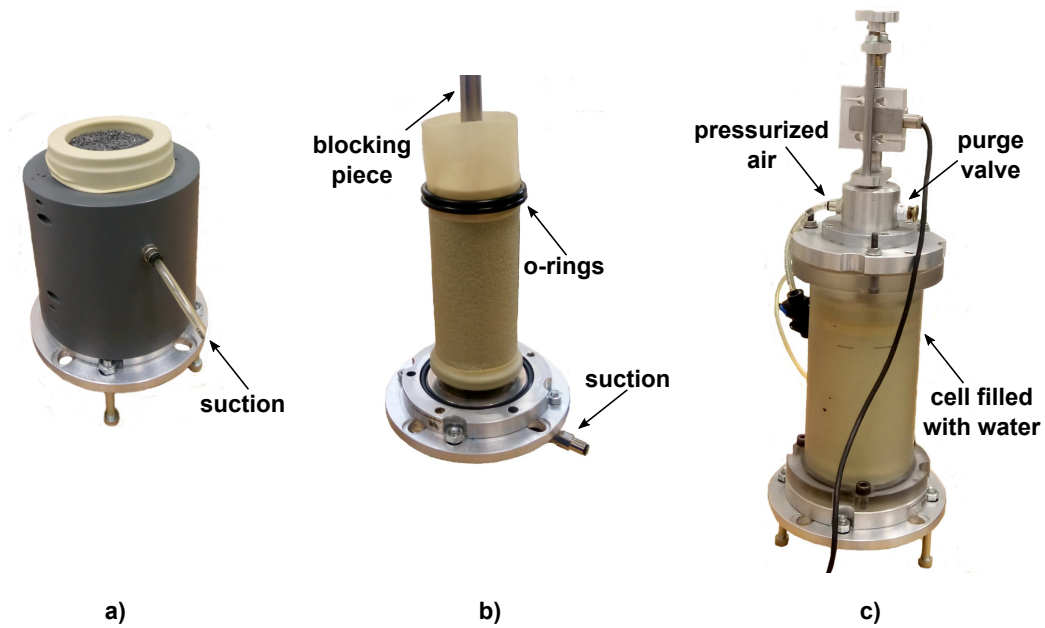


**Figure 4.13:** Different steps of sample preparation: a) sand deposition within a cylindrical mold, b) mold removal for the measurement of sample height and diameter and c) cell assembly

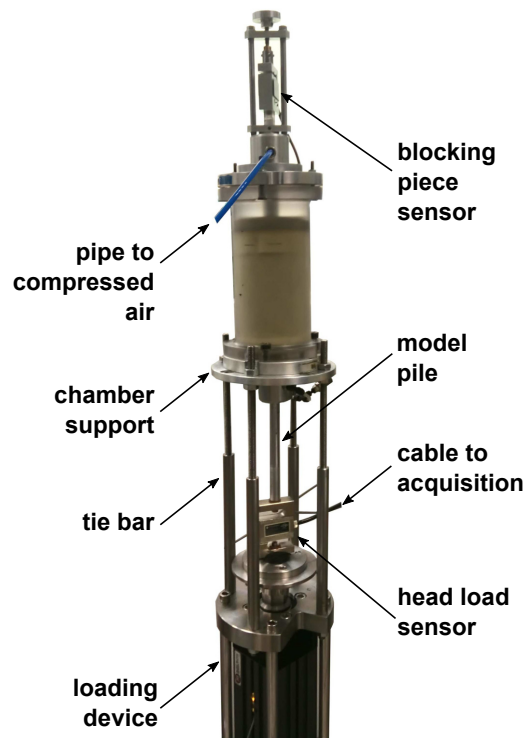


**Figure 4.14:** Experimental arrangement before pile installation for a test conducted outside the tomograph

Figure 4.15a shows the 3D porosity field at the initial state, *i.e.*, before pile embedment, for sample P-GLAG-16. The measurements were done over a REV of 50 voxels. Five horizontal layers of lower

porosity, of about 40 %, are observed in the 3D field. These layers are attributed to the sample preparation during which the sand is poured layer by layer and slightly tamped. A relatively uniform porosity, ranging from 44 to 49 %, can be observed in the vertical slice of Figure 4.15b. These values are consistent with the porosity measured macroscopically during the preparation of the sample for test P-GLAG-16, *i.e.*, 45 %. Horizontal slices taken through the 3D field reveal the effect of the tamping during sample preparation (Fig. 4.15c). The two slices taken at the elevations H1 and H3, at the limit between two layers of sand deposition, exhibit lower values of porosity.

The results presented in Figure 4.15 indicate that the porosity are lower on the boundaries of the sample (about 39 %). This phenomenon is believed to be mainly due to beam hardening. From Figure 3.5, the ratio of the gray level at the center of the image to the gray level on the circumference equals to 82 %. Similarly, the ratio of the porosity at the boundary to the porosity at the center of the sample equals to 85 %. As explained in Section 3.1.4, beam hardening leads to higher gray levels at the boundaries, *i.e.*, lower porosity values (grains and voids are associated with high and low gray levels, respectively). The lower porosity on the boundaries might also be due to a membrane-grains interaction. The angularity and the elongated shape of the grains might induce a particular alignment of the grains alongside the membrane during sample preparation.

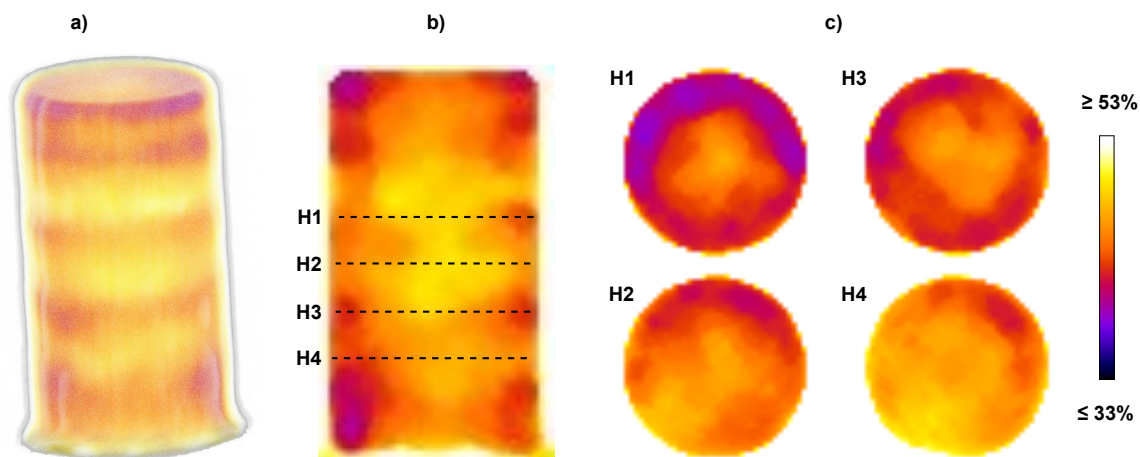


**Figure 4.15:** Porosity at the initial state for test P-GLAG-16: a) 3D field of porosity, b) Vertical slice through the 3D field, and c) horizontal slices taken at different elevations through the 3D field (H1, H2, H3, H4)

#### 4.4.3 Pile installation

In this study, the model pile was installed by monotonic jacking at a constant rate of  $25 \mu\text{m}/\text{s}$  until an initial embedment depth ranging from 45 to 65 mm. This embedment depth was selected for two reasons: with a depth higher than 70mm, the tip response is highly affected by the top metallic piece closing the sand sample; moreover, having the tip located at half of the sample height facilitates image acquisition. As illustrated by the typical head load profile shown in Figure 4.16, after the initial embedment the loading was interrupted and resumed according to the type of study: installation or loading cycles. In the case of a test that aims at studying the installation process, the monotonic loading was resumed and stopped every millimeter for image acquisition, until an additional embedment of 15 mm.

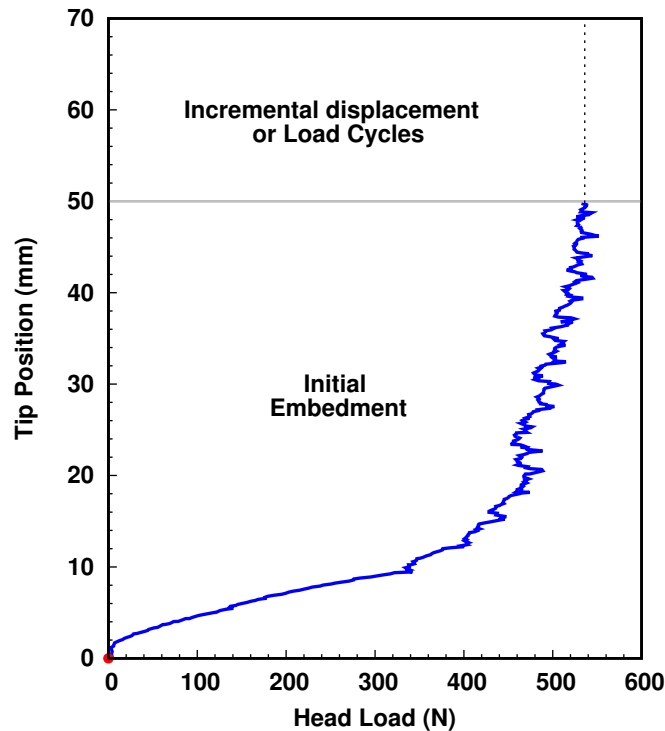
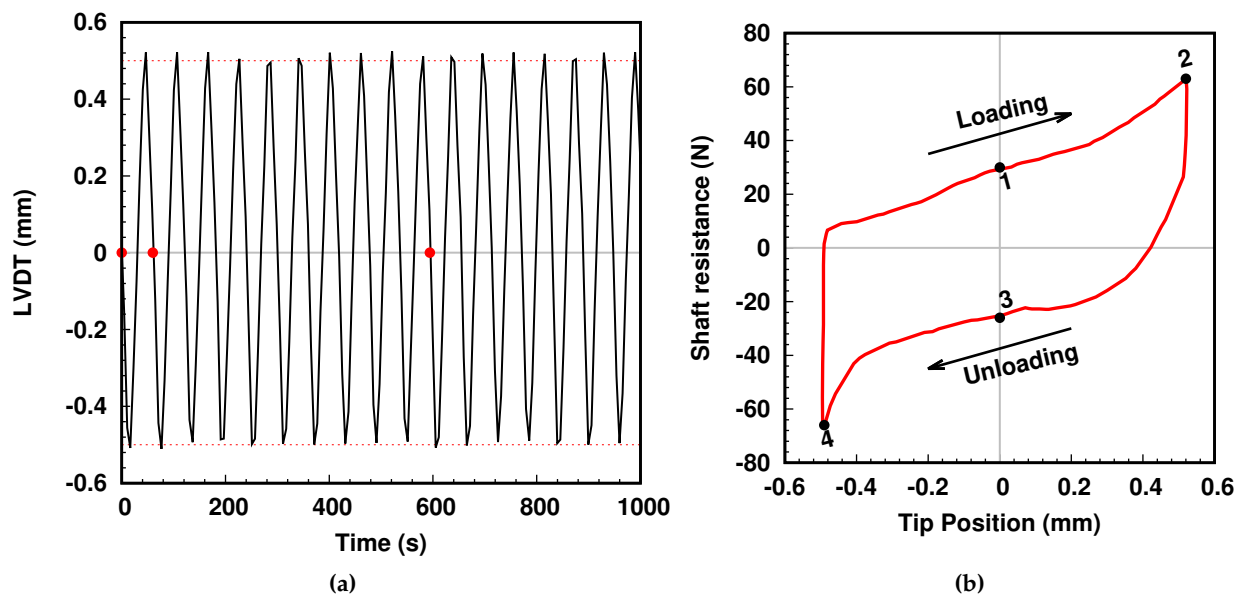


Figure 4.16: Typical head load profile during pile installation

#### 4.4.4 Displacement-controlled two-ways loading cycles

In the case of a test that aims at studying the behavior of the sand-pile interface during cyclic loading, multiple loading cycles were applied to the pile following the initial pile embedment. The model pile was submitted to up to one thousand axial displacement-controlled cycles. The cycles were performed at the same rate as for pile installation, with an amplitude of  $\pm 0.5$  mm or  $\pm 1.0$  mm around the pile-tip reference position, alternating between compression and tension phases (two-way cycles). //

Figure 4.17a shows the typical evolution of the displacement imposed to the pile by the LVDT during loading cycles. The red dots symbolizes the times when the scans were acquired: when the tip comes back to its reference position, which means when the LVDT is at 0 mm. In the example given in Figure 4.17a, scans were recorded before cycling, after one cycle and after ten cycles. It is important to note that the position imposed by the LVDT is stable in time. Figure 4.17b gives the evolution of shaft resistance (friction measured on the shaft) within a single cycle. During one of the tests using x-ray tomography, the loading was interrupted within a single cycle in order to study the behavior of the sand-pile interface during the tension and the compression phases of the cycle. The black dots on Figure 4.17b indicate when the loading was interrupted for scanning in such a test.



**Figure 4.17:** a) Typical displacement imposed to the pile during loading cycles; b) Typical shaft resistance evolution within a cycle. (red and black dots represent an x-ray scan acquisition)

## 4.5 Comparison with field pile testing conditions and scale effects

This section describes to what extent the mini-calibration chamber and the experimental procedure are comparable to large-scale experiments. Indeed, scaling effects result in distortion of the stresses and strains measured on the model and lead to results that cannot be directly extrapolated to field piles.

### Scale effects and boundary conditions

The main effect to be considered for small scale calibration chambers is that of chamber boundaries (Parkin and Lunne, 1982; Bellotti, 1985; Boulon and Foray, 1986). Due to the reduced size of the mini-calibration chamber, it is a main shortcoming of the present work. In an early study, Schnaid and Houlsby (1991) reported that this ratio affects substantially cone resistance, especially in the case of dense sands, and suggested that a ratio of at least 50 is required. Chamber size effects depends on the soil capacity to dilate radially. Thus, it should be higher in the case of low confining stresses and a dense sand. Later on, Balachowski (1995) and Salgado et al. (1998) suggested that values over 100 may be required in order to reach complete similitude with field behavior and neglect the size effects on penetration resistance, even for relatively dilative sand. Foray (1991) showed that, at a certain radial distance from the pile, pile penetration induces soil stresses that can be modeled by cavity expansion theory, with a loading and an unloading phase. The Author suggested to simulate an infinite lateral surrounding soil by applying a constant lateral stiffness at the boundaries that could reproduce the loading and unloading path. The use of such 'active' boundary conditions also proved to be the most adequate to model lateral shaft friction alongside a pile in sand (e.g., Boulon and Foray, 1986; Mortara et al., 2007; Pra-ai and Boulon, 2016).

A second important source of scale effects in model pile testing is the ratio of the pile diameter to the mean particle size. In the case of a coarse sand, the layer of grains around the shaft experiencing

shearing becomes too large, which can lead to excessive normal effective stress and affect directly the shaft resistance as reported by Lee et al. (2011). To minimize this effect the pile diameter should be at least 80 times the mean particle size according to Peterson (1988).

In the present study, the ratio of the chamber to the pile diameter and the ratio of the pile diameter to the mean particle size are respectively 5 and 14, which is far below the limits proposed in the literature and cannot reproduce field conditions. In the current setup, keeping a pile diameter of 14 mm, a chamber diameter of 140 cm would be required to limit scale effects. However, such a diameter is not compatible with x-ray imaging. The mean grain size should be of 140  $\mu\text{m}$ , which means that grains could not be tracked individually during mechanical loading. Adopting these conditions would make the benefits of a small-scale model, *i.e.*, applicability of high-resolution 3D imaging and extraction of grain-scale information, useless. Therefore, the scaling of the experimental arrangement used in this study is considered as a reasonable trade-off resulting from the limitations imposed by x-ray imaging and image-based measurements.

### Testing procedure

It is also important to mention that the testing procedure employed in this work does not reproduce faithfully the loading conditions encountered in the field. In fact, single displacement-controlled cyclic tests is just an example of a highly artificial case that is rarely encountered in the field, where piles that support bridges, towers, pylons, wind-turbines or offshore platforms have to sustain axial load-controlled cycles imposed by vehicles, winds, etc. However, displacement-controlled tests are more suitable to a grain-scale investigation of sand-pile interface as the zone of interest remain the same throughout the test. During load-controlled tests, the interface zone evolves in time as the displacement of the pile evolves. Load-controlled tests allows the evaluation of the sand-pile interface stability, which was not the objective of the present work.

The response of sand-pile interface is highly dependent on the stress level (mainly circumferential stresses). At earth gravity, stress similitude with field conditions cannot be achieved. In this work, the reduced height of the sample (about 130 mm) and the low confining pressure (100 kPa) highly reduce the magnitude of stress state in the model. This condition can lead to unrealistic failure mechanisms, especially near the pile.

## 4.6 Experimental program and tests naming

A total of 18 model pile tests using the mini-calibration chamber, 3 triaxial compression tests were conducted on Glageon sand. A series of 16 direct shear tests were also conducted as part of two MSc internships (Baydoun, 2017; Mohamed, 2017) on Glageon sand for comparison with model pile tests. The following naming convention was adopted:

- the first series of characters designate the type of test: P="Model Pile", TRIAX="Triaxial"
- the second series of characters designate the material used: GLAG="Glageon sand"
- the third series of characters designate the test number

Throughout the experimental campaign different testing parameters were varied in the model pile tests to study their effect on the cyclic behavior of sand-pile interface. Table 4.4 details the testing conditions for each test and Table 4.5 describes the main objectives and problem encountered for each test.

- Some of the tests were performed inside the 3SR tomograph to image phenomena at the interface during a test. These tests are attributed the variable "Imaging" = "Y". The remaining test were only analyzed at the macroscopic scale, without imaging.
- For all tests, the boundary conditions were CNL (Constant Normal Load), which means that the confining pressure was kept constant at 100 kPa during pile installation and cyclic loading. One test, P-GLAG-05 was conducted under constant volume conditions (CV).
- Tests were conducted on dense sand samples prepared by sand deposition as described in section 4.4.1 with an initial relative density ranging between 85% and 110%. Two tests have a slightly different initial state: P-GLAG-00 (medium dense) and P-GLAG-03 (very dense).
- To study the influence of the displacement amplitude of loading cycles, two different amplitudes were applied on the pile:  $\pm 0.5$  mm or  $\pm 1.0$  mm. For test P-GLAG-13, the amplitude was varied during a test from 0.5 to 1.0 mm.

**Table 4.4:** Summary of model pile tests conducted in the mini-calibration chamber

Test Name	Imaging	BC <sup>1</sup>	$D_r$ (%)	$n$ (%) <sup>2</sup>	Number of Cycles	Amplitude (mm)
P-GLAG-00 <sup>3</sup>	Y	CNL-100 kPa	61	48.2	-	-
P-GLAG-01	N	CNL-100 kPa	102	45.5	-	-
P-GLAG-02	N	CNL-100 kPa	85	46.6	1500	$\pm 0.5$
P-GLAG-03	Y	CNL-100 kPa	84	46.7	1000	$\pm 0.5$
P-GLAG-04	N	CNL-100 kPa	130	43.5	400	$\pm 0.5$
P-GLAG-05	N	CNL-100 kPa	110	44.9	1000	$\pm 1.0$
P-GLAG-06	Y	CV	102	45.5	2000	$\pm 0.5$
P-GLAG-07	N	CNL-100 kPa	85	46.6	500	$\pm 0.5$
P-GLAG-08	N	CNL-100 kPa	98	45.8	400	$\pm 0.5$
P-GLAG-09	Y	CNL-100 kPa	85	46.6	150	$\pm 1.0$
P-GLAG-10	N	CNL-100 kPa	98	45.8	315	$\pm 0.5$
P-GLAG-11	Y	CNL-100 kPa	102	45.5	130	$\pm 1.0$
P-GLAG-12	N	CNL-100 kPa	106	45.2	800	$\pm 0.5$
P-GLAG-13	N	CNL-100 kPa	117	44.4	1160	$\pm 0.5$
P-GLAG-14	N	CNL-100 kPa	104	45.4	175	$\pm 0.5 - 1.0$
P-GLAG-15	N	CNL-100 kPa	85	46.6	1000	$\pm 0.5$
P-GLAG-16 <sup>1</sup>	Y	CNL-100 kPa	110	44.9	500	$\pm 0.5$
P-GLAG-17	Y	CNL-100 kPa	84	46.7	-	-

<sup>1</sup> Lateral Boundary Conditions (BC).

<sup>2</sup> Initial porosity calculated after sample preparation.

<sup>3</sup> In this test the model pile was not instrumented yet. Only the head load was recorded.

<sup>4</sup> This test was imaged by global tomography whereas all the others were imaged by local tomography.

**Table 4.5:** Specific objectives and technical issues encountered for each test

<b>Test Name</b>	<b>Objectives</b>	<b>Technical Remarks</b>
P-GLAG-00	Investigate the grain-scale mechanisms governing the behavior of sand pile interface during pile installation.	Lower initial relative density due to the method of sand deposition.
P-GLAG-01	Test the accuracy of the model pile instrumentation for both monotonic and cyclic loadings.	None
P-GLAG-02	Examine the effect of axial cyclic loading on the macroscopic response of the interface.	None
P-GLAG-03	Investigate the grain-scale mechanisms governing the behavior of sand pile interface during cyclic loading.	None.
P-GLAG-04	Verify the reproducibility of the macroscopic results.	The loading device stopped working after only 400 cycles.
P-GLAG-05	Investigate the effect of a larger amplitude of cycles on the macroscopic behavior of the interface.	Error in the tip resistance values recorded by the strain gauges.
P-GLAG-06	Investigate the effects of constant volume boundary conditions on the cyclic behavior of the interface.	A deviation of the tip load measurements was observed.
P-GLAG-07	Test the model pile after a new calibration of strain gauges recording the tip resistance.	Error in the tip resistance values recorded by the strain gauges.
P-GLAG-08	Test a new acquisition system to solve the problem of the tip resistance measurements	Error in the tip resistance values recorded by the strain gauges.
P-GLAG-09	Investigate the effect of a larger amplitude of cycles on the grain-scale behavior of the interface.	The tip resistance could not be recorded.
P-GLAG-10	Test the model pile after isolating each electrical device.	None
P-GLAG-11	Examine the grain-scale mechanisms within a single cycle (during cyclic softening and during cyclic hardening).	None
P-GLAG-12	Verify the reproducibility of the macroscopic results.	Error in the tip resistance values recorded by the strain gauges
P-GLAG-13	Verify the reproducibility of the macroscopic results.	None
P-GLAG-14	Investigate the influence of a change in the amplitude of cycle within a single test.	None
P-GLAG-15	Investigate macroscopic response of the interface for a sand sample directly molded around the pile to stress the effect of the installation method.	None
P-GLAG-16	Investigate the global behavior of the sample by means of global tomography during cyclic loading.	None
P-GLAG-17	Test performed without any loading in order to verify the accuracy of the grain-scale measurements (porosity, grain kinematics, etc.).	None

## Chapter 5

# Macroscopic response of sand-pile interface

This chapter presents the results of model pile tests performed in the mini-calibration chamber. It examines particularly the evolution of the load applied to the pile when it is submitted to monotonic jacking (initial embedment phase) and when it is then submitted to a large number of displacement-controlled cycles. Different testing parameters affecting the macroscopic response of sand-pile interface during cyclic loading were varied:

- the amplitude of displacement imposed to the pile during loading cycles
- the boundary conditions (constant radial stress, constant volume)
- the method of pile installation (monotonic jacking, sand molding around the pile)

These various tests also aimed at producing a rather complete dataset to be compared to previous experimental work conducted on large-scale laboratory models. The objective was to validate the results obtained at the macro-scale within the mini-calibration chamber despite the expected scale-effects as described in Section 4.5. The specific objectives of each tests are detailed in Table 4.5, while Table 4.4 summarizes the testing parameters. The principal technical problems encountered during testing are also reported in Table 4.5.

### Layout of the chapter

This chapter starts with the presentation of the evolution of the loads applied to the pile during the first embedment phase (Section 5.1). The reproducibility of the results and the comparison with other studies from the literature are discussed. The influence of the interruption of the loading on the load evolution is also pointed out.

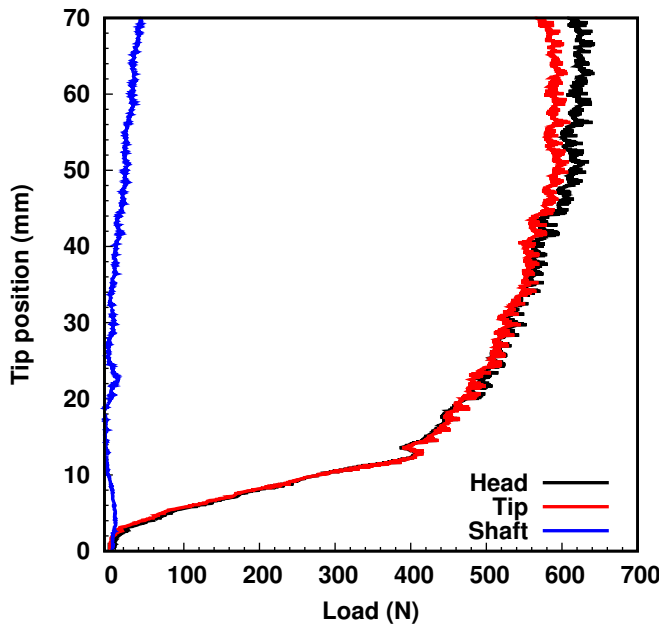
The following sections focus on the macroscopic behavior of the interface during the cyclic phase of the tests. Section 5.2.1 shows the identification of two different regimes in the evolution of shaft resistance. Section 5.2.2 details the problem encountered with the strain gauges measuring the load applied to the pile tip and how this problem affected the results of a few tests. The results of the tests conducted with a larger amplitude of the cycles, under constant volume and on a molded pile are presented in Sections 5.3, 5.4, and 5.5, respectively.

## 5.1 Typical response during pile installation

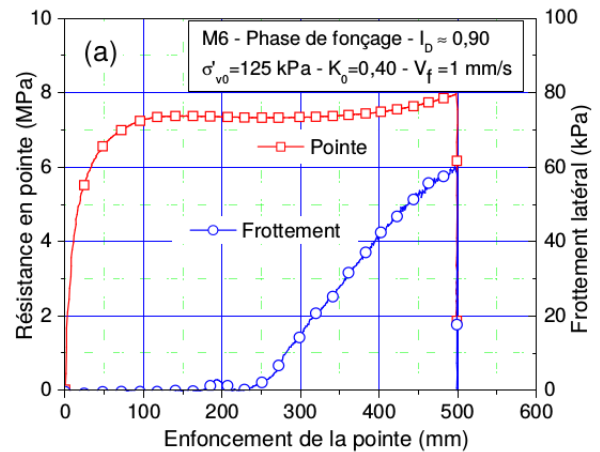
### 5.1.1 Evolution of the loads applied to the pile

Figure 5.1 shows the evolution of the loads applied to the pile during the initial embedment: the head load (total load), the tip resistance and the shaft resistance. The pile head load and the tip resistance

follow the same trend. Two distinct phases are observed. First, the tip resistance increases sharply and rapidly for the first 15 mm, which also corresponds to the height of the conical tip. After its rapid mobilization, the tip resistance tends to stabilize and reaches a plateau at a value of about 580 N. There is no visible change of tip resistance when the pile tip reaches a new layer of sand (each layer is about 2 cm thick). However, given the sub-optimal ratio of pile diameter to pile diameter, tip resistance measurements cannot be directly correlated to density variations in this specific study. The shaft resistance, is about 15 times lower than the tip resistance. Negligible at the very beginning of the installation, the shaft resistance starts increasing almost linearly after 20 mm embedment, as the surface in contact with the surrounding sand increases. At the end of the loading, the shaft resistance reaches 47 N. Tali (2011) observed similar results from large calibration chamber tests with similar testing conditions as illustrated in Figure 5.2. However, Tali (2011) pointed out a visible effect of the bottom of the calibration chamber on the tip measurements: the tip resistance increases again after reaching a plateau, as it gets closer to the bottom of the chamber. In Tali (2011), the distance from the pile tip to the bottom of the chamber was about 5.5 pile diameters. In the present study, the distance from the pile tip to the top of the sample is of about 5 pile diameters. The difference observed between the two studies is likely due to the different boundary conditions: constant volume in Tali (2011) and constant vertical stress in the present study.



**Figure 5.1:** Evolution of the loads applied on the pile during the initial embedment for test P-GLAG-01



**Figure 5.2:** Evolution of tip and shaft resistance during pile installation, after Tali (2011)

In sand, the unit shaft resistance at failure ( $q_{sL}$ ) is governed by Coulomb friction and depends on the normal effective horizontal stress ( $\sigma'_{rf}$ ) and the mobilized interface friction angle ( $\delta$ ) as presented in Equation 5.1.

$$\tau_{sf} = \sigma'_{rf} \tan(\delta) \quad (5.1)$$

A reliable value of  $\delta$  can be selected depending on the mean grain size and the normalized interface surface roughness using interface shear tests (Jardine et al., 1993). In a general framework for

the prediction of shaft resistance, White (2005) detailed how the stress of soil element adjacent to the pile changes at each stage of the installation from the initial state  $\sigma'_{h0}$  to  $\sigma'_{rf}$ , depending on the loading history. From centrifuge pile tests using different installation methods (monotonic, cyclically jacked and "pseudo-dynamic") White and Lehane (2004) showed that the horizontal stress normalized by the tip resistance remains constant throughout monotonic installation and is independent of the distance behind the pile tip. It is also shown that, unlike during cyclic installation, the horizontal stress increases during monotonic installation, with no friction fatigue (see Figure 5.3).

In the present work, it can be assumed that the radial stress applied to the shaft is equal to the confining stress (which should not be the case as evidenced by the studies described previously). With this assumption, by fitting a linear function to the shaft resistance evolution for a tip position ranging between 20 and 70 mm, the slope obtained gives an interface friction angle about  $12^\circ$ . This result is close to the residual interface friction angle measured during the monotonic direct shear interface test presented in Section 4.3.2 ( $14^\circ$ ).

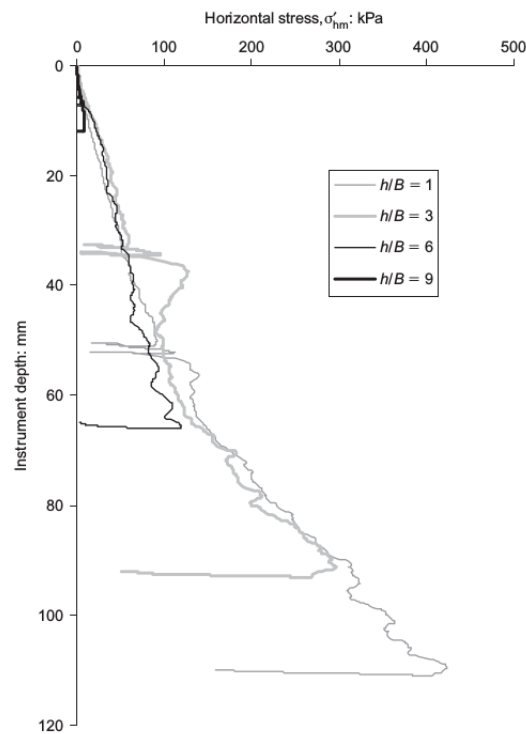


**Figure 5.3:** Horizontal stress measurement at different distances from the pile tip during monotonic installation, from White & Lehane (2004)

### 5.1.2 Reproducibility of the results

The measured load for several tests conducted under similar testing conditions are plotted in Figure 5.4. The tip and the shaft resistances of test P-GLAG-12 are not displayed, as they could not be measured during the test due to electrical interferences. The results show a good reproducibility of the measurements for the selected tests despite an initial density varying from 85 % to 110 %. Unlike test P-GLAG-01, two tests show a sudden change in the measured head load as indicated by the arrows in Figure 5.4a. This change, also visible from the tip resistance profiles given in Figure 5.4b, occurs respectively at 38 mm and 46 mm for test P-GLAG-02 and test P-GLAG-06 and may correspond to

the interface between two deposition layers. From Figure 5.4c, it can be seen that until 25 mm embedment, the measurements of shaft resistance are noisy, since the surface in contact with the grains is close to null. It is also observed that between test P-GLAG-01 and test P-GLAG-11 the shaft resistance nearly doubled. Despite the smoothing of the model pile with a very fine sandpaper before each experiment, a slight change in pile surface roughness is expected between the tests. From axial interface shear tests conducted on sub-angular sand, Hebler et al. (2015) reported the evolution of the peak and residual stress ratios (ratio between the shear stress and the normal stress) as a function of the maximum surface roughness  $R_{max}$ <sup>1</sup>. Their results show that when  $R_{max}$  increases from 0.01 mm (smooth conventional CPT) to about 0.125 mm the peak stress ratio increases from 0.2 to 0.3, which means that the interface friction angle increases from about 11 to 17°. It is believed that the repeated installations and removals of the model pile can induce such a surface roughness increase as illustrated by the photograph of the model pile taken after a typical test in Figure 5.5.

The fluctuations in the measured load are attributed to the small  $D/D_{50}$  ratio and not to potential measurement inaccuracies. Indeed, fewer grains are in contact with the tip and the shaft of the pile. Consequently, if one of those grains is displaced or broken due to the large stresses developed by the penetration of the pile, the resulting change in measured load will also be relatively large. However, it can be noted that test P-GLAG-11, conducted with the second loading device described in section 4.2, at a loading rate of 25  $\mu\text{m/s}$ , exhibits smoother results.

As a general remark, the measured tip resistance and shaft resistance are much lower than the one commonly obtained in full-scale conditions. There are several possible explanations to this significant difference. First, as described in section 4.1, Glageon sand is vulnerable to crushing, even at low stress levels. Hence, unlike siliceous sands, Glageon sand tends to exhibit a higher volumetric reduction upon shearing. The high compressibility of calcareous (or carbonate) sands has been reported as one of the main factor that leads to lower pile tip resistance and pile shaft friction as compared to siliceous sands (*e.g.*, Almeida et al., 1991; Parkin, 1991; Chin and Poulos, 1996; Klotz and Coop, 2001; Schneider et al., 2007). Schneider et al. (2007) also suggested that the higher friction angles of calcareous sands result in a faster radial decay of stress during cavity expansion.

A second, and rather straightforward explanation, is the scale effects due to the reduced size of the mini-calibration chamber. Parkin (1988) showed that a large chamber diameter to cone diameter ratio is needed before the cone resistance levels off to a constant value, especially in the case of dense sands. Salgado et al. (1998) also showed that under constant lateral stress, the penetration resistance is always smaller than the corresponding free-field values. Free-field conditions involves higher lateral stresses which are increasing at the same distance from the point of penetration. Based on the penetration resistance theory (R., 1993), Salgado et al. (1998) stated that a lower confining stress results in a lower stiffness, thus to higher hoop strains at the elastic-plastic interface illustrated in Figure 5.6a. Salgado et al. (1998) concluded that the higher initial relative density and the lower the initial confining stress, the higher will be the dilatancy of the plastic zone and the more pronounced the scale effects. Figure 5.6b also shows that a lower chamber diameter to cone diameter ratio leads to lower values of penetration resistance in comparison with free-field conditions. The experiments describe in the present work gather all the parameters reported in the literature as having an effect on pile tip and shaft resistance during pile installation: a crushable sand, a dense initial soil state, low confining stresses and a low chamber diameter to cone diameter ratio.

<sup>1</sup>The maximum surface roughness is defined as the absolute maximum distance between the highest peak and the lowest valley of the surface roughness profile.

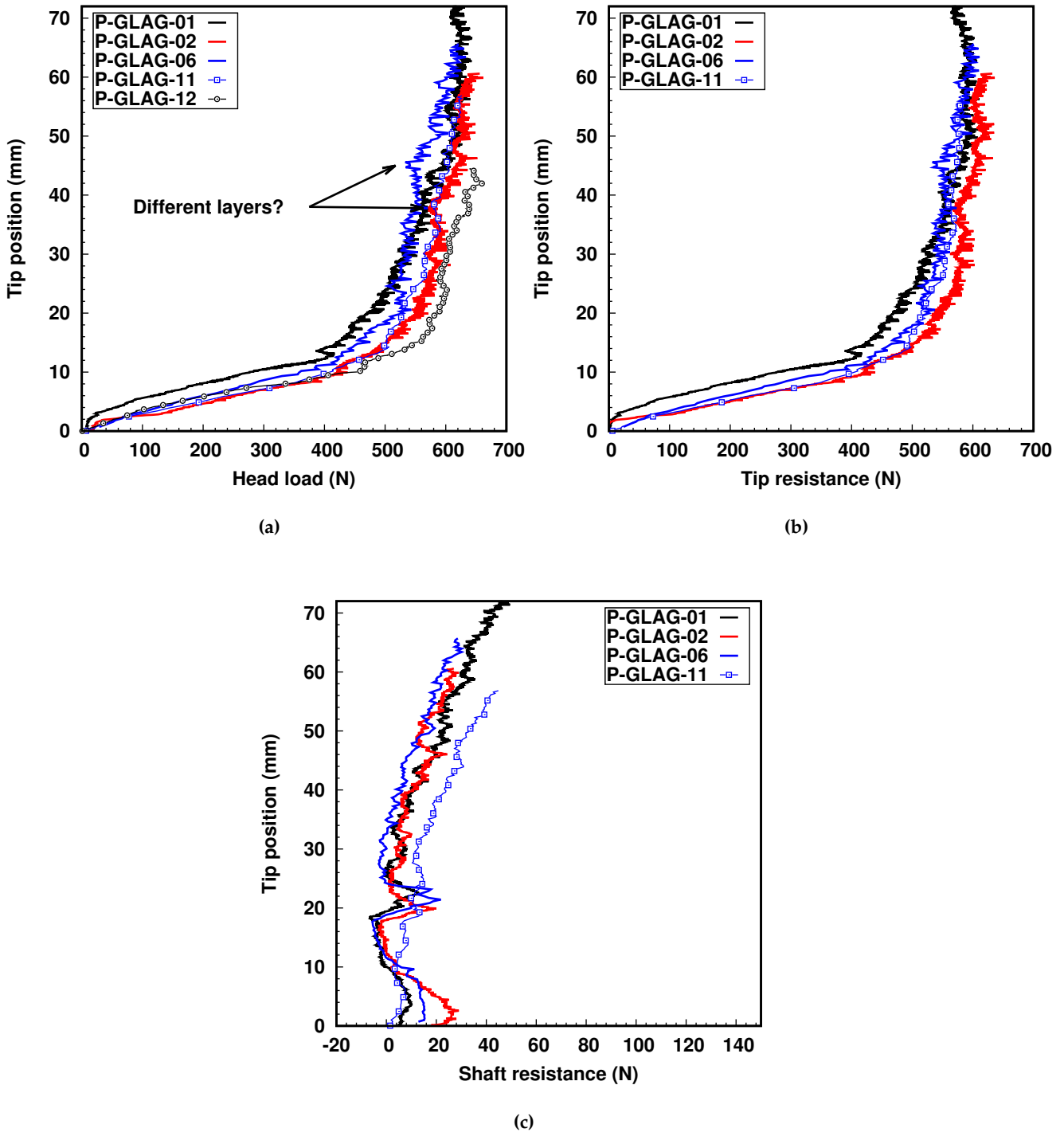


Figure 5.4: Load profiles during pile installation for different tests showing the reproducibility of the results (initial relative density between 85 % and 110 %): a) head load, b) tip resistance and c) shaft resistance. Note that the tip resistance and shaft resistance could not be recorded during test P-GLAG-12



Figure 5.5: Photograph showing the pile surface after a typical test in the mini-calibration chamber

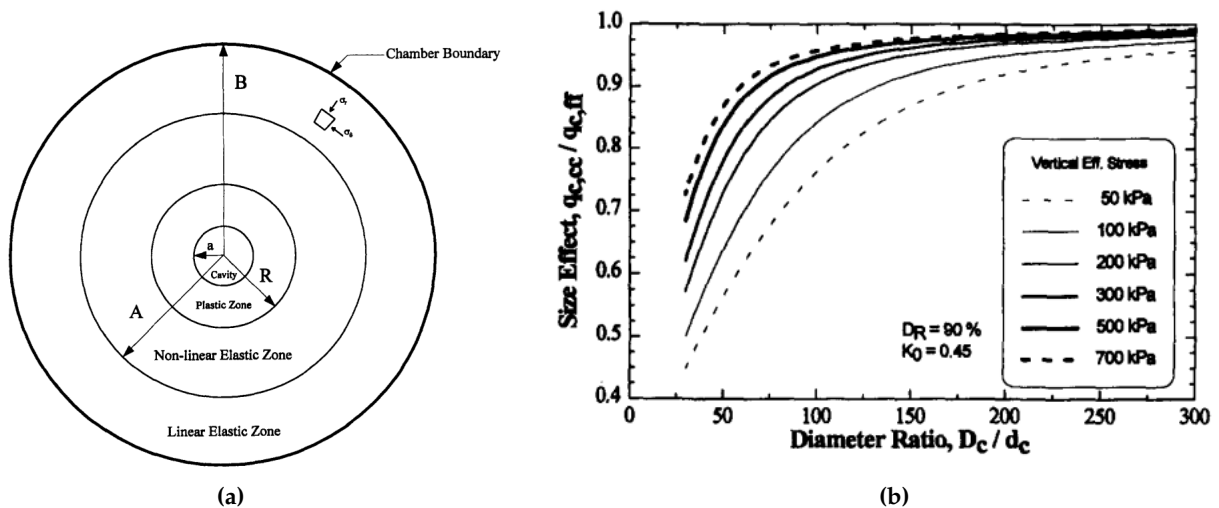


Figure 5.6: a) Different zones developing around the pile during cavity expansion and b) size effect curves for several vertical stress values (cc: calibration chamber, ff: free-field), after Salgado et al. (1998)

### 5.1.3 Typical response when the loading is stopped for image acquisition

In this work, the analysis of pile installation in sand also aimed at calibrating the image analysis tools described in chapter 3. For this reason, the experimental conditions of the test analyzed (test P-GLAG-00) were modified accordingly. For test P-GLAG-00, the pile was initially embedded with a low confinement pressure of about 20 kPa to limit the amount of grain breakage at the interface. When they break Glageon sand grains produce a powder that brings additional noise in the x-ray images and adds complexity to the analyses. After an initial embedment of 35mm, the confining pressure was increased until 100 kPa. Finally, 14 incremental displacements of 1 mm were applied to the pile. The loading rate was kept constant at 25  $\mu\text{m}/\text{s}$ .

Figure 5.7b shows the evolution of the pile head load during the 14 incremental displacements. The results show that, after a total embedment of 50 mm, the head load does not stabilize and reaches a maximum value of about 400N, which is two thirds of the value measured for the other tests (about

600 N). This is likely due to the lower stress level developed around the pile during the first embedment at lower confining pressure (20 kPa). The installation method of test P-GLAG-00 may be closer to the one of a non-displacement pile for which the sand is molded directly around the pile. Therefore, the analysis of the incremental loading was related to the region of interest illustrated in Figure 5.7b, meaning before the head load reaches a plateau.

At each increment, the loading was interrupted for image acquisition as symbolized by the red circles in Figure 5.7a. The interruption of the loading involves a phase of relaxation of the pile head load until it stabilizes again. This is likely due to the relaxation of the whole system (sand, loading device and pile). However, when the loading is resumed, the head load comes back to its previous value almost instantaneously and continue increasing. This phenomenon is classically observed and neglected for mechanical tests performed incrementally inside the x-ray scanner (see for instance Andò, 2013, Fonseca et al., 2013). Two jumps in head load values are indicated by the arrows in Figure 5.7a. These jumps corresponds to voltage drops due to an electrical interference during the test that did not influence the final results.

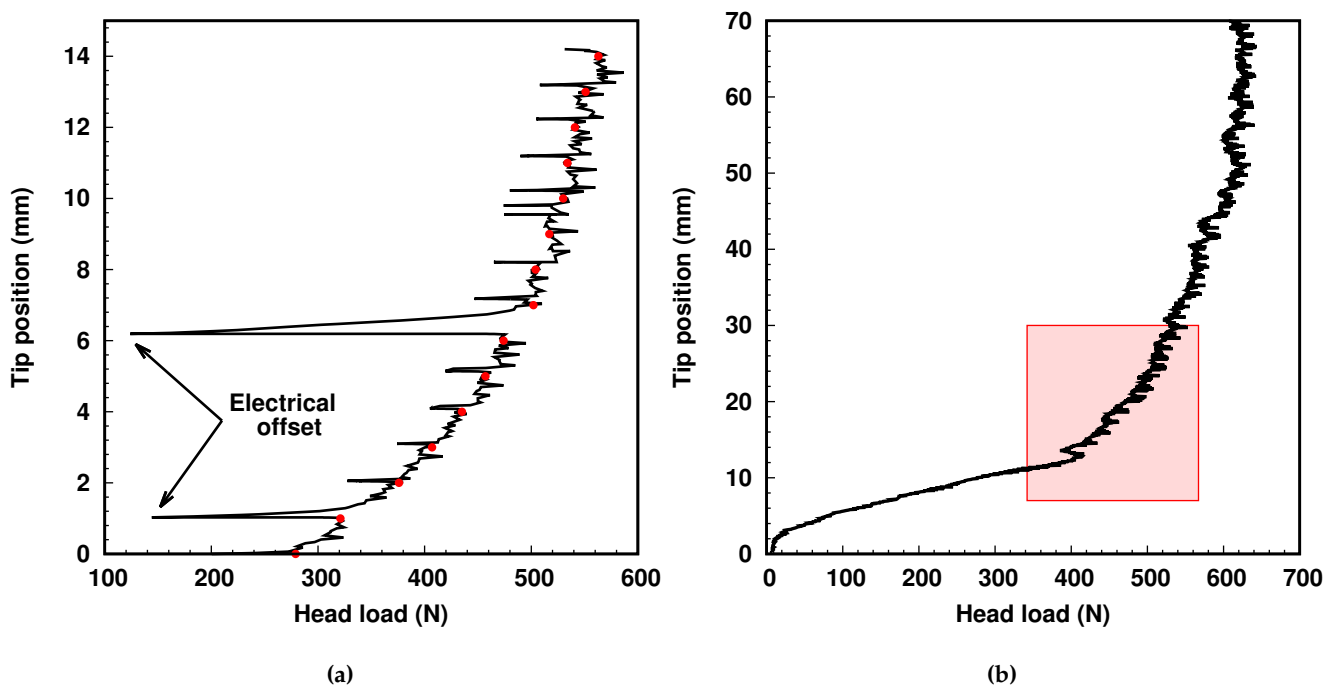


**Figure 5.7:** a) Incremental loading steps applied to the pile during scanning for test P-GLAG-00. The circles represents the steps when the loading was interrupted for scanning. b) Sketch of the region of interest analyzed by x-ray tomography during pile embedment

## 5.2 Typical evolution of tip and shaft resistance during loading cycles

### 5.2.1 Identification of two different phases in shaft resistance evolution.

Displacement-controlled cyclic tests allowed to follow the mobilization of the pile skin friction (thus shaft resistance) and of the pile tip resistance within a single cycle and after a series of loading cycles.

The applied loading can be described as follows:

1. The pile is installed by monotonic jacking until an initial embedment depth (between 45 and 70 mm). The tip position at the end of the installation is considered as the reference position (tip position equal to zero) during the cycles.
2. The pile is loaded further until the tip position reaches +0.5 mm
3. The pile is unloaded until the tip position reaches -0.5 mm
4. The pile is reloaded until its reference position when the tip is at zero.

Figure 5.8a shows the evolution of the total load applied to the pile vs. tip position as measured in test P-GLAG-02. It is observed that the first cycle differs significantly from the subsequent ones. This is likely due to a granular rearrangement around the pile as discussed in Section 6.3. After the first two cycles or so, three different phases are observed. At the very beginning of each cycle (phase I), the measured response is very stiff, which is expected because of load direction reversal. A sudden change in slope is then observed (phase II), which becomes more important after 50 cycles. The load increases slightly with a smaller tangential stiffness and less rapidly till a tip position of around -0.1 mm, where-after it starts increasing again (phase III).

From 50g centrifuge tests, Li et al. (2012) observed relatively similar response, with three different phases, in the case of pre-jacked piles. According to Li et al. (2012), the pre-jacked piles installed by monotonic jacking at 1g lead to very small locked-in stresses that are similar to the construction of a bored pile in the field. The Authors attributed the softening behavior observed during the second phase to a high densification of the sand at the pile base. In the present study, tomographic images taken at different stages of the loading reveal that in fact a gap forms between the pile tip and the grains, due to a high densification of the sand ahead of the pile tip (see section).

In Figure 5.8b, the evolution of the tip load indicates that during phase I and phase II, no load is actually applied to the tip of the pile, after the ten first cycles. The tip is mobilized only during the third phase of the loading. This phenomenon indicates that during phase I, the head load is only due to the friction on the shaft, while the tip is completely unloaded. Once the friction is mobilized, the head load does not vary significantly (phase II) until the tip comes again in contact with the grains (phase III). It can also be observed that the maximum tip load measured when the tip position reaches +0.5 mm decreases, at a smaller rate with increasing number of cycles.

Figure 5.9 shows the evolution of shaft resistance during the cycles. Two different phases can be identified. For the first fifty to hundred cycles, shaft resistance slightly decreases (of about 15N). For the subsequent loading cycles, shaft resistance increases continuously from about 20 N to 40 N, at the reference position of the tip. When the tip reaches  $\pm 0.5$  mm, the curves show a peak, which becomes increasingly marked with increasing number of cycles. In this work this peak is also referred as "maximum friction" for both tension and compression phases of the loading.

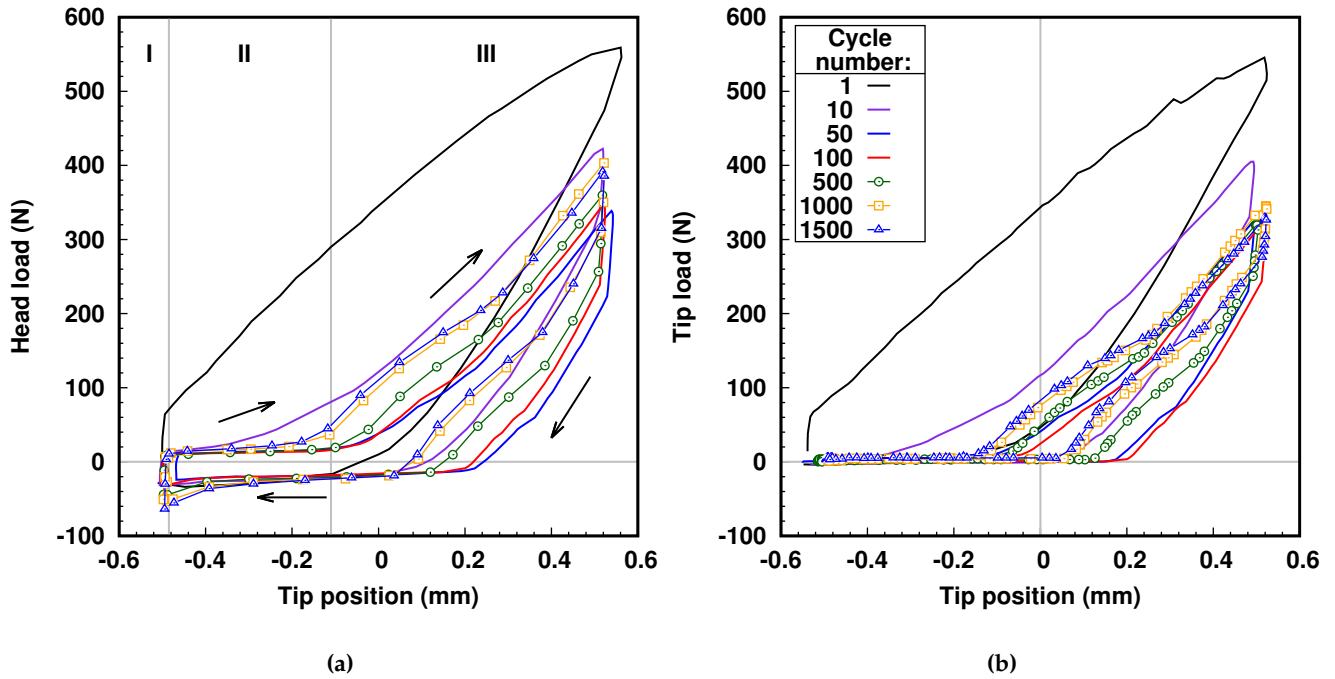


Figure 5.8: Evolution of a) head and b) tip load during displacement-controlled loading cycles for test P-GLAG-02 (amplitude of  $\pm 0.5$  mm). Arrows indicate the loading path within a single cycle

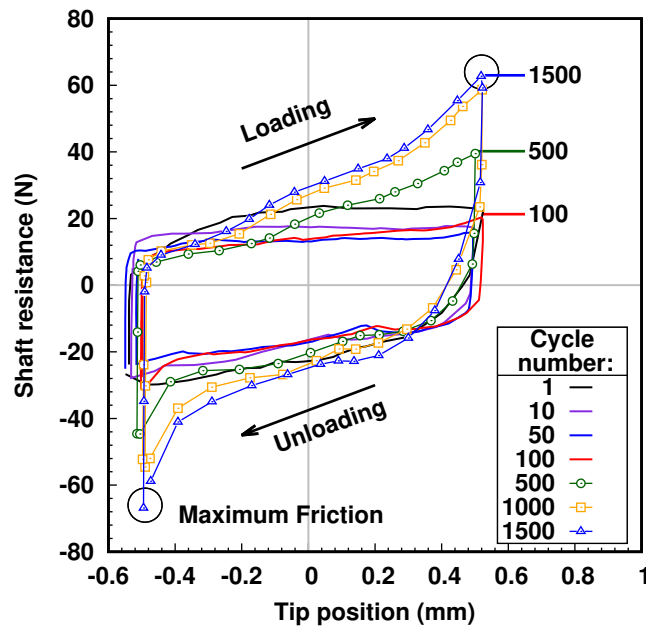


Figure 5.9: Evolution of shaft resistance during displacement-controlled loading cycles for test P-GLAG-02 (amplitude of  $\pm 0.5$  mm)

Figure 5.10 presents the force induced by friction measured at the peak for three tests performed with identical testing parameters. The three tests exhibit similar evolutions showing the reproducibility of the results. The shaft resistance at the end of the cycles is twice as big as the value measured during the first cycle. The transition between the two phases occurs between 50 and 100 cycles (shaded region in the figure). Even though similar trends are observed for the three selected tests, a difference in shaft resistance intensity is visible. The highest values are measured during test P-GLAG-04, for which the initial relative density was higher (130 % against 85 % for the two other tests). As for pile installation, the shaft surface roughness may vary slightly after being submitted to several cyclic tests. Thus, it may also affect the shaft resistance intensity between two tests.

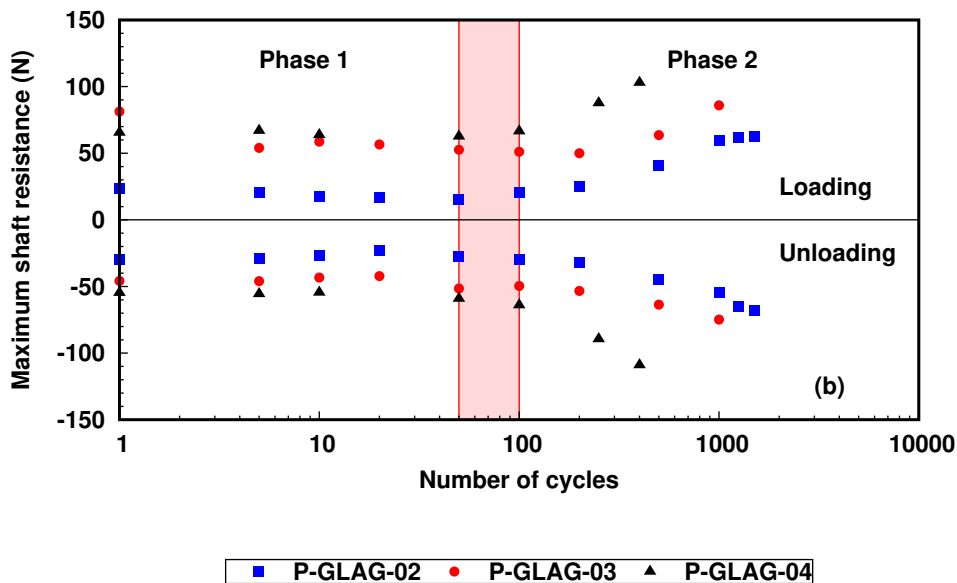


Figure 5.10: Evolution of the maximum friction measured with increasing number of cycles for tests P-GLAG-02, P-GLAG-03, P-GLAG-04

## 5.2.2 Problems encountered with the instrumentation of the model pile.

The analysis of the test P-GLAG-05, performed outside the tomograph, revealed a deviation in the measurements given by the instrumented pile as illustrated by Figure 5.11a. A clear shift in shaft resistance values is observed with increasing number of cycles, leading to inconsistent negative load measurements, even during the compressive phase of the loading. In fact, both the initial offset and the slope of the gages had changed during the test. In such a case, it was not possible to correct the measured values. A first assumption considered was that the strain gages accumulated a deformation with repeated tests or were damaged. The gages were therefore carefully tested and the model pile was re-calibrated.

The following test, P-GLAG-06 was conducted within the x-ray tomograph. Despite the new calibration, the tip load measured thanks to the gages showed a significant deviation in time. This deviation presented in Figure 5.11b was continuous, even when the loading was interrupted for image acquisition. The deviation increases almost linearly over time until 35 N, which is far above the measurement tolerance of the strain gages. A second assumption considered was the effect of

temperature on the strain gages response. Indeed, the temperature within the tomograph can vary of few degrees during a test. The strain gages have been tested under cyclic temperature variations with an amplitude of  $\pm 35^{\circ}\text{C}$  over one day (see Fig. 5.12, data provided by the manufacturer). Ando (2012) measured temperature variations within the tomograph over 5 days. The temperature change was of about  $+3^{\circ}\text{C}$  maximum. For such a limited variation, Figure 5.12 shows that the strain gages measurements varies of  $\pm 5\text{ N}$ . This result indicates that although temperature can potentially influence the measurements, it should have a limited effect in the present testing conditions.

The last option considered to ensure the quality of the measurements was to completely isolate the model pile from any other metallic parts of the setup, avoiding possible electrical interference. To this end, several parts of the setup were re-processed using insulating materials. This adaptations associated with a careful re-calibration of the model pile fixed the measurements deviations.

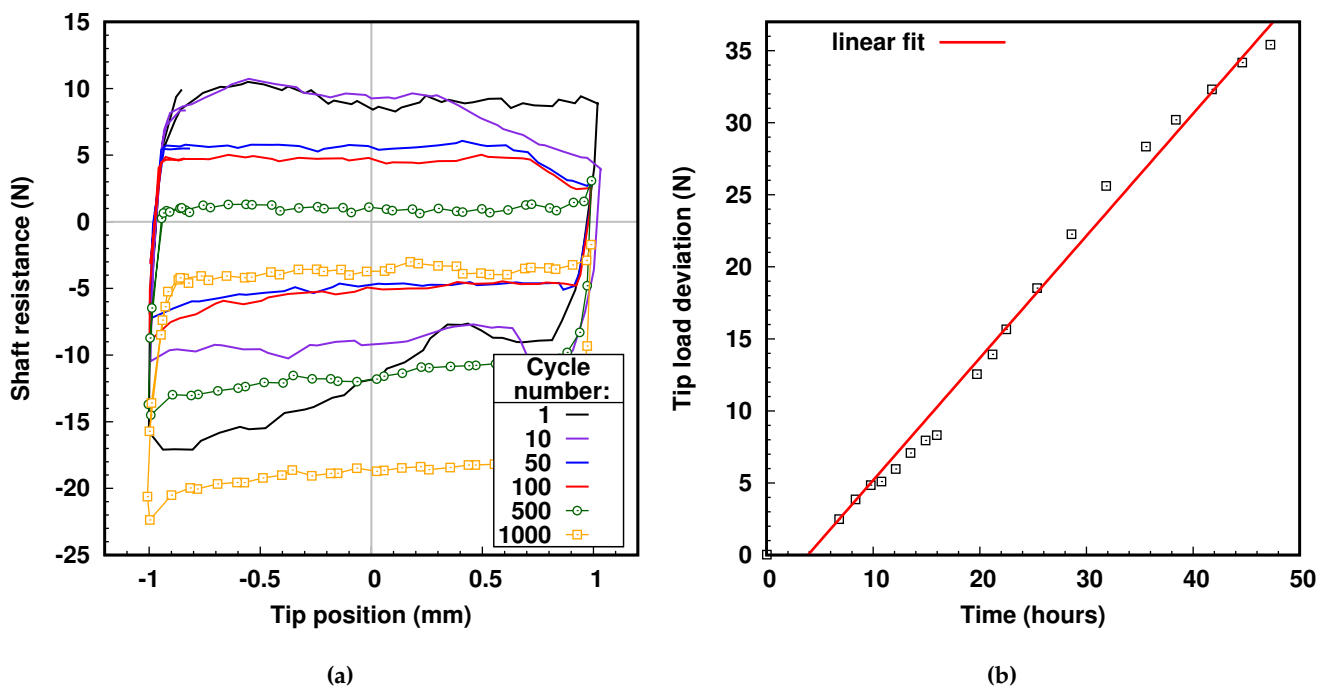


**Figure 5.11:** Deviation of the measurements given by the instrumented model pile: a) inconsistent shaft resistance values during test P-GLAG-05, b) tip load deviation during test P-GLAG-06 and its linear fit (inside the tomograph)

## 5.3 Influence of the amplitude of displacement applied during loading cycles

### 5.3.1 Influence of the amplitude on the two phases in shaft resistance evolution

Several cyclic tests were performed applying different values of amplitude of displacement during the cycles. Two kinds of test were carried out: the pile was submitted to *a series of loading cycles using only one amplitude* or the pile was submitted to *two subsequent series of cycles using two distinct amplitudes of displacement*. The objective of the first kind of test was to study the influence of the amplitude of displacement on the different regimes of shaft resistance described in section 5.2.1. The second

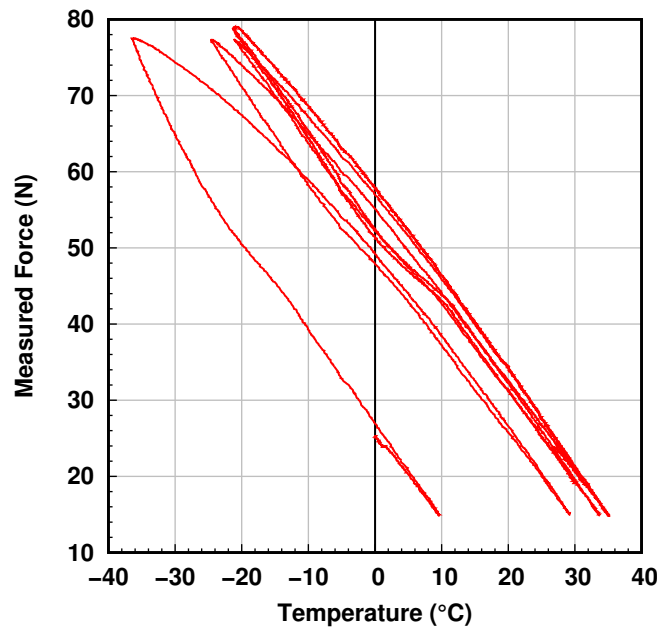


Figure 5.12: Evolution of the force measured using the strain gauges with temperature.

kind of test focused on the maximum shaft resistance measured at the loading reversal.

Figure 5.13 shows the evolution of shaft resistance during displacement-controlled loading cycles with an amplitude of  $\pm 1.0$  mm. The evolution of shaft resistance within a single cycle is similar to the one observed for a smaller amplitude of  $\pm 0.5$  mm. Two regimes are also observed. During the first tens of cycles the shaft resistance decreases of about 10 N, whereas it increases again for the subsequent cycles. The main difference between the two displacement amplitudes is the number of cycles required to reach the transition between the two phases. Indeed, with the highest amplitude, the increase in shaft resistance is triggered earlier, around the twentieth cycle.

The influence of the amplitude of displacement have already been reported by a number of authors: *e.g.*, Lee and Poulos (1990), Le Kouby (2003), Foray et al. (2010), Tali (2011). Le Kouby (2003) carried out a series of displacement-controlled cyclic tests on closed-ended pile, in silica sand, within the calibration chamber of CERMES. The piles were installed either by monotonic jacking or buried. Their results showed that an increase in the amplitude of cycle results in a more severe degradation at the interface in both cases. The degradation was higher for buried piles. Le Kouby (2003) also noted that, in the case of pile installed by monotonic jacking, low displacement amplitudes (inferior to 0.3 mm) lead to an increase in shaft friction whereas higher amplitudes had a negative effect on the shaft friction. From the same experimental campaign Le Kouby (2003) highlighted the importance of loading history by comparing the response of the pile after one series of cycles or after cumulated series of cycles with different amplitudes applied to the same sand-pile interface. The results for jacked piles (see Fig. 5.14) indicate that a cumulation of loading cycles applied to the same sand-pile interface leads to smaller benefits in shaft resistance for low amplitudes of displacement and to higher degradation for large amplitudes.

From displacement-controlled calibration chamber model pile tests, Tali (2011) and Silva Illanes (2014) also showed that a test conducted with a larger amplitude of displacement requires shows

benefit for the shaft resistance after fewer loading cycles. However, the transition between the two phases reported by these authors was found around 3000 cycles and 300 cycles respectively for an amplitude of cycle of  $\pm 0.5$  mm. The difference with the present work in the required number of cycles to gain shaft resistance is likely due to size effects as discussed in Section 4.5.

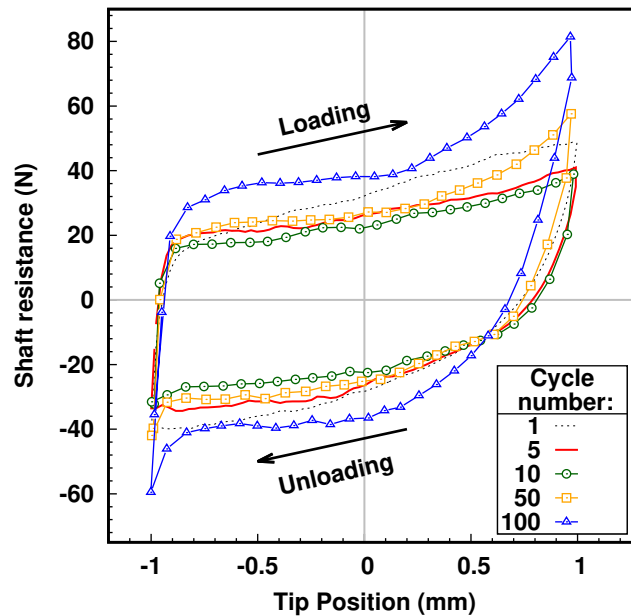


Figure 5.13: Evolution of shaft resistance during loading cycles for test P-GLAG-11 (amplitude of  $\pm 1.0$  mm)

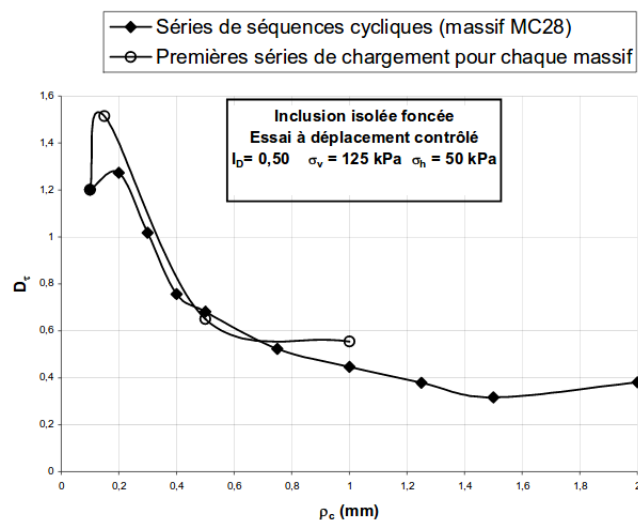


Figure 5.14: Evolution of the degradation of shaft resistance with the amplitude of loading cycles, from Le Kouby (2003). The degradation factor  $D_T$  was defined as the ratio between the limit shaft resistance after and prior to cyclic loading

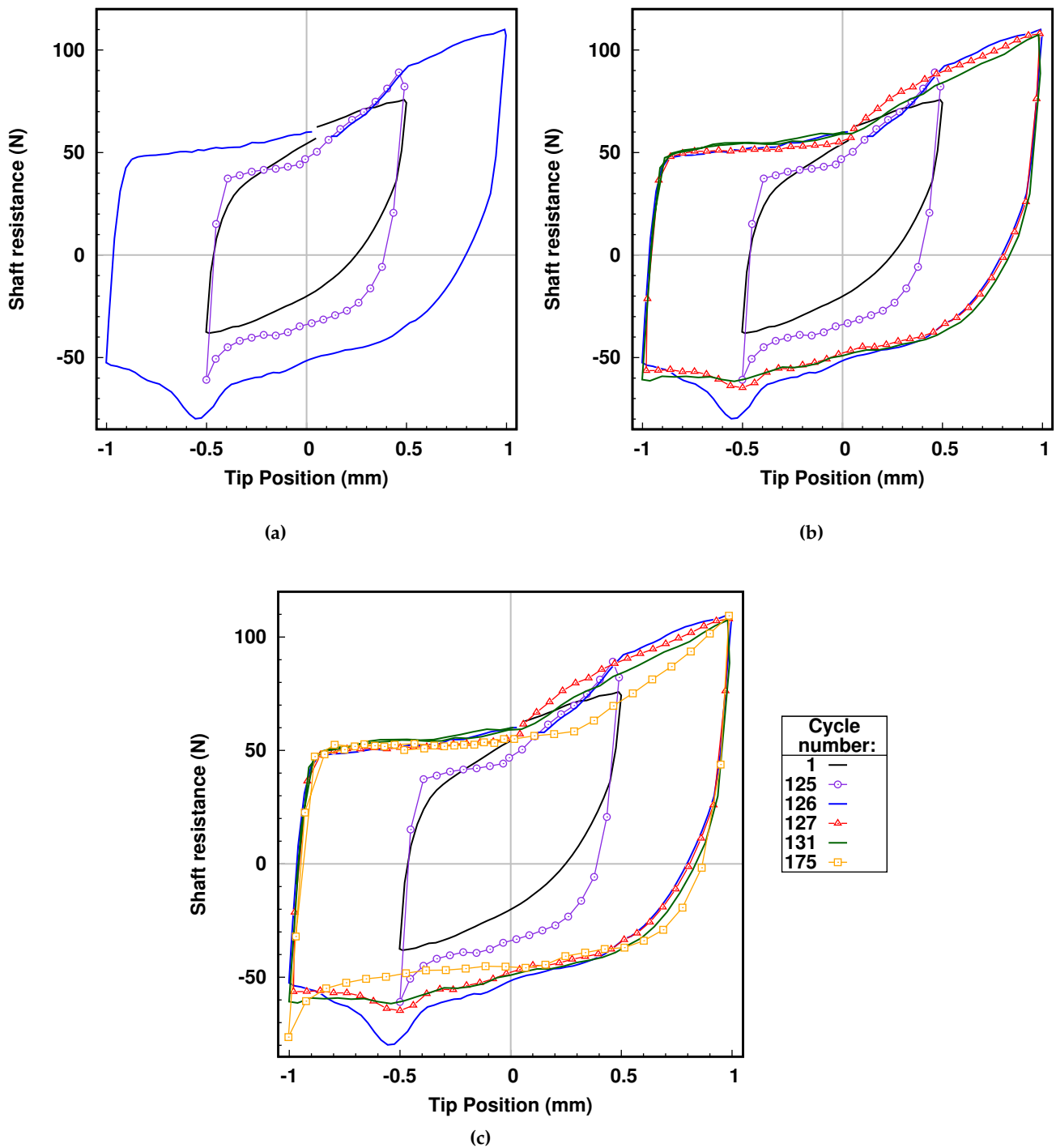
### 5.3.2 Variation of the amplitude within a single test

Figure 5.15 shows the evolution of shaft resistance after a given number of cycles, for two different amplitudes of displacement applied successively to the model pile. During test P-GLAG-14, 125 loading cycles of  $\pm 0.5$  mm were applied first. Figure 5.17a shows that after 125 cycles, the shaft resistance has increased and the peak at loading reversal is clearly marked. This result means that the second phase (of cyclic hardening) has been reached, consistently with the tests analyzed in Section 5.2.1. Without interruption, a second amplitude of  $\pm 1.0$  mm was applied to the model pile. The first cycle using this larger amplitude is the cycle  $n^\circ 126$  in Figure 5.15. At the beginning of the loading, the shaft resistance follows the same path as during the previous cycle ( $n^\circ 125$ ) until the tip position reaches  $+0.5$  mm. As the loading continues until  $+1.0$  mm, the shaft resistance continues increasing, but at a smaller rate. After the loading direction is reversed, the shaft resistance follows the same path as the previous cycle, but exhibits higher values (about  $+20$  N). When the tip position reaches  $-0.5$  mm, a peak is observed but it is less defined and followed by a drop in shaft resistance until  $-1.0$  mm. This observation suggests that the soil "remembers" the previous loading story it experienced. The following cycles  $n^\circ 127$  and  $131$ , plotted in Figure 5.17b, show that about five cycles are needed for the peak resistance measured at  $\pm 0.5$  mm to decrease. The last cycle  $n^\circ 175$ , plotted in Figure 5.17c, shows a smoother loading path within the cycle with two new sharp peaks resistance measured at  $\pm 1.0$  mm.

These possible explanations were examined through additional experimental tests: direct-shear tests on Glageon sand and shear tests performed on Schneebeli rods in the  $1\gamma 2\epsilon$  device of 3SR.

This phenomenon could come from different possible sources:

- boundary or scale effects
- the geometry of the interface
- the type of sand (grains can break and produce fine particles)
- a specific granular arrangement created by the mechanical loading



**Figure 5.15:** Evolution of shaft resistance when changing the amplitude of cycles from  $\pm 0.5$  mm to  $\pm 1.0$  mm: a) maximum peak shaft resistance "kept in memory" at  $\pm 0.5$  mm, b) smoothing of the first maximum peak shaft resistance and c) new maximum peak shaft resistance reached at  $\pm 1.0$  mm - test P-GLAG-14

### Direct-shear tests

A series of direct-shear tests was conducted on the direct shear box of Laboratoire 3SR, modified for different boundary conditions, *i.e.*, constant normal stress, constant volume and constant normal stiffness (see Fig. 5.16). A sample of Glageon sand was prepared at a relative density of 85 % and sheared against a smooth aluminum plate, using a constant normal stress of 100 kPa in order to keep similar testing conditions as in the mini-calibration chamber. The speed of the box was kept constant at 1.0 mm/s throughout the tests. The interface was subjected to shear until a maximum tangential relative displacement ( $[w]$ ) of +0.5 mm, then until -0.5 mm in the opposite direction, passing through the initial position 0 mm. Finally, the shear direction was reversed to go back to the initial position 0 mm. This loading sequence is a complete cycle and was repeated a certain number of times before increasing the maximum tangential displacement to  $\pm 1.0$  mm, and then to  $\pm 2.0$  mm. In this direct shear test, the number of cycles applied with each amplitude was respectively 15, 25 and 25.

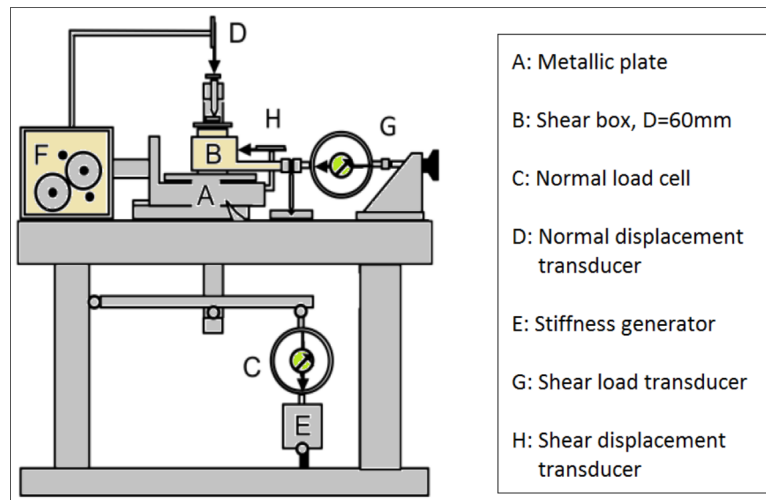


**Figure 5.16:** Schematic showing the modified direct shear device of Laboratoire 3SR

Figure 5.17 shows the evolution of the shear stress ( $\tau$ ) after a given number of cycles, for three different amplitudes of tangential displacement applied successively to the interface. For each amplitude, the curve plotted for the first and the last cycle show that the shear stress increases with increasing number of cycles. Contrary to model pile tests, no degradation was observed for the first cycles. The volumetric response revealed that the sample contracts continuously at a decreasing rate with increasing number of cycles (see Fig. 5.18). The objective of the test was to focus on the maximum peak shear stress measured when the shearing direction is reversed. Figure 5.17a shows that after 15 cycles, a sharp maximum peak shear stress is visible when  $w$  reaches  $\pm 0.5$  mm, whereas it is not observed for the first cycle. Figure 5.17b shows that, when the tangential displacement is increased to  $\pm 1.0$  mm, the maximum peak shear stress at  $\pm 0.5$  mm is "kept in memory" similar to the model pile test. However, the direct shear test exhibit a decrease in shear stress when  $[w]$  goes from 0.5 to 1.0 mm (or -0.5 to -1.0 mm). After 25 cycles at  $\pm 1.0$  mm, the maximum peak shear stress observed when  $[w]$  reaches  $\pm 0.5$  mm is smoothed and a second peak is visible when  $[w]$  reaches  $\pm 1.0$  mm. The same phenomenon was observed for a tangential displacement of  $\pm 2.0$  mm, as illustrated in Figure 5.17c. Further analysis of these results can be found in (Baydoun, 2017; Mohamed, 2017).

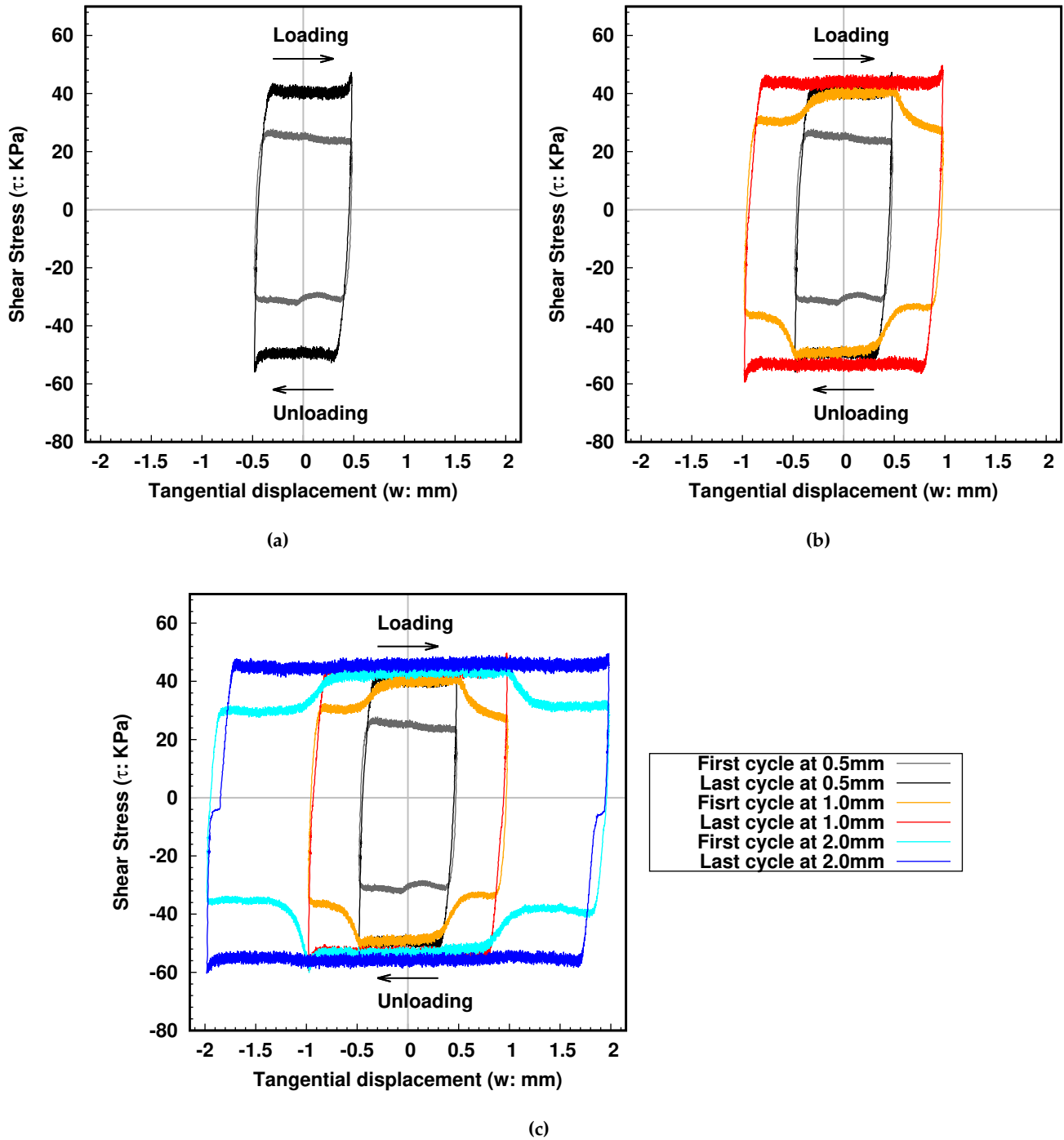
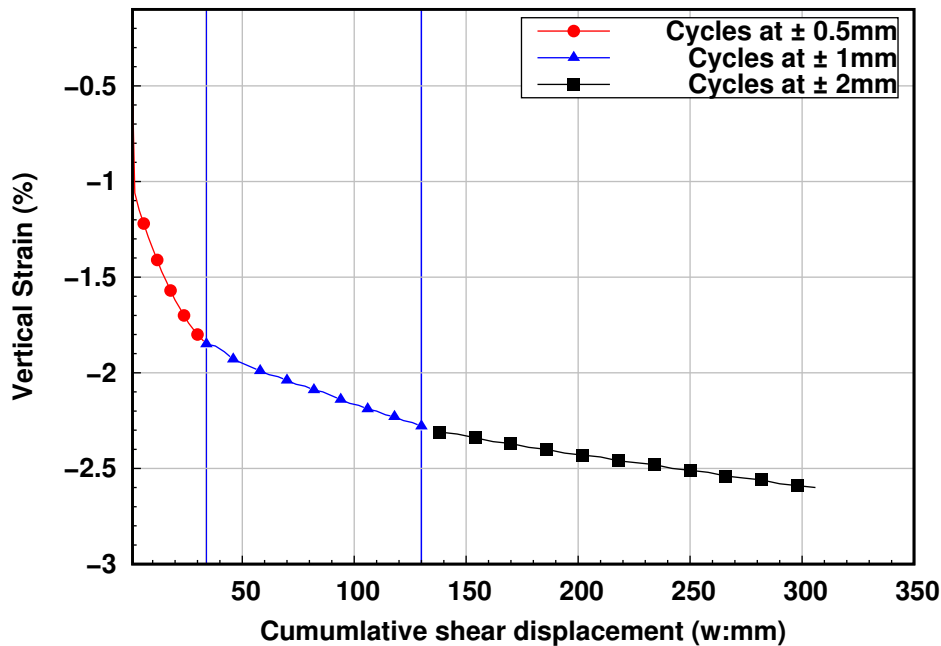


Figure 5.17: Evolution of the shear stress when changing the amplitude of cycles from  $\pm 0.5\text{mm}$  to  $\pm 1.0\text{mm}$  and to  $\pm 2.0\text{mm}$ : a) maximum peak shear stress visible at  $\pm 0.5\text{mm}$ , b) smoothing of the first maximum peak shear stress and new maximum peak shear stress visible at  $\pm 1.0\text{mm}$ , c) smoothing of the second maximum peak shear stress and new maximum peak shear stress visible at  $\pm 2.0\text{mm}$ . Please, note that the key is common to the three plots



**Figure 5.18:** Evolution of the axial shear strain with cumulative shear displacement when changing the amplitude of cycles from  $\pm 0.5\text{mm}$  to  $\pm 1.0\text{mm}$  and to  $\pm 2.0\text{mm}$  (associated with the test presented in Figure 5.17)

### $1\gamma 2\varepsilon$ shear test

A strain-controlled cyclic shear test was performed using  $1\gamma 2\varepsilon$  apparatus, at Laboratoire 3SR, which is essentially a plane stress version of the directional shear cell developed for testing soils (see Calvetti et al., 1997 for technical details). The sample is a 2D assembly of 6 cm long wooden rods as illustrated in Figure 5.19. In this case, the granular material is rigid and cannot crush or deform. The 2D assembly was submitted to a series of about 200 cycles by varying the shear angle  $\gamma$  from  $+2^\circ$  to  $-2^\circ$ . Without loading interruption, it was then submitted to 40 additional cycles using a shear angle of  $\pm 7^\circ$ . The shear stress ( $\tau$ ) was measured all along the cyclic shear test.

Figure 5.20 shows the evolution of the shear stress when changing the magnitude of the shear angle from  $\pm 2^\circ$  to  $\pm 7^\circ$ . For a shear angle of  $\pm 2^\circ$ , Figure 5.20a shows the shear stress measured during the first and the last loading cycle (*i.e.*, 200<sup>th</sup> cycle). Unlike the model pile tests and the direct shear-tests, only the peak shear stress increases. It can also be noticed that the peak shear stress is increasingly marked with loading cycles. Figure 5.20a shows that, when the shear angle is increased to  $\pm 7^\circ$ , the maximum peak shear stress at  $\pm 2^\circ$  is "kept in memory" similar to the model pile test and the direct shear test. When the shear angle increases from  $\pm 2^\circ$  to  $\pm 7^\circ$  the shear stress remains constant, whereas for the direct shear test a loss of shear stress was observed at this stage of the loading. Figure 5.20b indicates that after the peak shear stress measured at  $\pm 2^\circ$  is already smoothed. Finally, after 40 cycles with a shear angle of  $\pm 7^\circ$  the shape of the shear stress path is modified: there is no plateau for  $\gamma$  ranging between  $2^\circ$  and  $7^\circ$  and the peak shear stress starts increasing when  $\gamma$  reached  $\pm 7^\circ$ .

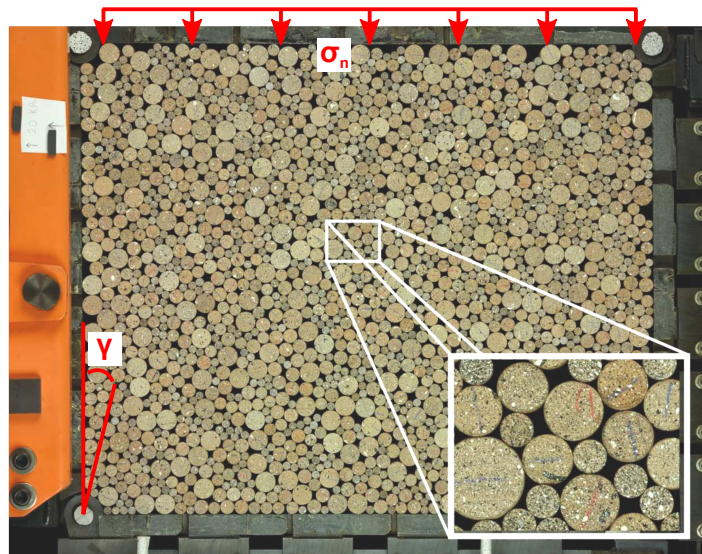


**Figure 5.19:** Image of an isotropically compressed sample in the  $1\gamma 2\epsilon$  device, with zoom on a small amount of grains to show the speckle pattern on their visible face, after Tolomeo et al. (2017) (the frame is 599.4 mm x 444.7 mm).  $\sigma_n$  and  $\gamma$  are the vertical stress and the shear angle imposed, respectively

### Conclusions about the evolution of the peak shear stress

The three types of tests conducted differ for many reasons: 3D versus 2D configuration, the shape of the grains, the grain size distribution, the material strength (crushable versus non-crushable), the type of mechanical loading, the presence of fines or not, etc. However, a similar phenomena was observed when changing the amplitude of the loading cycles during a single test. The peak shear stress measured at the loading reversal is increasing with loading cycles. This peak shear stress is "kept in memory" for several cycles (this number differs from one test to another) when the amplitude is increased. These common results refute most of the assumptions made previously to explain this phenomenon. The most likely reason remaining is that a specific granular arrangement is created by the mechanical loading and strengthens with increasing number of cycles. When the amplitude of loading is increased, this granular arrangement is "kept in memory" for few more cycles until its "collapse". Such a conclusion could be supported, hopefully, by a discrete element model allowing the analysis of the granular structure and of the contact forces network. From an experimental point of view, it would be interesting to see the influence of the order in which the different amplitudes are applied.

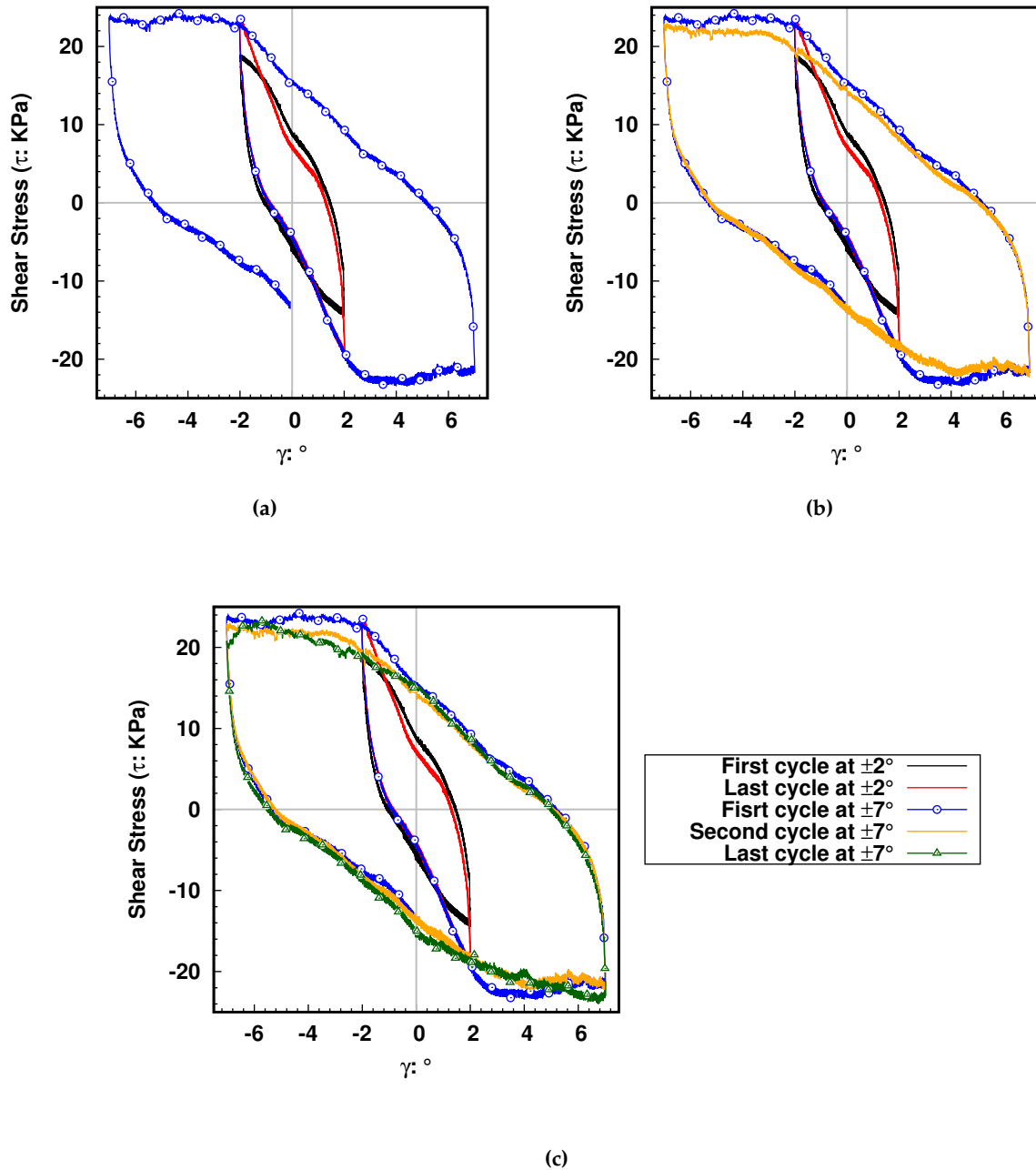


**Figure 5.20:** Evolution of the shear stress when changing the magnitude of the shear angle from  $\pm 2^\circ$  to  $\pm 7^\circ$ : a) maximum peak shear stress at  $\pm 2^\circ$ , b) smoothing of the first maximum peak shear stress, and c) new peak shear stress at  $\pm 7^\circ$ . Please, note that the key is common to the three plots

## 5.4 Effect of boundary conditions

The test P-GLAG-06 was conducted under constant volume keeping similar testing conditions as the tests conducted under constant radial stress for comparison. It should be noted that the pile was installed under constant stress. The boundary conditions were changed prior to the cyclic phase of the test in order to isolate the effect of such boundary conditions on the cyclic response of the pile only. The model pile was then submitted to 2000 displacement-controlled cycles, using an amplitude of displacement of  $\pm 0.5$  mm. Figure 5.21a presents the evolution of the pile head load during test P-GLAG-06. Unlike the tests performed under constant stress, the pile head load reduces continuously and significantly during cycles. The load mobilized is also much lower than under constant stress. The decreased of pile head load can be explained by an important degradation of both tip and shaft resistance.

After 50 cycles, the maximum tip resistance measured when the tip position is at +0.5 mm is already divided by four (see Fig. 5.21b). It is also observed that, after 1000 cycles, the tip is completely unloaded within the whole cycle (zero load recorded at the tip). X-ray images recorded during test P-GLAG-06 show that, in fact, the pile tip is still in contact with sand grains after 1000 cycles. However, as the experimental set-up is upside down, the constant volume boundary condition leads to an important stress relaxation around the pile, which results in a collapse of the soil located ahead of the tip after 1000 cycles.

Figure 5.9 shows the evolution of the shaft resistance during test P-GLAG-06. For the first 50 cycles, test P-GLAG-06 exhibits similar response as test P-GLAG-02 conducted under constant stress. The shaft resistance decreases at a similar rate, of about 15 N. For the subsequent cycles, during P-GLAG-06, the shaft resistance decreases until 100 cycles and then stabilizes whereas test P-GLAG-02 lead to an increase in shaft resistance after 50 cycles. At the end of test P-GLAG-06, the measured shaft resistance is minute, of about 5 N.

Similar results were reported by Silva Illanes (2014). The tests performed in the large calibration chamber of Laboratoire 3SR involved an installation by jacking under constant pressure, an ageing period of 15 days under constant volume and a series of displacement-controlled cyclic loading under constant volume. The results also showed a strong reduction in shaft resistance in the first 3000 cycles followed by a stabilization. The measurement of radial stresses indicated that the effective stress path at the interface moves at an early stage into the unstable zone (as defined by Tsuha et al., 2012) with a significant reduction in radial stresses. A decrease of the pressure applied to the circumferential membranes was attributed to a contraction of the sand mass surrounding the pile. During test P-GLAG-06, an important decrease of the confining pressure, from 100 kPa after the initial pile embedment until 17 kPa after 2000 cycles, indicates a volume reduction of the sand sample (see Fig.5.21d). The contraction of the sand mass around the model pile is clearly visible from the analysis of x-ray images presented in Chapter 6.

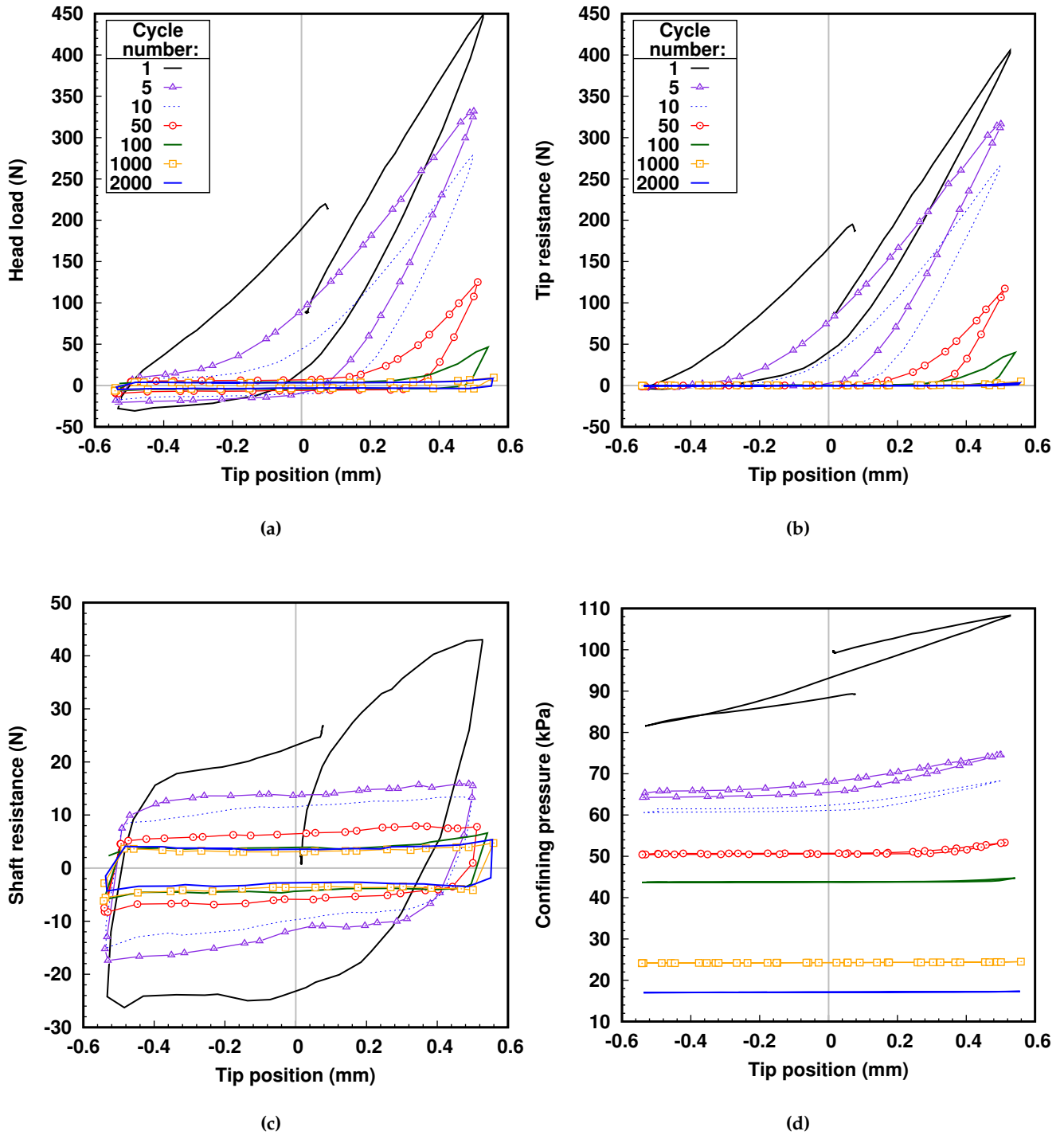


Figure 5.21: Test under constant volume boundary conditions (test P-GLAG-06): a) head load, b) tip resistance, c) shaft resistance and d) confining pressure evolution

## 5.5 Cyclic response of a molded pile

An additional test was conducted on a molded pile to emphasize the importance of the installation method as reported in the literature (*e.g.*, Deeks et al., 2005; El Haffar et al., 2018). In test P-GLAG-15, the pile was pre-installed in the mini-calibration chamber to an equivalent embedment depth of 45 mm. The sand was then deposited by layering directly around the model pile and confined at 100 kPa. Even though the stress conditions are not representative of free-field tests, test P-GLAG-15 was performed to mimic the case of a bored pile. After sample preparation, the first loading applied to the pile was a series of 1000 displacement-controlled cycles, under constant stress, using an amplitude of displacement of  $\pm 0.5$  mm.

Figure 5.22 shows the evolution of shaft resistance during test P-GLAG-15. In contrast with the tests performed on a monotonically jacked pile, during test P-GLAG-15 the loading cycles show no positive effect on shaft resistance. There is a significant degradation of the load measured on the shaft followed by a stabilization around a value of 10 N. It is also clear that the first cycle already leads to a large decrease in shaft resistance, in contrast with the jacked tests. From similar results, Le Kouby et al. (2004) showed that the negative effect of cyclic loading on pile capacity was amplified in the case of a bored pile. Le Kouby et al. (2004) estimated a loss of about 91 % in shaft friction and 46 % in tip resistance after a series of 50 displacement-controlled loading cycles.

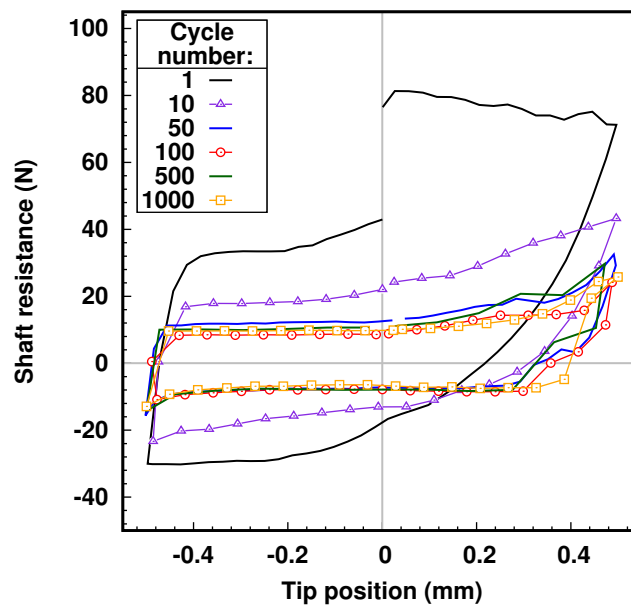


Figure 5.22: Evolution of shaft resistance during loading cycles for test P-GLAG-15 (pre-installed model pile)

## 5.6 Conclusions

The mini-calibration chamber and the experimental methodology used in this study were shown to be effective tools to investigate the behavior of sand-pile interface under axial loading. A comprehensive program of model pile tests was conducted to study the effect of axial cyclic loading on

sand-pile interface. The influence of the amplitude of loading cycles, of boundary conditions and of the method of installation was also investigated. Although testing conditions are not representative of real field piles, the trends measured macroscopically for the evolution of the loads on the pile are qualitatively similar to those obtained in previous studies performed with large-scale devices.

\* The cyclic tests revealed two distinct regimes in the evolution of shaft resistance. In the first regime, the shaft resistance decreases, whereas in the second regime it increases again significantly. This result is consistent with the potential gains in shaft capacity reported in the literature in the case of low level loading cycles.

\* Cyclic tests conducted with different values of amplitudes of loading cycles showed that, in the case of a lower amplitude, fewer cycles are needed to trigger the transition between the two regimes. The results also revealed that the peak shear stress measured when the loading direction is reversed increases with cyclic loading. When the amplitude of loading is increased within a single test, the peak shear stress associated with the first amplitude of loading is "kept in memory" for several cycles. Then, a new peak shear stress is observed at the loading reversal corresponding to the new (higher) amplitude of loading. From additional shear tests performed on a direct shear device and on  $1\gamma_2c$  device, it was concluded that a specific granular arrangement is created by the loading and collapses when the amplitude of loading is increased.

\* It was observed that, with constant volume boundary conditions, the loading cycles have a negative effect on shaft resistance. The load applied on the shaft decreases until it stabilizes after about 100 cycles. Similar results were obtained in the case of molded pile.

\* Finally, model pile tests repeated under identical conditions exhibited similar responses during both pile installation and axial cyclic loading, showing the reproducibility of the results.

## Chapter 6

# Image-based analysis of sand-pile interface

This chapter presents the results of the model pile tests performed in the mini-calibration chamber, using x-ray tomography. The chapter highlights the quantitative measurements made possible thanks to the different image analysis tools described in Chapter 3, including at the scale of the sand grains. The results mainly focus on grain kinematics, porosity changes, and on grain crushing. The objective of this chapter is to analyze and gather grain-scale information that can be used to characterize the micro-mechanisms controlling the macroscopic response of sand-pile interface during pile installation and subsequent loading cycles.

### Layout of the chapter

This chapter starts by a brief presentation of the methodology adopted to report the data obtained by image analysis (Section 6.1). All the analyses performed in this work are in 3D, which makes them difficult to be presented in 2D print. This is why the results are generally shown in vertical slices taken through a 3D field (of scalars or vectors). The slices are always taken in a vertical plane passing through the pile axis, assuming the axisymmetry of the results.

Section 6.2 examines the deformation mechanisms occurring during the installation of the pile. The soil displacement pattern is characterized by means of both continuum and discrete DIC, showing the possibilities offered by each approach (Section 6.2.1). Section 6.2.2 shows how individual grains rotate and are reoriented during the initial embedment of the model pile. Mesoscopic measurements of porosity and shear strains are then presented in Section 6.2.3. The analysis of pile installation ends with a first insight into grain crushing at the sand-pile interface.

Section 6.3 provides a detailed analysis of the mechanisms associated with the loading cycles. The analysis focuses on the evolution of grain kinematics during the two different phases identified for the evolution of shaft resistance (Section 6.3.1). Local density changes and the evolution of fines produced by grain crushing are also investigated during cyclic loading (see Sections 6.3.2 and 6.3.2, respectively).

Finally, a link between the microscopic and the macroscopic behavior of sand-pile interface submitted to axial loading is discussed.

## 6.1 Image analysis data reporting

In this work, a number of analyses are based on the assumption that the response of the sand-pile interface is axisymmetric. It is therefore crucial to justify this assumption. Continuum DIC results show that, in fact, the 3D-displacement field is axisymmetric. Figure 6.1 shows vertical slices taken at different angles through the 3D field of vertical displacements obtained for the increment 2-3 mm of test P-GLAG-00. Horizontal slices taken from the 3D field of horizontal displacements (in  $x$  and  $y$

directions) are also presented in Figure 6.2. As a reminder, in test P-GLAG-00, the pile was first installed until an embedment depth of 35 mm and then submitted to 14 additional increments of 1 mm. It means that the incremental displacements showed in the two figures were obtained between an image pair recorded when the pile tip moved from 37 mm up to 38 mm. The different slices selected within the vertical displacement field exhibit a similar pattern: the regions where displacements concentrate have the same extent around the pile and similar magnitudes. This result is also true for the horizontal displacement field.

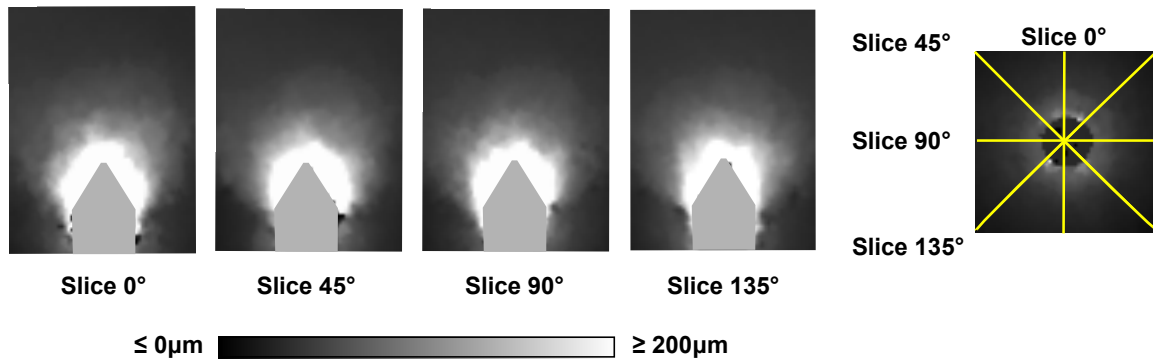


**Figure 6.1:** Vertical slices taken at different angular position within the 3D field of vertical displacements. These results were obtained with continuum DIC, for the increment 2-3 mm of test P-GLAG-00

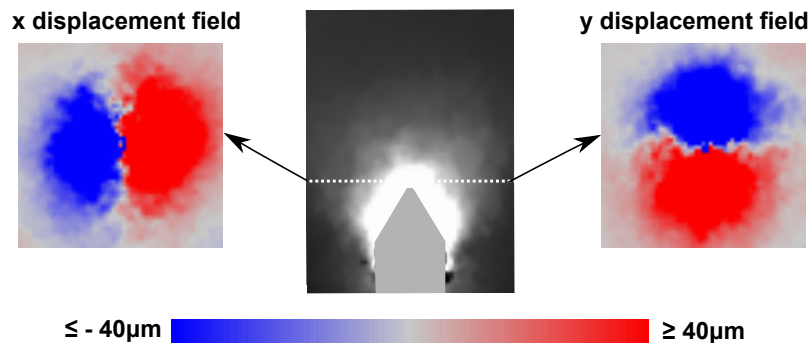


**Figure 6.2:** Horizontal slices taken within the 3D field of horizontal displacements in both x and y directions. These results were obtained with continuum DIC, for the increment 2-3 mm of test P-GLAG-00

Since the full-fields measured (porosity, kinematics, ...) are symmetric about the pile axis, in the following sections, the results are generally displayed as a single 2D slice taken through the 3D field. This 2D slice is considered to be representative of the 3D behavior of the soil mass. Figure 6.3a gives the coordinate system employed in this work for reporting the results of image analysis. In some cases, the results are averaged on the circumference of the sample within a toroidal subdomain obtained by revolution of a rectangular cross-section showed in Figure 6.3b around the pile axis. Such section has a width  $l$  and a length  $L$ , both expressed in function of the mean particle diameter. The position of the section is defined by the coordinates of its top corner ( $T_c$  in Fig. 6.3b): radial coordinate  $r$  and elevation  $h$ .

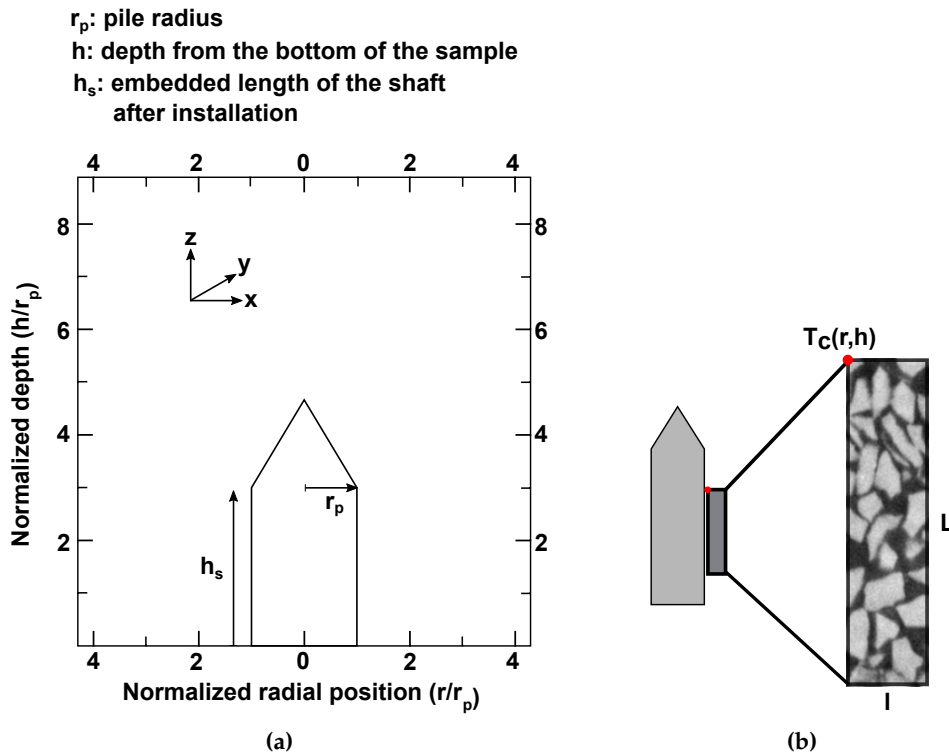


Figure 6.3: a) Coordinate reference system for image analysis data reporting. b) Schematic showing how a subdomain is defined for averaging micro-scale measurements on the circumference of the sample

## 6.2 Mechanical processes during pile installation

### 6.2.1 Soil displacement pattern during pile installation

#### Global behavior of the soil: continuum DIC

Continuum DIC was performed on consecutive scans during pile installation according to the method detailed in Section 3.4.2. As mentioned in Section 5.1.3, the scans were recorded every millimeter after an initial embedment depth of 35 mm, during test P-GLAG-00. Figures 6.4 and 6.5 show respectively vertical and horizontal displacements from continuum DIC calculations at different stages of the pile penetration. Although the results are obtained in 3D, only a vertical slice passing through the pile axis is presented for each increment to facilitate the interpretation of the displacement fields. The continuum DIC results were used to characterize qualitatively the displacements of the soil in the vicinity of the pile during installation. Figure 6.4 shows that vertical displacements concentrate in a zone with the shape of a bulb ahead of the pile tip. This region has a width of about one pile diameter. The rest of the soil mass has displacements close to zero. It can be noticed that the displacement patterns remain the same for all the increments. However, the pile engages more soil as the embedment depth increases. Figure 6.5 shows the displacements of the sand mass in the horizontal direction. The sand located ahead of the pile tip is pushed away from the face of the cone tip. On the contrary, the sand located behind the pile tip, around the pile shaft, tends to move in the opposite direction, *i.e.*, towards the pile. The horizontal displacements are measured in a wider area from the pile axis and at a lower depth than the vertical displacements.

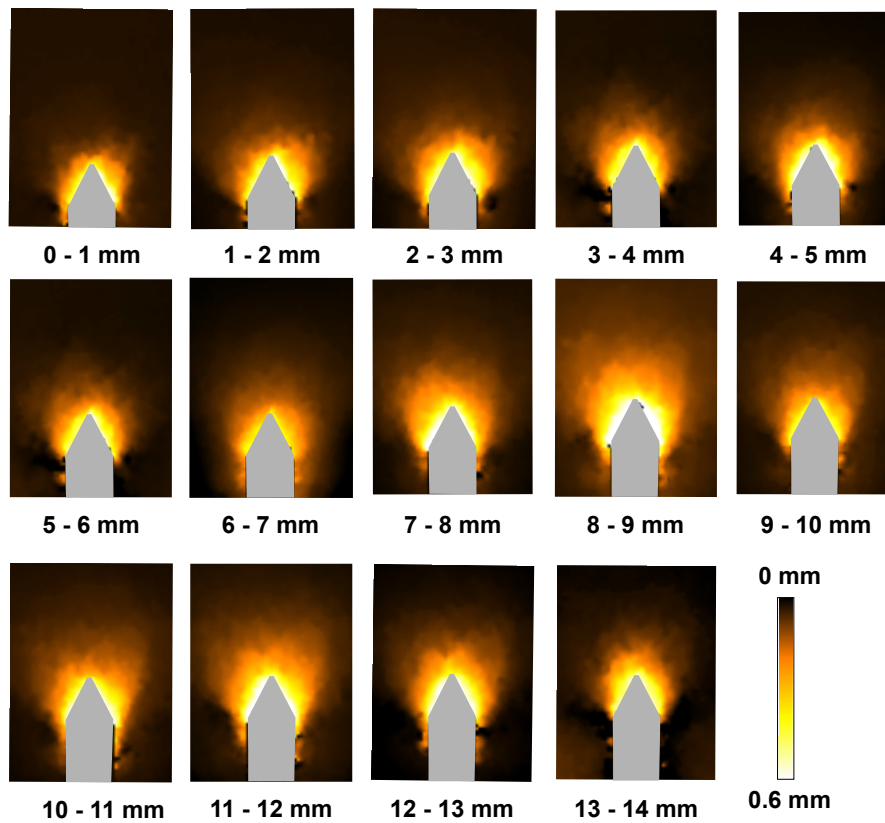


**Figure 6.4:** Vertical slices taken through the 3D field of vertical displacements obtained with continuum DIC (node spacing: 20 pixels, correlation window size: 40 voxels) for an incremental displacement of the pile tip of 1 mm until a maximum displacement of 14 mm (test P-GLAG-00)

### Characterization of different zones of displacements around the pile: discrete DIC

Figures 6.6a, b show individual grain displacements from discrete DIC, plotted in a vertical plane passing through the pile axis, when the pile tip moved up from  $h = 37\text{mm}$  to  $h = 38\text{mm}$  (increment 2-3 mm). Four regions where displacements concentrate can be identified (regions I, II, III and IV sketched in Fig. 6.6b). In region I, which extends down to two pile radii ahead of the pile tip, vertical displacements dominate. The maximum incremental displacements are measured for the grains directly in contact with the cone tip. Region II corresponds to a transition zone where the orientation of the incremental displacement rotates from a mainly vertical direction to an horizontal one. In region III, beneath the pile tip, grains move away from the pile as the pile advances, with a relatively large radial component. The incremental displacements in this region is similar to the one that would result from a cylindrical cavity expansion. In region IV, the incremental displacement is purely radial but with an opposite direction, *i.e.*, towards the pile shaft. These zones are similar to those observed thanks to continuum DIC. However, discrete DIC allows the observation of local discontinuities between grains that are not visible with continuum DIC.

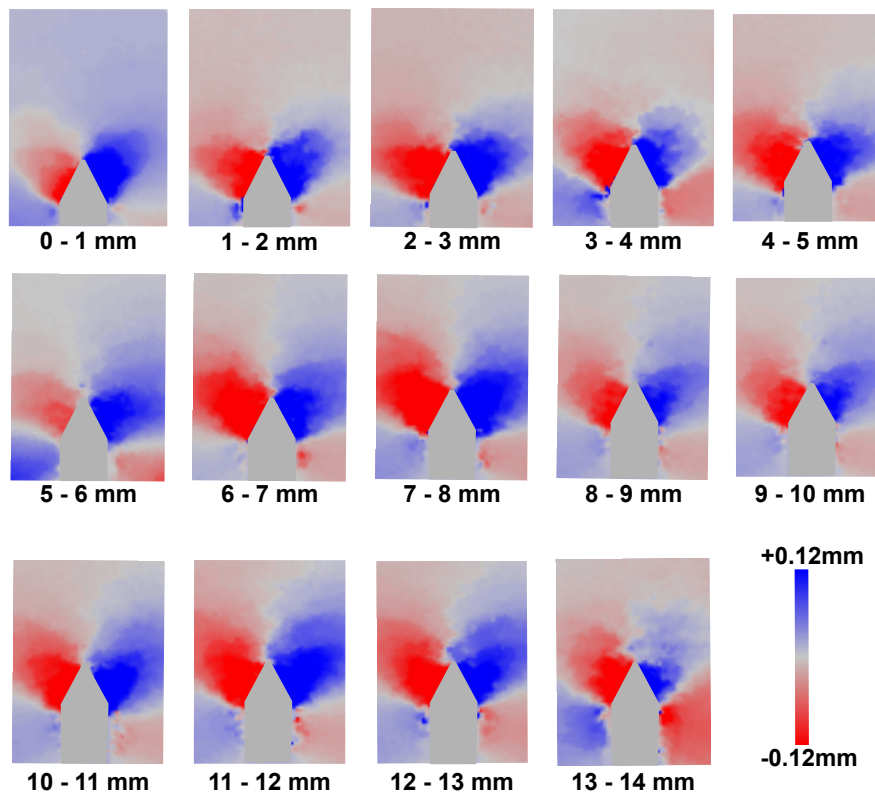


Figure 6.5: Vertical slices taken through the 3D field of horizontal displacements obtained with continuum DIC (node spacing: 20 pixels, correlation window size: 40 voxels) for an incremental displacement of the pile tip of 1 mm until a maximum displacement of 14 mm (test P-GLAG-00)

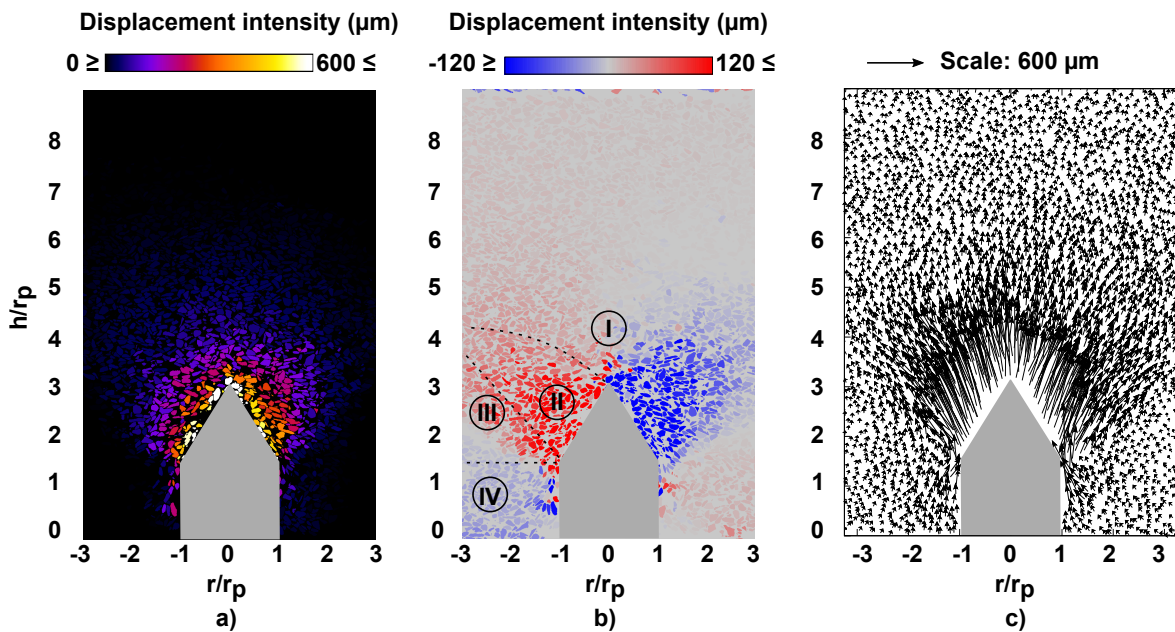


Figure 6.6: Typical individual grain displacements from discrete DIC, plotted in a vertical plane passing through the pile axis, when the pile tip moved up from  $h = 37\text{mm}$  to  $h = 38\text{mm}$  (increment 2-3 mm): a) vertical displacements; b) horizontal displacements; c) individual displacement vectors for the same loading increment. These results are from test P-GLAG-00. Dashed lines delimit the different zones of displacement

It can also be noticed that few grains alongside the shaft experience a vertical displacement. The limited amount of grains engaged by the pile shaft is due to the low roughness of the pile shaft surface. As stated in Section 4.3.2, Hebel et al. (2015) showed that shearing against smooth CPT sleeves is not influenced by sand grains angularity and results in sliding at the soil-continuum interface with negligible soil shearing (see results presented in Section 6.2.3). In the present study, sand grains obviously tend to slide alongside the shaft; however, relative displacements between grains, *i.e.*, grain rearrangement occurs – and is measured – around the pile during its embedment.

The individual displacement vectors of each grain (vertical and horizontal components of Figs. 6.6a, b) are plotted in Figure 6.6c. These vectors highlight the change in the direction of the displacements of the grains located ahead of the pile tip (pushed towards the chamber boundaries) and the grains beneath the pile tip (pushed towards the pile shaft). This result is consistent with the "recirculation" of the sand grains observed in the vicinity of the pile by White and Bolton (2004) and Silva et al. (2013).

The locations where the pile tip is not in contact with any grain are believed to regions where severe grain crushing occurs. Grains that could not be tracked with discrete DIC are not displayed in the figure. It can be assumed that the sand grains undergo a rigid body motion (translation and/or rotation) or do break. Discrete DIC proved to be able to capture a rigid body motion. Thus, any failure to track a grain can be attributed to breakage. Grain wear or breakage modifies the shape of the grain, resulting in a poor correlation. Following breakage thanks to discrete DIC has been successfully employed previously by Karatza (2017) and Guida et al. (2018).

Figure 6.7 shows the grains that are experiencing a rotation for the same loading increment as in Figure 6.6, during test P-GLAG-00. The rotations are concentrated in a limited region around the pile tip. Except for a few grains directly in contact with the pile tip, the intensity of rotation is relatively small (about  $3^\circ$ ). These rotations were measured for an incremental displacement of the pile of 1.0 mm. Grains are expected to undergo larger rotations during the complete installation process. The region where rotations occur is the region where most of the granular rearrangement takes place as noted in Figure 6.6. Alongside the pile shaft, grains do not rotate. This observation supports the fact that the kinematics of the grains in contact with the pile shaft are dominated by a sliding mechanism.

## 6.2.2 Grains orientations

In this section, the orientations of individual sand grains are compared before and after pile installation. Figure 6.8 shows the normalized distribution of grains orientations measured within a subdomain obtained by revolution of the rectangular cross-section shown in Figure 6.3a, with  $l = 5 \cdot D_{50}$ ,  $L = 9 \cdot D_{50}$ ,  $r = 2.15 \cdot r_p$  and  $h = h_s - 4 \cdot D_{50}$ , for test P-GLAG-03. The results show that Legendre polynomial expansion truncated at order 4 (Eq. 3.9) provides a good fit of the PDF of  $|x|$  ( $P(|x|) = 2p(x)$ ) distribution prior to (Fig. 6.3a) and after pile installation (Fig. 6.3b). There is also a clear evolution of the distribution between the two loading stages. The sample is initially rather anisotropic. The fit gives a value of 0.088 for  $\tilde{a}$  (defined as the level of anisotropy in Section 6.2.2), which means that the second moment is relatively far from its isotropic value ( $\frac{1}{3}$ ). From this measurement, it can be concluded that grains are preferably oriented in the horizontal direction ( $\cos\theta$  close to 0), due to the sand deposition procedure. After pile installation, the number of grains with  $\cos\theta$  close to zero (horizontally oriented grains) decreases whereas that closer to one increases (vertically oriented grains). This leads to a less anisotropic distribution of grain orientations, with  $\tilde{a} = 0.045$ . This result shows that the installation of the pile into the sand mass involves a reorientation of the

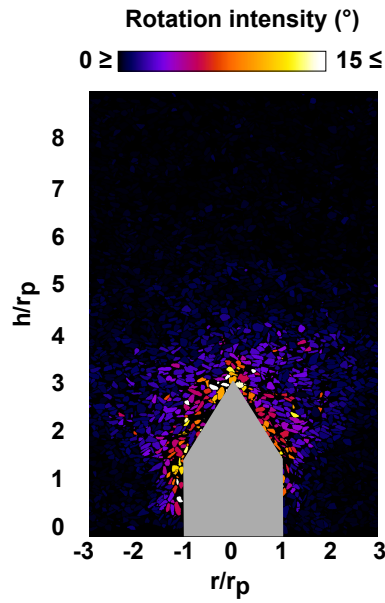


**Figure 6.7:** Individual grain rotations plotted in a vertical plane passing through the pile axis, when the pile tip moved up from  $h = 37\text{mm}$  to  $h = 38\text{mm}$  (increment 2-3 mm) during test P-GLAG-00. The color scale represents the rotation intensity in degrees

grains.

In the present study, it was assumed that the sample was homogeneous at the initial state and that  $\tilde{a}$  was similar over the whole sample. Table 6.1 gives values of  $\tilde{a}$  measured over a same subdomain, but at different arbitrary locations within the 3D image. The results show that, *locally*,  $\tilde{a}$  is ranging between 0.085 and 0.103. A deeper statistical analysis could have been conducted. However, since the values of  $\tilde{a}$  obtained after pile installation are much lower than the one obtained at the initial state, the value of  $\tilde{a}$  measured *globally*, on the whole image was kept as a reference value to characterize the initial state:  $\tilde{a} = \tilde{a}_{initial} = 0.095$ .

Contrary to the initial state, spatial variations of  $\tilde{a}$  are expected after pile installation, as grains do not have a preferred orientation anymore. In order to analyze the spatial evolution of the level of anisotropy,  $\tilde{a}$  was also measured over smaller subdomains defined with  $l = 1 \cdot D_{50}$ ,  $L = 21 \cdot D_{50}$ ,  $r \in [1.0, 3.9] \cdot r_p$  and  $h = h_s$ , after pile installation, for test P-GLAG-03. The ratio between  $\tilde{a}$  and  $\tilde{a}_{initial}$  is plotted against the distance to the pile axis in Figure 6.9a. The figure shows that the highest difference between the two loading states ( $\tilde{a}/\tilde{a}_{initial}$  about 35 %) is reached at a distance of 2.5 pile radii from the pile axis. Closer to the pile axis, the ratio is lower,  $\tilde{a}/\tilde{a}_{initial}$  about 60 %. At a distance  $r$  greater than  $2.5 \cdot r_p$ , the ratio increases continuously and significantly until a value close to 100 % at  $r = 3.5 \cdot r_p$ . These results can be interpreted as follows:

- Close to the pile surface, grains are reoriented and tend to align along a preferred direction. In x-ray images, the majority of the grains is visibly aligned vertically alongside the pile shaft (see region 3 in Fig. 6.9b).
- At a distance  $r$  greater than  $3 \cdot r_p$ , the orientations of the grains are similar to the one measured at the initial state, which means in the horizontal direction (see the region 5 in Fig. 6.9b).

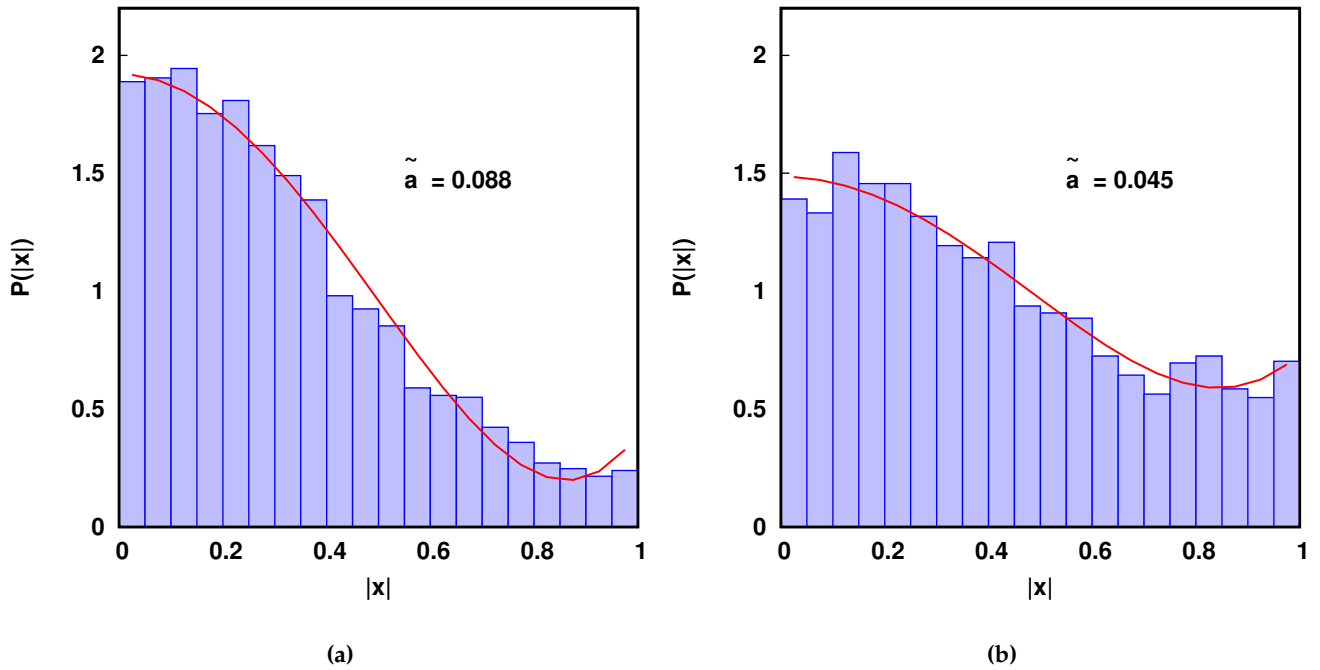


**Figure 6.8:** Distribution of grains orientations and its representation using Legendre polynomials expansion truncated at the 4th order ( $P(|x|) = 2p(x)$ ) a) prior to and b) after pile installation

**Table 6.1:** Coefficient  $\tilde{a}$  measured locally at different locations in the 3D image recorded at the initial state.

$\frac{r}{r_p}$	$h$	$\tilde{a}$
0.00	$h_s + 4 \cdot D_{50}$	0.098
0.00	$h_s$	0.103
0.00	$h_s - 4 \cdot D_{50}$	0.085
1.00	$h_s + 4 \cdot D_{50}$	0.098
1.00	$h_s$	0.098
1.00	$h_s - 4 \cdot D_{50}$	0.096
2.00	$h_s + 4 \cdot D_{50}$	0.092
2.00	$h_s$	0.097
2.00	$h_s - 4 \cdot D_{50}$	0.086
3.00	$h_s + 4 \cdot D_{50}$	0.099
3.00	$h_s$	0.095
3.00	$h_s - 4 \cdot D_{50}$	0.093

- The region where the highest value of  $\tilde{a} / \tilde{a}_{initial}$  is measured appears like a transition zone where grains orientations change from the horizontal to the vertical direction as illustrated in the region 4 of Figure 6.9b.

The level of anisotropy was also estimated around the pile tip, after pile installation. In this case,

$\tilde{a}$  was determined over two subdomains associated with the regions 1 and 2 in Figure 6.9b. Region 1 was defined with  $l = 10 \cdot D_{50}$ ,  $L = 4.5 \cdot D_{50}$ ,  $r = 0$  and  $h = h_s + 9 \cdot D_{50}$ . Region 2 was defined with  $l = 14 \cdot D_{50}$ ,  $L = 4.5 \cdot D_{50}$ ,  $r = 0$  and  $h = h_s + 4.5 \cdot D_{50}$ . The distribution of the orientations of these two subdomains are plotted in Figures 6.10a and b respectively. In the subdomain closer to the pile tip extremity (region 1), the level of anisotropy is lower than the initial state:  $\tilde{a}/\tilde{a}_{initial} = 64\%$ . From the images, it is observed that intact grains tend to align alongside the cone surface and are surrounded by a large amount of broken grains, the orientation of which is difficult to estimate. In the subdomain closer to the shaft (region 2), the preferred orientation of the grains alongside the cone is better defined with fewer broken grains. This is confirmed by the value of  $\tilde{a}/\tilde{a}_{initial}$  that reaches 53 %.

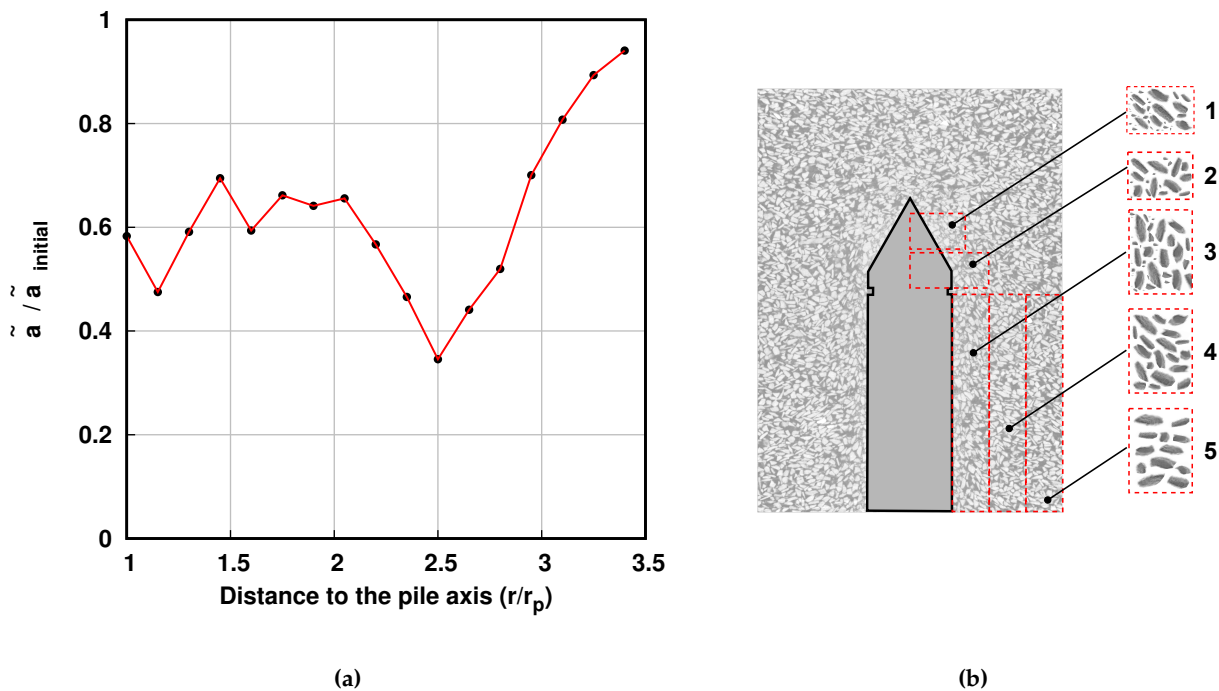


**Figure 6.9:** a) Radial evolution of the ratio between  $\tilde{a}$  and  $\tilde{a}_{initial}$  showing the change in anisotropy prior to and after pile installation. b) Schematic illustrating the fabric formed following pile penetration at different locations around the pile tip and the pile shaft. In this figure,  $\tilde{a}_{initial}$  was obtained over all grains at the initial state and its value is 0.095

These results suggest that the (re)orientation of the grains is linked to the kinematics of the grains measured during pile installation by 3D DIC. The aforementioned grain-scale observations can be interpreted as follows. The relatively large displacements and rotations measured in a relatively small region around the tip indicate that the movement of the pile tip causes the grains to rearrange and to rotate. As the pile advances, grains located in front of the cone tip are pushed away from the pile path, mainly in the horizontal direction. Grains located immediately near the cone face are given a preferred orientation almost parallel to the cone surface, which induces a relatively high level of anisotropy. As the cone shoulder reaches their elevation, these sand grains are pushed in the opposite direction, *i.e.*, towards the pile shaft, by the surrounding grains (sand flow measured in the vicinity of the pile). When these grains come in contact with the pile shaft, their major axes tend to align alongside the pile shaft surface. At this stage of the installation, these grains slide vertically due to

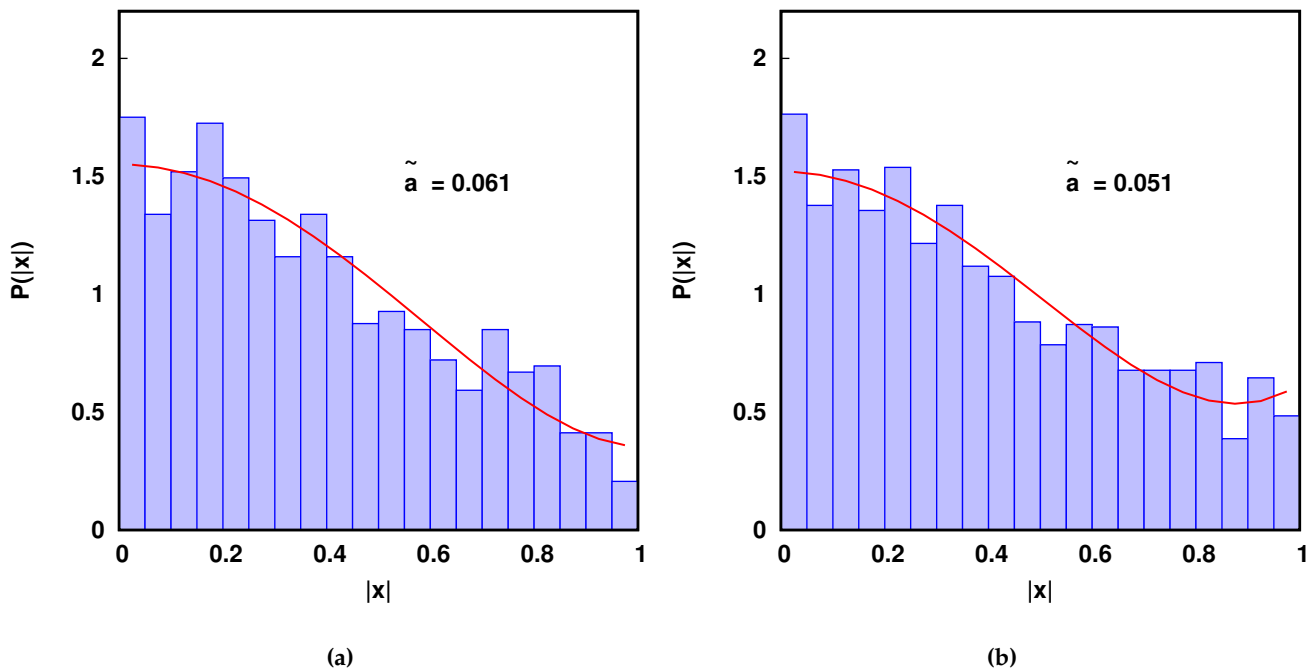


**Figure 6.10:** Distribution of grains orientations and its representation using Legendre polynomials expansion truncated at the 4th order after pile installation. The level of anisotropy was estimated by determining  $\tilde{a}$  over two subdomains located around the pile tip corresponding to the regions 1 and 2 in Figure 6.9b

the low roughness of the model pile. The angularity and the shape of Glageon grains facilitate their (re)orientation during pile penetration.

### 6.2.3 Volumetric and shear behaviors

Figure 6.11 shows vertical slices taken through the 3D field of porosity before and after pile installation during test P-GLAG-16. In this test, 3D images were recorded in global tomography allowing the global characterization of the sand sample. The measurements of porosity were obtained following the mesoscopic approach described in Section 3.3 with a REV measuring  $50 \text{ pixel}^3$ . After pile installation (Fig. 6.11b), a zone ahead of the pile tip exhibits porosity values of about 53 %, which is 8% higher than the one measured for the initial state (Fig. 6.11a). This result indicates a loosening of the soil around the pile tip, as reported by Chong (1988) and Nes (2004). Similar results are observed around the pile shaft, within a region that extends until one pile diameter away from the shaft surface. The region where dilation of the soil occurs is delimited by the dotted line in Figure 6.11a. Figure 6.11c shows that the sample, initially cylindrical, deformed. Its volume obviously increased around the pile.

A thin layer of lower porosity (less than 33 %) is visible near the pile tip and the pile shaft. The lower porosity of this layer is attributed to the presence of fines produced by grain crushing during the installation as illustrated in Section 6.2.4. As observed in the images, fines are filling the pores at the interface, leading to a local densification. A quantitative study of local density changes around the pile will be presented in Section 6.3.2 for cyclic loading.

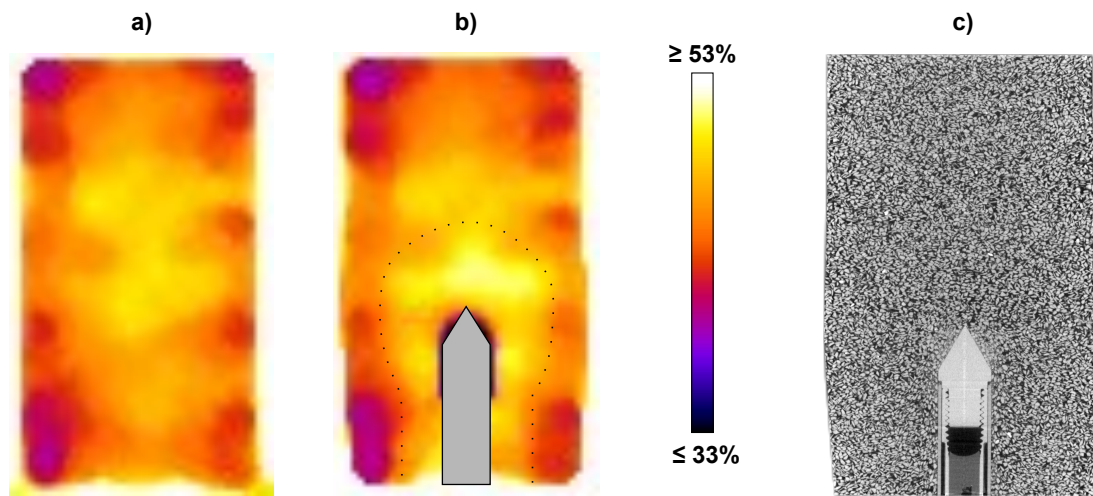


**Figure 6.11:** Vertical slices selected through the measured 3D field of porosity a) before and b) after pile installation, for test P-GLAG-16. c) Same vertical slice through the 3D reconstructed volume showing the global volume change of the sample after pile installation

When comparing the measurement of porosity and the orientations of the sand grains, it can be noted that in the region where the soil contracts, grains are preferably aligned, parallel to the shaft or to the cone surface. Dilative regions are associated with the grains that undergo large displacements and have relatively random orientations. Paniagua et al. (2018) observed similar results for the penetration of a cone in a silty soil. The Authors showed that the compressive and dilative zones observed around the cone in Paniagua et al. (2013) correlate well with the statistical orientation of the grains traduced by a level of anisotropy. In particular, the Authors identified two types of soil fabric (due to the presence of flaky grains): (1) an "open-fabric" where the grains reorient with random orientations creating large voids between them and (2) a "closed-fabric" where the grains align along a well-defined orientation forming a more compacted structure with small voids within.

Figure 6.12 shows vertical slices through the incremental 3D field of maximum shear strain during pile installation, for test P-GLAG-00. It can be observed that the shear strain concentrates in a relatively small region around the pile tip. This region correlates well with the one where grain displacements and rotations occur (Figs. 6.6 and 6.7). The maximum value, about 10%, is measured ahead of the pile tip. In the rest of the sand mass and around the pile shaft no shear strain is measured. These results support the fact that pure sliding dominates alongside the pile shaft, due to its low roughness. It is also noteworthy that the output from Tomowarp2 appears to be more noisy for the strain field than for the displacement field. This is likely due to the fact that the sub-pixel search of the DIC algorithm has some preferential values (at 0.5 pixels displacement in the case of Tomowarp2), which add noise to the calculation of the gradient of the displacements, *i.e.*, strain.

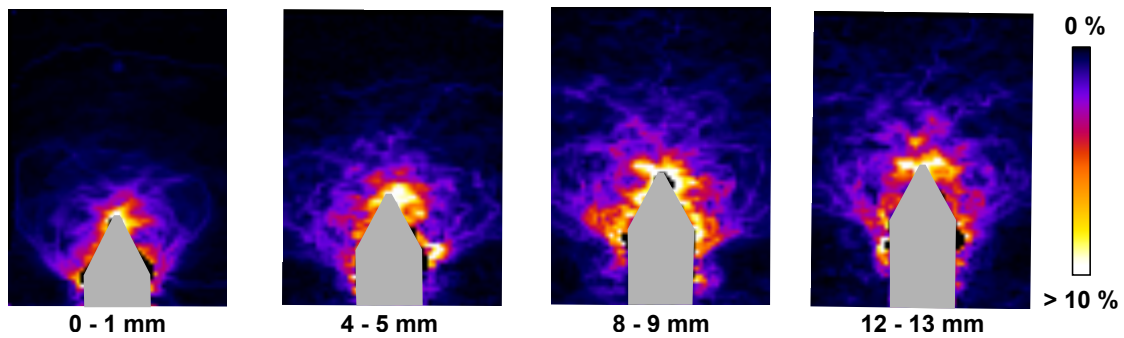


Figure 6.12: Vertical slices through the 3D deviatoric strain field (*i.e.*, maximum shear strain) calculated from continuum DIC kinematics for test P-GLAG-00

#### 6.2.4 Grain crushing

At the end of the tests, the set up was dismantled and the sand above the pile tip was carefully removed from the sample in order to let the interface visible. Post-mortem photographs of the interface show a thin layer of the powder produced by grain crushing around the pile tip and pile shaft. There was no visible abrasion of the shaft surface contrary to what is generally observed (*e.g.*, Yang et al., 2010; Arshad et al., 2014).

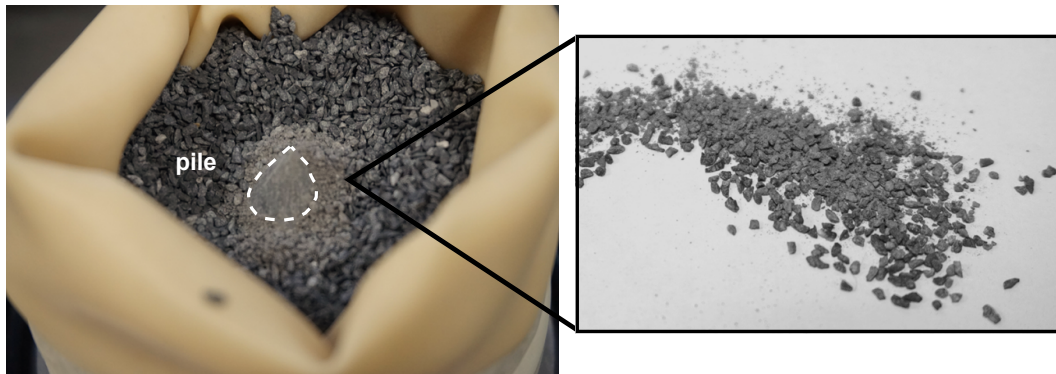
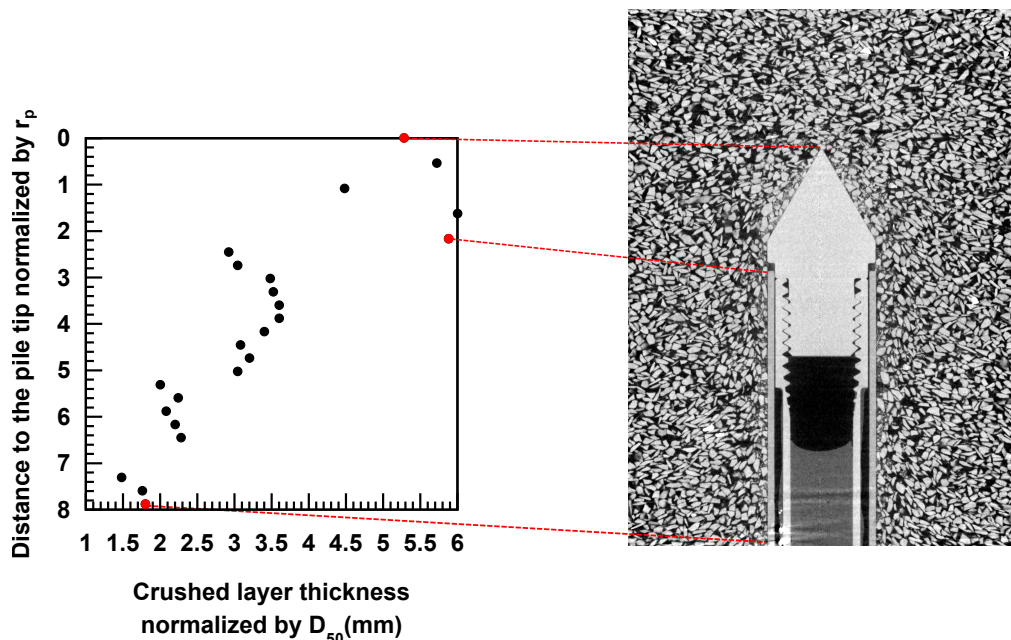


Figure 6.13: Photograph of the sample when the setup was disassembled after pile installation. A light-gray powder can be seen around the pile, which is delimited by the dashed line. A zoom into the material sampling at the interface shows the powder produced by grain crushing

Thanks to x-ray imaging, a further analysis of the thin layer of fines produced by grain crushing at the interface was conducted. Figure 6.14 shows a vertical slice from test P-GLAG-09, after the installation of the pile until an embedment depth equals to 70 mm. A thin layer where fines are interlocked between the bigger grains (or fragments of grains) can be seen around the pile tip and pile shaft. The thickness of this layer was directly measured at different elevations alongside the pile shaft, every 50 pixels (*i.e.*,  $2 \cdot D_{50}$ ), with a standard deviation of  $\approx 1 \cdot D_{50}$ . Around the pile tip, the thickness of the layer was measured perpendicularly to the tip surface. The results obtained on 2D slices are plotted in Figure 6.14. The larger thickness, about  $6 \cdot D_{50}$  is measured around the pile tip. This results suggests that most of grain crushing occurs ahead of the pile tip as the pile advances. Along the pile shaft, the measurements are relatively scattered. However, there is a clear trend showing that

the thickness decreases when increasing the distance from the pile tip: it goes from  $3.5 \cdot D_{50}$  to  $1.5 \cdot D_{50}$ .

From a series of CPTS tests conducted on three types of silica sand with different crushability, Arshad et al. (2014) observed a very thin crushed particle band of thickness ranging between  $1.5$  and  $4 \cdot D_{50}$  for the most crushable sand. This thin particle band was surrounded by a  $4 \cdot D_{50}$ -thick band consisting of moderately crushed sand particles. Similar results were reported by Yang et al. (2010) for large calibration chamber pile tests. The Authors suggested that the crushed material is displaced radially, developing concentric zones around the pile shaft involving different degrees of particle crushing. The thickness of the band near the pile tip found by the Authors was about  $2.4 \cdot D_{50}$ , similarly to White and Bolton (2004). In this study, only one band of crushed grains was observed. This major difference with previous studies is due to the relatively small amount of shearing at the interface. The fines are not migrating radially away from the pile shaft surface. Moreover, the upside-down configuration of the setup may induce a vertical migration of the fines due to their own weight. As a consequence, the fines produced ahead of the pile tip are displaced as the pile tip advances but remain roughly in the same position around the pile shaft for the rest of pile installation.



**Figure 6.14:** Evolution of the thickness of the layer of soil alongside the pile where grain crushing occurs and vertical slice showing this layer after pile installation during test P-GLAG-09

## 6.3 Mechanical processes during cyclic loading

### 6.3.1 3D displacement fields

Typical results from 3D discrete DIC are presented in Figure 6.15. Two pairs of 3D images were analyzed, one from 10 to 50 cycles (Figs. 6.15a, b) and one from 500 to 1000 cycles (Figs. 6.15c, d). These two increments respectively fall in the first and second phase of behavior of the shaft resistance defined in Section 5.2.1. Cyclic loading induces significant displacements, mainly in the horizontal direction. Grains globally move towards the shaft for both loading steps leading to a radial contraction of the soil mass (Figs. 6.15b, d). Vertical displacements are relatively small – less than  $20\mu\text{m}$  in the second increment (Fig. 6.15c). In Figure 6.15a, two distinct zones can be observed in the vertical displacement field. Grains located ahead of the pile tip move upwards, which indicates a local densification ahead of the pile of the soil, whereas grains located alongside the pile shaft move in the opposite direction.

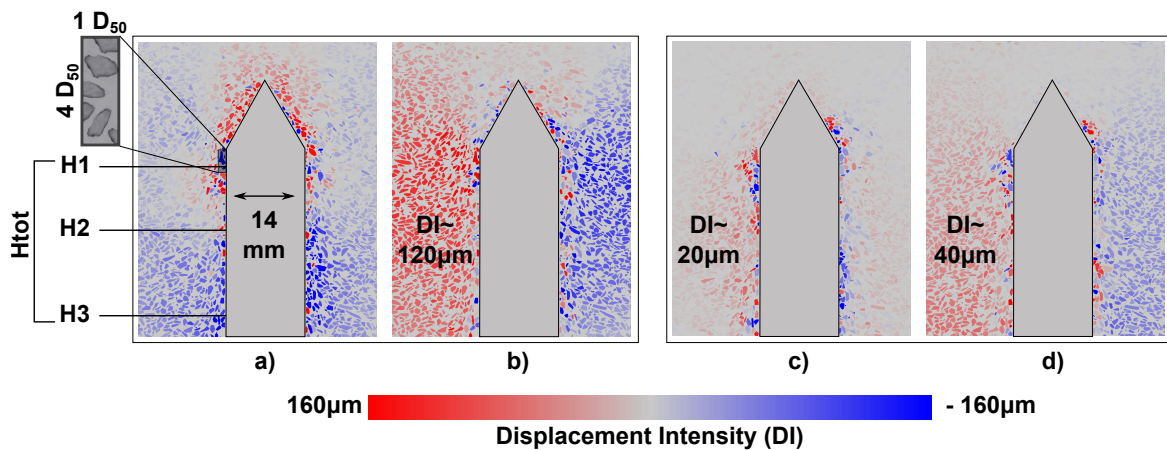


**Figure 6.15:** Typical individual grain displacements from discrete DIC, plotted in a vertical plane passing through the pile axis and showing the evolution of displacement intensity (DI) during loading cycles: a) vertical displacements, b) horizontal displacements between cycles 10 and 50; c) vertical displacements, d) horizontal displacements between cycles 500 and 1000. These results are from test P-GLAG-03 (amplitude  $\pm 0.5$  mm)

Individual displacement vectors for the same two loading increments are shown in Figure 6.16. Ahead of the pile tip, the displacement vectors are nearly vertical and relatively minute, while around the shaft the displacement vectors have a much larger radial component. The displacement fields also reveal, in both increments, a thin layer around the shaft where the grains are highly affected by the loading and difficult to track from one image to another. In the first of the two increments shown, (Fig. 6.16a), grains are clearly moving downwards. This is likely due to a reduction of the hoop stresses created during pile installation. This effect is erased in the later increment.

The radial displacements were then calculated from vertical and horizontal displacements using the axis of the pile as the axis of symmetry. Radial displacements were averaged (arithmetic mean) within a toroidal subdomain of soil obtained by revolution of the rectangular cross-section shown in Figure 6.15a, defined by its distance from the shaft ( $d$ ), normalized by  $D_{50}$ . Three such sub-domains

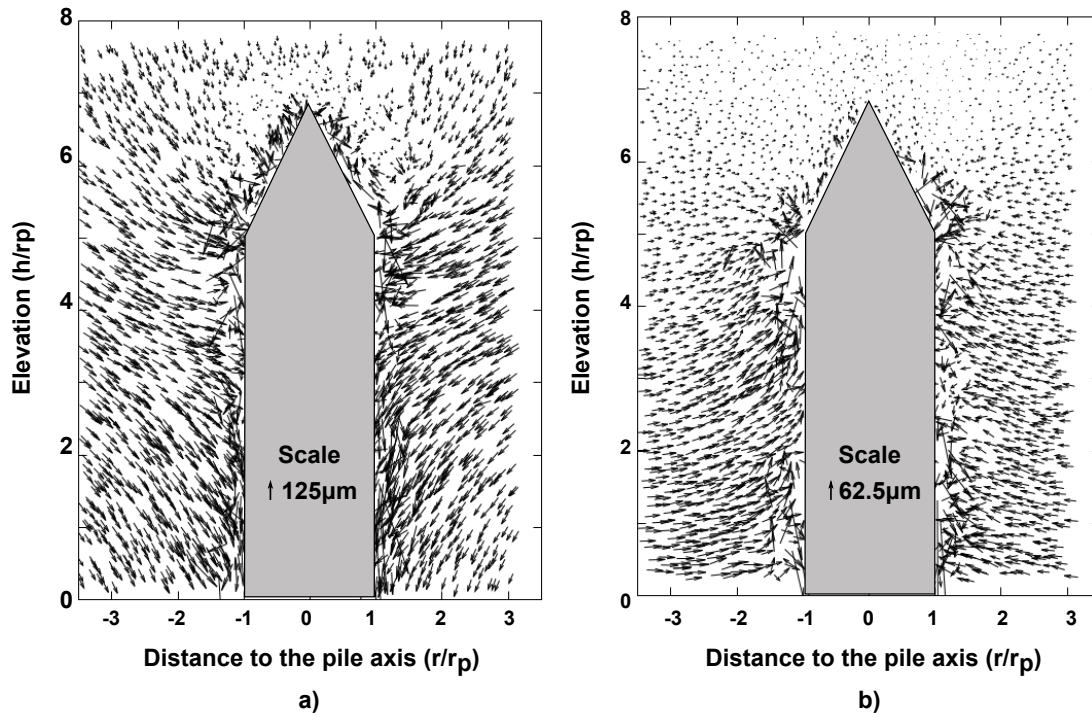
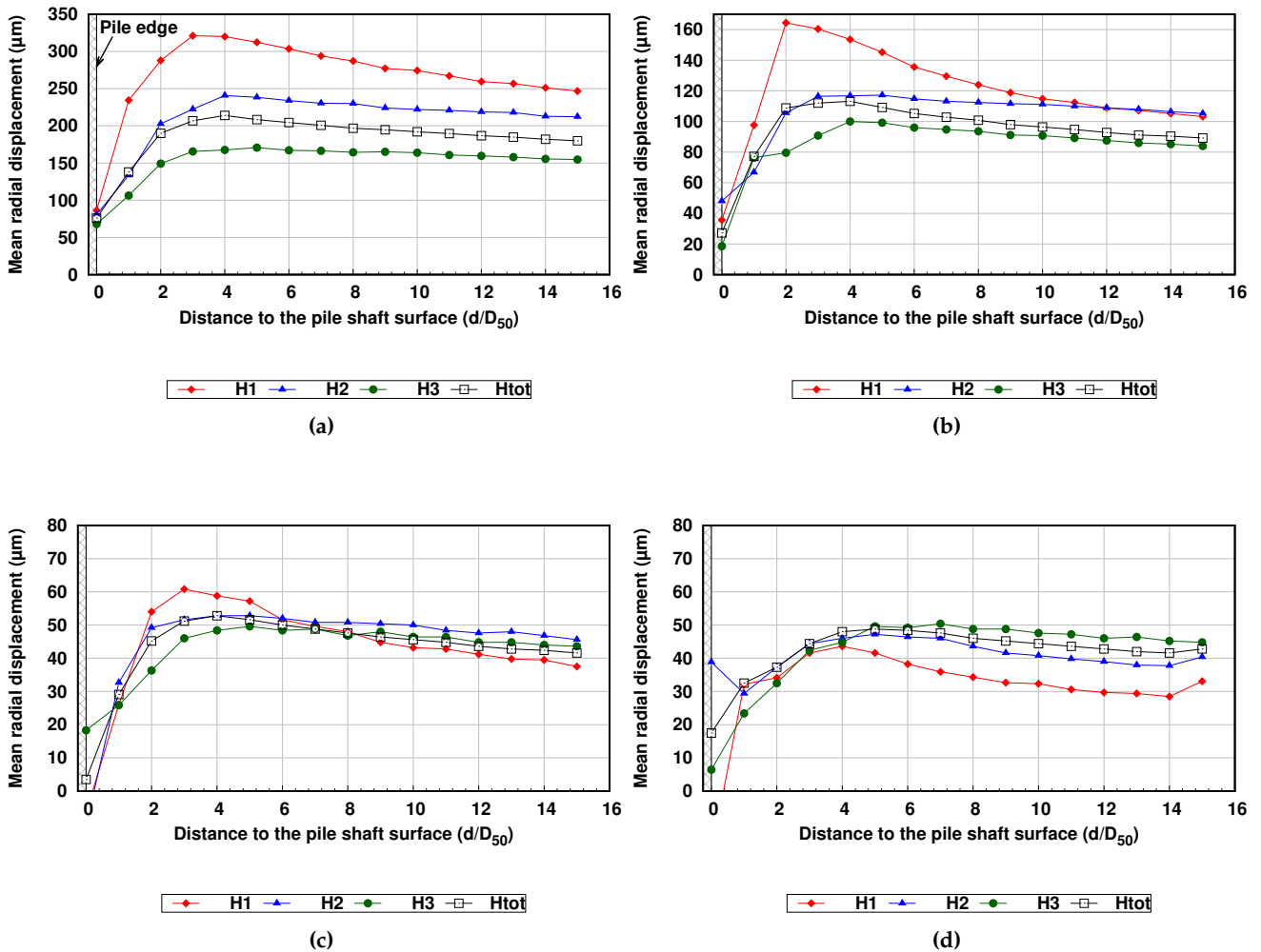


**Figure 6.16:** Individual displacement vectors obtained for the same loading increments as Figure 6.15, plotted in a vertical plane passing through the pile axis: a) between cycles 10 and 50 and b) between cycles 500 and 1000. Note that the scale is different in figures a and b

were studied, at three different elevations alongside the pile shaft (H1, H2 and H3 in Fig. 6.15). Finally, the analysis was also applied to the entire length of the pile shaft (Htot in Fig. 6.15).

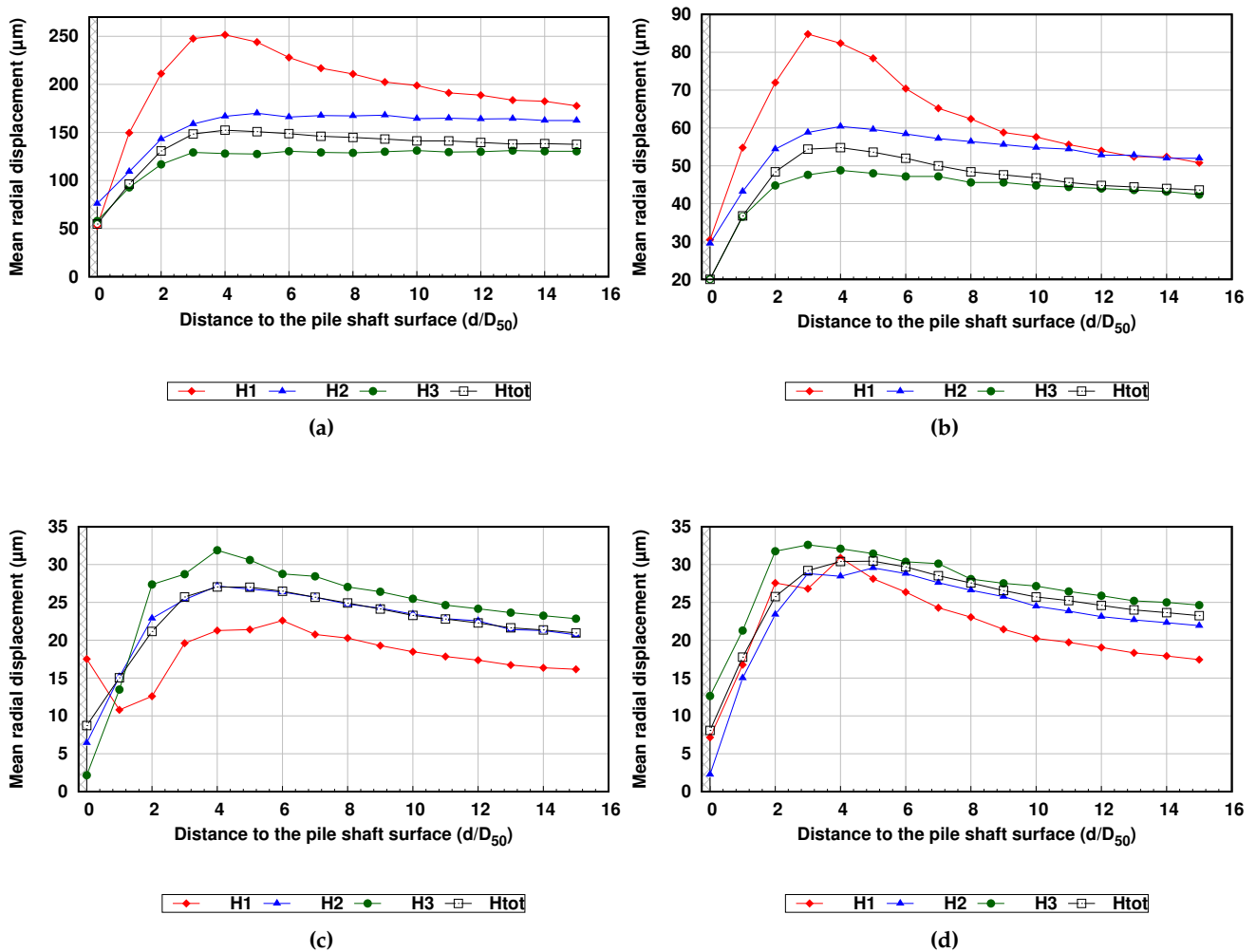
In Figure 6.17, average radial displacements are plotted against the normalized distance from the shaft surface for test P-GLAG-03 (amplitude  $\pm 0.5$  mm). At a distance between  $3$  and  $6 \cdot D_{50}$ , the highest radial displacements take place. As one goes closer to the shaft, grains displacements decrease significantly. This region corresponds to a layer of soil with a high percentage of fines interlocked between grains where high porosity changes take place (see Section 6.3.2). Although grains are mainly sliding alongside the pile shaft during cyclic loading, non-zero displacements are measured on the shaft surface ( $d/D_{50} = 0$ ). This is likely due to the reorientation of some of the grains due to the global radial contraction of the soil mass. At a distance greater than  $6 \cdot D_{50}$ , sand grains are moving homogeneously towards the shaft. It is also noteworthy that the closer the grains are to the tip (elevation H1), the more they are affected by the loading.

By comparing radial displacements after 50 cycles (Fig. 6.17b) and 1000 cycles (Fig. 6.17d), two different trends can be identified. The first tens of cycles cause higher grain movements (100 to 300  $\mu\text{m}$ ). After 50 cycles, displacement intensity is almost divided by 6 and it is essentially the same at all elevations. This result shows that, in the second regime, when the shaft resistance increases, grains hardly move and granular rearrangement is almost inhibited after 50 cycles.



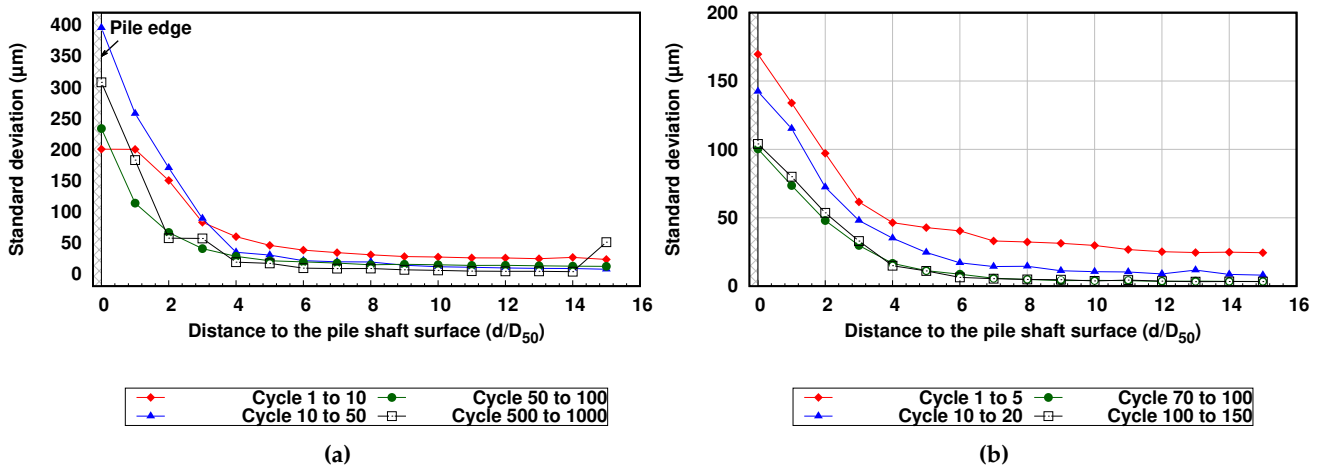
**Figure 6.17:** Mean radial displacements obtained from discrete DIC for different loading stages: a) cycles 1-10, b) cycles 10-50, c) cycles 50-100 and d) cycles 500-1000. Radial displacements are averaged within a toroidal subdomain of soil obtained by revolution of the rectangular cross-section shown in 6.15a. These results are from test P-GLAG-03 (amplitude  $\pm 0.5$  mm)

Figure 6.18 shows the averaged radial displacements obtained for test P-GLAG-09 (amplitude  $\pm 1.0$  mm). With a higher amplitude of cycles, the same trends as for the lower amplitude can be observed. The majority of the radial displacements occurs for the first tenth of cycles, which means in the first regime, when the shaft resistance decreases. Later on, the measured radial displacements are relatively small, about  $30 \mu\text{m}$ . This magnitude of displacement is close to the resolution of the discrete DIC when using a subpixel search. This means that, as for a lower amplitude of cycles, kinematics are minute in the second regime, when the shaft resistance increases again.



**Figure 6.18:** Mean radial displacements obtained from discrete DIC for different loading stages: a) cycles 1-5, b) cycles 10-20, c) cycles 70-100 and d) cycles 100-150. Radial displacements are averaged within a toroidal subdomain of soil obtained by revolution of the rectangular cross-section shown in 6.15a. These results are from test P-GLAG-09 (amplitude  $\pm 1.0$  mm)

Figure 6.19a, b show respectively the standard deviation of the radial displacements of test P-GLAG-03 and test P-GLAG-09. The standard deviation is 20 and 10 times higher for the grains close to the pile ( $d \leq 3 \cdot D_{50}$ ) in each test. This relatively large variability can be explained by the heterogeneous behavior of the grains at the interface but also, and above all, by the difficulty to follow grains that are in contact with the pile. However, at a distance greater than  $3 \cdot D_{50}$  the standard deviation is relatively low and the same for all elevations, supporting the assumption of an axisymmetric field of displacements.



**Figure 6.19:** Evolution of the standard deviation of the radial displacements for the elevation H1 during cycles: a) test P-GLAG-03 of Fig. 6.17, b) test P-GLAG-09 of Fig. 6.18

### 6.3.2 Porosity changes

The evolution of porosity during test P-GLAG-03 is plotted in Figure 6.20. This test was conducted on a sample with an initial relative density of 84% and an amplitude of displacement of  $\pm 0.5$  mm for the loading cycles. The estimation of the volume of each phase (expressed in percentage of voxels) was done thanks to the method presented in Section 3.3. It is important to note that the measurements for the first two points of each curve are highly affected by the binary mask on the pile that can increase the percentage of pores. In the figure, the terms "grain phase" refers to the solid phase without fines, *i.e.*, non-broken grains or relatively large pieces of broken grains. The results show an increase of the percentage of voxels associated to grains with increasing number of cycles in the vicinity of the pile. Close to the interface, the quantity of grains is 20% higher after 1000 cycles, which indicates a local densification. It can also be observed that the thickness of the region affected by such densification is about  $2 \cdot D_{50}$  for cycle 1 and  $4 \cdot D_{50}$  for cycle 1000. In the rest of the sand mass, the proportion of grains and pores remains constant throughout the test.

Figure 6.21 shows the same results obtained during test P-GLAG-09, which was conducted on a sample with a similar initial relative density (85%) but with an amplitude of displacement of  $\pm 1.0$  mm. The results exhibit a similar trend as the one obtained for test P-GLAG-03. The percentage of the grain phase is 20% higher after 150 cycles. It is interesting to note that the results give similar percentages of grains (about 50%) and pores (about 37%) in the region that is not affected by the loading cycles (at least in terms of density changes) for both tests.

These results indicate that the thickness of the band adjacent to the shaft is related to the displacements that the grains undergo and to the local shearing loading history. Yang et al. (2010) also reported a shear zone  $2.4 \cdot D_{50} - 8.6 \cdot D_{50}$  wide, after cyclic jacking installation, in their large calibration chamber tests on NE34 Fontainebleau sand ( $D_{50} = 0.21\text{mm}$ ). Similar to Silva et al. (2013), in their post-mortem analysis, Yang et al. (2010) suggested that the shear zone thickness grows with the vertical distance from the pile tip, especially when the installation is not monotonic, and is augmented

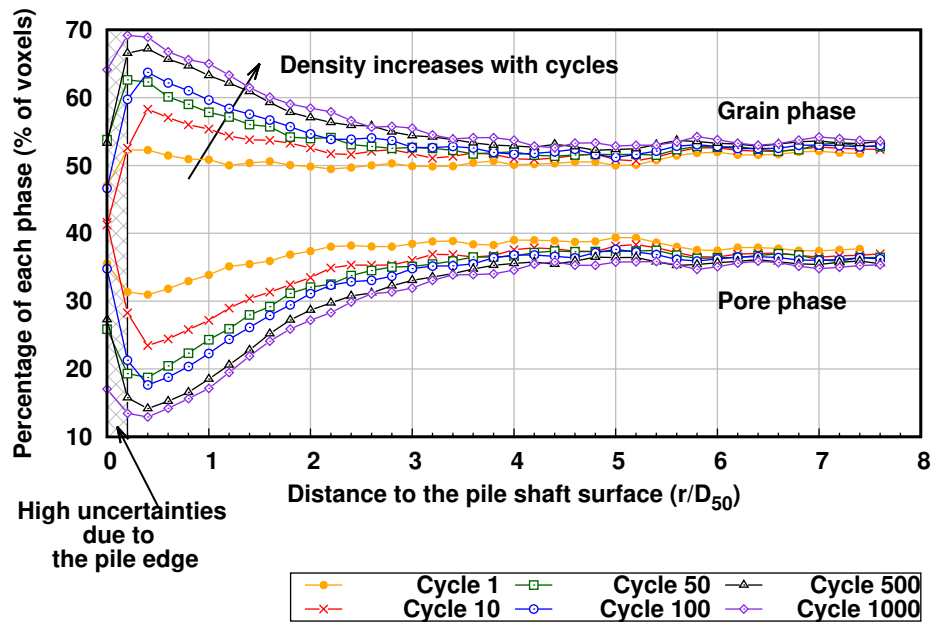


**Figure 6.20:** Radial evolution of grain (without fines) and pore phases volume during loading cycles for test P-GLAG-03 (amplitude of displacement  $\pm 0.5$  mm, initial relative density of 84 %). The x-axis scale is such that a radial distance of 7 is equal to one pile radius. For a given curve, each symbol represents one measurement obtained by thresholding the gray-scale image at a distance  $r$  from the shaft (over a cylindrical subdomain as defined in Section 3.3)

by later static or cyclic loading.

Figures 6.22aa and b give the evolution of the percentage of the grain and pore phases at different distances from the pile surface, with increasing number of cycles, for test P-GLAG-03 and test P-GLAG-09. The results indicate that although the percentage of grains keeps increasing with increasing number of cycles, the rate of densification decreases for these two tests. It is also observed that the closer to the pile surface, the higher the densification. Finally, it is noteworthy that the results for both tests almost overlap. However, for test P-GLAG-09 (amplitude of  $\pm 1.0$  mm), the increase in grain percentage is about 12 % after only 150 cycles, while the same increase is reached after about 500 cycles in the case of test P-GLAG-03 (amplitude of  $\pm 0.5$  mm).

Figure 6.23 shows the radial evolution of the percentage of grains and pores after 150 cycles, during test P-GLAG-09. The data were obtained from two different x-ray scans recorded when 150 cycles were reached (referred as 150 and 150 bis). This figure aims at showing the reproducibility of the methodology. Indeed, the results for the two scans perfectly overlap despite the time difference between the two acquisitions (3 hours for each scan).

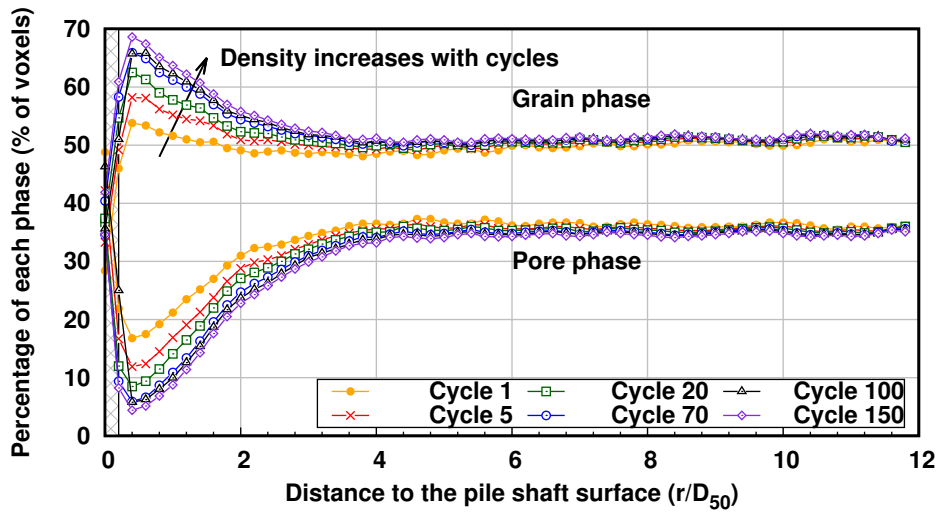


Figure 6.21: Radial evolution of grain (without fines) and pore phases volume during loading cycles for test P-GLAG-09 (amplitude of displacement  $\pm 1.0$  mm, initial relative density of 85 %). The x-axis scale is such that a radial distance of 7 is equal to one pile radius. For a given curve, each symbol represents one measurement obtained by thresholding the gray-scale image at a distance  $r$  from the shaft (over a cylindrical subdomain as defined in Section 3.3)

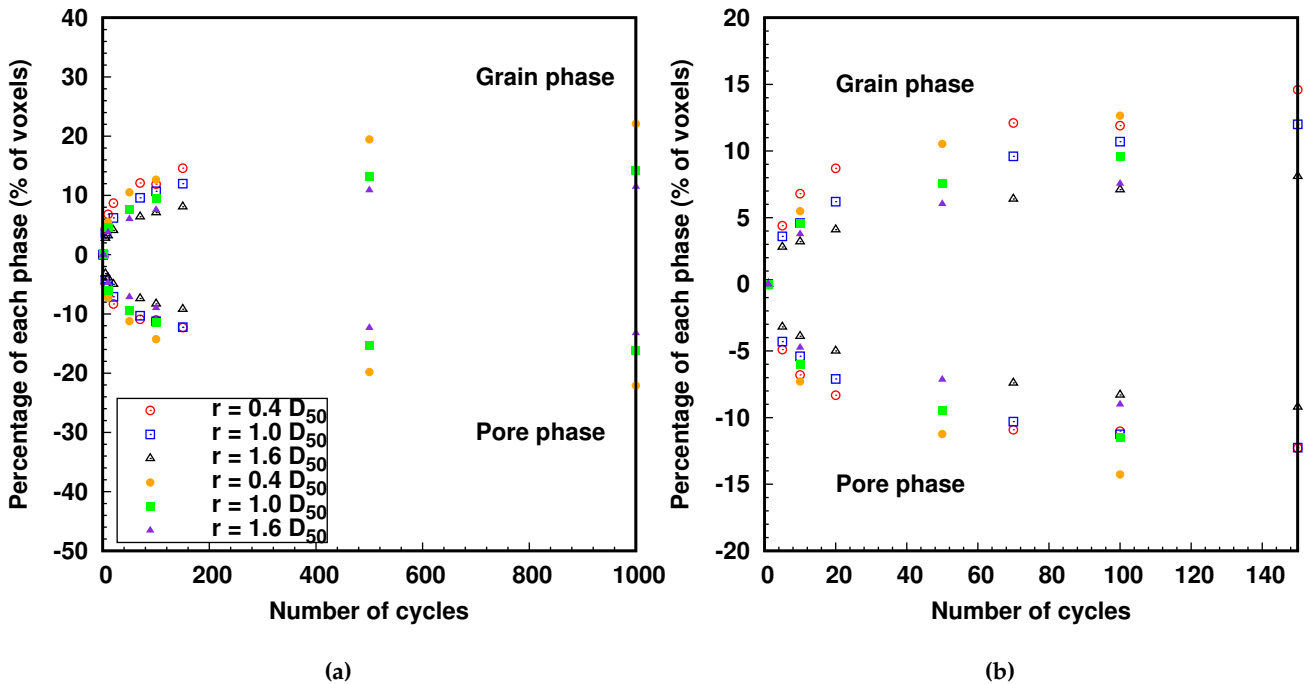
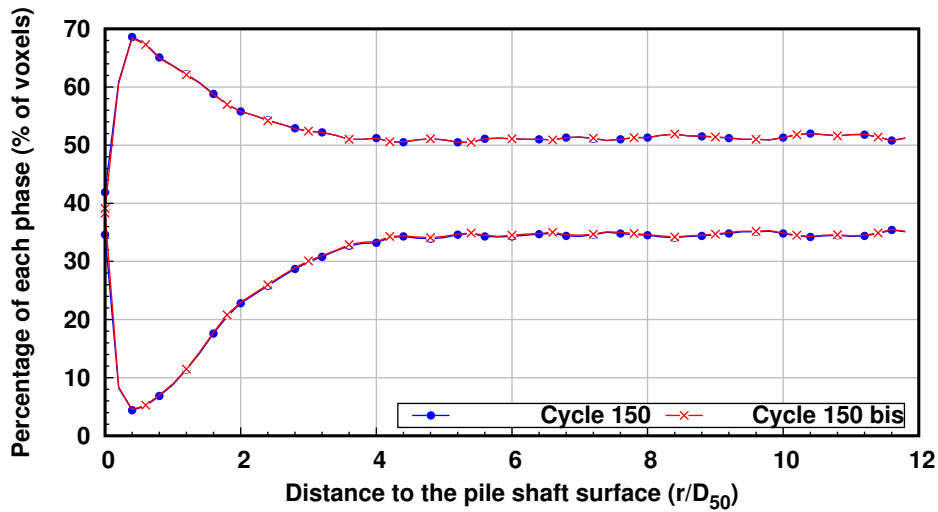


Figure 6.22: a) Density evolution at different distances "r" from the pile surface when increasing the number of loading cycles and b) zoom into the first 150 cycles. The results obtained for test P-GLAG-03 are plotted with filled symbols and the one obtained for test P-GLAG-09 are plotted with empty symbols. To meaningfully compare the two tests, the initial percentage measured for the first cycle was subtracted from all values

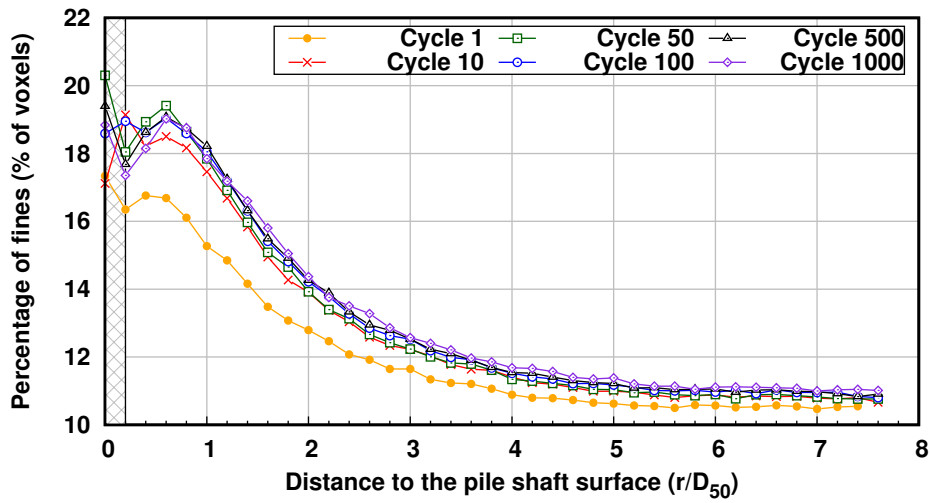


**Figure 6.23:** Radial evolution of grain (without fines) and pore phases volume for two different x-ray scans recorded after 150 cycles during test P-GLAG-09. The measurements done on two scans show the reproducibility of the methodology described in Section 3.3

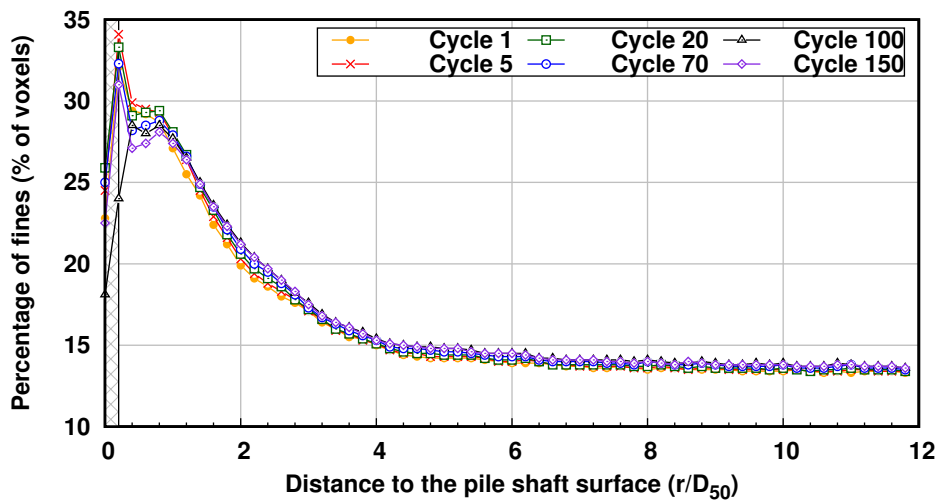
### 6.3.3 Grain crushing

Figure 6.24 shows the radial evolution of the quantity of fines (volume) with increasing number of cycles during test P-GLAG-03. The quantity of fines increases of about 2% between the first and the tenth cycle. It is believed that this increase is linked to the upside down configuration of the test. Due to their own weight, fines located ahead of the pile tip rearrange around the shaft during the first loading and unloading steps, which may explain this apparent increase. For a larger amount of cycles, the percentage of fines remains stable, indicating that most of particle crushing occurred during pile installation. The region where fines are produced has a thickness of  $4 \cdot D_{50}$ . At a greater radial distance, the percentage of fines is of about 11 % whereas it should be close to zero. The quantity of fines measured far from the pile surface is likely due to the partial volume effect mentioned in Section 3.3. It is not possible to simply subtract this value from all the measurements. Indeed, the partial volume effect depends on the surface of the grains. At the interface, grains are broken during pile installation which means that the grain size distribution is changing - and so does the surface of the grains.

By comparing the results between test P-GLAG-03 (Fig. 6.24) and test P-GLAG-09 (Fig. 6.25), the same observation can be made. The quantity of fines does not vary during the cyclic phase of the test. The results also indicate that for test P-GLAG-09, the maximum percentage of fines measured at  $r = 0.5 \cdot D_{50}$  is twice the percentage measured for test P-GLAG-03. This difference may be explained by the fact that the initial embedment depth was 70 mm for test P-GLAG-09 while it was 50 mm for test P-GLAG-03, which means that grain crushing was more important for test P-GLAG-09. Finally, as for the grains and pores quantities, Figure 6.26 shows the reproducibility of the measurements for two scans taken of the same state, *i.e.*, after 150 cycles during test P-GLAG-09.



**Figure 6.24:** Radial evolution of the quantity of fines during loading cycles for test P-GLAG-03 (amplitude of displacement  $\pm 0.5$  mm, initial relative density of 84 %). The x-axis scale is such that a radial distance of 7 is equal to one pile radius. For a given curve, each symbol represents one measurement obtained by thresholding the gray-scale image at a distance  $r$  from the shaft (over a cylindrical subdomain as defined in Section 3.3)



**Figure 6.25:** Radial evolution of the quantity of fines during loading cycles for test P-GLAG-09 (amplitude of displacement  $\pm 1.0$  mm, initial relative density of 85 %). The x-axis scale is such that a radial distance of 7 is equal to one pile radius. For a given curve, each symbol represents one measurement obtained by thresholding the gray-scale image at a distance  $r$  from the shaft (over a cylindrical subdomain as defined in Section 3.3)

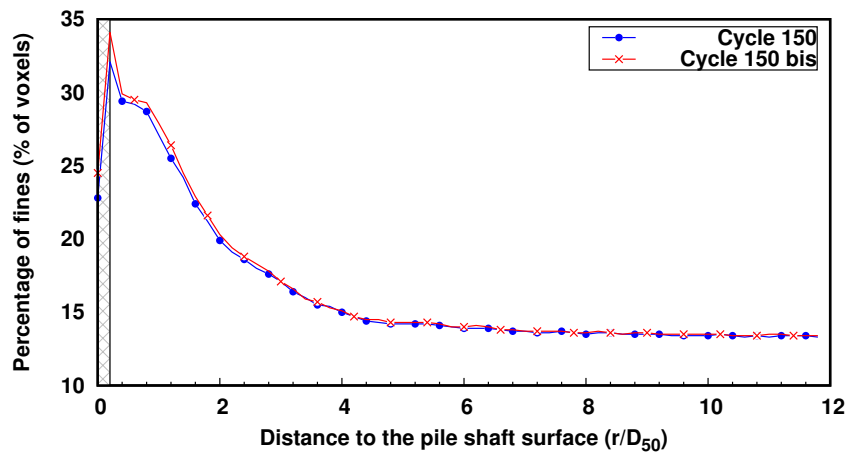


**Figure 6.26:** Radial evolution of the quantity of fines for two different x-ray scans recorded after 150 cycles during test P-GLAG-09. The measurements on two scans show the reproducibility of the methodology described in Section 3.3

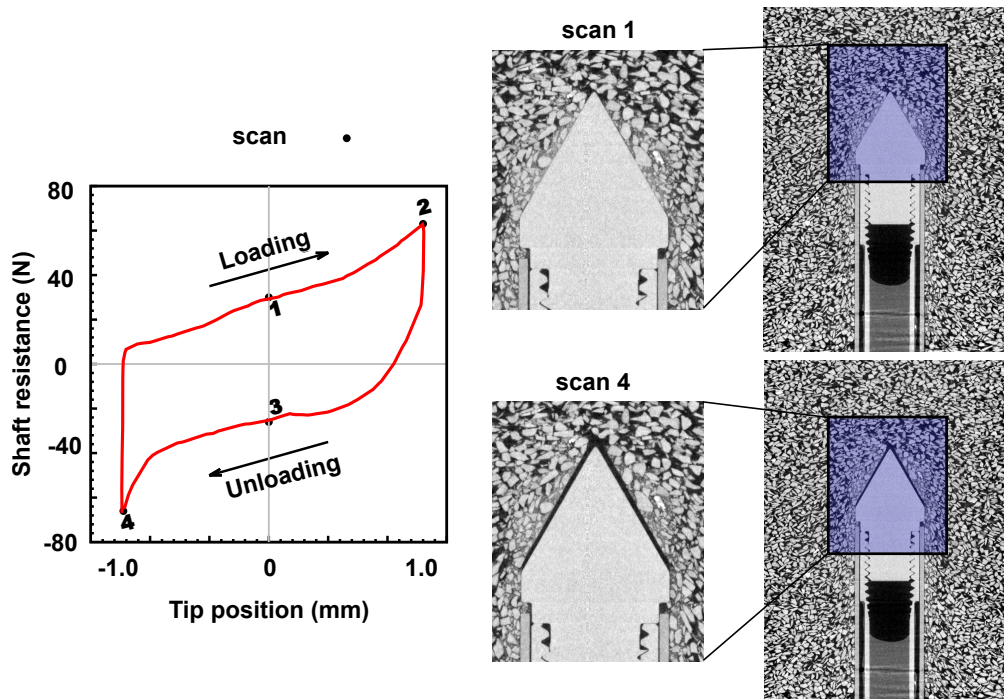


**Figure 6.27:** Sketch showing the high densification of the sand ahead of the pile tip during test P-GLAG-11. The numbers placed on the curve showing the typical evolution of shaft resistance indicate when the loading was interrupted for x-ray scanning. The two vertical slices (on the right) were taken through the 3D images recorded after the tenth cycle, when the tip was at 0 mm (scan 1) and at -1.0 mm (scan 4). The zooms into the slices illustrate the densification at the tip

## 6.4 Behavior of sand-pile interface across the scales: discussion

### Pile installation

A thin layer of crushed grains forms along the surface of the cone tip and shaft. The sand grains crushed ahead of the pile tip are displaced radially as the pile advances, and stay roughly at the same location around the shaft as the pile embedment continues increasing. The maximum thickness of this layer ranges between 3 and  $4 \cdot D_{50}$ .

DIC results showed that grain kinematics are localized near the pile tip. It is believed that a less crushable sand (*e.g.*, a silica sand) would undergo displacements with a higher magnitude in a region that extends further radially from the pile tip, as suggested by Arshad et al. (2014). In this study, these differences between a crushable and a less-crushable sand are expected to be clear as the testing conditions are closer to the one of a shallow penetration. For deep penetration, at high stress levels, the differences may be less pronounced. The different zones identified within the 3D displacement field showed that, immediately ahead of the pile tip, the displacement of the grains is purely vertical, while close to the pile tip shoulder, the displacements are mainly radial. This observation is consistent with the displacement field that would be created during the expansion of a cylindrical cavity.

The measurement of local porosity shows good agreement with the reorientation of the grains induced by the installation of the pile. In the region where grains have a preferred orientation, and are aligned with the pile surface, the field of porosity showed a dense layer of sand. On the contrary, in the dilative regions significant grain rearrangement occurs (ahead of the tip) and grains do not have a preferred orientation (further away from the pile shaft). It was also observed that grains rotate mainly ahead of the pile tip, where the highest values of maximum shear strain are measured.

### Axial loading cycles

During axial cyclic loading, the behavior of the sand grains was investigated in the two regimes observed for the macroscopic evolution of shaft resistance. A different behavior of the sand mass was observed in each regime.

In the first regime, when the shaft resistance decreases, large individual displacements were measured. The sand grains undergo radial displacements towards the shaft, with a magnitude similar to the one measured during the installation of the pile. The individual displacement vectors from discrete DIC also showed that the grains move vertically, downwards. These results suggest that the tensile hoop stresses built during pile installation collapsed during the first tenth of loading cycles. Moreover, the analysis of local density changes showed that the radial contraction of the sand mass is accompanied by a local densification in a region that is  $4 \cdot D_{50}$  thick. The densification rate is higher during the first 50 loading cycles. It was also observed that, in the case of a smooth shaft surface, grain crushing does not occur during cyclic loading, rather it takes place during pile installation. However, fines are rearranged between grains around the shaft during the first cycle.

In the second regime, when the shaft resistance increases again, relatively small displacements were measured. DIC results showed no vertical displacements and radial displacements with an amplitude divided by 6 compared to the one measured in the first phase of cyclic loading. After 50 cycles, density keeps increasing at the interface but at a lower rate. These results suggest that, after a given number of loading cycles, the sand mass reaches a threshold density for which granular kinematics are constrained leading to an increase in shaft resistance. The repeated loading cycles may also lead to an increase in pile shaft surface roughness as mentioned in Chapter 5. However, it is

believed that the increase in surface roughness due to the loading cycle is relatively low compared to one induced by the initial monotonic loading (*i.e.*, pile installation). The total magnitude of displacement imposed within a single cycle is of 1.0 mm (in the case of a cyclic amplitude of  $\pm 0.5\text{mm}$ ), which is close to the mean grain size. Moreover, the cumulated displacement that corresponds to 1000 cycles of  $\pm 0.5\text{ mm}$  equals to 2.0 cm, while during pile installation the embedment depth ranges between 5 and 7 cm. Thus, a simple change in surface roughness cannot explain alone the measured increase of shaft resistance.

During cyclic loading two main mechanisms occur: a reduction of the hoop stresses, *i.e.*, the arching effect of pile installation is reducing, and a local densification of the sand mass at the interface. It can be concluded that, the reduction of hoop stresses is the dominant mechanism during the first regime, which leads to a decrease in radial stresses and in shaft resistance (*i.e.*, interface shear stress decreases). In the second regime, the densification of the sand mass takes over, leading to an increase in radial stresses and in shaft resistance.

## 6.5 Conclusions

The analyses presented in this chapter showed that the image-based methodology employed in this work allows the characterization of deformation mechanisms taking place at the grain-scale.

### Kinematics

3D Digital Image Correlation (DIC) provided full-field kinematics at sand-pile interface during both pile installation and subsequent loading cycles. Different regions where granular rearrangement concentrate were identified and characterized. Individual grain kinematics obtained from discrete DIC revealed a displacement field consistent with the cavity expansion theory during pile embedment. On the contrary, following loading cycles induce a significant radial contraction of the sand mass during the first regime observed for shaft resistance evolution. In the second regime, when the shaft resistance increases, grain kinematics are almost inhibited. A reorientation of the grains was also measured during pile installation, showing the ability to access essential information at the grain-scale that allow the description of soil fabric.

### Volumetric and shear behavior

Porosity measurements showed that the installation of the pile leads to a dilative behavior of the sand around the pile, except in a thin layer in contact with the pile surface, where grain crushing occurs. The shear strain field showed that pile installation induce relatively small shear strains ahead of the pile tip. Due to the low roughness of the pile, no shear strain was measured alongside the shaft. This result indicates that the interaction between the grains and the shaft is dominated by a sliding mechanism. During cyclic loading, 3D image analysis revealed a densification in a region that is  $4D_{50}$ -thick. The rate of this local densification decreases in the second regime observed for the evolution of shaft resistance.

### Grain crushing

A thin layer of crushed particles was observed in the images, after pile installation. The maximum thickness of this layer, about  $6D_{50}$ , was measured near the pile tip. It was showed that the fines are produced by grain crushing ahead of the pile tip and are displacement as the pile advances. During cyclic loading, the quantity of fines does not evolve, showing that grain crushing takes place only

during pile installation, due to the low roughness of the interface.

Both qualitative and quantitative results showing the behavior the sand mass located in the vicinity of the pile when it is submitted to axial loading were linked to the macroscopic observations described in chapter 5. However, despite the valuable aspect of the data produced, it is imperative to note the limitations of the experimental setup used to obtain these data. The conclusions derived throughout this work should therefore be interpreted in realization of these limitations, including: the low roughness of the pile compared to the mean grain size, the size effects, and the boundary conditions (constant radial stress). The apparent benefit in shaft resistance caused by axial cyclic loading and the related deformation mechanisms cannot and should not be directly extrapolated to real field piles.

## Chapter 7

# Summary, conclusions & perspectives

### 7.1 Summary

This doctoral work deals with an experimental investigation into the mechanisms governing the macroscopic response of sand-pile interface during monotonic installation and subsequent axial cyclic loading. An innovative approach combining x-ray tomography and advanced image analysis tools was employed to extract information at different scales, including micro-scale, i.e., the scale of sand grains. The quantitative analysis of the behavior of individual sand grains in the vicinity of the pile offers valuable three-dimensional (3D) data set against which theoretical or numerical approaches could be tested.

#### Macro-scale experiments

A series of tests was run on an instrumented close-ended conical model pile installed by monotonic jacking in a dense calcareous sand sample. A total of 17 model pile tests were performed. Following the installation, the model pile was submitted to a few thousands axial displacement-controlled loading cycles under constant radial stress. The tests were performed in a mini-calibration chamber that allows the acquisition of high resolution x-ray 3D images at different stages of the loading. Several testing parameters affecting the macroscopic response of sand-pile interface during cyclic loading were varied from one test to another: the amplitude of displacement imposed to the pile during loading cycles, the boundary conditions (constant radial stress, constant volume), and the method of pile installation (monotonic jacking, sand molding around the pile). The loads applied to the pile, including both tip and shaft resistances, were measured for every test.

#### Imaging at the grain-scale

Some of the model pile tests were conducted inside the x-ray scanner of Laboratoire 3SR. 3D scans were recorded during both pile installation and following loading cycles. The 3D images resulting from the reconstruction of the x-ray scans were used to follow the behavior of the sand mass at the interface across different scales (meso and micro). Full-kinematics and shear strain fields were measured thanks to the 3D DIC code TomoWarp2 developed at 3SR. Various advanced image analysis techniques were used and adapted to the study of sand-pile interface, showing the ability to explore local porosity changes, grain crushing and fabric anisotropy (in terms of grains orientations).

### 7.2 Conclusions

#### 7.2.1 Macro-scale observations

The cyclic tests revealed two distinct phases in the evolution of shaft resistance. In the first phase, the shaft resistance decreases, whereas in the second phase it increases again significantly. After 1000

cycles, the load measured on the shaft nearly doubled. This observation was made for both amplitudes of loading cycles, *i.e.*,  $\pm 0.5$  mm and  $\pm 1.0$  mm. However, the results showed that for the larger amplitude, the transition between the two phases is reached for a smaller number of cycles. In addition, model pile tests conducted under identical conditions exhibited similar responses during both pile installation and axial cyclic loading, showing the reproducibility of the results.

An effort was made to explain to what extent the physical model developed in this work can be compared to field pile testing conditions. It is acknowledged that the scaling and the specific loading conditions employed are not representative of real engineering applications, where piles that support bridges, wind-turbines or offshore platforms have to sustain safely severe axial load-controlled cycles due to their environment. In this study, the apparent benign outcomes of displacement-controlled loading cycles cannot be extrapolated to field pile design. However, the mini-calibration chamber proved to be able to reproduce qualitatively trends that are similar to those obtained at the macro-scale on large-scale experiments and allows the observation of deformation mechanisms taking place at the micro-scale.

### 7.2.2 Image-based analysis

#### Pile installation

X-ray imaging allowed the observation of a thin layer of crushed grains and fines along the surface of the cone tip and shaft. The maximum thickness of this layer was measured directly in the images and ranges between 3 and  $4 \cdot D_{50}$ . It was also observed that the sand grains crushed ahead of the pile tip are displaced radially as the pile advances, and stay roughly at the same location around the shaft as the pile embedment continue increasing.

Different zones where displacements concentrate during pile installation were identified and thoroughly characterized thanks to 3D Digital Image Correlation (DIC). Discrete DIC proved to be an efficient tool to access the full-kinematics of individual sand grains, including 3D rotations. Individual displacement vectors revealed a recirculation of the grains close to the pile shaft, as the pile advances. The analysis of grain kinematics was supplemented by the measurement of sand grains orientations. The novel results showed a reorientation of the grains due to pile installation. The elongated shape of the grains employed in this study facilitated their alignment along the pile tip and the pile shaft surfaces.

The measurement of local porosity showed a dilative behavior of the sand mass induced by the installation of the pile. However, a contractive behavior was observed in a limited region around the pile, where grain crushing occurs. The 3D porosity field showed good agreement with the maximum shear strain field and with the reorientation of the grains.

#### Axial loading cycles

During axial cyclic loading, the behavior of the sand grains was investigated in the two phases observed for the macroscopic evolution of shaft resistance. A different behavior of the sand mass was observed in each phase.

In the first phase, when the shaft resistance decreases, grain kinematics obtained from 3D DIC showed a radial contraction of the sample accompanied with a downward movement of the grains. It is believed that the first tens of cycles induce a collapse of tensile hoop stresses created during the installation of the pile. A local densification of the sand mass was also measured at the interface. The analysis of the production of fines by grain crushing showed that, in the present study, the loading

cycles did not lead to additional grain breakage.

In the second phase, when the shaft resistance increases, it was observed that density keeps increasing at the interface but at a lower rate than in the first phase. DIC results did not show any granular rearrangement. Only relatively small radial displacements of the grains were measured in the second phase. These results suggest that, after a given number of loading cycles, the sand mass reaches a threshold density for which granular kinematics are inhibited.

Two main mechanisms compete during cyclic loading: a reduction of the hoop stresses, *i.e.*, a loosening of the arching effect built up during pile installation, and a densification of the sand mass at the interface. During the first phase, the reduction of hoop stresses is the dominant mechanism leading to a decrease in radial stresses and in shaft resistance. In the second phase, the first mechanism fades out while the densification of the sand mass takes over, leading to an increase in radial stresses and in shaft resistance.

## 7.3 Perspectives

### Interface roughness

The influence of surface roughness on shear resistance has been established by several researchers. Therefore, it would be interesting to repeat similar model pile tests with a rough pile shaft surface. The imaging tools used in this PhD work could reveal the influence of the pile shaft roughness on the observed grain kinematics, interface shearing, and grain crushing. It would also be possible to explore and compare the behavior of the interface during both tension and compression phases of a single cycle. Taken together with the DIC results obtained for a series of tension-compression static loading tests performed on instrumented model piles by Galvis-Castro et al. (2018), a 3D investigation by x-ray tomography could provide a better understanding of the interface response when the loading direction is reversed.

To reach an interface friction angle close to the one measured for field piles, *i.e.*,  $30^\circ$ , a normalized roughness of about 0.25 should be applied. Such a normalized roughness can be achieved by sticking silica sand grains, such as Hostun sand grains, directly on the shaft surface. A preliminary test was performed inside the x-ray scanner of Laboratoire 3SR.

### Boundary conditions

In order to limit size effects caused by the reduced scale of the physical model, active boundary conditions, *i.e.*, constant stiffness, could be applied to the sand sample. To achieve these conditions, the vertical stress applied at the top of the sample and the horizontal stress applied on the circumference of the sample should be controlled individually. Thus, two different membranes are required, as proposed by Eissautier (1986). Figure 7.1 shows the top membrane used to impose  $\sigma'_v$  and the lateral membrane used to apply  $\sigma'_h$ , which varies as a function of the radial volumetric change  $\Delta V_h$ .

### Different material

To evaluate the importance of the crushability of the sand on the interface response, a material which is less vulnerable to crushing, such as silica sand, could be employed. A valuable comparison with the results obtained for Glageon sand could be provided about the full-kinematics, the interface layer thickness, the occurrence or non-occurrence of breakage, the measured shaft resistance.

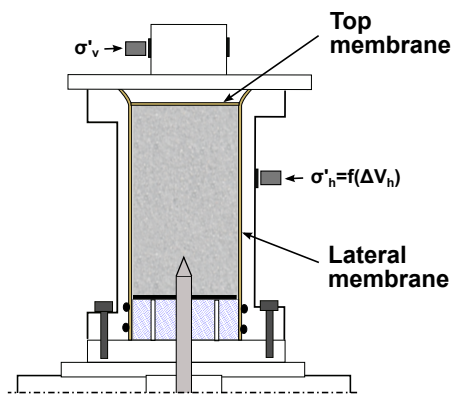


Figure 7.1: Sketch showing a possible modification of the mini-calibration chamber for the application of active radial boundary conditions

### Grain crushing and contact detection

Further quantification of the extent and nature of grain crushing and the analysis of fabric changes in terms of inter-granular contacts are two important future steps that remain very challenging as pointed out by Andò et al. (2013b). To achieve accurate measurements of features that are smaller than the grain-scale, very high spatial resolution images are required. However, with the objective of gaining understanding in geomechanics, relatively large sand volume are required. Such large samples limit the minimum resolution of the 3D images. For this reason, new non-conventional image analysis tools must be developed. This is one objective of two ongoing PhD projects at Laboratoire 3SR: see for instance Okubadejo et al. (2017) for tracking breakage and Wiebicke et al. (2017) for measuring contact fabric evolution.

### Numerical Modeling

A rather straightforward perspective to this PhD work would be to use the set of data obtained thanks to x-ray imaging in order to validate multi-scale models, in which different scales are explicitly simulated (*e.g.*, the so-called FEM-DEM approach). These kinds of models require accurate references of the evolution of the micro-structure of real granular materials as those presented in this research work.

First, a DEM model able to reproduce the mini-calibration tests performed in this study would already be of major interest. Indeed, a DEM model could provide essential information that could not be measured experimentally. In particular, measuring the stresses developing on and around the pile would allow a direct link between the macroscopic response of the interface and the stress-strain behavior of the sand. 3D effects could be investigated by evaluating the contact forces network and the hoop stresses developed around the pile. These results could be compared with theoretical models, such as the cavity expansion theory. An additional series of tests conducted on an artificial granular material, such as glass beads, would provide interesting data to be used as a first calibration for such DEM model.

# Bibliography

- Ahrens, J., Geveci, B., and Law, C. (2005). "Paraview: An end-user tool for large data visualization". In: *The visualization handbook* 717.
- Alawneh, A., Husein Malkawi, A., and Al-Deeky, H. (1999). "Tension tests on smooth and rough model piles in dry sand". In: *Canadian Geotechnical Journal* 36, pp. 746–753.
- Almeida, M., Jamiolkowski, M., and Peterson, R. (1991). "Preliminary result of CPT tests in calcareous Quiou sand". In: *Proceedings of the International Symposium on calibration chamber testing*. Ed. by A. Huang. Postdam: Elsevier, pp. 41–53.
- Als-Nielsen, J. and McMorrow, D. (2001). *Elements of Modern X-ray Physics*. Wiley.
- Andò, E. (2013). "Experimental investigation of microstructural changes in deforming granular media using x-ray tomography". Theses. Université de Grenoble.
- Andò, E., Viggiani, G., Hall, S. A., and Desrues, J. (2013a). "Experimental micro-mechanics of granular media studied by x-ray tomography: recent results and challenges". In: *Géotechnique Letters* 3.3, pp. 142–146.
- Andò, E., Viggiani, G., Hall, S. A., and Desrues, J. (2013b). "Experimental micro-mechanics of granular media studied by x-ray tomography: recent results and challenges". In: *Géotechnique Letters* 3.3, pp. 142–146.
- Arshad, M., Tehrani, F., Prezzi, M., and Salgado, R. (2014). "Experimental study of cone penetration in silica sand using digital image correlation". In: *Géotechnique* 64.7, pp. 551–569.
- Balachowski, L. (1995). "Différents aspects de la modélisation physique du comportement des pieux: Chambre d'Etalonnage et Centrifugeuse". Theses. Institut National Polytechnique de Grenoble.
- Batiste, S., Alshibli, K., Sture, S., and Lankton, M. (2004). "Shear Band Characterization of Triaxial Sand Specimens Using Computed Tomography". In: *Geotechnical Testing Journal* 27, 568–579.
- Baydoun, S. (2017). "Influence of cyclic loading on sand-pile interface: investigation through direct shear interface tests". MA thesis. Université Grenoble Alpes.
- Bekki, H., Canou, J., Tali, B., Dupla, J., and Bouafia, A. (2013). "Evolution of local friction along a model pile shaft in a calibration chamber for a large number of loading cycles". In: *Comptes Rendus Mécanique* 341.6, pp. 499–507.
- Bekki, H., Tali, B., Canou, J., Dupla, J., and Bouafia, A. (2014). "Behavior of Soil-structure interfaces under cyclic loading for large numbers of cycles: Application to piles". In: *J. Appl. Eng. Sci. Technol.* 1.1, pp. 11–16.
- Bekki, H., Tali, B., Canou, J., Dupla, J., and Bouafia, A. (2016). "Influence of the cyclic loading of very large number of cycles on the pile capacity". In: *J. Appl. Eng. Sci. Technol.* 2.2, pp. 51–55.
- Bellotti, R. (1985). "Chamber size effects and boundary conditions effects". In: *Seminar of cone penetration testing in the laboratory*, pp. 26–29.
- Benzaria, O., Puech, A., and Le Kouby, A. (2013). "Cyclic axial load tests on bored piles in dense sands". In: *Proceedings of the 18th International Conference on Soil Mechanics and Geotechnical Engineering. Challenges and innovations in geotechnics*. Ed. by P. des ponts. Paris, pp. 2323–2326.
- Bornert, M. et al. (2009). "Assessment of Digital Image Correlation Measurement Errors: Methodology and Results". In: *Experimental Mechanics* 49.3, pp. 353–370.

- Boulon, M. and Foray, P. (1986). "Physical and numerical simulation of lateral shaft friction along offshore piles in sand". In: *Proceedings of the 3rd International Conference on Numerical methods in Offshore piling*. Nantes, pp. 127–147.
- Butlanska, J., Arroyo, M., Gens, A., and O'Sullivan, C. (2014). "Multi-scale analysis of cone penetration test (CPT) in a virtual calibration chamber". In: *Canadian Geotechnical Journal* 51.1, pp. 51–66.
- Calvetti, F., Combe, G., and Lanier, J. (1997). "Experimental micromechanical analysis of a 2D granular material: relation between structure evolution and loading path". In: *Mechanics of Cohesive-frictional Materials* 2.2, pp. 121–163.
- Chan, S and Hanna, T. H. (1980). "Repeated loading on single piles in sand". In: *Journal of the Geotechnical Engineering Division, American Society of Civil Engineers* 106.2, pp. 171–188.
- Chen, Z., Li, K., Omidvar, M., and Iskander, M. (2017). "Guidelines for DIC in geotechnical engineering research". In: *International Journal of Physical Modelling in Geotechnics* 17.1, pp. 3–22.
- Chin, J. and Poulos, H. (1996). "Tests on Model Jacked Piles in Calcareous Sand". In: *Geotechnical Testing Journal* 19.2, pp. 164–180.
- Cho, G., Dodds, J., and Santamarina, J. (2006). "Particle Shape Effects on Packing Density, Stiffness, and Strength: Natural and Crushed Sands". In: *Journal of Geotechnical and Geoenvironmental Engineering* 132.5, pp. 591–602.
- Chong, M. (1988). "Density changes of sand on cone penetration resistance". In: *In Proceedings of the first international symposium on penetration testing ISOPT-1*. Orlando, 707–714.
- Coop, M., Sorensen, K., Bodas Freitas, T., and Georgoutsos, G. (2004). "Particle breakage during shearing of carbonate sand". In: *Géotechnique* 54.3, pp. 157–163.
- Cui, L. and Bhattacharya, S. (2016). "Soil-monopile interactions for offshore wind turbines". In: *Proceedings of the Institution of Civil Engineers - Engineering and Computational Mechanics*. Vol. 169. 4, pp. 171–182.
- Cundall, P. and Strack, O. (1979). "A discrete numerical model for granular assemblies". In: *Géotechnique* 29.1, pp. 47–65.
- D4253-16, A. *Standard Test Methods for Maximum Index Density and Unit Weight of Soils Using a Vibratory Table*. Tech. rep.
- D4254, A. (2000). *Standard Test Methods for Minimum Index Density and Unit Weight of Soils and Calculation of Relative Density*. Tech. rep.
- D698-12e2, A. *Standard Test Methods for Laboratory Compaction Characteristics of Soil Using Standard Effort (12 400 ft-lbf/ft<sup>3</sup> (600 kN-m/m<sup>3</sup>))*. Tech. rep.
- Deeks, A., White, D., and Bolton, M. (2005). "A comparison of jacked, driven and bored piles in sand". In: *In Proceedings of the 16th international conference on soil mechanics and geotechnical engineering*. Vol. 3. Osaka, Japan: Rotterdam, the Netherlands: Millpress Science Publishers, pp. 2103–2106.
- DeJong, J., Randolph, M., and White, D. (2003). "Interface load transfer degradation during cyclic loading: a microscale investigation". In: *Soils and Foundations* 43.4, pp. 91–94.
- DeJong, J., White, D., and Randolph, M. (2006). "Microscale observation and modelling of soil–structure interface behaviour using PIV". In: *Soils and Foundations* 46.1, pp. 15–28.
- Desrues, J., Nguyen, T., Combe, G., and Caillerie, D. (2015). "FEMxDEM Multi-scale Analysis of Boundary Value Problems Involving Strain Localization". In: *Bifurcation and Degradation of Geomaterials in the New Millennium*. Ed. by K.-T. Chau and J. Zhao. Springer International Publishing, pp. 259–265.
- Dijkstra, J. and Broere, W. (2010). "New Method of Full-Field Stress Analysis and Measurement Using Photoelasticity". In: *Geotechnical Testing Journal* 33.6, pp. 469–481.

- Dijkstra, J., Broere, W., and Tol, A. van (2010). "Measuring the apparent density change near a cyclically loaded displacement pile in sand". In: *Physical Modelling in Geotechnics, Two Volume Set: Proceedings of the 7th International Conference on Physical Modelling in Geotechnics*. Ed. by C. Press. Zurich, pp. 913–918.
- Duan, N. and Cheng, Y. (2016). "A Discrete Element Method Centrifuge Model of Monopile under Cyclic Lateral Loads". In: *International Journal of Environmental, Chemical, Ecological, Geological and Geophysical Engineering* 10.2, pp. 189–194.
- D'Aguiar, S., Modaresi-Farahmand-Razavi, A., Santos, J., and Lopez-Caballero, F. (2011). "Piles under cyclic axial loading: Study of the friction fatigue and its importance in pile behavior". In: *Canadian Geotechnical Journal* 48.10, pp. 1537–1550.
- Einav, I. (2007). "Soil mechanics: breaking ground". In: *Philosophical Transactions of the Royal Society of London A: Mathematical, Physical and Engineering Sciences* 365.1861, pp. 2985–3002.
- Eissautier, M. (1986). "Frottement latéral des pieux en milieu pulvérulent: expérimentation en petite chambre de calibration". PhD thesis. Institut National Polytechnique de Grenoble.
- El Haffar, I., Blanc, M., and Thorel, L. (2018). "Effect of the installation methods of piles in cohesionless soil on their axial capacity". In: *Physical Modelling in Geotechnics*. Ed. by M. et al. (Eds). London, UK: Taylor & Francis Group, pp. 1341–1346.
- Emam, S., Canou, J., Corfdir, A., Dupla, J. C., and Roux, J. (2006). "Elaboration et comportement mécanique de matériaux granulaires solides modèles: expériences et simulations numériques." In: *Rhéologie des pâtes et des matériaux granulaires, volume SI12 of Etudes et Recherches des Laboratoires des Ponts et Chaussées*. Ed. by B. Cazacliu and J. R. (Eds.) Paris: Presses du Laboratoire Central des Ponts et Chaussées.
- Falagush, O., McDowell, G., and Yu, H. (2015). "Discrete Element Modeling of Cone Penetration Tests Incorporating Particle Shape and Crushing". In: *International Journal of Geomechanics* 15.6, pp. 1–14.
- Feia, S., Clain, X., Canou, J., Sulem, J., and Ghabezloo, S. (2017). "Fine particles production in sand under triaxial compression". In: *Journal of Applied Engineering Science and Technology* 3.1, pp. 1–6.
- Fioravante, V. (2002). "On the shaft friction modeling of non-displacement piles in sand". In: *Soils and Foundations* 42.2, pp. 23–33.
- Fonseca, J., Bésuelle, P., and Viggiani, G. (2013). "Micromechanisms of inelastic deformation in sandstones: an insight using x-ray micro-tomography". In: *Géotechnique Letters* 3.2, pp. 78–83.
- Foray, P. (1991). "Scale and boundary effects on calibration chamber pile tests". In: *Proceedings of the First International Symposium on Calibration Chamber Testing/ISOCCT1*. Ed. by A. Huang. Postdam: Elsevier, pp. 147–160.
- Foray, P., Tsuha, C., Silva, M., Jardine, R., and Yang, Z. (2010). "Stress paths measured around a cyclically loaded pile in a calibration chamber". In: *Physical Modelling in Geotechnics, Two Volume Set: Proceedings of the 7th International Conference on Physical Modelling in Geotechnics*. Ed. by S. et al. (Eds). Zurich: CRC Press, pp. 933–939.
- Frost, J. D. and DeJong, J. (2005). "In situ assessment of role of surface roughness on interface response". In: *Journal of Geotechnical and Geoenvironmental Engineering* 131.4, pp. 498–511.
- Fu, P. and Dafalias, Y. (2011). "Study of anisotropic shear strength of granular materials using DEM simulation". In: *International Journal for Numerical and Analytical Methods in Geomechanics* 35, pp. 1098–1126.
- Galvis-Castro, A., Tovar-Valencia, R., Salgado, R., and Prezzi, M. (2018). "Effect of loading direction on the shaft resistance of jacked piles in dense sand". In: *Géotechnique, Ahead of Print*, pp. 1–13.
- Guida, G., Casini, F., Viggiani, G. M. B., Andò, E., and Viggiani, G. (2018). "Breakage mechanisms of highly porous particles in 1D compression revealed by X-ray tomography". In: *Géotechnique Letters* 8.2, pp. 155–160.

- Hall, S., Bornert, M., Desrues, J., Pannier, Y., Lenoir, N., Viggiani, G., and Bésuelle, P. (2010). "Discrete and continuum analysis of localised deformation in sand using X-ray  $\mu$ CT and volumetric digital image correlation". In: *Géotechnique* 60.5, pp. 315–322.
- Hebeler, G., Martinez, A., and Frost, J. (2015). "Shear zone evolution of granular soils in contact with conventional and textured CPT friction sleeves". In: *KSCE Journal of Civil Engineering* 20.4, pp. 1267–1282.
- Heerema, E. (1980). "Predicting pile driveability: heather as an illustration of the friction fatigue theory". In: *Ground Engng* 13, pp. 15–37.
- Hsieh, J. (2003). *Computed Tomography: Principles, Design, Artifacts, and Recent Advances*. SPIE Press monograph. SPIE Press.
- Iskander, M. (2010). *Modelling with Transparent Soils: Visualizing Soil Structure Interaction and Multi Phase Flow, Non-Intrusively*. Springer Series in Geomechanics and Geoengineering. Springer Berlin Heidelberg.
- Jardine, R. and Standing, J. (2000). *Pile load testing performed for HSE cyclic loading study at Dunkirk, France*. Vol. 1. Offshore technology report. Health and Safety Executive.
- Jardine, R. and Standing, J. (2012). "Field axial cyclic loading experiments on piles driven in sand". In: *Soils and Foundations* 52.4, pp. 723–736.
- Jardine, R., Lehane, B., and Everton, S. (1993). "Friction Coefficients for Piles in Sands and Silts". In: *Offshore Site Investigation and Foundation Behaviour: Papers presented at a conference organized by the Society for Underwater Technology and held in London, UK, September 22–24, 1992*. Ed. by D. A. Arduş, D. Clare, A. Hill, R. Hobbs, R. J. Jardine, and J. M. Squire. Dordrecht: Springer Netherlands, pp. 661–677.
- Jardine, R., Zhu, B., Foray, P., and Dalton, C. (2009). "Experimental arrangements for investigation of soil stresses developed around a displacement pile". In: *Soils and Foundations* 49.5, pp. 661–673.
- Jardine, R., Zhu, B., Foray, P., and Yang, Z. (2013). "Interpretation of stress measurements made around closed-ended displacement piles in sand". In: *Géotechnique* 63.8, pp. 613–627.
- Jin, W. and Zhou, J. (2010). "A Coupled Micro-Macro Method for Pile Penetration Analysis". In: *Soil Behavior and Geo-Micromechanics*. Shanghai, pp. 234–239.
- Johnston, I., Lam, T., and Williams, A. (1987). "Constant normal stiffness direct shear testing for socketed pile design in weak rock". In: *Géotechnique* 37.1, pp. 83–89.
- Karatza, Z. (2017). "A study of temporal and spatial evolution of deformation and breakage of dry granular materials using X-ray computed tomography and the discrete element method." PhD thesis. The University of Edinburgh.
- Ketcham, R. and Carlson, W. (2001). "Acquisition, optimization and interpretation of X-ray computed tomographic imagery: applications to the geosciences". In: *Computers & Geosciences* 27.4, pp. 381–400.
- Khalili, M., Roux, J., Pereira, J., Brisard, S., and Bornert, M. (2017). "Numerical study of one-dimensional compression of granular materials. I. Stress-strain behavior, microstructure, and irreversibility". In: *Phys. Rev. E* 95 (3), p. 032907.
- Kishida, H. and Uesugi, M. (1987). "Tests of the interface between sand and steel in the simple shear apparatus". In: *Géotechnique* 37.1, pp. 45–52.
- Klotz, E. and Coop, M. (2001). "An investigation of the effect of soil state on the capacity of driven piles in sands". In: *Géotechnique* 51.9, pp. 733–751.
- Le Kouby, A. (2003). "Etude du Comportement Mécanique de Micropieux sous Chargements Monotones et Cycliques Verticaux. Application aux Effets de Groupe." Theses. Ecole Nationale des Ponts et Chaussées, Cermes.
- Le Kouby, A., Canou, J., and Dupla, J. (2004). "Behaviour of model piles subjected to cyclic axial loading". In: *Cyclic Behaviour of Soils and Liquefaction Phenomena: Proceedings of the International Conference*. Ed. by T. (Ed). Bochum: CRC Press, pp. 159–166.

- Lee, C. and Poulos, H. (1990). "Axial response analysis of piles in vertically and horizontally non-homogeneous soils". In: *Computers and Geotechnics* 9.3, pp. 133–148.
- Lee, J., Prezzi, M., and Salgado, R. (2011). "Experimental Investigation of the Combined Load Response of Model Piles Driven in Sand". In: *Geotechnical Testing Journal* 34.6, pp. 653–667.
- Lehane, B. M. and Gill, D. (2004). "Displacement fields induced by penetrometer installation in an artificial soil". In: *International Journal of Physical Modelling in Geotechnics* 4.1, pp. 25–36.
- Lenoir, N., Bornert, M., Desrues, J., Bésuelle, P., and Viggiani, G. (2007). "Volumetric Digital Image Correlation Applied to X-ray Microtomography Images from Triaxial Compression Tests on Argillaceous Rock". In: *Strain* 43.3, pp. 193–205.
- Li, Z., Bolton, M., and Haigh, S. (2012). "Cyclic axial behaviour of piles and pile groups in sand". In: *Canadian Geotechnical Journal* 49.9, pp. 1074–1087.
- Liu, J. and Iskander, M. (2010). "Modelling capacity of transparent soil". In: *Canadian Geotechnical Journal* 47.4, pp. 451–460.
- Lobo-Guerrero, S. and Vallejo, L. (2005). "DEM analysis of crushing around driven piles in granular materials". In: *Géotechnique* 55.8, pp. 617–623.
- Lobo-Guerrero, S. and Vallejo, L. (2007). "Influence of pile shape and pile interaction on the crushable behavior of granular materials around driven piles: DEM analyses". In: *Granular Matter* 9.3, pp. 241–250.
- Martinez, A. and Frost, J. D. (2017). "The influence of surface roughness form on the strength of sand–structure interfaces". In: *Géotechnique Letters* 7.1, pp. 104–111.
- Martinez, A. and Frost, J. (2014). "Axisymmetric Shearing of Sand-Steel Interfaces under Axial and Torsional Loading". In: pp. 644–653.
- Mohamed, T. (2017). "Sand-pile interface under cyclic loading". MA thesis. Grenoble INP, ENSE3.
- Mortara, G., Mangiola, A., and Ghionna, V. (2007). "Cyclic shear stress degradation and post-cyclic behaviour from sand-steel interface direct shear tests". In: *Canadian Geotechnical Journal* 44.7, pp. 739–752.
- Nakata, A., Hyde, M., Hyodo, H., and Murata (1999). "A probabilistic approach to sand particle crushing in the triaxial test". In: *Géotechnique* 49.5, pp. 567–583.
- Nes, J. van (2004). "Application of computerized tomography to investigate strain fields caused by cone penetration in sand". MA thesis. Delft, the Netherlands: Delft University.
- Ngan-Tillard, D., Cheng, X., Nes, J. van, and Zitha, P. (2005). "Application of X-ray Computed Tomography to Cone Penetration Tests in Sands". In: *Geo-Frontiers 2005: Site characterization and modelling*. Ed. by M. et al. (Eds). Reston, VA: ASCE, pp. 1–12.
- Oda, M. (1972). "Initial fabrics and their relations to mechanical properties of granular material". In: *Soils and Foundations* 12.1, pp. 17–36.
- Oda, M., Nemat-Nasser, S., and Konishi, J. (1985). "Stress-induced anisotropy in granular masses". In: *Soils and Foundations* 25.3, pp. 85–97.
- Okubadejo, O., Karatza, Z., Andò, E., Bonnaud, L., Dalla Mura, M., and Viggiani, G. (2017). "Identification and tracking of particles undergoing progressive breakage under stress with 3D+t image analysis (Extended Abstract)". In: *3rd International Conference on Tomography of Materials and Structures*. Lund, Sweden.
- Omidvar, M., Doreau-Malioche, J., Chen, Z., Iskander, M., and Bless, S. (2015). "Visualizing Kinematics of Dynamic Penetration in Granular Media Using Transparent Soils". In: *Geotechnical Testing Journal* 38.5, pp. 656–672.
- Ooi, L. and Carter, J. (1987). "A Constant Normal Stiffness Direct Shear Device for Static and Cyclic Loading". In: *Geotechnical Testing Journal* 10.1, pp. 3–12.
- O'Sullivan, C., Cui, L., and O'Neill, S. (2008). "Discrete element analysis of the response of granular materials during cyclic loading". In: *Soils and Foundations* 48.4, pp. 511–530.

- Otsu, N. (1979). "A Threshold Selection Method from Gray-Level Histograms". In: *IEEE Transactions on Systems, Man, and Cybernetics* 9.1.
- Paniagua, P., Andò, E., Silva, M., Emdal, A., Nordal, S., and Viggiani, G. (2013). "Soil deformation around a penetrating cone in silt". In: *Géotechnique Letters* 3.4, pp. 185–191.
- Paniagua, P., Fonseca, J., Gylland, A., and Nordal, S. (2018). "Investigation of the change in soil fabric during cone penetration in silt using 2D measurements". In: *Acta Geotechnica* 13.1, pp. 135–148.
- Parkin, A. K. and Lunne, T. (1982). "Boundary effects in the laboratory calibration of a cone penetrometer in sand". In: *Proceedings of the 2nd European Symposium on Penetration Testing (ESOPT II)*. Ed. by R. Balkema. Vol. 2. Amsterdam, pp. 761–768.
- Parkin, A. (1988). "The calibration of cone penetrometers". In: *Proceedings of the 1st International Symposium on Penetration Testing, ISOPT-1*. Orlando, pp. 221–243.
- Parkin, A. (1991). "Chamber testing of piles in calcareous sand and silt". In: *Proceedings of the International Symposium on calibration chamber testing*. Ed. by A. Huang. Postdam: Elsevier, pp. 289–302.
- Peterson, R. (1988). "Laboratory investigation of the penetration resistance of fine cohesionless materials". In: *Proceedings of the 1st International Symposium on Penetration Testing, ISOPT-1*. Orlando: Rotterdam: A A Balkema, pp. 895–901.
- Poulos, H. (1989). "Cyclic axial loading analysis of piles in sand". In: *Journal of Geotechnical and Geoenvironmental Engineering* 115.6, pp. 836–851.
- Pra-ai, S. and Boulon, M. (2016). "Post-cyclic Behavior of Granular Soil-structure Interface Direct Shear Tests". In: *International Journal of GEOMATE* 11.24, pp. 2328–2334.
- Puech, A. and Garnier, J. (2017). *Design of Piles Under Cyclic Loading: SOLCYP Recommendations*. Wiley.
- R., S. (1993). "Analysis of penetration resistance in sands". Theses. University of California, Berkeley, Calif.
- Robinsky, E. and Morrison, C. (1964). "Sand Displacement and Compaction around Model Friction Piles". In: *Canadian Geotechnical Journal* 1.2, pp. 81–93.
- Salgado, R., Mitchell, J. K., and Jamiolkowski, M. (1997). "Cavity Expansion and Penetration Resistance in Sand". In: *Journal of Geotechnical and Geoenvironmental Engineering* 123.4, pp. 344–354.
- Salgado, R., Mitchell, J., and Jamiolkowski, M. (1998). "Calibration Chamber Size Effects on Penetration Resistance in Sand". In: *Journal of Geotechnical and Geoenvironmental Engineering* 124.9, pp. 878–888.
- Schindelin, J., Arganda-Carreras, I., Frise, E., Kaynig, V., Longair, M., Pietzsch, T., Preibisch, S., Rueden, C., Saalfeld, S., Schmid, B., et al. (2012). "Fiji: an open-source platform for biological-image analysis". In: *Nature methods* 9.7, pp. 676–682.
- Schnaid, F. and Houlsby, G. (1991). "An assessment of chamber size effects in the calibration of in situ tests in sand". In: *Géotechnique* 41.3, pp. 437–445.
- Schneider, J., White, D., and Lehane, B. (2007). "Shaft Friction Of Piles Driven In Siliceous, Calcareous And Micaceous Sands". In: *Proceedings of the 6th International Offshore Site Investigation and Geotechnics Conference: Confronting New Challenges and Sharing Knowledge*. London: Society of Underwater Technology, pp. 367–382.
- Silva, I. M., Combe, G., Foray, P., Flin, F., and Lesaffre, B. (2013). "Postmortem analysis of sand grain crushing from pile interface using X-ray tomography". In: vol. 1542. 1, pp. 297–300.
- Silva, M. and Combe, G. (2015). "Soil-pile interaction during pile installation. Observations from x-ray tomography and 3D-DIC". In: *Deformation Characteristics of Geomaterials*. Ed. by V. R.e.a. E. IOS Press, pp. 600–607.
- Silva Illanes, M. F. (2014). "Experimental study of ageing and axial cyclic loading effect on shaft friction along driven piles in sands". Theses. Université de Grenoble.
- Tabucanon, J., Airey, D., and Poulos, H. (1995). "Pile Skin Friction in Sands from Constant Normal Stiffness Tests". In: *Geotechnical Testing Journal* 18.3, pp. 350–364.

- Tali, B. (2011). "Behaviour of the soil-structure interface under cyclic axial loading : application to the deep foundations computation". Theses. Université Paris-Est.
- Tatsuoka, F., Jardine, R., Lo Presti, D., Di Benedetto, H., and Kodaka, T. (1997). "Characterising the pre-failure deformation properties of geomaterials: theme lecture for plenary session no.1". In: *Proceedings of the 14th International Conference on Soil Mechanics and Geotechnical Engineering*. Vol. 4. Hamburg, pp. 2129–2164.
- Tehrani, F., Han, F., Salgado, R., Prezzi, M., Tovar, R., and Castro, A. (2016). "Effect of surface roughness on the shaft resistance of non-displacement piles embedded in sand". In: *Géotechnique* 66.5, pp. 386–400.
- Tolomeo, M., Richefeu, V., Combe, G., Roux, J., and Viggiani, G. (2017). "Assessing contact forces in granular materials from experimental measurements of kinematics". In: *EPJ Web Conf.* 140.02012.
- Tsuha, C., Foray, P., Jardine, R., Yang, Z., Silva, M., and Rimoy, S. (2012). "Behaviour of displacement piles in sand under cyclic axial loading". In: *Soils and Foundations* 52.3, pp. 393–410.
- Tudisco, E., Andò, E., Cailletaud, R., and Hall, S. A. (2017). "TomoWarp2: A local digital volume correlation code". In: *SoftwareX* 6, pp. 267–270.
- Uesugi, M., Kishida, H., and Tsubakihara, Y. (1988). "Behavior of sand particles in sand-steel friction". In: *Soils and Foundations* 28.1, pp. 107–118.
- Viggiani, G. and Hall, S. (2012). *Full-field measurements in experimental geomechanics: historical perspective, current trends and recent results*. eng. Ed. by G. Viggiani, S. Hall, and E. Romero. ALERT Doctoral School 2012: Advanced experimental techniques in geomechanics. ALERT Geomaterials, pp. 3–68.
- Viggiani, G., Andò, E., Takano, D., and Santamarina, J. (2015). "X-ray tomography: a valuable experimental tool for revealing processes in soils". In: *Geotechnical Testing Journal, ASTM* 38.1, pp. 61–71.
- Wang, J. and Zhao, B. (2014). "Discrete-continuum analysis of monotonic pile penetration in crushable sands". In: *Canadian Geotechnical Journal* 51.10, pp. 1095–1110.
- White, D. J. and Bolton, M. D. (2004). "Displacement and strain paths during plane-strain model pile installation in sand". In: *Géotechnique* 54.6, pp. 375–397.
- White, D. (2005). "A general framework for shaft resistance on displacement piles in sand". In: *First International Symposium on Frontiers in Offshore Geotechnics*. Ed. by Gourvenec and C. (Eds). Taylor & Francis, pp. 697–703.
- White, D. and Lehane, B. (2004). "Friction fatigue on displacement piles in sand". In: *Géotechnique* 54.10, pp. 645–668.
- Wiebicke, M., Andò, E., Viggiani, G., and Herle, I. (2015). "Towards the measurement of fabric in granular materials with x-ray tomography". In: *In Proceedings of the 6th International Symposium on Deformation Characteristics of Geomaterials*. Buenos Aires.
- Wiebicke, M., Andò, E., Herle, I., and Viggiani, G. (2017). "On the metrology of interparticle contacts in sand from x-ray tomography images". In: *Measurement Science and Technology* 28.12, p. 124007.
- Wils, L., Impe, W., Van Impe, P., and Haegeman, W. (2013). "Laboratory testing issues related to crushable sands". In: *In Proceedings of the 18th International Conference on Soil Mechanics and Geotechnical Engineering*. Paris.
- Yang, Z., Li, X., and Yang, J. (2008). "Quantifying and modelling fabric anisotropy of granular soils". In: *Géotechnique* 58.4, pp. 237–248.
- Yang, Z., Jardine, R., Zhu, B., Foray, P., and Tsuha, C. (2010). "Sand grain crushing and interface shearing during displacement pile installation in sand". In: *Géotechnique* 60.6, pp. 469–482.
- Youd, T. (1972). "Factors Controlling Maximum and Minimum Densities of Sands". In: *ASTM Special Technical Publication* 523, pp. 98–112.

- Zhang, C., Yang, Z. X., Nguyen, G. D., Jardine, R. J., and Einav, I. (2014). "Theoretical breakage mechanics and experimental assessment of stresses surrounding piles penetrating into dense silica sand". In: *Géotechnique Letters* 4.1, pp. 11–16.
- Zhao, J. (2008). *Multiscale Modeling of Granular Media*. URL: [http://jzhao.people.ust.hk/research\\_multiscale.html](http://jzhao.people.ust.hk/research_multiscale.html).
- Zhao J.D., G. N. (2015). "Bridging micro and macro in granular media: a computational multiscale paradigm". In: *Proceedings of the Second International Symposium on Geomechanics from Micro to Macro 2014*. Ed. by S. et al. (Eds.) Vol. 1. Cambridge: CRC Press, Taylor & Francis, pp. 747–752.
- Zhou, J., Jian, Q., Zhang, J., and Guo, J. (2012). "Coupled 3D discrete-continuum numerical modeling of pile penetration in sand". In: *Journal of Zhejiang University SCIENCE A* 13.1, pp. 44–55.